UNIVERSITY OF SOUTHAMPTON

FACULTY OF ENGINEERING, SCIENCE & MATHEMATICS

School of Physics & Astronomy

Spin Fluctuations in Manganese Intermetallics

by

Clare Jane Horn

Thesis for the degree of Doctor of Philosophy

July 2007

UNIVERSITY OF SOUTHAMPTON

ABSTRACT

FACULTY OF ENGINEERING, SCIENCE & MATHEMATICS

SCHOOL OF PHYSICS & ASTRONOMY

Doctor of Philosophy

SPIN FLUCTUATIONS IN MANGANESE INTERMETALLICS

By Clare Jane Horn

Magnetic ground states and dynarrnics in manganese systems have been investigated for two different types of structure, the binary β-$Mn_{1-x}M_x$ and ternary RMn_4Al_8 intermetallics where M represents cobalt or ruthenium and R is a rare earth element/yttrium/scandium.

For β-Mn alloys containing cobalt impurities, a static ground state of spin glass-like character has been stabilised for concentrations above 5% Co; there is an absence however of long range order in these systems, up to the highest measured concentration of 25at.% Co. The β-$Mn_{1-x}Ru_x$ alloys enter a spin glass-type state for all measured concentrations (above $x = 0.03$), in conjunction with a higher-temperature transition to a long range antiferromagnetically ordered state for $x = 0.12$, co-existent with the spin glass phase. These findings are evidenced by peaks in the muon spin relaxation rate, with a characteristic stretched exponential relaxation function observed below the spin glass transition temperature. Further support is provided by susceptibility and polarized neutron measurements. Clear magnetic Bragg peaks in neutron powder diffraction data, in addition to specific heat anomalies, confirm the presence of the long-range ordered state in the ruthenium alloys. Neutron lineshapes in a number of samples of both series may also imply Non-Fermi liquid scaling.

These results are of particular significance in view of the fact that cobalt and ruthenium solutes are shown to substitute onto Site I of the β-Mn crystal structure, as opposed to the more strongly magnetic Site II as for previously reported spin glass alloy systems, in which the impurity lifts magnetic frustration by removal of configurational degeneracy. Expansion appears to play a key role in β-$Mn_{1-x}Ru_x$, with the introduction of ruthenium appearing to drive the system to an intermediate state between the weak itinerant and localized moment regimes.

In the RMn_4Al_8 compounds, a range of interesting behaviour has been observed: this includes the first evidence of a magnetic phase transition in $LaMn_4Al_8$, in the form of a peak in the low temperature μSR data together with weak Bragg peaks in polarized neutron measurements; $PrMn_4Al_8$ has shown an oscillatory muon response, indicative of long range order in the Mn sublattice since inelastic neutron data shows Pr^{3+} to be in a singlet ground state. For systems with heavy rare earths (R = Er, Tb, Dy, Gd and Ho), interaction between the R and Mn sublattices has been implied by μSR measurements, in which separate relaxation contributions have been ascribed to each species.

For the RMn_4Al_8 with R = Y, Ce and Sc, a spin gap reported previously has been directly observed with inelastic neutron scattering. This is reflected in a two-featured response in $LaMn_4Al_8$, and may have its origins in a quasi-one dimensional Mn sublattice.

Contents

List of Tables

List of Figures

Acknowledgements

The author wished to gratefully acknowledge the assistance and support of the following individuals and organisations in the preparation of this thesis:

University of Southampton:

Denis Torkington, for practical assistance with laboratory equipment during sample making procedures;

ISIS Facility/ Rutherford Appleton Laboratory:

Adrian Hillier, for technical and analytical assistance concerning muon spin relaxation experiments, as well as data acquisition and handling;

Devashibhai Adroja, for practical assistance with inelastic neutron experiments, phonon simulation software and data acquisition/handling;

Rob Bewley, for technical assistance with inelastic neutron measurements;

Jon Taylor, for guidance concerning phonon simulation software;

Ron Smith and Winfried Kockelmann, for practical assistance with diffraction experiments, data acquisition, corrections and Rietveld refinement of neutron powder diffraction data;

Steve Hull, for technical advice with regard to powder diffraction experiments and data correction;

Pascal Manuel, for practical assistance concerning vibrating sample magnetometry and specific heat measurements;

Institut Laue Langevin:

Ross Stewart, for guidance and technical support in all aspects of polarized neutron measurements, as well as general experimental and analytical assistance in regard to studies of β-$Mn_{1-x}M_x$ systems;

University College London/University of Warwick:

Arthur Lovell (UCL) and Nicola Wilson (Warwick) for advice and valuable discussion concerning aspects of refinement software;

University of Oxford:

Peter Baker, for valuable discussion with regards to aspects of muon spin relaxation experiments;

Thanks are also expressed to those numerous individuals who have offered additional technical assistance during preparation for, and execution of experimental procedures at both ISIS and ILL.

The author acknowledges the financial support of the Engineering and Physical Sciences Research Council in providing sponsorship for this PhD.

Finally and most importantly, the author wishes to express sincere gratitude to Brian Rainford for providing a great deal of assistance in his capacity as a supervisor, and to Gary Horn for providing support, motivation and displaying superhuman patience in his capacity as a husband.

1. Introduction

Magnetic systems based on the 3d transition element manganese are known to exhibit a wide range of interesting, sometimes highly complex, behavioural properties. Nonmagnetic, long-range ordered and static disordered states are all represented, whereby the interactions may be of local atomic moment or itinerant electron origin, or lying somewhere between these limits. Numerous materials are found to undergo transitions between these states under certain conditions, as a result of subtle structural changes. This behaviour has been studied more extensively and productively since the development of spin fluctuation theory has made possible explanations of observed phenomena.

Starting with the simplest composition and considering only the pure element, the beta phase of manganese is the only recognized allotrope displaying paramagnetism at all temperatures, despite strong antiferromagnetic interaction. Through the study of β-Mn, aspects of crystal structure, interatomic spacing and their impact on the magnetic state continue to be explored. The physical properties of β-Mn may be described using the Self-Consistent Renormalization (SCR) theory of spin fluctuations, a model fully capable of accounting for the characteristics of metallic magnets, as well as successfully interpreting transitions from an itinerant to a localized-moment system. As one of the more well known examples of a geometrically frustrated magnet, the effects of substituting impurities – both magnetic and nonmagnetic - on both lattice spacing and ground state degeneracy has been extensively investigated.

These theoretical principles may be extended to manganese intermetallics: within the ternary RMn_4Al_8 series where R is a rare earth element, little historical evidence of long range magnetic order has emerged despite ordering transitions occurring in isostructural alloys e.g. RFe_4Al_8. This has led to significant research into the nature of the Mn sublattice, with SCR spin fluctuation theory once again invoked to account for experimental observations. This is especially recognized in the case of $LaMn_4Al_8$, whose identification as a nearly-antiferromagnetic metal prompted much of the work featured in this thesis. Despite an interatomic separation in the critical region for moment stability, strong antiferromagnetically correlated spin fluctuations persist in the Mn sublattice, which due to a quasi-one dimensional arrangement does not show long-range order in most of the compounds. Studies of the RMn_4Al_8 intermetallics provide an excellent means of probing the effects of lattice separation, with the Mn-Mn distance driven further from the critical value as R moves across the 4f series as a result of the lanthanide contraction. Additionally, spin fluctuation behaviour

and its significance for the magnetic ground state is brought into context in conjunction with low dimensionality effects, in this particular case as a possible mechanism inducing gaps in the spin excitation spectrum.

This thesis reports the results of experimental studies into the magnetic behaviour of two structurally very different systems, in which the magnetism arises from or is strongly influenced by the manganese component. As such the latter section is divided into two halves, with the first part comprising a complete study of β-Mn alloys containing cobalt and ruthenium impurities. Secondly, a chronological account of major findings concerning the RMn_4Al_8 intermetallics is presented, together with the second set of experimental data. A breakdown of the subsequent chapters is as follows:

In Chapter 2, theoretical aspects pertinent to these metallic magnetic systems are discussed, in which a number of common themes for both types of system are evident. This includes a summary of local moment and itinerant electron models of magnetism, and an introduction to the Self-Consistent Renormalization theory, together with its implications for observed experimental behaviour in spin fluctuation systems. Concepts of magnetic frustration and suppression of ordering in one (RMn_4Al_8) and three (β-$Mn_{1-x}M_x$) dimensions are also discussed. Other behavioural classifications of magnetic systems that come into play for these materials, such as heavy-fermion (HF) and non-Fermi liquid (NFL) characteristics are included where relevant, in terms of the various models given.

The majority of experimental work undertaken for this thesis has involved the complementary fields of muon spin relaxation and neutron scattering: it is beneficial, and sometime necessary, to utilize such methods in conjunction in order to gain an understanding of the microscopic nature of the magnetic ground state, in addition to the dynamical processes occurring in these systems. Chapters 3 – 5 are concerned with introducing basic fundamental principles associated with the experimental techniques. Chapter 3 covers the theory and practical aspects of muon spin relaxation measurements, with details of instrumentation and relaxation functions used in data analysis. In Chapter 4, a similar treatment is given to the extensive subject of neutron scattering. Basic scattering theory is outlined, along with a summary of the information that can be extracted from such measurements and its relevance to these studies. The remainder of the chapter is devoted to a detailed description of each of the areas of inelastic and diffraction measurements, including specific instrumentation used in this work. Neutron polarization analysis (NPA) is dealt with separately in Chapter 5. This covers theory specific to NPA and the separation of nuclear and magnetic information. A brief general introduction to instrumentation is followed by details of experiments and instrumentation utilized specifically for these studies.

Chapter 6 examines the various methods used in the subtraction of phonon scattering from inelastic neutron data. This procedure has formed a large part of the data preparation prior to analysis of the data presented in this thesis, and is essential in any study of magnetic dynamics. For those experiments for which polarized neutrons have been unavailable, subtractions have been carried out using a combination of Monte Carlo simulations and "phonon blank" samples, both of which are explained here.

In Chapter 7 the β-Mn alloys are introduced in terms of previous and current work, and the results of experimental studies of the β-$Mn_{1-x}M_x$ (x = Co, Ru) systems carried out for this thesis are presented and discussed. Data presented in this chapter include structural and magnetic characterization from neutron diffraction, magnetometry and specific heat, together with studies of spin dynamics performed using muon spin relaxation, neutron polarization analysis and inelastic neutron scattering.

A summary of prior research involving the RMn_4Al_8 compounds is given in Chapter 8, together with experimental studies concerned with determination of magnetic character of the Mn sublattice. The data encompass neutron diffraction, susceptibility, polarized neutron and μSR spectra. Secondly, this chapter focuses specifically on the spin gap excitations observed in a number of these systems, and presents inelastic neutron spectra recorded for this thesis, which forms an extension to this work.

Conclusions and suggestions for further work in this field are given in Chapter 9.

2. Theoretical Models of Metallic Magnets

2.1 Local Moment versus Itinerant Magnetism

In order to understand the nature of the magnetism in intermetallics systems, it is necessary to consider the contrasting theoretical models associated with the character of the unfilled electron orbitals. For example, the rare earth elements occurring in RMn_4Al_8 (generally as trivalent ions) have a partially filled 4*f* shell, lying inside the 5*p* shell and conduction bands. These orbitals are shielded from broadening and retain localized character. Alternatively the unfilled orbitals may take the form of a conduction band, as occurs in the transition elements such as manganese. The local moment and itinerant models developed to account for observed behavioural properties, and situations in which these break down, will be summarized in this chapter. The SCR theory, initially developed as a successor to the itinerant models and more recently extended to the limit of moment localization, will subsequently be introduced.

The Local Moment Model

A fixed magnetic moment resulting from unpaired electrons in localized orbitals is given by

$$\mu = \mu_B(\boldsymbol{L}+2\boldsymbol{S}) = \mu_B g_J \langle \boldsymbol{J} \rangle = \mu_B g_J \sqrt{\boldsymbol{J}(\boldsymbol{J}+1)}$$

where the Bohr magneton $\mu_B = \frac{e\hbar}{2m}$ and g_J is the Lande g-factor:

$$g = \frac{3}{2} + \frac{1}{2}\left[\frac{\boldsymbol{S}(\boldsymbol{S}+1) - \boldsymbol{L}(\boldsymbol{L}+1)}{\boldsymbol{J}(\boldsymbol{J}+1)}\right]$$

J is the total angular momentum ***J*** = ***L*** ± ***S***, associated with a (2*J* + 1) - degenerate energy eigenstate, and is well separated from other ***J***-states for a fixed atomic moment. In the rare earth

elements, the spin-orbit coupling is small compared to the 4*f* Coulomb interaction, and ***S***, ***L*** and ***J*** are good quantum numbers [1].

In an applied field the fixed moment will have energy

$$U = m_J g_J \mu_B B$$

The assumption of Boltzmann statistics allows the derivation of the Curie law of paramagnetic susceptibility for non-interacting moments, extended to the Curie-Weiss law to take into account exchange coupling between spins

$$\chi = \frac{\mu_0 \boldsymbol{M}}{\boldsymbol{B}} = \frac{C}{T - \theta_{CW}}$$

where the Weiss parameter is defined as

$$\theta_{CW} = \frac{\mathrm{J}C}{g_J^2 \mu_B^2}$$

The exchange parameter $\mathcal{J}$ contained within the familiar Heisenberg Hamiltonian

$$H = -\sum_{i,j \neq i} \mathcal{J}_{i,j} (\boldsymbol{S}_i \cdot \boldsymbol{S}_j)$$

may be generalized to represent antiferromagnetic and ferromagnetic coupling, hence reflecting a real space variation of exchange interactions. This takes a wavevector-dependent form:

$$\mathcal{J}(\boldsymbol{q}) = \sum_{q} \mathcal{J}_{i,j} e^{i\boldsymbol{q} \cdot (\boldsymbol{R}_i - \boldsymbol{R}_j)}$$

with modulation wavevector ***q***. The wavevector-dependent susceptibility may be defined therefore as

$$\chi(\boldsymbol{q}) = \frac{C}{T - \dfrac{\mathcal{J}(\boldsymbol{q}) C}{g_J^{\,2} \mu_B^{\,2}}}$$

with the Curie temperature T_C, or Neel temperature T_N given by the divergence of the susceptibility

$$T_{C,N} = \frac{\mathcal{J}(q)C}{g_J{}^2 \mu_B{}^2}$$

Direct Heisenberg exchange is uncommon in local moment systems; in the rare earth elements, where negligible overlap of the 4*f* electron wavefunctions precludes direct Coulomb interaction, exchange is mediated via polarization of the conduction electrons - the *Ruderman-Kittel-Kasuya-Yosida* (RKKY) interaction. For the simplified case of a free electron gas with a spherical Fermi surface of radius k_F[1], the exchange parameter is obtained by [2]

$$\mathcal{J}_{i,j} \propto \frac{1}{\boldsymbol{R}_{ij}^3}\left[\cos\left(2\boldsymbol{k}_F\boldsymbol{R}_{ij}\right) - \frac{\sin\left(2\boldsymbol{k}_F\boldsymbol{R}_{ij}\right)}{2\boldsymbol{k}_F\boldsymbol{R}_{ij}}\right]$$

This gives rise to an oscillatory, long-range modulation producing a wide variety of possible magnetic structures, including long range ordered states.

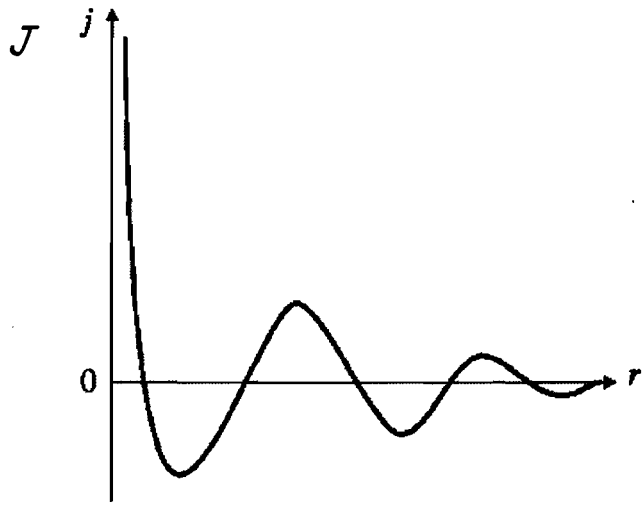

Figure 2.1: The oscillatory RKKY interaction (simplified case)

The theoretical model of local moment magnetism is generally successful in derivations of ferromagnetism, antiferromagnetism and other forms of modulated structure. The discussion here has been restricted to models that rely on the *mean-field* concept (the effective exchange field

[1] In real systems, allowance must be made for anisotropic exchange and realistic Fermi surfaces

required for the Curie-Weiss law); this carries associated problems in attempting to account for critical behaviour, giving rise to values for measurable properties that do not accord with experiment. The correlation length of order parameter fluctuations tends to infinity in the vicinity of a critical point, and removes the condition of uniformity across a system [3]. This results in an inaccurate power law prediction for the critical magnetic susceptibility.

Crystal Field Effects

The magnetic electrons of an ion in a real solid are subject to a charge distribution arising from the surrounding crystalline environment. The resulting perturbations constitute the *crystal field potential*, which reflects the point symmetry of the lattice [4]. The effects of crystal fields vary depending on the nature of the magnetic orbitals, as a result of the variation in angular distributions, as well as due to the symmetry of the environment. The five *d*-orbitals are divided into two groups, the e_g and t_{2g} orbitals, according to the orientation of the lobes. In an octahedral environment aligned with the axes, the t_{2g} orbitals experience a smaller degree of overlap and are lowered in energy, while the energy of the e_g orbitals is raised. This situation is reversed in a tetrahedral environment [3].

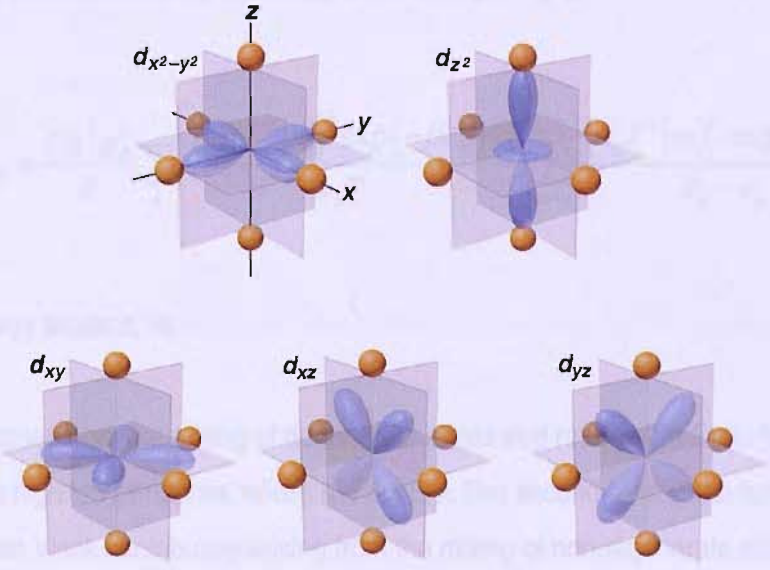

Figure 2.2: The e_g (top) and t_{2g} (bottom) groupings of d-orbitals [5]

As a result, for the case of 3d insulators, orbital filling by electrons is complicated by competition between double-occupation Coulomb and crystal field energies. The relative strengths of these may be assessed via comparison of experimentally determined effective moments, and predicted values. It is found however that in transition metals, where the crystal field is large compared to the spin-orbit coupling, these predictions can break down as a result of the 3*d* orbital moments becoming quenched. In the rare earths, screening of the 4*f* shell means that the crystal field may be treated as a perturbation on the Hund's rule ground state, and lifts the $(2J + 1)$ degeneracy.

According to Kramer's Law, an ion with an odd number of electrons must have a ground state that is at least doubly degenerate, irrespective of the symmetry of the crystal field [1]. In rare earth ions, splitting of the ground state multiplet is typically in the range 1- 100meV, and may be determined directly from inelastic neutron scattering experiments.

Wavefunctions for an ion in a crystal field are obtained by a mixing of the $\boldsymbol{m_J}$ states and the magnetic moment of the new ground state is given by [6]:

$$\langle \mu_\alpha \rangle = g \mu_B \langle \psi_0 | \boldsymbol{J}^\alpha | \psi_0 \rangle$$

where ψ_0 is the ground state wavefunction and α represents Cartesian directions *x*, *y* and *z*.

The static magnetic susceptibility becomes, in the limit of $\boldsymbol{H} \rightarrow 0$:

$$\chi^\alpha_{H\to 0} = \frac{Ng^2\mu_B^2}{Z} \sum_n \left[\frac{\left|\langle n|\boldsymbol{J}^\alpha|n\rangle\right|^2 \exp\left(-\beta\varepsilon_n^0\right)}{k_B T} - 2\sum_{m\neq n} \frac{\left|\langle n|\boldsymbol{J}^\alpha|m\rangle\right|^2 \exp\left(-\beta\varepsilon_n^0\right)}{\varepsilon_n - \varepsilon_m} \right]$$

for excited energy levels *n*, *m*.

The first term arises from the mixing of degenerate states and returns the Curie form of the susceptibility at high temperatures, where $k_B T >> E_{CF}$. The second term is the temperature-independent Van Vleck contribution arising from the mixing of nondegenerate states.

Crystal field effects will also be reflected in the thermodynamic properties of a material, such as the maximum or *Schottky anomaly* produced in the specific heat capacity of a material due to the changing population of excited crystal field states with temperature. The entropy of a system may be

calculated by integration of the heat capacity, and this is related to the degeneracy of the populated levels by [7]

$$S = k_B \ln(2\boldsymbol{J}+1)$$

The Kondo Effect/Heavy Fermion Scaling

Measurable thermodynamic properties of a rare earth system are also influenced by the nature of the *s-f* coupling responsible for RKKY exchange. A shallow minimum occurs in the low temperature resistivity of some alloys, due to conduction electrons scattering from localized spins [8]. Strong coupling may result in formation of spin singlets leading to a decrease in the local magnetic moment with decreasing temperature, and a low temperature peak in the specific heat.

The **Anderson Model** [9] provides a simple description of these phenomena, collectively referred to as the *Kondo effect*, by considering a single magnetic impurity in a metallic host. The density of 4f states features a sharp peak near the Fermi energy known as the Kondo resonance, which arises dynamically from the hybridization of the 4f level with the host conduction band. The displacement of this resonance from E_F defines a Kondo temperature T_K, which sets a hybridization energy scale typically of the order of 1 - 100meV.

$$k_B T_K = \frac{1-n_{fs}}{n_{fs}} N_f N(0) \left|V_{fk}\right|^2$$

In this expression, $N(0)$ is the single spin Fermi density of states, N_f is the $4f$ degeneracy, n_{fs} is a $4f$ electron number operator and V_{fk} parameterizes the hybridization strength.
T_K becomes large in strong hybridization limit, which may lead to $4f$ delocalization and intermediate valence behaviour. In the weak hybridization limit, the favourable regime for the existence of a localized impurity moment, T_K tends to zero and the $4f$ level occupancy approaches unity.

The idea may be extended to more complicated arrangements, including the "Kondo Necklace" spin chain for which weak antiferromagnetic moments may exist in an ordered state between limits of strong and weak coupling. In a three dimensional Kondo lattice the magnetic properties are

governed by competition between *f-s* hybridization and the RKKY interaction, which may be related in terms of the RKKY energy scaling by:

$$T_{RKKY} \propto \left(\rho J_{sf}\right)^2$$

where ρ represents the density of conduction states [10]. There is a crossover from a magnetically ordered ground state to a spin compensated ground state at a critical value of the parameter ρJ_{sf} [11]. In the magnetic phase, moments may still be reduced by the Kondo effect [12].

The frequency dependent (dynamical) susceptibility for the Kondo lattice is given by [13]:

$$\chi(\boldsymbol{q},\omega) = \frac{\Gamma(\boldsymbol{q})\chi(\boldsymbol{q})}{\Gamma(\boldsymbol{q}) - i\omega}$$

where $\Gamma(\boldsymbol{q})$ is the wavevector dependent Lorentzian linewidth.

The imaginary part of the dynamical susceptibility is used to define the following expression:

$$\frac{1}{\omega}\chi''(\boldsymbol{q},\omega) = \frac{\chi(\boldsymbol{q})\Gamma(\boldsymbol{q})}{\Gamma(\boldsymbol{q})^2 + \omega^2}$$

These relations can be experimentally tested with inelastic neutron scattering. In particular the linewidth $\Gamma(J \rightarrow 0)$ is a measure of the Kondo temperature.

For such lattices, anomalous magnetic phenomena may arise from Kondo – RKKY competition, which are of the same order of magnitude due to the proximity of the 4*f* and Fermi energies. The class of *f-s* coupled compounds encompasses those systems known as *heavy fermions*, so named because of their particularly large electronic specific heat coefficients [14]. Hybridization strengths in these compounds ranges from a few tenths of a Kelvin to a few tens of K.

The magnetic susceptibility of heavy fermions flattens at low temperatures from a Curie-Weiss form at high temperatures, becoming temperature independent as $T \rightarrow 0$ and suggesting Kondo quenching of local moments [15]. The magnitude of the low temperature susceptibility is enhanced compared to normal metals. Well below the Kondo temperature, the resistivity shows a linear or quadratic temperature dependence, associated with entrance into a coherent regime in which the heavy fermion quasiparticles become long-lived Bloch states.

Itinerant Electron Models

In the **Nearly-Free Electron Model** itinerant conduction electrons occupy states characterized by wavevector ***k***, according to the Pauli Exclusion Principle and obeying Fermi-Dirac statistics. The spin degeneracy of these states is lifted on application of a magnetic field ***B***, splitting the density of states into parallel and antiparallel spin bands. The potential energies of these bands may be equalized at the Fermi energy as a result of a number of higher energy electrons ΔN changing spin state, giving rise to a magnetization per unit volume in the direction of ***B*** and defining the temperature-independent *Pauli susceptibility*:

$$\chi = \frac{\mu_0 M}{B} = \frac{\mu_0 \Delta N \mu_B}{B} = \mu_0 \mu_B^2 D(E_F)$$

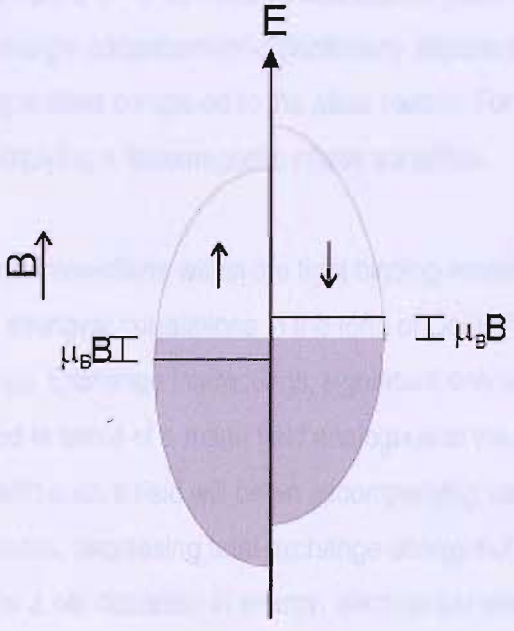

Figure 2.3: density of states representation for the appearance of Pauli paramagnetism in itinerant electron systems [16]

Implementation of the **Fermi Liquid Model** [17] accounts for electron-electron scattering processes, in addition to modifications of one-electron (Hartree-Fock) energies as a result of interactions. The Pauli Exclusion Principle allows only scattering into unoccupied states, and so at temperature T only electrons within $k_B T$ of the Fermi energy are available.

In the interacting Fermi liquid system, the perturbed wavefunction is assigned to quasiparticles rather than the original electrons, utilising the principle of adiabatic continuity. These quasiparticles are then considered to be only weakly interacting, for ***k***-states close to the Fermi surface. Certain intrinsic properties such as spin and charge are shared with the free electrons, while for others interactions are absorbed, reflecting a backflow in the Fermi sea caused by the moving quasiparticles; these include the effective mass m^* and F^a_0 (related to the sum of interdependent quasiparticle energies) - the so-called Landau parameters [18].

Creation of quasiparticles above the Fermi energy has an associated energy that will affect the number of occupied states in the presence of an applied field. The paramagnetic susceptibility is therefore adjusted according to [4]

$$\chi = \frac{1+\frac{1}{3}A_1}{1+B_0}\chi_{Pauli}$$

with parameter A_1 dependent on effective mass m*, and B_0 related to the quasiparticle spatial distribution function. B_0 falls from 0 to –1 as electron interactions become stronger, leading to a large susceptibility. This *exchange enhancement* is particularly apparent in transition metals (e.g. Pd), which have large susceptibilities compared to the alkali metals. For $B_0 = -1$, there is a divergence of susceptibility implying a ferromagnetic phase transition.

Treatment of electron-electron interactions within the tight binding model is the focus of the **Stoner Model** [19], in which only the strongest correlations in the form of Coulomb repulsions between opposing spins are considered. Exchange interactions, significant only for itinerant *d*-electrons on the same ionic site, are described in terms of a mean field analogous to the Weiss molecular field for local moments. Associated with such a field will be an accompanying transfer of electrons from antiparallel to parallel spin states, decreasing total exchange energy but increasing kinetic energy of each transferred electron. For a net decrease in energy, electron transfer between spin bands occurs spontaneously. This is represented by the *Stoner Criterion*:

$$ID(E_F) > 1$$

where *I*, the Stoner parameter, is a measure of the mean exchange energy per electron. The occurrence of ferromagnetism in itinerant systems is closely related to the band structure in the vicinity of the Fermi energy, with the Stoner Criterion likely to be satisfied for a narrow, peaked density of states at the Fermi level, a characteristic feature of the *d*-electron transition metals.

In the case that the Stoner criterion is not satisfied, the molecular exchange field still affects the relative energy splitting of the spin bands in the presence of a magnetic field and adjusts the paramagnetic susceptibility [20]

$$\chi = \frac{\chi_{Pauli}}{1 - ID(E_F)}$$

This is of the same form as the Fermi liquid prediction of exchange-enhanced susceptibility.

As in the local moment case, the shape of the Fermi surface has an important effect on the exchange interactions, and may cause a $\boldsymbol{q}$-dependence and spatially varying mean field. Within the Random Phase Approximation[2] an expression for wavevector-dependence may be derived:

$$\chi(\boldsymbol{q}) = \frac{\chi_0(\boldsymbol{q})}{1 - \frac{2I\chi_0(\boldsymbol{q})}{Ng_s^2\mu_B^2}} = \frac{\chi_0(\boldsymbol{q})}{1 - \alpha\chi_0(\boldsymbol{q})}$$

where $\chi_0(q)$ is the non-interacting susceptibility given, for the case of a spherical Fermi surface, by the Lindhard function [4]:

$$\chi(\boldsymbol{q}) = \frac{12\mu_0\mu_B^2 N}{16E_F}\left[1 + \frac{4\boldsymbol{k}_F^2 - \boldsymbol{q}^2}{4\boldsymbol{k}_F}\ln\left|\frac{2\boldsymbol{k}_F + \boldsymbol{q}}{2\boldsymbol{k}_F - \boldsymbol{q}}\right|\right]$$

In the case of antiferromagnetic exchange, as may be expected for a manganese system, $\chi(\boldsymbol{q})$ diverges at $\boldsymbol{q} = \boldsymbol{G}/2$ where $\boldsymbol{G}$ is a reciprocal lattice vector. The effective exchange field is defined in terms of a staggered magnetization $M_s = M_a - M_b$, for sublattice magnetizations $\boldsymbol{M_a}$ and $\boldsymbol{M_b}$. The staggered susceptibility associated with this may be defined as

$$\chi_S = \chi(\boldsymbol{q} = \boldsymbol{G}/2)$$

Within the Stoner model, excitations of *d*-band electrons across the Fermi surface (Stoner excitations) may occur, creating an electron-hole pair or "quasiparticle". This in turn leads to a fluctuation of spin density, affecting the equilibrium state. A more general itinerant electron theory was developed along these lines [21], whereby the dynamical susceptibility may be defined and takes

[2] The assumption of independent Fourier components of the exchange interaction

the form of the wavevector-dependent susceptibility above, replacing $\chi_0(q)$ by $\chi_0(q,\omega)$, the non-interacting frequency-dependent susceptibility.

The dynamical susceptibility can be expressed (within RPA) in terms of the frequency distribution of spin fluctuations $\Gamma(q)$ as

$$\chi(q,\omega) = \frac{\chi(q)}{1-\frac{i\omega}{\Gamma(q)}}$$

Taking the imaginary part of the dynamical susceptibility gives

$$\frac{1}{\omega}\chi''(q,\omega) = \frac{\chi(q)\Gamma(q)}{\Gamma(q)^2+\omega^2}$$

a Lorentzian function of $\Gamma(q)$ and linewidth $\chi(q)$ centred at zero frequency. As for the Kondo lattice dynamical susceptibility expression of the same form, this can be directly measured via inelastic neutron scattering experiments.

2.2. Self-Consistent Renormalization Theory

While the Stoner model of itinerant electron magnetism is consistent with many observations in real systems - such as moments which are non-integer multiples of μ_B - it fails to predict high temperature behaviour such as the Curie-Weiss susceptibility seen above T_C in many transition metals, and gives inaccurate predictions for the Curie temperature itself. Extending the theory to incorporate the effect of spin fluctuations is similarly unsuccessful, largely due to the failures of the Random Phase Approximation at high temperatures. The RPA description of spin fluctuations involves excited electron quasiparticle states which move independently, with only bound electron-hole states undergoing exchange interactions. Interactions between unbound electrons and holes constituting dissipative excitations are neglected, and hence exchange enhancement at high temperatures is not considered.

The Self-Consistent Renormalization (SCR) theory [22] redresses many of the problems encountered by previous models, invoking the key principle of a coupling mechanism between spin fluctuation modes. This manifests itself as a spin-correlation potential term in the Hamiltonian, and represents a renormalization of the equilibrium state. SCR theory seeks to determine a suitable form for this spin-correlation term, whereby the static susceptibility may be calculated from the Hamiltonian and this in turn from the dynamical susceptibility, in a self-consistent fashion. It has been demonstrated [23] that a self-consistent solution for the renormalized energy can only be obtained for a dynamical susceptibility of the form

$$\chi(\boldsymbol{q},\omega) = \frac{\chi_0(\boldsymbol{q},\omega)}{1-\alpha\chi_0(\boldsymbol{q},\omega)+\lambda(\boldsymbol{q},\omega)}$$

The term $\lambda(\boldsymbol{q},\omega)$ in the denominator is known as the *renormalization term*, and is dependent on the nature of the spin correlations.

By considering intermode coupling, the renormalization term may be expressed in terms of the thermal averages of longitudinal spin density amplitude fluctuations, and transverse spin density orientational fluctuations [22]. Where the spin fluctuations are ferromagnetically correlated, the renormalization term is given by

$$\frac{\lambda(\boldsymbol{q},\omega)}{\chi_0(\boldsymbol{q},\omega)} = \frac{5}{3}F_l S_L^2(\boldsymbol{q},\omega)$$

where $\chi_0(\boldsymbol{q},\omega)$ is the non-interacting susceptibility, F_l is the mode-mode coupling constant and $S_L(\boldsymbol{q},\omega)$ is the thermal average of local longitudinal and transverse spin density fluctuations. The local susceptibility (the sum over all $\boldsymbol{q}$ of $\chi(\boldsymbol{q})$) may be extracted from $\left\langle S_L^2 \right\rangle$, and this may be shown to take a Curie Law form. Substituting the ferromagnetic expression for the renormalization term given above into the SCR dynamical susceptibility returns a Curie-Weiss type function for the $\boldsymbol{q} = 0$ component, $\chi(0)$, provided S_L^2 increases linearly with T.

For antiferromagnetic correlations, a renormalization term $\lambda(\boldsymbol{Q})$ is defined where

$$\frac{\lambda(Q)}{\chi_0(Q)} = F_s\left(\frac{5}{3}S_L^2 + M_S^2(0)\right)$$

where F_S is the intermode coupling for Fourier components of the spin density around the antiferromagnetic wavevector $\boldsymbol{Q}$, and $M_S(0)$ is the staggered magnetization per atom at 0K. The magnetic susceptibility at $\boldsymbol{q} = \boldsymbol{Q}$ can then also be shown [24] to take a Curie-Weiss form, with the reciprocal susceptibility having a negative intercept for both antiferromagnetic metals, and those with antiferromagnetic correlations in the paramagnetic phase, known as *nearly-antiferromagnetic metals*.

It is possible, using SCR theory, to predict the nature of physical properties of itinerant electron systems. For the case of weakly antiferromagnetic metals, the electronic coefficient of specific heat (Sommerfeld constant) has a predicted form [25]

$$\gamma = \gamma_0 - \nu T_N^{4/3}$$

where ν is a constant. Specific heat measurements on a number of alloyed β-Mn systems [26] have confirmed this relation; this is discussed in more detail in Chapter 7.

In nuclear spin relaxation techniques, the SCR form of the nuclear spin relaxation rate $1/T_1$ above T_N is found to follow [27]:

$$\frac{1}{T_1} \propto \frac{T}{(T - T_N)^{1/2}}$$

where a Curie-Weiss type staggered susceptibility is assumed. This has been supported in studies of pure β-Mn and β-$Mn_{1-x}Al_x$ alloy systems by nuclear magnetic resonance [28, 29, 30], discussed fully in Chapter 7. The intermetallic system $LaMn_4Al_8$ has more recently been identified as a nearly-antiferromagnetic metal on the basis of NMR data showing this relation [31], reported in Chapter 8. Below T_N the relaxation follows

$$\frac{1}{T_1} \propto \frac{T}{M(T)}$$

while for $T >> T_N$:

$$\frac{1}{T_1} \propto \sqrt{T}$$

The key principle of SCR theory, that the physical properties of itinerant electron systems depend purely on the nature of spin density fluctuations in those systems, may also be extended to the local moment limit and successfully interpolates between the two extreme cases [32]. The spin density fluctuation amplitude $\langle S_L^2 \rangle$ in a local moment system is fixed, being consistent with moments localized in real space. In contrast, $\langle S_L^2 \rangle$ is temperature-dependent and tends be of smaller magnitude in itinerant systems, with fluctuations that are extended and hence localized only in reciprocal space. Magnetic materials may be thus classified, based on the amplitude and spatial extent of spin fluctuations [22].

In Section 2.1, the conditions for the appearance of local moments in a local moment/metallic host system were discussed. If the presence of exchange between two localized bound states is considered, the condition for the appearance of localized, antiferromagnetically-coupled moments is [33]

$$\frac{(U+4J)}{\Delta} > \pi\left[\frac{(V/\Delta)}{\tan^{-1}(V/\Delta)}\right]$$

Where U represents Coulomb repulsion between opposite spins in the localized orbital, $\boldsymbol{J}$ is the exchange energy, V is a *s-d* mixing or "hopping" term, and Δ is the bound state bandwidth. Large values of U and $\boldsymbol{J}$, together with small V and Δ terms, constitute favourable conditions for the appearance of localized moments.

The importance of interatomic distance in local moment formation is notably demonstrated in the Laves phase compounds RMn_2, for which the 3d bandwidth may be controlled by the substitution of various R species, where R = rare earth or yttrium. The magnetic properties of these systems are strongly dependent on lattice parameter [34, 35, 36], with stable Mn moments appearing for a lattice parameter in excess of ~ 7.52Å. In YMn_2, a large discontinuous increase of around 5% in the unit cell volume occurs on cooling to 92.5K, corresponding to a first order structural phase transition to a tetragonal, antiferromagnetically ordered state with helical modulation [37, 38]. Above T_N, YMn_2 displays an enhanced thermal expansion coefficient together with a slow increase in magnetic susceptibility, attributed to antiferromagnetic spin fluctuations that increase in amplitude up to at least $6T_N$ [39]. μSR experiments have highlighted a critical slowing of longitudinal spin fluctuations

approaching T_N, found to be due to an underlying second order phase transition corresponding to a crossover from itinerant to local moment regimes [38].

The Neel temperature may be suppressed as a result of applied hydrostatic or chemical pressure, with the latter achieved by substitution of elements causing volume shrinkage of the lattice [39, 40]. Conversely, substituting Al atoms onto the Mn sites suppresses the volume change at T_N [39, 41], with the transition becoming second order for Al concentrations above 3% [43]. These results reflect a transition of the system from itinerant to local moment character with increasing impurity concentration. Above 10at.% Al, the susceptibility becomes Curie-Weiss like [44], and the Mn moment (= 2.7μ_B) becomes independent of temperature.

A single susceptibility equation may be formulated in the unified SCR theory [22], which is consistent with both local moment and itinerant models. For ferromagnetic exchange this is expressed as:

$$\frac{1}{\chi(0)} = \frac{4k_B I^2}{T_0 N \mu_B} \sum_q \left(\frac{T}{1/\chi(0) + 2V(0) - 2V(\boldsymbol{q})} - \frac{T_c}{2V(0) - 2V(\boldsymbol{q})} \right)$$

the parameter $V(\boldsymbol{q}) = I / S_L^2(\boldsymbol{q})$, and T_0 represents a quantity termed the *longitudinal stiffness constant*, quantifying the resistance of the system to a change in spin fluctuation amplitude. Where $T_0 \rightarrow 0$, the longitudinal stiffness is increased to the extent that the system enters a local moment regime and the susceptibility is given by

$$\chi_0 = \frac{N\mu_B^2 S_L^2}{3k_B(T - T_C)}$$

Small values of T_0 result in an S_L^2 that increases rapidly in temperature, up to a saturation point corresponding to the formation of a temperature induced local moment – this is expected for magnetic metals in the intermediate regime, and has significance for some compounds of the RMn_4Al_8 series. The concept of temperature induced local moments in relation to spin gap-like experimental features is discussed in the following subsection.

For the limit of large T_0, the susceptibility becomes:

$$\frac{1}{\chi_0} = \frac{4nI^2\mu_B S_L^2(T)(T - T_C)}{3k_B T_0 T_C}$$

with the Curie-Weiss dependence arising from the linear increase in S_L^2 with temperature. The predictions of SCR theory in terms of spin fluctuation amplitudes for various regimes are summarized in Figure 2.4.

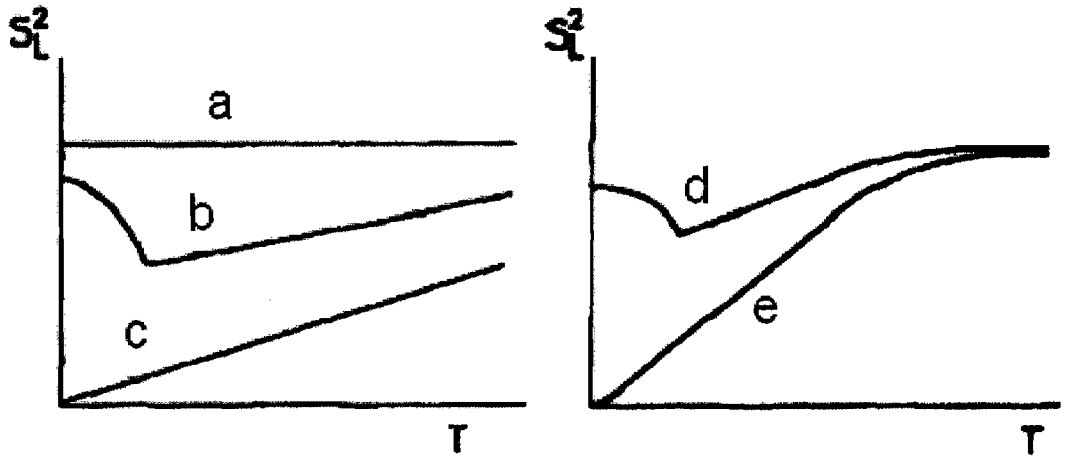

Figure 2.4: temperature dependence of spin fluctuation amplitudes as predicted by SCR theory: a) local moment system; b) weakly-ferromagnetic system, showing a collapse in $\langle S_L^2 \rangle$ at TC; c) nearly-antiferromagnetic metal; d) antiferromagnetic metal with temperature-induced local moments; e) nearly-antiferromagnetic system with temperature-induced local moments

2.3. Geometrical Frustration and Reduced Dimensionality

The presence of large effective moments and/or strong exchange coupling may lead to long-range magnetic ordering in both local moment and itinerant systems; however this is not guaranteed as the presence of some other feature may prevent of a static alignment of spins within a material. Such mechanisms include competing interactions, low dimensionality of the magnetic sublattice, or geometrical arrangements inherent to the crystallography. In Section 2.1 the concept of competition between the long range, oscillatory RKKY interaction and the Kondo effect was introduced. While this may be expected to play a part in influencing the magnetic behaviour of local moment metals, in alloys of manganese ordering is more likely to be suppressed by frustration or dimensionality effects. The geometrical arrangement of β-Mn systems constitutes a well-established example of a 3-D frustrated system. In the case of the RMn_4Al_8 series, in which the interactions of the manganese rather than the rare-earth sublattice appear dominant, the pseudo-one dimensional arrangement of the Mn sublattice is found to strongly influence magnetic ordering.

3-Dimensional Frustration and Spin Glass Order

Where it is possible to minimize simultaneously the energy associated with all spin interactions, a single well-defined ground state will result. For the case of antiferromagnetic interactions in a triangular lattice, this is not possible: the minimum-energy antiparallel alignment can only exist for two of any three nearest-neighbour spins.

Two well-known examples in which this type of frustrated arrangement is found are the two-dimensional Kagome planes and the three-dimensional pyrochlores [45]. The former class of compounds feature magnetic spins located on a lattice of corner-sharing triangles of the type shown in Figure 2.4, whereas the latter consist of a network of comer-sharing tetrahedra.

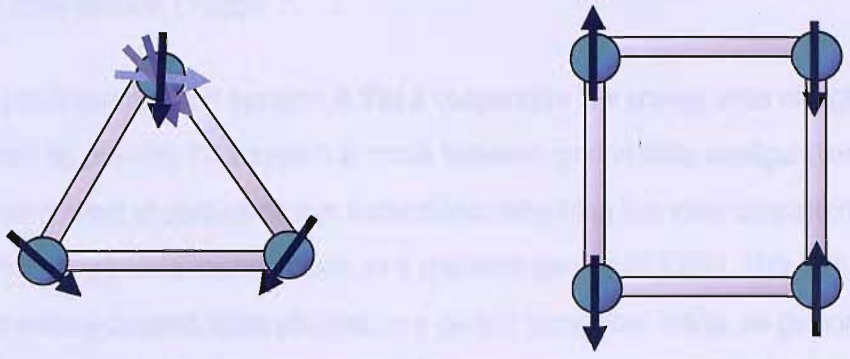

Figure 2.5: frustrated antiferromagnetically-coupled spins on a triangular lattice; in contrast a square lattice allows the exchange energy to be simultaneously minimized for all spins

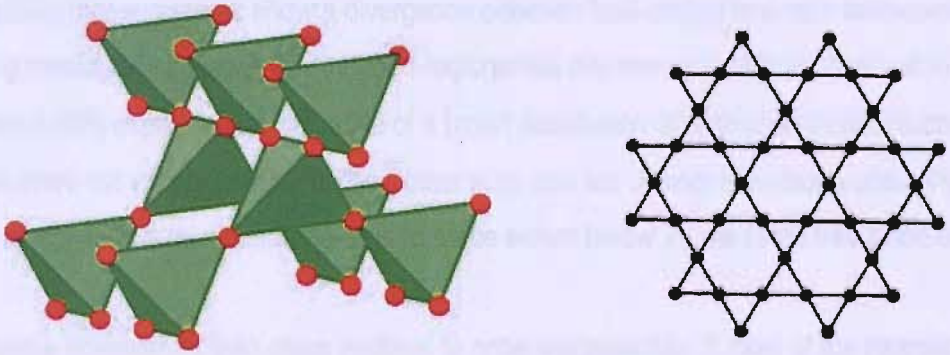

Figure 2.6: the geometrically frustrated pyrochlore (left) [46] and Kagome [47] arrangements

The concept of geometrical frustration in systems with antiferromagnetic interactions was initially employed in the description of magnetic behaviour in insulators, such as the Kagome, pyrochlore and spinel compounds. The idea was extended to metallic antiferromagnets more recently, despite the general association with long-range magnetic interactions in such materials. A well-documented example studied experimentally [48] and theoretically [49, 50, 51] is that of the Laves phase RMn_2 systems. The C15 cubic, heavy fermion-like compound $Y(Sc)Mn_2$ has a disordered ground state in which itinerant Mn moments form on a sublattice of the pyrochlore type. The β-Mn crystallography

investigated in the current study has features in common with both Kagome and pyrochlore structures, with magnetic manganese sites on a triangular lattice forming a tetrahedral 3-D structure together with nonmagnetic sites. The characteristic "distorted windmill" crystal structure of β-Mn is presented in more detail in Chapter 7.

The general prediction for such systems is that a cooperative low energy state of high degeneracy will form. It may be possible for a system to move between ground state configurations down to zero temperature as a result of zero-point spin fluctuations, remaining in a state characterized by dynamical short-range correlations, known as a *quantum spin liquid* (QSL). This is the case for antiferromagnetically coupled spins situated on a perfect pyrochlore lattice, as demonstrated by numerical simulations [45]. A dilute arrangement of randomized spins may alternatively undergo a transition at a characteristic temperature T_G, at which the spins "freeze" into a static but disordered configuration, forming a metastable state known as a *spin glass*. As the temperature is lowered, thermal fluctuations slow down, allowing the spins to form locally correlated clusters that increase progressively as the freezing transition is approached and the range of the fluctuations extends.

There are a number of experimental signatures by which spin glasses may be identified: magnetic susceptibility measurements show a divergence between field-cooled and zero field-cooled data reflecting metastability. A root- or stretched-exponential asymmetry profile is observed in muon spin relaxation (μSR) experiments, indicative of a broad distribution of relaxation times. Fluctuations within clusters will vary according to the cluster size, and are distinct from those occurring in regions outside clusters. This distribution persists to some extent below T_G, as some free spins can persist.

It is possible however for spin glass systems to order magnetically. If most of the nearest neighbours of a magnetic spin within a cluster are also magnetic, ordering can develop within a cluster that will influence the whole sample to a greater extent as the sample cools and the clusters increase in size. These systems display spin glass behaviour to a degree but have incipient long range order. In the percolation (very high concentration) limit, interactions between nearest-neighbour ions throughout the sample can produce long range order [52].

The addition of an impurity species may cause a quantum spin liquid to enter a spin glass state at finite temperature. The substitution of nonmagnetic aluminium atoms into a corner-sharing tetrahedral sublattice leads to the formation of local Mn moments, and a static ground state in $Y(Sc)(Mn_{1-x}Al_x)_2$ [53, 54, 55]. β-Mn shares a number of physical properties with this system, and similar conclusions have been drawn concerning the analogous β-$Mn_{1-x}Al_x$ series [56, 57], with the introduction

of Al responsible for partial lifting of the spin configurational degeneracy in the magnetic sublattice (in addition to expansion effects). Details of these studies will be reported later in this thesis.

Quasi-one Dimensional Magnetism and Spin Gap Formation

The Ising model of one-dimensional spins simplifies the Heisenberg Hamiltonian to a scenario in which each spin consists only of a *z*-component. For a one-dimensional lattice only nearest-neighbour interactions are considered and the exchange Hamiltonian for ferromagnetic spins becomes

$$H = -2\boldsymbol{J}\sum_{i=1}^{N} S_i^z S_{i+1}^z$$

for a chain of N + 1 spins.

A spin flip constituting a chain defect is therefore associated with an energy cost of $\boldsymbol{J}$, but will also bring about an entropy gain of $S = k_B \ln N$, as the defect can occur in any one of N locations. For real spin chains, where effectively $N \rightarrow \infty$, the entropy increase is such that the free energy $F = E - TS$ remains near - ∞. The energy cost per defect remains at $\boldsymbol{J}$, so for any finite temperature defects form spontaneously. Long-range order is therefore not expected in one dimension, for which the critical temperature may be given as zero [57]. The problem has also been solved in two dimensions [58], for which the defect energy cost and entropy gain both scale with defect perimeter. The system can hence achieve a minimum free energy state via either the presence or absence of a spin flip.

Spin chains may be of Ising, XY (2-D) or Heisenberg (3-D) type depending on the anisotropy of the particular system. Anisotropy effects may also lead to an additional energy cost for rotating spins for all but the smallest-radius excitations, a mechanism which allows magnetic order to develop in two-dimensional lattices [57].

The excitations in a 3-d Heisenberg magnet are massless Goldstone modes (namely the spin waves), of integer spin and hence bosons. In an Ising spin chain, flipping one spin creates a pair of walls at finite energy cost, leading to a gapped dispersion relation. In the case of antiferromagnetic chains of $S = ½$ spins, the excitations are known as spinons, and are of a fermionic nature.

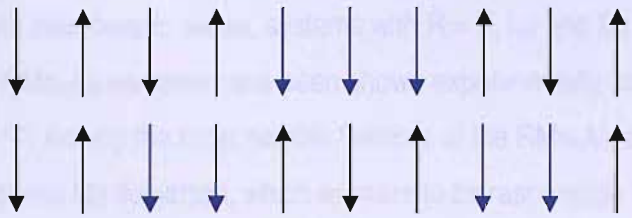

Figure 2.7: creation and propagation of a spinon excitation

Magnon and spinon excitations may be probed experimentally with the technique of inelastic neutron scattering. A neutron can create or annihilate a single magnon, whereas in a one-dimensional system a scattering interaction will set up the propagation of a spinon pair. The resulting spinon excitation spectrum is a continuum, reflected in the measured inelastic cross-section.

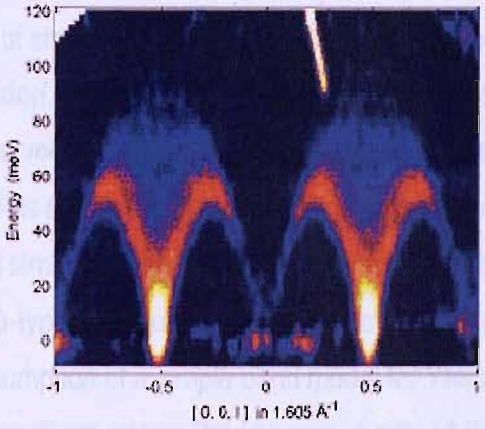

Figure 2.8: a single-crystal spinon excitation spectrum recorded using MAPS spectrometer (ISIS), bounded by the dispersion relation [59]

Examples of gapped excitation spectra occur in Haldane systems with integer spin chains, and at spin-Peierls transitions. The latter occur in antiferromagnetic spin-1/2 chains below a temperature T_{SP}. Above this temperature, the exchange coupling between nearest neighbours is uniform, but as T drops below T_{SP} elastic distortions cause spin dimerization and give rise to two unequal exchange

integrals. An energy gap is then created between the ground state and lowest lying excited state band [57].

Within the RMn_4Al_8 intermetallic series, systems with R = Y, Lu and Sc in addition to intermediate composition (La-Y)Mn_4Al_8 samples have been shown experimentally to exhibit spin gap-like phenomena[60, 61, 62]. Among the most notable features of the RMn_4Al_8 structure is the existence of a quasi-one dimensional Mn sublattice, which appears to be responsible for the suppression of magnetic ordering in $LaMn_4Al_8$ [63] (discussed in Chapter 8 of this thesis). In the gapped system YMn_4Al_8, the intrachain interatomic distance of 2.55Å and interchain separation 4.43Å [64, 65] suggest a similar quasi-1D form for the magnetic interaction. The observed temperature dependence of the magnetic susceptibility in these RMn_4Al_8 is characteristic of a one-dimensional antiferromagnetic system [66], in which a spin gap could be explained in terms of a spin-Peierls type instability.

However, with the classification of YMn_4Al_8 as an itinerant electron magnet, it has been identified as a suitable candidate for description in terms of spin fluctuation theory [60]. There exists a theory of itinerant electron magnetism in which a unified treatment is given for spin fluctuations with general amplitudes, interpolating between the weakly and strongly ferromagnetic limits [67]. In this model it is possible for the amplitude of local spin density fluctuations to increase rapidly with temperature up to a saturation point, above which the spin fluctuations may be regarded as a set of interacting local moments retaining a degree of short-range order [68]. This concept - of a temperature-induced localized moment - has provided a satisfactory explanation of some narrow band systems, and has been able to account for observed thermodynamic behaviour in the nearly-ferromagnetic semiconductor, FeSi [69]. FeSi is a rare example of a 3d transition metal compound with a correlated gap, and shares a number of similarities with YMn_4Al_8 such as a broad peak in $\chi(T)$ at a similar temperature [70], and Korringa-type temperature dependence of the NMR spin lattice relaxation time [71, 72]. This has led to the assumption of a simple band model for YMn_4Al_8 [60] as for FeSi, with a rapid increase in $1/T_1$ at high temperatures suggestive of a gap at around E_F, while the low temperature Korringa temperature dependence constitutes typical metallic behaviour, and indicates finite DOS within the gap.

A high semiconductor-metal transition observed in very high applied fields for FeSi [73] is also considered as having some possible bearing on the appearance of a gap. The degree of overlap with the physics of YMn_4Al_8 may suggest a similar mechanism operating in the manganese intermetallics. Interestingly, it has been observed that off-stoichiometric RMn_4Al_8 compounds exhibit semiconductor-like behaviour at low temperatures [74, 75] suggesting an electronic structure marginal to the metal-semiconductor boundary. A further possibility is explored in terms of the Kondo insulator

model originally applied to unstable 4*f* systems [76]. The renormalization of the density of states within a hybridization gap may account for the apparent partial filling, a scenario in accordance with an observed large value for γ (the enhancement of which implies a finite and enhanced DOS at the Fermi energy). An alternative scenario involves the partially filled gap originating from the bare electronic structure, with the R and Al atoms contributing electrons to wide conduction bands. This may have been discounted by recent DOS calculations for $LaMn_4Al_8$, performed parallel to these experimental studies using the Stuttgart TB-LMTO program. Separation of total density of states into orbital band contributions from each atom suggests that *s* and *p* contributions are negligible, with the main features above the Fermi energy coming from Mn-*d* and La-*f* electrons[3].

2.4. Non-Fermi Liquids

The physics of the Fermi liquid state constitutes an extensive subject, addressing some of the most fundamental concepts within the understanding of the metallic state. In recent years a growing number of examples within the class of strongly correlated electron systems have been found to show departure from Fermi liquid scaling via a range of experimental measurements. The significance of such discoveries cannot be understated, as prior to this the Fermi liquid model proved sufficient in the description of even "extreme" cases whereby interactions may have been expected to invalidate it, such as in the case of heavy fermion compounds.

At low temperatures corresponding to small excitations, the stability of Fermi liquid quasiparticles may be estimated, using Fermi's Golden Rule and assuming constant scattering matrix elements to obtain a scattering rate proportional to $(\Delta E)^2$ where ΔE is the energy of an excited quasiparticle above the Fermi surface. For small ΔE this results in quasiparticle states that are long lived on the perturbation timescale, and leads to a temperature dependence of the scattering rate of the form

$$\frac{1}{\tau} = A + B(k_B T)^2$$

where A is the scattering rate at $T = 0$, and the coefficient B is independent of T. Hence scattering-related transport properties – such as electronic resistivity - will show T^2 dependence at low temperatures.

[3] Preliminary LMTO DOS calculations carried out by B. D. Rainford and W. Temmerman, using the Stuttgart TB-LMTO program (O. Jepsen and O. K. Andersen)

The predicted scaling of measurable quantities for Fermi liquid systems are summarized in Table 2.1. In a number of cases the behaviour of metallic systems is described by an alternative relation, characterizing those materials as *Non-Fermi liquids* (NFLs). The most common examples of these are given together with the Fermi liquid predictions:

Quantity	Fermi liquid	Non-Fermi liquid
C/T	= constant	~ $\ln T/T_0$
χ	~ constant (metallic)	~ $1 - \sqrt{T}$
ρ	$\rho_0 + AT^2$	~ T

Table 2.1: temperature dependences of measurable quantities in FL and NFL systems

The Fermi liquid description fails to apply in a number of scenarios [77]. For example, where excitations occur corresponding to large energy transfers, constant scattering matrix elements can no longer be assumed, with consequences for the scattering time. In the vicinity of a quantum critical point, fluctuations in the order parameter slow down and increase in wavelength, increasing the mutual influence of the quasiparticles and enhancing the scattering cross-section. The scattering rate may be defined, for a system of dimension *d*, as [77]:

$$\frac{1}{\tau_{\Delta E}} = \frac{2\pi}{\hbar}\int_0^{\Delta E} D(E_F)\omega d\omega \int_{\omega/\hbar v_F}^{2k_F} \frac{q^{d-1}dq\left|D(q,\omega)\right|^2}{(2\pi/L)^d(\hbar v_F q)^2}$$

where $D(q,\omega)$ is the matrix element for all scattering processes. If this term is independent of q and ω then the integral in q is independent of energy transfer, and gives the expected Fermi liquid result whereby the scattering rate is proportional to the square of the quasiparticle energy. In one dimension however, the singular nature of the q integral leads to a decay proportional to ΔE to this order, even if $D(q,\omega)$ is invariant. The quasiparticle is hence not well defined anywhere, with the concept of adiabatic continuity no longer applicable (there is no one-to-one mapping of quasiparticle states and real, long-lived electron eigenfunctions).

The scattering matrix integrals may also become singular in higher dimensions [77]. The Coulomb interactions present in all metals would be a suitable candidate; however screening effects reduce

the long-range potential to a short-range Yukawa-type interaction, the scattering rate remains low and the quasiparticle state is preserved. The Amperian interaction is also long-range, and although it is much weaker, the effects manifest themselves if the temperature is sufficiently low. The screening length corresponding to the skin depth diverges in the low energy limit, allowing the scattering cross section to grow continuously. The matrix elements associated with the Amperian interaction are also nearly identical to those associated with a ferromagnetic QCP.

A double-channel Kondo effect, in which interactions of an impurity with two identical, independent conduction seas is considered, also leads to a Fermi liquid breakdown. As the temperature is lowered, a point is approached at which a bound singlet would ordinarily form. As one channel cannot be favoured within the symmetry constraints of the system, the bound quasiparticles associated with the single-channel Fermi Liquid state do not form.

The experimental analysis of non-Fermi liquids has been addressed by Bernhoeft [78], using a unifying model based on self-consistent renormalization of the dynamical magnetic susceptibility. This interpretation treats $\chi(\omega)$ at each wavevector $\boldsymbol{q}$ as an incoherent sum over a distribution of relaxation rates, $D(\Gamma)$, of susceptibilities $\chi(\Gamma;\omega)$ for the relaxational dispersion of magnetization density fluctuations with characteristic rate Γ:

$$\chi(\omega) = \int d\Gamma D(\Gamma)\chi(\Gamma;\omega)$$

A normal Fermi liquid with a single exponential decay rate will have $D(\Gamma)$ clustered around a central value, and this generalised susceptibility form will not yield any extra information about the system. For the NFL case, the distribution width is key in elucidating the form of non-exponential relaxation.

The key thermodynamic signatures of the NFL regime and observed features of inelastic neutron measurements are all fully accounted for by a fixed, flat, compact ("top hat") distribution bounded by lower and upper limits Γ_1 *and* Γ_2, where Γ_1 scales with temperature and Γ_2 is temperature-independent.

An expression for the dynamical susceptibility in relation to magnetic fluctuations of rate $\Gamma(\boldsymbol{q})$ has previously been introduced:

$$\chi(\Gamma;\boldsymbol{q},\omega) = \frac{\chi(\boldsymbol{q})\Gamma(\boldsymbol{q})}{\Gamma(\boldsymbol{q}) - i\omega}$$

The non-Fermi liquid generalization is given by:

$$\chi(\omega) = \int d\Gamma D(\Gamma)\left[\frac{u}{\Gamma - i\omega}\right]$$

where $\Gamma(\boldsymbol{q}) = u(\boldsymbol{q})\,\chi^{-1}(\boldsymbol{q})$. The form of the dynamical susceptibility for each wavevector is obtained by integration over the "top hat " distribution:

$$\chi(\omega) = \frac{u}{\Gamma_2 - \Gamma_1}\ln\left[\frac{\Gamma_2 - i\omega}{\Gamma_1 - i\omega}\right]$$

The imaginary part of the susceptibility may be expressed as (Bernhoeft's function):

$$\chi''(\omega) = \frac{u}{\Gamma_2 - \Gamma_1}\left[\tan^{-1}\left(\frac{\omega}{\Gamma_1}\right) - \tan^{-1}\left(\frac{\omega}{\Gamma_2}\right)\right]$$

where the response is peaked at $\sqrt{\Gamma_1\Gamma_2}$. At high temperatures where Γ_1 approaches Γ_2, a conventional paramagnetic relaxation rate $\Gamma_{para} = \sqrt{\Gamma_1\Gamma_2}$ may be defined and the familiar dynamical susceptibility term corresponding to single exponential relaxation is recovered.

As a system displaying a transition to an NFL state will in general show measurable trends as a function of a number of tuning parameters (such as composition, pressure or applied fields), an index of the Fermi liquid state has been developed in line with this theoretical treatment. The non-Fermi liquid parameter is defined as the ratio of the fluctuation distribution width to the susceptibility response peak, or mode frequency:

$$NFL = \frac{(\Gamma_2 - \Gamma_1)}{\sqrt{\Gamma_1\Gamma_2}}$$

this ratio tends toward zero as Γ_1 and Γ_2 tend to a common relaxation rate as expected for the Fermi liquid case, and diverges as the distribution width becomes large with increasing non-Fermi liquid order.

Since the scattering correlation function measured in a neutron experiment is directly related to the imaginary part of the dynamical susceptibility, the Bernhoeft function provides a means of directly confirming non-Fermi liquid states in real systems. An example of this scaling, assessed via inelastic neutron measurements of β-Mn, is reported in Chapter 7.

References

Local Moment and Itinerant Models:

[1] N. W. Ashcroft and N. D. Mermin, *Solid State Physics*, CBS Publishing Asia Ltd. 1987

[2] R. J. Elliot, *Magnetic Properties of Rare Earth Metals*, Plenum Press, 1972

[3] S. Blundell, *Magnetism in Condensed Matter*, Oxford University Press, 2001

[4] R. M. White, *Quantum Theory of Magnetism*, Springer-Verlag, 1983

[5] Picture taken from: http://www.tcd.ie/Chemistry/Under/6

[6] B. D. Rainford, *Magnetism and Neutron Scattering*, in *Neutron Scattering at a Pulsed Source* (R. J. Newbury, B. D. Rainford and R. Cywinski), Adam Hilger Press, 1988

[7] K. N. R. Taylor and M. I. Darby, *Physics of Rare Earth Solids*, Chapman and Hall, 1972

[8] J. Kondo, Progr. Theor. Phys. **32** (1964) 37

[9] P. W. Anderson, Phys. Rev. **124** (1961) 41

[10] B. A. Jones, C. M. Varma and J. W. Wilkins, Phys. Rev. Lett. **61** (1988) 125

[11] P. Coleman, Phys. Rev. B **28** (1983) 5255

[12] C. Lacroix, J. Magn. Magn. Mater. **100** (1991) 90

[13] C. Broholm, J. K. Kjems, G. Aeppli, Z. Fisk, J. L. Smith, S. M. Shapiro and G. Shirane, Phys. Rev. Lett. **58** (1987) 917

[14] P. Fulde, J. Phys. F: Met. Phys. **18** (1988) 601

[15] G. R. Stewart, Rev. Mod. Phys. **56** (1984) 755

[16] Diagram taken from P. A. J. de Groot, (PHYS3004) *Crystalline Solids*, undergraduate lecture notes (University of Southampton)

[17] L. D. Landau, Zh. Eksp. Teor. Fiz. 30 (1956) 1058

[18] A J Schofield, Contemporary Physics **40** (1999) 2

[19] E. C. Stoner, Acta Metal. **2** (1954) 260

[20] J. Hubbard, Proc. Roy. Soc. (London) **276A** (1963) 238

[21] T. Izuyama, D. J. Kim and R. Kubo, J. Phys. Soc. Japan **18** (1963) 1025

[22] T. Moriya, *Spin Fluctuations in Itinerant Electron Magnetism* (Springer-Verlag, 1985)

[23] T. Moriya and A. Kawabata, J. Phys. Soc. Japan **34** (1973) 639

[24] T. Moriya, Y. Takahashi and K. Ueda, J. Phys. Soc. Japan **59** (1990) 2905

[25] H. Hasegawa, J. Phys. Soc. Japan **38** (1975) 107

[26] J. Shinkoda, K. Kumagai and K. Asayama, J. Phys. Soc. Japan **46** (1979)

[27] K. Ueda and T. Moriya, J. Phys. Soc. Japan **38** (1975) 32

[28] S. Akimoto, T. Kohara and K. Asayama, Solid State Comm. **16** (1975) 1227

[29] Y. Nakamura, K. Yoshimoto, M. Shiga, M. Nishi and K. Kakurai, J. Phys. Cond. Matt. **9** (1997) 4701

[30] Y. Kohori, Y. Iwamoto, Y. Muro and T. Kohara, Physica B **237** (1997) 455

[31] T. Yamasaki, K. Matsui, H. Nakamura and M. Shiga, Solid State Comm. **119** (2001) 415

[32] T. Moriya and Y. Takahashi, J. Phys. Soc. Japan **45** (1978) 397

[33] T. Moriya, Progr. Theor. Phys. **33** (1965) 157

[34] K. Shimizu, S. K. Dhar, R. Vijayaraghavan et al, J. Phys. Soc. Japan **50** (1981) 1200

[35] K. Yoshimura and Y. Nakamura, J. Phys. Soc. Japan **53** (1984) 3611

[36] M Shiga, Physica B **149** (1988) 293

[37] Y. Nakamura, M Shiga and S. Kawano, Physica B **120** (1983) 212

[38] R. Cywinski, S. H. Kilcoyne and C. A. Scott, J. Phys. Cond. Matt. **3** (1991) 6473

[39] T. Freltoft, P. Böni, G. Shirane and K. Motoya, Phys. Rev. B **37** (1988) 3454

[40] K. Yoshimura, M. Takigawa, H. Yasuoka, M Shiga and Y. Nakamura, J. Magn. Magn. Mater. **54-57** (1986) 1075

[41] H. Nakamura, H. Wada, K. Yoshimura, M Shiga, Y. Nakamura, J. Sakurai and Y. Komura, J. Phys. F: Met. Phys. **18** (1988) 981

[42] M Shiga, H. Wada, H. Nakamura, K. Yoshimura and Y. Nakamura, Phys. F: Met. Phys. **17** (1987) 1781

[43] H. Wada, H. Nakamura, E. Fukami, K. Yoshimura, M Shiga and Y. Nakamura, J. Magn. Magn. Mater. **70** (1987) 17

[44] M Shiga, H. Wada, K. Yoshimura and Y. Nakamura, **54-57** (1986) 1073

[45] B. Canals and C. Lacroix, Phys. Rev. Lett. **80** (1998) 2933

[46] Picture taken from: http://www-drfmc.cea.fr/Phocea/Vie_des_labos/Ast

[47] Picture taken from: www.rsc.org/ej/JM/2001/b003682j/

[48] M. Shiga, J. Magn. Magn. Mater. **129** (1994) 17

[49] R. Ballou, C. Lacroix and M. D. Nunez Reguerio, Phys. Rev. Lett. **66** (1991) 1910

[50] M. D. Nunez Reguerio and C. Lacroix, Phys. Rev. B **50** (1994) 16 063

[51] C. Pinettes and C. Lacroix, J. Phys.: Cond. Matt. **6** (1994) 10 093

[51] S. Blundell, *Magnetism in Condensed Matter*, Oxford University Press, 2001

[52] M. Shiga, K. Fujisawa and H. Wada, J. Phys. Soc. Japan **62** (1993) 1329

[53] M. Mekata, T. Asano, T. Sugino, H. Nakamura, N. Asai, M. Shiga, A. Keren, K. Kojima, G. M. Luke, W. D. Luke, W. D. Wu, Y. J. Uemura, S. Dunsinger and M. Gingras, J. Magn. Magn. Mater. **140-144** (1995) 1767

[54] H. Nakamura, F. Takayanigi, M. Shiga, M. Nishi and K. Kakurai, J. Phys. Soc. Japan **65** (1996) 2779

[55] H. Nakamura, K. Yoshimoto, M. Shiga, M. Nishi and K. Kakurai, 1997, J. Phys.: Cond. Matt.**9** (1997) 4701

[56] J.R. Stewart and R. Cywinski, Phys. Rev. B **59** (1999) 4305

[57] S. Blundell, *Magnetism in Condensed Matter*, Oxford University Press, 2001

[58] L. Onsager, Phys/ Rev. 65 (1944) 117

[59] Image taken from: www.isis.rl.ac.uk/science

[60] H. Nakamura, S.Giri and T. Kohara, J. Phys. Soc. Japan **73** (2004) 2971

[61] H. Nakamura, Y. Muro, S. Giri, J. Umemura, H. Kobayashi, T. Koyama and T. Kohara, J. Phys. Soc. Japan **74** (2005) 2421

[62] Y. Muro, H. Nakamura and T. Kohara, J. Phys. Cond. Matt. **18** (2006) 3931

[63] T. Yamasaki, K. Matsui, H. Nakamura and M. Shiga, Solid State Comm. **119** (2001) 415

[64] I. Felner and I. Nowik, J. Phys. Chem. Sol. **40** (1979) 1035

[65] K. H. J. Buschow, J. H. N. van Vucht and W. W. van den Hoogenhof, J. Less Comm. Met. **50** (1976) 145

[66] J. G. Bonner and M. E. Fisher, Phys. Rev. **135A** (1964) 640

[67] T. Moriya and Y. Takahashi, J. Phys. Soc. Japan **45** (1978) 397

[68] T. Moriya, Solid State Commun. **26** (1978) 483

[69] Y. Takahashi and T. Moriya, J. Phys. Soc. Japan **46** (1979) 1451

[70] V. Jaccarino, G. K. Wertheim, J. H. Wernick, L. R. Walker and S. Arajs, Phys. Rev. **160** (1976) 476

[71] S. Takagi, H. Yasuoka, S. Ogawa and J. H. Wernick, J. Phys. Soc. Japan **50** (1981) 2539

[72] M. Corti, S. Aldrovandi, M. Fanciulli and F. Tabak, Phys. Rev. B **67** (2003) 172408

[73] Y. B. Kudasov, A. I. Bykov, M. I. Dolotenko, N. P. Kolokol'chikov, M. P. Monakhov, I. M. Markevtsev, V. V. Platonov, V. D. Selemir, O. M. Tatsenko, A. V. Filippov, A. G. Volkov, A. A. Povzner, P. V. Bayankin and V. G. Guk, JETP Lett. **68** (1998) 350

[74] Y. Kotur, A. M. Palasyuk, E. Bauer, H. Michor and G. Hilscher, J. Phys. Cond. Matt. **13** (2001) 9421

[75] A. M. Palasyuk, B. Y. Kotur, E. Bauer, H. Michor and G. Hilscher, J. Alloys Comp. **367** (2004) 205

[76] G. Aeppli and Z. Fisk, Comment. Cond. Matt. Phys. **16** (1992) 155

[77] A J Schofield, Contemporary Physics **40** (1999) 2

[78] N. Bernhoeft, J. Phys. Cond. Matt. **13** (2001) R771 – R816

3. Muon Spin Relaxation Experiments

3.1 Introduction

The widespread use of muons in condensed matter research is based on the extreme sensitivity of the muon to the presence of microscopic fields within a sample, as well as to the distribution and dynamics of these fields. In the case of dynamical studies, fluctuations may be recorded either as a result of genuine time-varying fields present at a particular muon site, or of muons moving through a sample: in the latter case presenting an alternative use as a probe of diffusion. It is commonly found that when muon spin techniques are used in conjunction with neutron scattering, the information extracted is maximised [1].

Muon facilities may be established together with accelerator-based spallation sources of neutrons. High-energy (>500MeV) proton beams directed at a graphite target produce pions, which decay with $t_{½}$ = 26.03ns. Positive pions at rest near the surface of the target emit positive muons accompanied by muon neutrinos, isotropically and with energy 4.119MeV in the rest frame.

The neutrino has negative helicity (antiparallel spin and momentum) as a result of maximal parity violation, and so the muon is constrained similarly. Hence a number of muons transported towards a sample in a beam pipe constitute a 100% spin-polarised pulse or beam.

Condensed matter research utilizes positive muons, since when implanted into solids these sit away from the nucleus in regions of high electron density; negative muons are less useful as they are attracted by the nucleus and displace electrons [2]. The properties of positive muons are summarised in the table below:

Mass	$m_\mu = 208.6\ m_e = 0.113\ m_p$
Charge	+e
Spin	½
Magnetic moment	$\mu_\mu = 4.8 \times 10^{-3}\ \mu_B = 3.183\ \mu_N$

Table 3.1: Summary of properties of positive muons

On implantation into a sample, formation of a *muonium* (μ^+e^-) state occurs, with subsequent loss of an electron. Rapid thermalisation ensure the muons come to rest with negligible depolarisation (muons are thermalised on a timescale ~ 1ns [1,2]). Implanted muons decay after a time t with a probability proportional to e^{-t/τ_μ} ($\tau_\mu = 2.197\mu s$ for positive muons, equal to the vacuum lifetime[1]). A 3-body decay process results in an electron neutrino, muon antineutrino and a positron. Due to parity violation the positron is emitted preferentially in the direction of the muon spin vector.

The positron emission is according to the probability function

$$P(\theta) = 1 + a_0 \cos\theta$$

where is the angle between the direction of muon spin and the direction of positron emission. The parameter a_0 is known as the asymmetry parameter and depends on the emitted positron energy[2]. The distribution becomes isotropic when the positron energy is half of the maximum. When averaged over all positron energies, a_0 becomes 1/3.

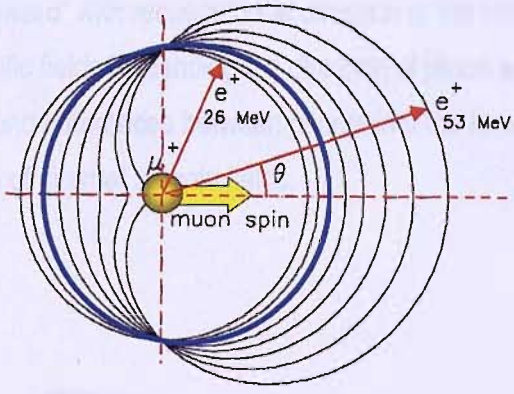

Figure 3.1: the probability distribution function for positrons emitted in the muon decay process: the functions for E_{max} to $E_{max}/2$, corresponding to $a_0 = 1$ and 0 respectively, are shown. $P(\theta)$ for the averaged energies ($a_0 = 1/3$) is shown in blue

It is therefore not possible to determine the orientation of a muon spin from a single decay positron, but the average polarisation is obtained from a collection of positrons emitted from muons throughout the sample.

---

[1] The lifetime of negatively charged muons implanted in a material depends on the atomic number of that material [3,4].

[2] a_0 varies between 1 for the maximum emitted positron energy, to 0 for half the maximum energy.

Each muon has a magnetic moment 4.49×10^{-26} JT^{-1} ($= 4.8 \times 10^{-3}$ μ_B), which couples to any local field experienced at the site of implantation. Local fields as experienced by the muon originate from dipolar interactions with surrounding nuclear or electronic spins, and from hyperfine fields associated with the spin density at the muon site [1]. A muon moment will Larmor precess with frequency $\omega_\mu = \gamma_\mu \boldsymbol{B}$ around such fields, where $\gamma_\mu = 136$ $MHzT^{-1}$.

The time evolution of the direction of muon spin vectors in the sample therefore depends on the nature of the magnetic environments experienced by the muon population. If a uniform off-axis magnetic field exists in the sample, the muon ensemble precesses coherently at the corresponding Larmor frequency. This gives rise to an oscillatory signal described below. If there is a spatial variation in magnetic field, there will be a dephasing (depolarisation) effect.

3.2 Principles of Muon Spin Relaxation Experiments

The basic experimental geometry involves two positron detector banks on either side of the sample, termed "forward" and "backward" with respect to the direction of the initial muon spin vector (-z axis). Applied and internal magnetic fields influencing the direction of muon spin will affect the positron counts in these detectors, and differences between counts into the forward and backward directions are used to infer the nature of internal sample fields.

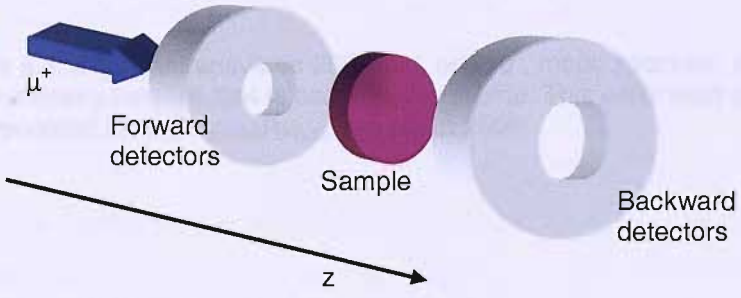

Figure 3.2: the basic arrangement for μSR experiments. The muon beam direction defines the z-axis, and in relaxation experiments longitudinal fields may be applied along this axis

If a transverse magnetic field is applied, Larmor precession occurs around the field axis and a muon decaying immediately will emit positrons into the forward detector - while one surviving for half a revolution emits in the backward direction.

The time evolution of the emissions to each detector set - $N_B(t)$ and $N_F(t)$ - is given by an exponential decay superimposed with an oscillatory function. The normalised difference between these is the *asymmetry function*

$$A(t) = \frac{N_F(t) - \alpha N_B(t)}{N_F(t) + \alpha N_B(t)}$$

The parameter α takes into account the relative detector efficiency and anisotropic absorption. The value of α is determined for each sample via a calibration spectrum recorded with a small, applied transverse field (20G in the case of instrumentation used here), producing an oscillatory signal as described.

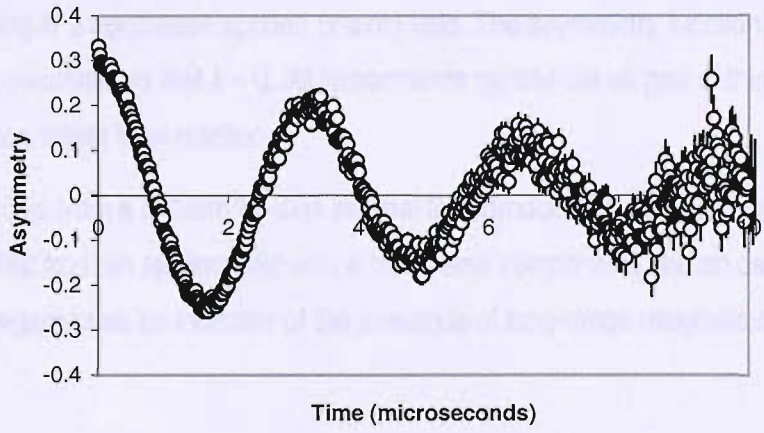

Figure 3.3: a typical transverse 20G field, or"T20", muon spectrum showing an asymmetry function that is oscillatory with time. This calibration spectrum was recorded for a β-$Mn_{0.81}Ru_{0.19}$ sample at 250K

The transverse asymmetry function has the specific form

$$A_x(t) = \frac{N_F(t) - \alpha N_B(t)}{N_F(t) + \alpha N_B(t)} = a_0 G_x(t)\cos(\omega_L t) + a_b \cos(\omega_L t) + k$$

where $G_x(t)$ is a sample field-dependent relaxation function, k is the offset of the spectrum from the centred position about zero, and a_b is a background asymmetry term arising from muons thermalised in the sample holder. A least-squares fit of a T20 spectrum to this function is used to adjust α until the offset k is zero. The calculable maximum asymmetry a_0 depends on the initial beam polarisation (usually ~ 1), intrinsic asymmetry of the weak decay as mentioned above, and detector efficiency as a function of positron energy. These factors typically bring the observed maximum asymmetry down to ~ 0.25 [2].

Muon spin *relaxation* is the term used generally to describe the change in initial longitudinal polarisation due to sample fields, either in zero applied field (purely to observe the field distribution of a sample) or in longitudinal applied fields, to assess the strength of field required to decouple the muon spins. In this case the asymmetry function is simplified to

$$A_z(t) = \frac{N_F(t) - \alpha N_B(t)}{N_F(t) + \alpha N_B(t)} = a_0 G_z(t) + (background)$$

Muon spin *rotation* tends to be used to describe the dephasing effect of local fields on an ensemble of muons precessing in a transverse applied (x-axis) field. The asymmetry function is as for the calibration set-up, corrected so that $k = 0$. All experiments carried out as part of this work involve muon spin relaxation rather than rotation.

The asymmetry profile from a uniform off-axis internal field produced by the sample will follow a similar pattern to that from an applied field with a transverse component, and an oscillatory signal can therefore be regarded as an indicator of the presence of long-range magnetic order.

3.3 Muon Sources

Pulsed sources or continuous beams of muons may be utilised. In the latter case a mechanism – coincidence technique - needs to be in place whereby single muon arrival times can be recorded (low arrival rate is desirable) as it is unknown where or at what time each detected positron originated. A high background is also unavoidable, as positrons from muons arriving less than a few lifetimes apart must be rejected. However, a continuous-beam instrument (such as those at PSI and TRIUMF facilities) also provides an intrinsic time resolution determined only by the detection system.

A pulsed source (those at the ISIS and KEK facilities) eliminates the background problem (the high sensitivity allows events to be recorded further than 10 muon lifetimes[3] into the measurements), although the time resolution, limited by the pulse width of typically ~ 70 ns, precludes measurements of extremely fast relaxation or large fields causing rapid precession. For a pulsed source, the width of the pulse must be significantly shorter than the muon lifetime to minimise the spread of detection times, and the repetition rate must be longer [2]. For fields of more than approximately 50mT causing coherent precession, a continuous muon beam should be used [1].

Muon Spin Relaxation at ISIS

All samples in the present thesis were investigated using the MuSR instrument at the ISIS pulsed source facility, Rutherford Appleton Laboratory. The instrument records positron arrivals using 64 scintillation detectors, arranged in two arrays around the sample position. These are concentric with the coils of the main Helmholtz magnet, which can be rotated between the transverse and longitudinal geometries (as can the detectors). Maximum fields of 600G and 2500G respectively are useable in these configurations [5].

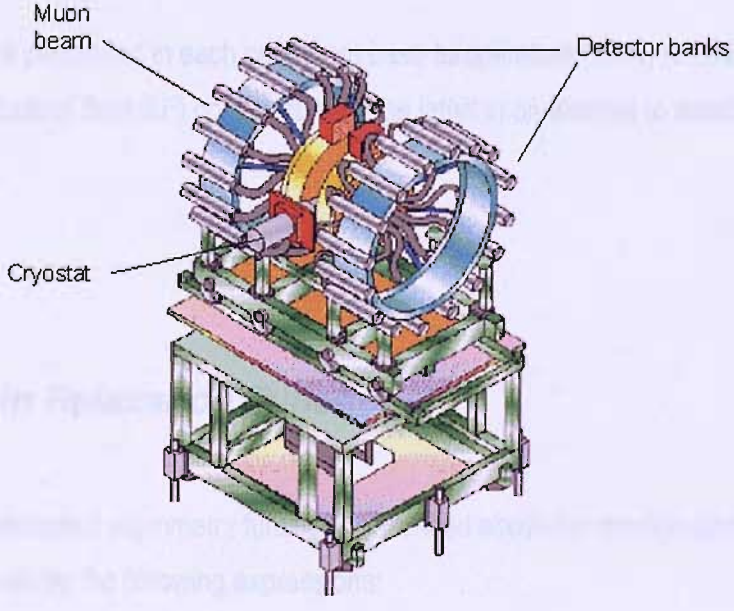

Figure 3.4: the ISIS MuSR instrument [5]

[3] At the ISIS facility data is routinely collected for ~ 32μs or 2000 bins

A "*T20*" run was performed prior to recording spectra for each sample, in order to determine the parameter α and correct for offset as described.

In experiments involving the RMn_4Al_8 and β-$Mn_{(1-x)}M_x$ samples, the prepared ingots were crushed to a fine powder and inserted into a holder composed of a recessed silver backing plate with an mylar cover. These materials are used specifically as silver causes negligible spin depolarisation (with negligible atomic and nuclear moments), and mylar is transparent to muons. This assembly was then inserted into a cryostat positioned in the muon beam, between the detector arrays.

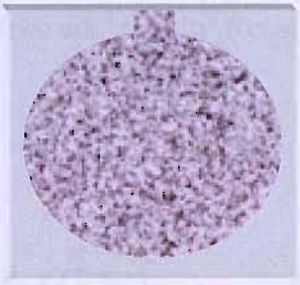

Figure 3.5: representation of the sample holder inserted into the MuSR cryostat

Measurements were performed in each case from base temperature (1.4K) to over 100K, and in zero field (ZF) and longitudinal field (LF) configurations, the latter in an attempt to establish the decoupling field.

3.4 Muon Spin Relaxation Functions

The background-subtracted asymmetry functions described above for rotation and relaxation experiments are given by the following expressions:

$$A_x(t) = a_0 G_x(t)\cos(\omega_L t)$$

$$A_z(t) = a_0 G_z(t)$$

These contain the transverse $G_x(t)$ and longitudinal $G_z(t)$ terms. Muon experiments seek to determine the form of these functions for a given sample. The experiments described in this thesis involved only relaxation techniques: henceforth only the *longitudinal relaxation function* $G_z(t)$ and its origins will be considered.

In a magnetic field at an angle θ to the z-axis, the z-component of the muon spin will have a time-independent $\cos^2\theta$ component and a time-dependent $\sin^2\theta$ component which precesses at frequency $\omega_L = \gamma_\mu B$. Hence the variation with time of the spin z-component is [6]

$$s_z(t) = \cos^2\theta + \sin^2\theta \cos(\gamma_\mu B t)$$

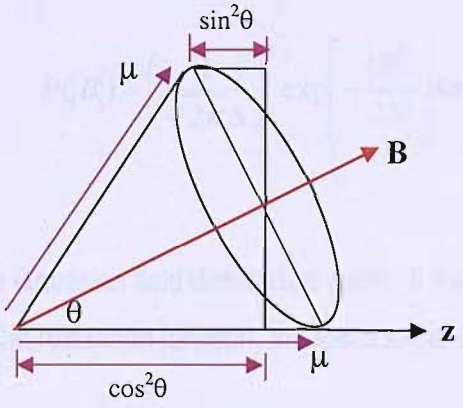

Figure 3.6: precession of muon spin component μ_z around field ***B***

The relaxation function is then obtained by taking the statistical average of all $s_z(t)$:

$$G_z(t) = \iiint s_z(t) P(B_x) P(B_y) P(B_z) dB_x dB_y dB_z$$

The terms $P(B_i)$ are the probability distributions for the x-, y- and z-components of the internal fields.

As mentioned, in the case of a fully magnetically ordered sample this function will have an oscillatory nature as for the transverse field asymmetry function. In a sample lacking long-range order, the internal magnetic field may vary from site to site in direction and magnitude, and there will be a distribution of precession frequencies and axes.

Static Relaxation

In a system of randomly oriented, concentrated static moments, the probability distributions of the *x*, *y* and *z* field components are Gaussian.

$$P(B_i) = \frac{1}{\sqrt{2\pi}\Delta} \exp\left[\frac{-B_i^2}{2\Delta^2}\right] \quad (i = x, y, z)$$

The probability distribution of the resultant magnitude of such fields has the form of a Maxwell-Boltzmann function:

$$P(|B|) = \left(\frac{1}{\sqrt{2\pi}\Delta}\right)^3 \exp\left[-\frac{|B|^2}{2\Delta^2}\right] 4\pi |B|^2$$

The parameter Δ is the Gaussian field distribution width. If these *P(Bi)* are used in the integrals given above to obtain the relaxation function, the result is the *Gaussian Kubo-Toyabe* relaxation function [7]:

$$G_z^{GKT}(t) = \frac{1}{3} + \frac{2}{3}(1-\sigma^2 t^2) \exp\left[-\frac{\sigma^2 t^2}{2}\right]$$

In this expression the relaxation rate parameter σ is related to the second moment of the field distribution Δ^2 as $\sigma^2 = \gamma_\mu^2 \Delta^2$. The factor 1/3 arises as a result of the fact that in a system of randomly-oriented dipoles, on average 1/3 of the muons in the ensemble will sense a field only along the z-direction, and will have no precessing spin component.

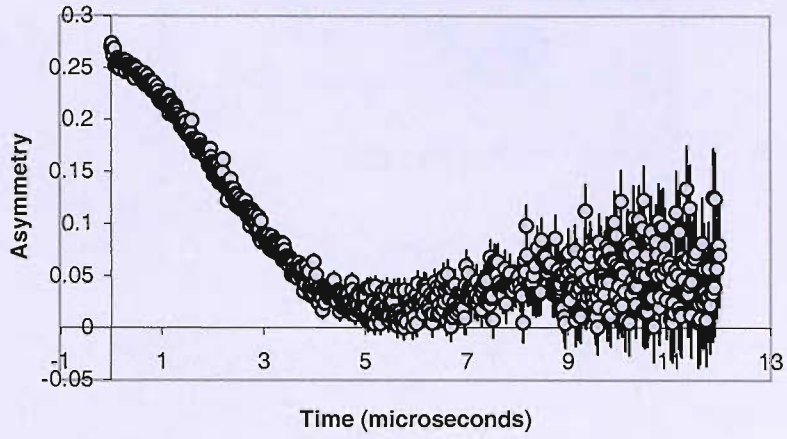

Figure 3.7: Gaussian Kubo-Toyabe relaxation in $PrMn_4Al_8$ at 70K. The asymmetry tail at ~ $a_0/3$ represents the 1/3 of the muon ensemble whose spin vectors only see a field along z

Where the static dipole system is more dilute, the fields experienced by the muons have a Lorentzian distribution of width λ. The probability distributions of the x-, y- and z-components take the form

$$P(B_i) = \frac{\gamma_\mu \lambda}{\pi(\lambda^2 + \gamma_\mu^2 B_i^2)} \quad (i = x, y, z)$$

In such a system the implanted muons experience a greater range of field environments, giving rise to the sharp peak of the distribution centred on zero (from muons located far from magnetic spins) and broader tails (from those in close proximity). A similar statistical averaging treatment to the Gaussian case gives rise to the *Lorentzian Kubo-Toyabe* (LKT) relaxation function:

$$G_z^{LKT}(t) = \frac{1}{3} + \frac{2}{3}(1 - \lambda t)\exp[-\lambda t]$$

The Lorentzian relaxation spectrum has an initial exponential decay, and a shallower, broader minimum than the Gaussian relaxation, consistent with the broader tails of the field distribution. Both relaxation profiles converge to a value of 1/3.

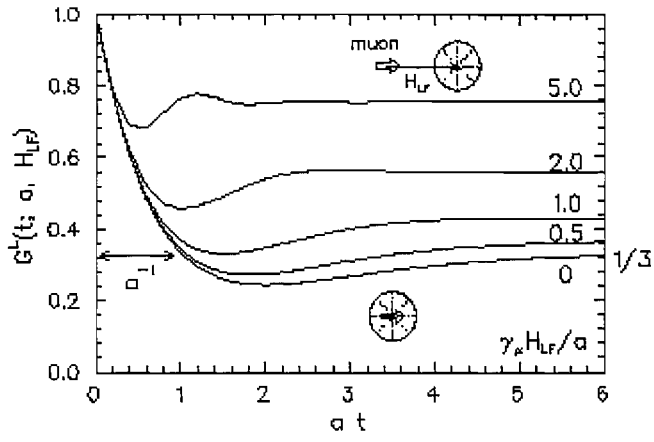

Figure 3.8: The effect of a longitudinal magnetic field on muon spin relaxation; the ***B*** = 0 curve corresponds to Lorentzian Kubo-Toyabe relaxation [8]

The Gaussian and Lorentzian forms of Kubo-Toyabe relaxation apply to the concentrated and dilute limits; in the intermediate regime, the zero-field KT-type relaxation can be generalised to a function that interpolates between these limits:

$$G(t) = \frac{1}{3} + \frac{2}{3}(1-(at)^{\alpha})\exp\left[\frac{-(at)^{\alpha}}{\alpha}\right]$$

Here and λ are generalised to *a*. The value of α ranges from 1 to 2, going from the dilute to the concentrated limit. This function corresponds to Voigtian probability distributions for the internal field components [9].

Relaxation in an External Field

If a longitudinal magnetic field is applied along *z*, then $B_{i=z}$ should be replaced by $B_z + B_{ext}$ before the statistical averaging integral is performed. For Gaussian field distributions this then leads to the expression [6]:

$$G_z^{GKT}(t,\omega_L) = 1 - \frac{2\sigma^2}{\omega_L^2}\left(1-\cos(\omega_L t)\exp\left[-\frac{\sigma^2 t^2}{2}\right]\right) + \frac{2\sigma^4}{\omega_L^3}\int_0^t \sin(\omega_L \tau)\exp\left[-\frac{\sigma^2\tau^2}{2}\right]d\tau$$

This assumes that the external field does not reorient the dipoles of the sample system. The effect of a longitudinally applied external field is shown in Figure 3.8.

Where the muon spins are subject to an internal field arising form long-range magnetic order, the relaxation function is given by:

$$G_z(t) = \frac{1}{3} + \frac{2}{3}\cos\left(\gamma_\mu |B| t\right)$$

Dynamical Relaxation and Muon Diffusion

The KT relaxation expressions given above are obtained by considering a system in the static limit. In many cases however the fields affecting a muon spin are time varying, either as a result of the muon diffusing or "hopping" between sites, or spin fluctuations of the magnetic system. Such effects can be accounted for within the *strong collision approximation* [10]. This assumes that the local field changes direction at a time t according to the probability distribution:

$$P(t) = \exp[-\nu t]$$

and that the field after this event is entirely uncorrelated with that before. The fluctuation rate ν can be defined as the (exponential) decay rate of the local fields' autocorrelation function [8].

Within the strong collision model, muons are grouped according to the number of fluctuations experienced within a time interval. A dynamical relaxation function is obtained by summing contributions to the total polarisation from all groups. The probability that a given muon has not experienced a field change by time t is $e^{-\nu t}$, and so the contribution to the total polarisation from that muon group seeing no fluctuations is:

$$G_z^{(0)}(t) = G_z(t)\exp[-\nu t]$$

A muon experiencing exactly one fluctuation in this interval, at time t', has an associated probability of $e^{-\nu(t-t')}$ and the contribution to the total polarisation from all such muons is

$$G_z^{(1)}(t) = \nu \int_0^{\infty} G_z(t') \exp[-\nu t] G_z(t-t') \exp[-\nu(t-t')] dt'$$

All higher order terms may then be derived using the recurrence relation:

$$G_z^n(t) = \nu \int_0^t G_z^{(0)}(t') G_z^{(n-1)}(t-t') dt'$$

The dynamic Kubo-Toyabe function is then obtained by summing over all *n*:

$$G_z^{DKT}(t) = G_z^{(0)}(t) + \sum_{n=1}^{\infty} \nu \int_0^t G_z^{(0)}(t') G_z^{DKT(n-1)}(t-t') dt'$$

The expression can be evaluated by numerical integral for a given internal field distribution with or without an applied field [11]. However over most of the dynamic range, it is sufficient to use analytical approximations. For example, where fluctuations are slow, the relaxation has a similar form to the static case, the only difference being a suppression of the "1/3 tail" by an exponential factor so that [1]

$$G_z^{tail}(t) = \frac{1}{3} \exp\left[-\frac{2}{3}\nu t\right]$$

For an intermediate situation the 1/3 factor disappears completely and for Gaussian distributions the relaxation becomes an *Abragam* function [1]:

$$G_z^{DKT}(t) = \exp\{-\lambda[\exp(-\nu t) - 1 + \nu t]\}$$

In the fast fluctuation regime, the total relaxation function is approximated by an exponential

$$G_z^{DKT}(t) = \exp[-\Lambda t]$$

with $\Lambda = 2\sigma^2/\nu$.

The relaxation rate is found to decrease with faster fluctuations, which the muons are unable to follow. This effect is referred to as *motional narrowing.*

For Lorentzian distributions, the situation is complicated by the fact that those muons situated far from a magnetic spin experience a different environment to those in close proximity, and direct summation as mentioned earlier leads to an unphysical result in which motional narrowing does not occur. An alternative approach involves decomposing the distribution into a number of Gaussian distributions, finding the dynamical functions and re-combining [8].

It is commonplace to describe fluctuations as "fast" when $R = \nu/\sigma > 10$, as "intermediate" when $1 < R < 10$, and "slow" when $R < 1$ [1].

For atomic spin fluctuations, the fast relaxation rate Λ can be directly related to the fluctuating local fields via the autocorrelation function:

$$\Lambda = G \sum_{\alpha=x,y} \int_0^\infty \langle B_\alpha(0) B_\alpha(t) \rangle dt$$

where G is a coupling constant.

It can be shown [12] that

$$\Lambda(T) = G \frac{k_B T}{N} \sum_q \frac{\chi(q)}{\Gamma(q)}$$

where $\chi(q)$ is the wavevector-dependent susceptibility, $\Gamma(q)$ is the linewidth of the fluctuations and the sum is taken over the Brillouin zone. $\chi(q)$ and $\Gamma(q)$ can be measured directly with inelastic neutron scattering, so that using this relation neutron and muon measurements of temperature-dependent spin fluctuations become comparable. In a number of itinerant antiferromagnets, the q-dependence of Γ is weak and the relaxation rare may be defined as

$$\Lambda = \frac{G k_B T \chi_L}{\Gamma}$$

where χ_L is the *local susceptibility*:

$$\chi_L = \frac{1}{N} \sum_q \chi(q)$$

A comparison of neutron linewidth and relaxation rate data determined by μSR is given below for YMn_2 alloys [13]:

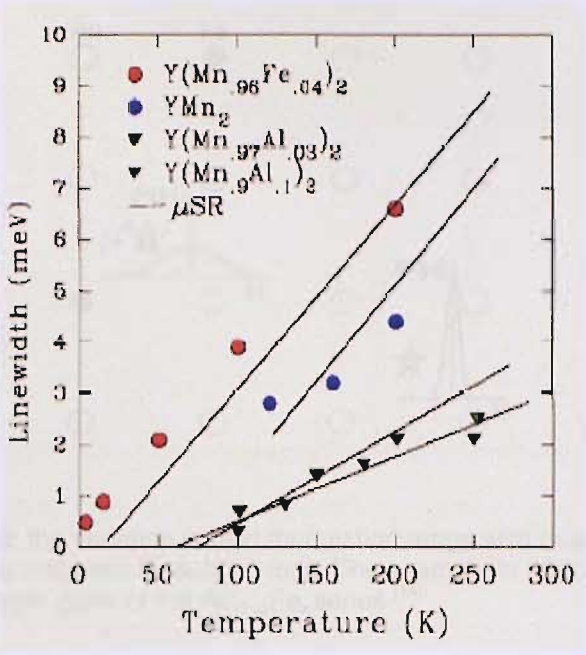

Figure 3.9: fluctuation linewidths from neutron and muon measurements in alloys of YMn_2 [13]: coloured symbols represent neutron data; lines represent μSR data

For paramagnetic spin fluctuations, the fast muon spin relaxation rate Λ is determined by the sum over the entire Brillouin zone, and accounts for long- and short-range dynamic correlations of the neighbouring atomic spins. If however there is long range order giving rise to coherent fields, the length scale of correlations and the muon site may be crucially important.

μSR Studies of Spin Glasses

Materials classified as spin glass systems require an alternative description of their muon relaxation behaviour.

Conventional dilute spin glasses (those with a small concentration of magnetic impurities) are successfully described by a model taking into account the fluctuations of the magnetic impurity spins, and their effect on the field modulations at the muon site [14]. The dynamic range of these time-modulated fields is dependent on the proximity of a muon site to the fluctuating spin, with fields at muon sites closer to magnetic ions modulated over a wider range than those at sites further away.

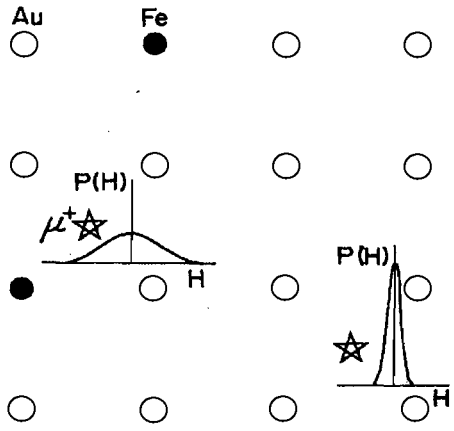

Figure 3.10: the variation in field modulation range with muon proximity to magnetic fluctuating ions. The example in this case is a dilute spin glass of the $Au_{(1-x)}Fe_x$ series [14]

The dynamic range in this model may be approximated to a Gaussian distribution:

$$P^G(B_i) = \frac{\gamma_\mu}{\sigma\sqrt{2\pi}} \exp\left[-\frac{\gamma_\mu^2 B_i^2}{2\sigma^2}\right] \quad (i = x, y, z)$$

The probability of a muon being located at a site with σ ($\sigma = \Delta\gamma_\mu$ where Δ is the distribution width) is given by

$$\rho(\Delta) = \sqrt{\frac{2}{\pi}} \frac{a}{\sigma^2} \exp\left[-\frac{a}{2\sigma^2}\right]$$

The total field distribution is extracted via a summation over all sites weighted by their corresponding probabilities. This results in a Lorentzian distribution of width a/γ_μ

$$P^L(B_i) = \int_0^\infty P^G(B_i)\rho(\sigma)d\sigma$$

Above T_g and in the fast fluctuation limit, a dilute spin glass therefore follows the *root exponential* relaxation function

$$G_z^{DSG}(t,a,\nu) = \exp\left[-\sqrt{\frac{4a^2t}{\nu}}\right]$$

Where the spin glass system is more concentrated, the relaxation function takes the form of a *stretched exponential*:

$$G_z^{CSG}(t) = \exp\left[-(\lambda t)^{\beta}\right]$$

In this case all muon sites are in close proximity to magnetic spins, removing the wide range of field distributions encountered in the dilute case. An exponential relaxation function would be expected; however it emerges that the spin autocorrelation function is itself stretched-exponential.

It has been hypothesised that the distribution of fluctuation frequencies broadens as the temperature decreases towards T_g, which would also lead to a broad distribution in . The temperature dependence of β is often found to closely reflect the dependence found in Monte Carlo relaxation calculations of the Ising spin glass autocorrelation function [15]:

$$\langle S(0)S(t)\rangle \propto \exp\left[-\left(\frac{t}{\tau}\right)^{\beta}\right]$$

where the autocorrelation function exhibits Kohlrausch relaxation with a broad distribution of relaxation times, τ.

The relaxation rate λ is found to diverge as T_g is approached, [1] and the exponent β is also temperature dependent, often increasing from 1/3 at the transition T_g to 1 at high temperatures (~4T_g [1])

Stretched exponential relaxation has been observed in a number of concentrated spin glass systems, notably in alloyed systems of β-Mn [16].

References

[1] R. Cywinski, Physica B **350** (2004) 17-25

[2] S. J. Blundell, Contemporary Phys. **40** (1999) 175

[3] M. Conversi, E. Pancini and O. Piccioni, Phys. Rev. **68** (1945) 232

[4] M. Conversi, E. Pancini and O. Piccioni, Phys. Rev. **71** (1947) 209

[5] MuSR instrument user guide, ISIS facility, RAL

[6] R. Cywinski, *Muon Spin Relaxation Functions*, ISIS Muon Training Course lecture material (2005)

[7] R. Kubo and T. Toyabe, in *Magnetic Resonance and Relaxation* (1967)
(ed. R. Blinc) 810

[8] PhD thesis of K. Kojima, University of Tokyo (1995)

[9] M. R. Crook and R. Cywinski, J Phys Condensed Matter **9** (1997) 1149

[10] R. Kubo, J. Phys. Soc. Japan **9** (1954) 935

[11] R. S. Hayano, Y. J. Uemura, J. Imazato, N. Nishida, T. Yamazaki and R. Kubo, Phys. Rev. B **20** (1979) 850

[12] R. Cywinski, *Complementarity of Muons and Neutrons*, ISIS Muon Training Course lecture material (2005)

[13] B. D. Rainford, R. Cywinski and S. J. Dakin, JMMM **140** (1992) 805

[14] Y. J. Uemura, T. Yamazaki, D. R. Harshman, M. Senba and E. J. Ansaldo, Phys. Rev. B **31** (1985) 546]

[15] T. Ogielski, Phys. Rev. B **32** (1985) 7384

[16] J. R. Stewart and R. Cywinski, Phys. Rev. B **59** (1999) 4305

4. Theory of Neutron Scattering

4.1. Introduction: Properties of the Neutron

A diverse range of techniques involving neutrons may be employed in order to fully investigate the magnetic properties of a material. In addition to structural analysis, dynamical processes may also be observed; neutron studies are therefore a useful complement to those laboratory methods that only evaluate static properties.

Neutrons interact with the nucleus rather than the electrons of an atom (unlike probes such as X-rays) and the atomic cross section for neutron scattering does not depend strongly on atomic number. Hence the signals from light elements are not masked, and isotopes or neighbouring elements in the Periodic Table can be differentiated. Additionally, and of great importance in these investigations is the fact that the neutron possesses a magnetic moment of magnitude 1.04×10^{-3} μ_B, which interacts with moments of a magnetic material according to $\boldsymbol{\mu} \cdot \boldsymbol{B}$. By this means studies can be made of magnetic structures and excitations on a microscopic scale.

Neutrons are advantageous in that they are available for scattering experiments at energies comparable to many processes at the atomic level: thermal neutrons typically have energies in the range 10 meV – 100 meV. The kinetic energy of a neutron is related to its wavelength by:

$$E = \frac{\hbar^2 k^2}{2m_n} = \frac{81.72(meVAng.^{-2})}{\lambda^2}$$

Consequently neutron wavelengths at these energies are on the same scale as atomic spacings: 1 – 3 Å typically in the thermal range. As a result, structure - both crystalline and magnetic – can be investigated via diffraction effects. Meanwhile dynamics (for example phonon excitations, crystal field splittings, spin waves, spin fluctuations and other magnetic excitations) may be explored by means of energy transfers to and from the scattering system. The interaction of neutrons with nuclei is weak

and this, coupled with the neutron's electrical neutrality, means that they penetrate samples effectively[1] and with minimal destructive effect.

Mass	$m_n = 1.675 \times 10^{-27}$kg
Charge	0
Spin	½
Magnetic moment	$\mu_n = -1.913\mu_N = -9.66 \times 10^{-27}$ JT^{-1}

Table 4.1: a summary of properties of the neutron

4.2. Neutron Sources

Neutrons for scattering experiments can be obtained from reactor or accelerator (spallation) sources. A reactor core comprises an array of fuel elements enriched in ^{235}U: neutrons produced by the fission process, with energies in the MeV range, are slowed to thermal energies via elastic collisions with molecules of the moderator. The flux of thermal neutrons sustains a chain reaction by inducing fission in the fuel elements (cross sections for nuclear fission are greater for less energetic neutrons).[2]

Moderators are composed of low mass, non-absorbing nuclei and commonly consist of hydrogenous materials (water, light/heavy water, methane) or graphite, ensuring maximum energy transfer from the nuclei. The flux emerging from a reactor through a beam tube is close to a Maxwellian distribution in the thermal region:

$$\Phi(v) \propto v^3 \exp\left[\frac{-\frac{1}{2}mv^2}{k_B T}\right]$$

The peak flux attained is for neutrons in thermal equilibrium with the moderator and so is at a neutron speed corresponding to the moderator temperature

[1] While this is usually the case, there are materials (such as cadmium) with particularly high neutron absorption cross-sections, in which attenuation is high.

[2] In reactor sources the moderators for sustaining fission and experimental procedures may be separate [1].

$$v = \left(\frac{3k_B T}{m} \right)^{\frac{1}{2}}$$

This corresponds to a kinetic energy:

$$E = \tfrac{1}{2} m v^2 = \tfrac{3}{2} k_B T$$

Reactor sources therefore produce high fluxes at lower energies, but are limited at high energies by achievable moderator temperatures. A wide range of wavelengths is also produced and the necessary monochromation reduces the flux further.

A significant part of the experimental work for this thesis was carried out at the Institut Laue-Langevin in Grenoble, the source of the world's most intense neutron beams. The neutron flux produced in the reactor is 1.5×10^{15}n/s cm^2, with a thermal power of 58.3MW, using a single fuel element with a heavy water moderator. The thermal flux, in equilibrium with the heavy water moderator at 300 K, has a peak wavelength at 1.2 Å. In addition, a hot source consisting of 10 litres of graphite at 2400K is available for enhancing the flux below 0.8 Å, and two cold sources (liquid deuterium at 25K) are available for enhancing flux above 3 Å [2].

Spallation sources use a beam of charged particles accelerated to GeV energies to eject neutrons from heavy target nuclei. Early systems used a linac to collide relativistic electrons with a uranium target, and the subsequent bremsstrahlung cascade and photon-neutron reaction to produce neutrons. Modern sources use a much more efficient linac-synchrotron combination to accelerate proton beams, with a heavy metal target (Ta, U or W) giving up neutrons via spallation. This production method comes without the chain reaction of nuclear fission, or the need to remove large amounts of energy from the system as generated in a reactor. The neutrons ejected from the target nuclei are again in the MeV energy range, and so spallation sources also require the use of a moderator. Accelerator sources are usually pulsed (at around 50Hz) and so are suited to the time-of-flight diffraction and spectroscopy techniques.

The ISIS facility at the Rutherford Appleton Laboratory, at which most of the neutron scattering studies in this work were carried out, produces a pulsed neutron beam. The time averaged heat generation in the target is 160kW, but for the duration of the pulse the intensity exceeds that of a steady state source. The acceleration process, repeated 50 times per second, involves a H^- beam from which electrons are removed using a stripping foil, the resulting 800 MeV protons each

releasing approximately 15 neutrons from the tantalum spallation target. The three moderators are ambient temperature water, liquid methane at 100K and liquid hydrogen at 20K, and each is constrained to be small (containing around 0.5 litres of material) to avoid excessive over-broadening of the 0.4 μs initial pulse. This under-moderation contributes to the relatively high flux of epithermal neutrons compared to a reactor source, and the pulse sharpness facilitates both high instrument resolution and the use of time-of-flight techniques with the polychromatic neutron beams [3].

4.3. Principles of Neutron Scattering Experiments

The interactions of neutrons with the nuclei and electrons of a sample change the measurable properties of the incident beam with respect to the scattered beam. Momentum, discussed in terms of wavevector, and energy can both change, depending on whether the scattering processes are elastic or inelastic. At its most basic, a neutron scattering experiment may be described as a count of scattered neutrons against wavevector transfer $\boldsymbol{q}$ and energy transfer $\hbar\omega$. The exact way both of these values are changed is sample-dependent and it known as the scattering function $S(\boldsymbol{q}, \omega)$. To relate this to what is measured in an experiment, the principle of neutron cross-sections must first be considered:

1. The *total cross-section* (σ) is defined as the total number of neutrons scattered into all directions per second, normalised by the incident flux.

2. The *differential cross-section* ($d\sigma/d\Omega$), is defined as the cross-section per solid angle, i.e. the number of neutrons per second scattered into a solid angle $d\Omega$ in the direction θ, ϕ, given the incident flux into that solid angle.

3. The *double-differential cross-section* ($d^2\sigma/d\Omega dE$) is the scattered neutron count into the solid angle $d\Omega$ and energy interval dE, given the incident flux into the same.

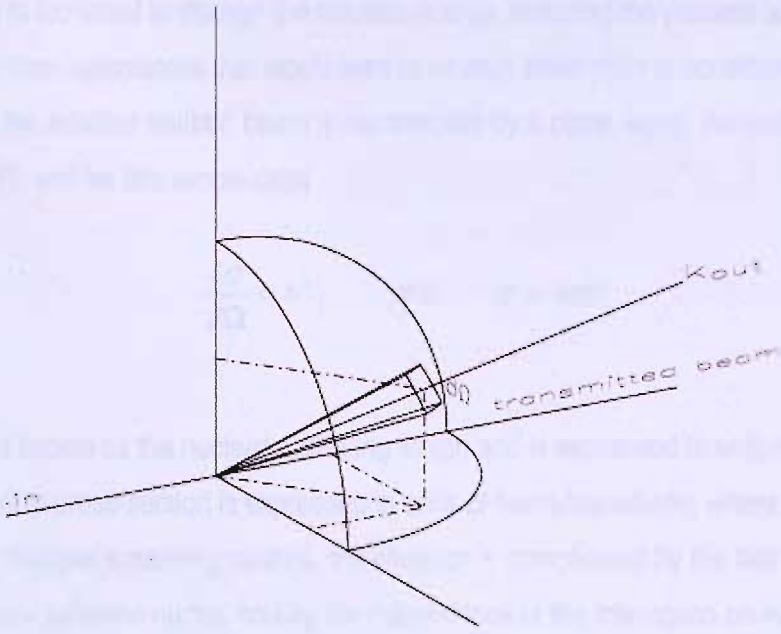

Figure 4.1: schematic of a neutron scattering experiment [4]

Hence the differential cross-section is obtained by integrating the partial differential cross-section over all energy

$$\frac{d\sigma}{d\Omega} = \int_0^\infty \frac{d^2\sigma}{d\Omega dE'} d\Omega dE'$$

(where E' is the final neutron energy) and in turn the total cross-section is obtained by integrating the differential cross-section over 4π steradians

$$\sigma = \int_0^{4\pi} \int_0^\infty \frac{d^2\sigma}{d\Omega dE'} d\Omega dE'$$

Elastic Nuclear Scattering

Expressions for the scattering cross-sections may be derived by considering the simplest model: elastic scattering from a single, fixed nucleus. The range of the nuclear force is small compared to the neutron wavelength, leading to point-like, spherically symmetric scattering [5]. The energy of a

thermal neutron is too small to change the nucleus energy, ensuring the process is elastic, and only scattering away from resonances that would lead to neutron absorption is considered. Under these approximations the incident neutron beam is represented by a plane wave, the scattered wave by a spherical wave [5], and for this simple case

$$\frac{d\sigma}{d\Omega} = b^2 \qquad \text{and} \qquad \sigma = 4\pi b^2$$

The quantity *b* is known as the nuclear scattering length and is expressed in units of Fermi (f) = 10^{-15}m. The differential cross-section is expressed in units of barns/steradians, where1 barn = 10^{-28} m^2. For a system of multiple scattering centres, the situation is complicated by the fact that *b* does not vary systematically between nuclei, and by the dependence of the interaction on nuclear spin, which will in general vary randomly. Identical scattering cannot therefore be expected from all nuclei in a sample of the same element, or even the same isotope.

Applying Fermi's Golden Rule and box normalisation [5] leads to the development of a mathematical expression for the partial differential cross-section [5, 6]:

$$\frac{d^2\sigma}{d\Omega dE'} = \frac{k'}{k}\left(\frac{m_n}{2\pi\hbar^2}\right)^2 \sum_{\Lambda,\Lambda'} p_\Lambda \left|\left\langle k\Lambda\left|V\right|k'\Lambda'\right\rangle\right|^2 \delta(E_\Lambda - E_{\Lambda'} + \hbar\omega)$$

where $\boldsymbol{k}$ and $\boldsymbol{k'}$ are the initial and final neutron wavevectors respectively, and Λ and Λ' the initial and final quantum states describing the sample. *V* is the interaction potential, and the delta function is included to ensure conservation of energy in a scattering event; the scattering cross section is zero unless the change in sample energy is equal to the change in neutron energy. The partial differential cross-section is then the sum over all possible states, weighted by the probability p_Λ.

The nuclear potential may be represented by the Fermi pseudopotential,

$$V(r) = \frac{2\pi\hbar^2}{m_n} b\delta(\boldsymbol{r} - \boldsymbol{R})$$

This does not correspond to the actual potential, and so its use is strictly unrealistic. Similarly, Fermi's Golden Rule uses first order perturbation theory, the conditions of which do not apply to

nuclear scattering of thermal neutrons. However, in conjunction these two concepts are used to achieve the correct result of isotropic scattering for a fixed nucleus [5].

For an assembly of nuclei in the scattering target, and at large distances, the spherical scattered waves from each nucleus add to give a plane wave. Taking into account the path lengths from each nucleus to the detector, the expression for the differential cross-section becomes

$$\frac{d\sigma}{d\Omega} = \left| \sum_n b_n \exp[i\boldsymbol{q} \cdot \boldsymbol{r}_n] \right|^2$$

where $\boldsymbol{q} = (\boldsymbol{k}_i - \boldsymbol{k}_f)$ and $\boldsymbol{r}_n$ is the position vector of the nth nucleus.
The elastic differential cross-section is the sum of two contributions, the *coherent* and *incoherent* cross-sections. The coherent term depends on correlations between the same nucleus, and between different nuclei, over time. Hence coherent scattering is used to infer the nature of crystal structures, concerning both long- and short-range order. The incoherent term depends only on correlations between positions of the same nucleus at different times. There is no interference, therefore incoherent scattering is isotropic and manifests itself as a flat background in measured spectra. The physical origin lies in the fact that solely coherent scattering would arise in a system in which all scattering lengths = $\overline{b}$. Addition of the incoherent term is necessary to take account of the random distribution of deviations in b from the mean value, and therefore obtain scattering due to the real system [5].

Assuming the distribution of isotopes and spin states is random and uncorrelated between nuclear sites m and n, ensemble averaging gives [7]

$$\left.\frac{d\sigma}{d\Omega}\right|_{coherent} = \sum_n \sum_m \overline{b}_n \overline{b}_m \exp[i\boldsymbol{q} \cdot (\boldsymbol{r}_n - \boldsymbol{r}_m)]$$

$$\left.\frac{d\sigma}{d\Omega}\right|_{incoherent} = \sum_{n=m} \left(\left(\overline{b_n^2}\right) - \left(\overline{b}_n\right)^2 \right)$$

Coherent elastic scattering is essentially Bragg scattering: the coherent differential cross-section corresponding to one unit cell of volume V is [5]

$$\left.\frac{d\sigma}{d\Omega}\right|_{coherent} = \frac{(2\pi)^3}{V} \sum_{h,k,l} \delta(\boldsymbol{q} - \boldsymbol{G}_{hkl}) \left| F(\boldsymbol{G}_{hkl}) \right|^2$$

$\boldsymbol{G}_{hkl}$ is the reciprocal lattice vector for the (hkl) planes, and the delta function represents the (hkl) Bragg peak corresponding to wavevector $\boldsymbol{q}$ satisfying the Laue condition:

$$|\boldsymbol{q}| = |\boldsymbol{G}_{hkl}|$$

The measured intensity of a given Bragg reflection is proportional to the square of the *nuclear structure factor* $F(\boldsymbol{G}_{hkl})$,

$$F(G_{hkl}) = \sum_d b_d \exp[i(\boldsymbol{G}\cdot\boldsymbol{d})] = \sum_d b_d \exp\left[2\pi i\left(hx_d + ky_d + lz_d\right)\right]$$

for atomic position vectors d within the unit cell.

A temperature factor also needs to be introduced in order to account for thermal vibration of atoms around their equilibrium positions. The squared structure factor is therefore multiplied by the *Debye-Waller* factor [8]

$$e^{-2W} \simeq e^{-Pq^2T}$$

where P is a constant.

The Debye-Waller factor reduces constructive interference and hence intensity of all Bragg reflections with increasing temperature and becomes more significant for larger values of $|\boldsymbol{q}|$.

Elastic Magnetic Scattering

If initial and final spin states of the scattered neutrons are taken into account, the elastic partial differential cross-section is modified from the simplified nuclear case, to

$$\left(\frac{d^2\sigma}{d\Omega dE'}\right) = \frac{k'}{k}\left(\frac{m}{2\pi\hbar^2}\right)^2 \left|\langle k's'\Lambda'|V_m|ks\Lambda\rangle\right|^2 \delta(E_\Lambda - E_{\Lambda'} + \hbar\omega)$$

The potential V_m acts between the neutron and all the electrons within the scattering system. A full evaluation of $\langle k's'\Lambda'|V_m|ks\Lambda\rangle$ is given in Reference [5]; $\langle k'|V_m|k\rangle$ is determined initially by integration over the spatial coordinates of the neutron, with the spin and orbital parts of V_m treated separately. This leads to the expression

$$\left.\frac{d^2\sigma}{d\Omega dE'}\right|_{\sigma\lambda\to\sigma'\lambda'} = [\gamma r_0]^2 \frac{k'}{k}\left|\langle\sigma'\lambda'|\boldsymbol{\sigma}\cdot\boldsymbol{\kappa}_\perp|\sigma\lambda\rangle\right|^2 \partial[E\lambda - E\lambda' + \hbar\omega]$$

where the operator $\boldsymbol{\kappa}_\perp$ is defined accordingly

$$\boldsymbol{\kappa}_\perp = \sum_i \exp[i\boldsymbol{q}\cdot\boldsymbol{r}_i]\left\{\hat{\boldsymbol{q}}\times[\boldsymbol{s}_i\times\hat{\boldsymbol{q}}] + \frac{i}{\hbar q}[\boldsymbol{p}_i\times\hat{\boldsymbol{q}}]\right\}$$

considering the contribution due to the ith electron of the system with position $\boldsymbol{r}_i$, spin $\boldsymbol{s}_i$ and momentum operator $\boldsymbol{p}_i$. $\hat{\boldsymbol{q}}$ is a unit vector in the direction of $\boldsymbol{q}$. Operator $\boldsymbol{\kappa}_\perp$ can be shown to be related to the magnetization of the system [5], considering spin and orbital components::

$$\boldsymbol{\kappa}_\perp = \boldsymbol{\kappa}_{\perp S} + \boldsymbol{\kappa}_{\perp L} = \hat{\boldsymbol{q}}\times(\boldsymbol{\kappa}\times\hat{\boldsymbol{q}})$$

where

$$\boldsymbol{\kappa} = \boldsymbol{\kappa}_S + \boldsymbol{\kappa}_L = \frac{1}{2\mu_B}\boldsymbol{M}(\boldsymbol{q})$$

So that operator $\boldsymbol{\kappa}$ is effectively the Fourier transform of $\boldsymbol{M}(\boldsymbol{r})$. Since $\boldsymbol{\kappa}_\perp$ is the vector projection of $\boldsymbol{\kappa}$ on the plane perpendicular to $\hat{\boldsymbol{q}}$, it follows that

$$\boldsymbol{\kappa}_\perp = \boldsymbol{\kappa} - (\boldsymbol{\kappa}\cdot\hat{\boldsymbol{q}})\hat{\boldsymbol{q}}$$

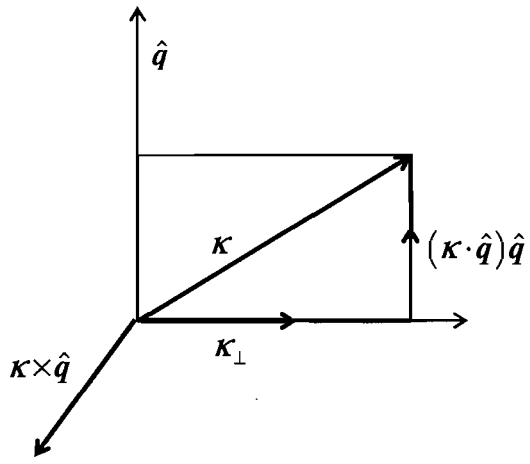

Figure 4.2: relation between κ and $\kappa_\perp$ [5]

In order for an atom to contribute to the magnetic scattering intensity, there must be a component of its magnetic moment perpendicular to the scattering vector.

The elastic magnetic differential cross-section can be written as

$$\left.\frac{d\sigma}{d\Omega}\right|_{magnetic} = (\gamma r_0)^2 \left|\tfrac{1}{2} gf(\boldsymbol{q})\right|^2 \exp[-2W] \sum_{\alpha,\beta} (\delta_{\alpha\beta} - q_\alpha q_\beta) \sum_{i,j} \exp\left[i\boldsymbol{q}\cdot(R_i - R_j)\right] \left\langle S_i^\alpha \right\rangle \left\langle S_j^\beta \right\rangle$$

where r_0 is the classical electron radius = e^2/m_e, and γ is a positive constant = 1.913, related to the neutron magnetic moment as $\mu_n = -\gamma \mu_N \sigma$. The sum is over spin sites *i* and *j* and Cartesian directions α and β. $\left\langle S_i^\alpha \right\rangle$ and $\left\langle S_j^\beta \right\rangle$ are the time-averaged spin components on sites *i* and *j*.

Magnetic scattering occurs via the $\boldsymbol{\mu}\cdot\boldsymbol{B}$ dipole interaction, the range of which is comparable to the neutron wavelength. Angular dependence is introduced and there is an attenuation as with X-ray scattering, represented by the term $f(\boldsymbol{q})$, the *magnetic form factor*. This is the Fourier transform of the magnetisation density around the magnetic ion, and has the effect of reducing the magnetic scattering intensity with increasing $\boldsymbol{q}$

The form factors of rare earth and transition metal elements have been parameterised, as a function of q [9]. In the case of manganese, the magnetic species in all systems studied here, the form factor is expressed as

$$f(S) = A\exp\left[-aS^2\right] + B\exp\left[-bS^2\right] + C\exp\left[-cS^2\right] + D$$

with $S = q/4\pi$

Species	A	a	B	b	C	c	D
Free Mn	0.2438	24.963	0.1472	15.673	0.6189	6.54	-0.0105
Mn^{2+}	0.4220	17.684	0.5948	6.005	0.0043	-0.609	-0.0219
Mn^{3+}	0.4198	14.283	0.6054	5.469	0.9241	-0.009	-0.9468

Table 4.2: magnetic form factor parameters for manganese species [9]

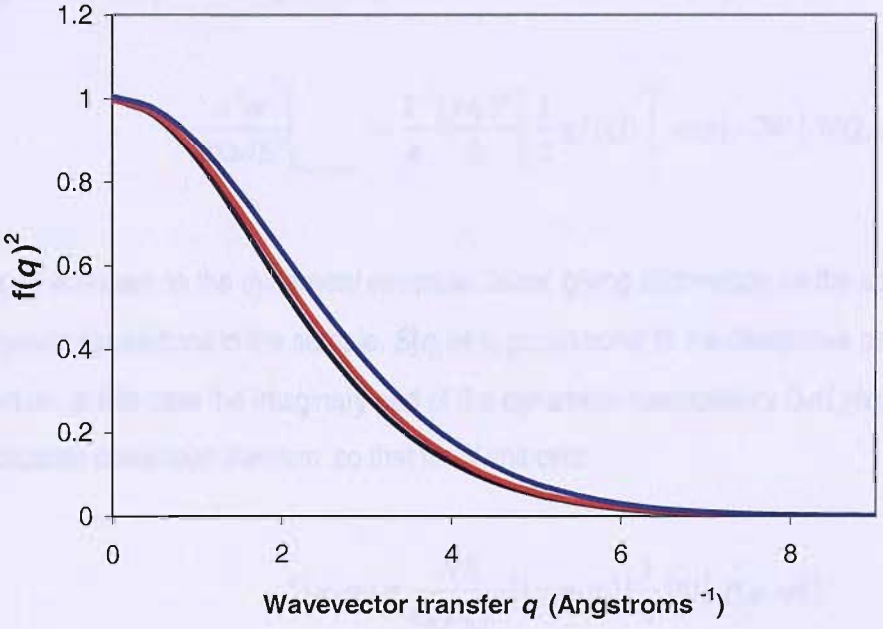

Figure 4.3: squared form factor contribution to the elastic magnetic cross-section, plotted using the relation and parameter values from [9]. Key: black curve = Mn^{2+}; red curve = Mn^{3+}; blue curve = free Mn

For an antiferromagnetic structure with modulation vector $\boldsymbol{Q}$, magnetic Bragg peaks occur for [10]

$$\boldsymbol{q} = \boldsymbol{G}_{hkl} + \boldsymbol{Q}$$

Antiferromagnetic diffraction peaks therefore appear at different positions in a diffraction pattern from the nuclear peaks (for a ferromagnetic material these would coincide).

Inelastic Scattering

An inelastic scattering event involves a transfer of energy between neutron and sample, via the creation or annihilation of excitations involving either magnetic or nuclear lattices. These may include single ion crystal field transitions and collective, coherent dynamics such phonons and spin waves, with characteristic excitation energies. Diffusive processes such as magnetic spin fluctuations give rise to intensity around the elastic line, the so-called quasielastic scattering.

For inelastic scattering, the magnetic partial differential cross-section is determined using linear response theory, describing the response of a system to a varying field

$$\left.\frac{d^2\sigma}{d\Omega dE'}\right|_{magnetic} = \frac{k'}{k}\frac{(\gamma r_0)^2}{\hbar}\left[\frac{1}{2}gf(Q)\right]^2 \exp[-2W]S(\boldsymbol{Q},\omega)$$

$S(\boldsymbol{q},\omega)$ is known as the *dynamical structural factor*, giving information on the spatial and temporal magnetic correlations in the sample. $S(\boldsymbol{q},\omega)$ is proportional to the dissipative part of the response function, in this case the imaginary part of the dynamical susceptibility $\Im m[\chi(\boldsymbol{q},\omega)]$, according to the *fluctuation dissipation theorem* so that for N unit cells

$$S(\boldsymbol{q},\omega) = \frac{N\hbar}{(g\mu_B)^2}[1+n(\omega)]\frac{1}{\pi}\mathrm{Im}[\chi(\boldsymbol{q},\omega)]$$

$[1+n(\omega)]$ is the *detailed balance factor*, and takes account of the fact that the probability of an energy-gain or energy-loss process depends on the temperature of the system and hence on relative thermal populations [6]. The detailed balance factor takes the form

$$[1+n(\omega)] = \frac{1}{1-\exp\left[\frac{-\hbar\omega}{k_B T}\right]}$$

The imaginary part of the dynamical susceptibility of a magnetic system is thus directly calculable from an inelastic scattering experiment, and this can be related to the wavevector-dependent static susceptibility $\chi(\boldsymbol{q})$ via the *Kramers-Kronig* relation [10]

$$\chi(\boldsymbol{q}) = \frac{1}{\pi}\int_{-\infty}^{\infty}\frac{\chi''(\boldsymbol{q},\omega)}{\omega}d\omega$$

The measured inelastic cross-section includes magnetic scattering, together with the response from coherent and incoherent vibrational excitations, i.e. phonons. The phonon response must therefore be subtracted from inelastic data in order to extract information concerning magnetic dynamics. Scattering from coherent excitations leads to peaks in $S(\boldsymbol{q},\omega)$ for the conditions [7]

$$\hbar\omega = \pm\hbar\omega_{\substack{SW \\ Ph}}$$

$$\hbar\boldsymbol{q} = \hbar(\boldsymbol{G}_{hkl} \pm \boldsymbol{q}_{\substack{SW \\ Ph}})$$

for energies and wavevectors of the phonon or spin wave processes. As the magnetic form factor decreases scattering intensity with increasing $\boldsymbol{q}$, it is possible to separate phonon and magnetic inelastic processes at large $\boldsymbol{q}$ where phonon scattering is maximised. The process of phonon subtraction will be discussed fully in Chapter 6.

4.4 Neutron Powder Diffraction Experiments

In diffraction experiments involving crystal structures, interference between scattered wavefronts from the periodic atomic array gives rise to a characteristic diffraction pattern, used to identify positions of atoms. Constructive interference produces intensity peaks for neutrons scattered into well-defined directions, for which the Bragg condition

$$n\lambda = 2d\sin\theta$$

is satisfied by some set of planes.

Available values of wavevector transfer q that can be measured are given by the scattering triangle for elastic processes, in which $|\boldsymbol{k}_i| = |\boldsymbol{k}_f|$:

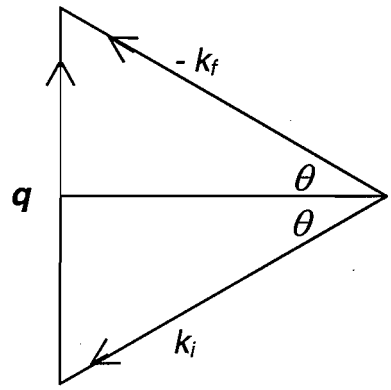

Figure 4.4: the scattering triangle for diffraction experiments

For elastic scattering the wavevector transfer q is given by

$$q = \frac{4\pi \sin\theta}{\lambda} = \frac{2\pi}{d}$$

For a known wavelength (for a monochromated beam or calculated via neutron time of flight) and scattering angle 2θ (detector position) the interplanar separations can be calculated, and from this dimensions and symmetry of the unit cell. For nuclear scattering, atomic positions are measured directly, unlike X-ray experiments in which electron density maps are obtained, and from this nuclear positions deduced. Within a magnetically ordered phase, dipole interactions between neutron and atomic spins allow the structure of the magnetic lattice (which often differs from the crystal lattice) to be simultaneously determined.

For single crystal measurements, the relative positions of sample and detector need to be changed in order to observe reflections from different sets of *hkl* planes. In a powder sample however, the large number of small, randomly oriented crystallites mean that for each *hkl* reflection a finite number of planes are inclined at the correct angle for constructive interference to occur. The orientation of

the planes around the incident beam is also not fixed, and so cones of scattered intensity are produced, the half-angle of which correspond to the scattering angles. These *Debye-Scherrer* cones are produced simultaneously for all *hkl*.

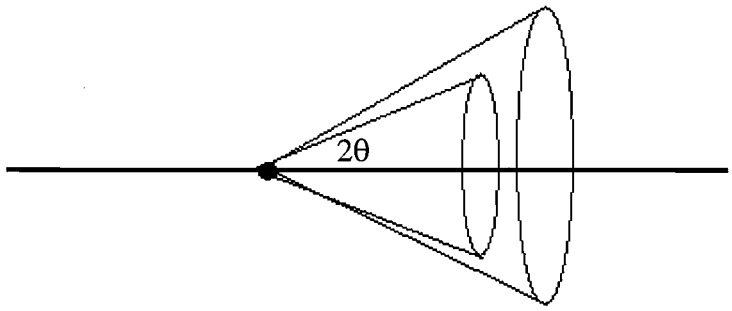

Figure 4.5: Debye-Scherrer intensity cones in a neutron powder diffraction measurement

For a powder sample the integrated intensity of each nuclear Bragg peak of multiplicity Z_N is then

$$\sigma_{hkl} = \frac{\lambda^3 Z_N}{V 4\sin\theta} \left| F(\boldsymbol{G}_{hkl}) \right|^2 \exp[-2W]$$

for a unit cell of volume V. For magnetic Bragg peaks of multiplicity Z_M, the integrated intensity is:

$$\sigma_{hkl} = (r_0\gamma)^2 \frac{1}{4} \langle S \rangle^2 \left[\tfrac{1}{2} g f(q) \right]^2 \exp[-2W](1-q_z^2) \frac{\lambda^3 Z_M}{V 4\sin\theta}$$

This expression contains the time-averaged spin value $\langle S \rangle^2$, and the factor $(1\text{-}q_z^2)$ is the orientation factor.

The traditional experimental set-up involves a monochromatic incident beam and measures scattered neutron intensity as a function of detector angle 2θ. An alternative method, utilising *time of flight* (TOF) white-beam instrumentation for powder diffraction has been extensively developed at pulsed neutron sources, and the work done for this thesis has largely involved such techniques. A wavelength-distributed pulse of neutrons is incident upon the sample, with

$$\lambda = \frac{ht}{mL}$$

where t is the TOF and L is the flight path length. This facilitates simple calculation of d-spacing using

$$d = \frac{nht}{2mL\sin\theta}$$

Hence using a polychromatic incident pulse, a complete powder diffraction pattern may be obtained using a single fixed detector (although to minimise counting times practical diffractometers typically have large numbers of detectors, arranged into banks with characteristic d-spacing range, count rate and resolution.

For a given wavelength, the measurable limit is given by $d_{min} = \lambda/2$ for a detector at 180°. Since pulsed sources yield higher epithermal fluxes, they are advantageous for measuring very small d-spacings. The resolution function is dependent on the type of instrumentation: for TOF, the resolution function is given by partial differentiation of the previous equation[3] and is [11]:

$$\frac{\Delta d}{d} = \left(\left(\frac{\Delta t}{t} \right)^2 + \left(\frac{\Delta L}{L} \right)^2 + (\Delta\theta\cot\theta)^2 \right)^{1/2}$$

Rietveld Refinement of Powder Diffraction Data

Single-crystal neutron diffraction measurements allow the necessary structure factor information to be determined from measured intensities. There are then a number of techniques available for structural solution and refinement. It is not so straightforward however, to perform the same analysis with a polycrystalline sample: unless the unit cell is very small and the degree of symmetry high enough to allow the separation, identification and integration of a sufficient number of intensities, peak overlap means an alternative solution is required.

[3] Assuming independent variables, hence addition in quadrature.

By treating each point in the diffraction pattern as an individually observed intensity, the Rietveld method avoids this problem. The crystal structure is modelled and this, together with information on diffractometer parameters describing reflection shape/width, allows intensities for a diffraction pattern to be calculated. This modelled pattern is compared against the experimental data and iteratively adjusted using least-squares fitting.

The model from which the theoretical intensity is calculated contains up to 400 independent parameters that may be adjusted during a refinement. The major parameter inputs can be listed:

Scale factor – this accounts for the measured integrated intensity
Background - an appropriate polynomial function
Unit cell constants and **atomic coordinates** – this defines the contents of the assumed cell, allowing calculations of locations and intensities of Bragg reflections.
Zero shift – to allow for adjustment of the zero point of measurements.
Isotropic temperature factors - this adjusts Bragg intensities according to the Debye-Waller factor
Absorption correction – needed due to isotopic dependence of neutron absorption
Peak shape – determined by instrument intrinsic lineshape

The intensity at each point in the diffraction pattern is calculated according to [11]:

$$Y_{ic} = Y_{ib} + \sum_{k=k_1}^{k=k_2} G_{ik} I_k$$

Y_{ic} = calculated intensity at point i
Y_{ib} = background intensity at point i
G_{ik} = value of the normalised peak profile function at point i for reflection k
I_k = Bragg intensity of reflection k
$k = k_1$ to k_2, reflections contributing intensity to point i

This allows for partial or complete overlap.

The quality of the fit is quantified by **R-factors**:

1) Bragg R-factor R_B, sum of magnitude of residuals for each Bragg reflection. This is then normalised to the total intensity of all the Bragg reflections.
2) Profile R-factor R_P, sum of residuals for each point in the powder pattern, normalised to the total integrated intensity of the pattern.
3) Weighted profile R-factor R_{WP}, as for R_P but the residual for each point is squared and weighted, and the square root is taken after summation.
4) Expected R-factor R_{exp}, defined so that $(R_{WP}/R_{exp})^2 = \chi^2$.

Instrumentation:

POLARIS

Polaris is a medium-resolution, high-intensity powder diffractometer at the ISIS facility, RAL. Incident wavelengths range from 6 – 0.1Å (corresponding to energies of 20meV – 10eV). The sample is positioned 12m from the moderator, and there are 4 banks of detectors at various positions relative to the sample [12]. Each of these banks is optimised for a particular *d*-range.

The Polaris detectors are resolution- rather than time-focused: the elements of each detector bank are arranged to have approximately constant resolution (rather than the same TOF for neutrons scattered from a given *hkl*). This is achieved by considering the dominant term in the resolution function for high or low angles - whichever is appropriate - and adjusting the positions of the detectors in the bank to keep $\Delta d/d$ constant.

The data collected are binned as histograms of counts versus total TOF, and spectra within each bank are summed, normalised to counting time (divided by incident monitor counts), and the instrument background spectrum is subtracted. The raw data files are divided by a vanadium spectrum[4], which normalises to the incident energy distribution, taking into account detector efficiency as a function of energy. The TOF axes may also be converted to *d*-spacings. Sample absorption corrections must also be performed on the data prior to any analysis, and important procedure since absorption effects are wavelength-dependent and can differ strongly for different

[4] This has been pre-corrected for absorption and multiple scattering effects (see Appendix A).

atoms and isotopes. As the resolution varies between banks, each bank is treated separately when normalising data.

Using this instrument, diffraction spectra were recorded for the β-$Mn_{1-x}Ru_x$ sample series at intervals from 4.2K to room temperature.

ROTAX

The multipurpose diffractometer ROTAX (ISIS) utilises a wavelength distribution of 0.6 – 5.2 Å at a maximum incident flux of $10^6/cm^2sec$. The total flight path is variable between 14.5 and 17.6m, and the linear position-sensitive detectors are arranged to accommodate scattering angles from 10 - 170°. In this set-up, the accessible *d*-spacings range from 0.2 - 50 Å, and the maximum resolution $\Delta d/d$ = 0.35% [13].

Diffraction patterns were obtained on ROTAX for RMn_4Al_8 with R = La, Pr, and Y at room temperature, in addition to low temperature measurements performed on $LaMn_4Al_8$.

GEM

Another ISIS instrument, GEM is a high intensity, high resolution diffractometer suited to the study of crystalline powders. The incident flight path is 17m and the instrument uses scintillator detectors (covering a solid angle ~ 3.5 steradians) organised into six banks, covering a wide range in scattering angle, 1.1 – 169.3°. GEM also features adjustable beam apertures, a nimonic chopper to cut out fast neutrons and disc choppers to reduce wavelength range where necessary [14].

Room temperature diffraction patterns have been obtained using GEM, for β-$Mn_{1-x}Co_x$ with x = 0.25, 0.10 and 0.05.

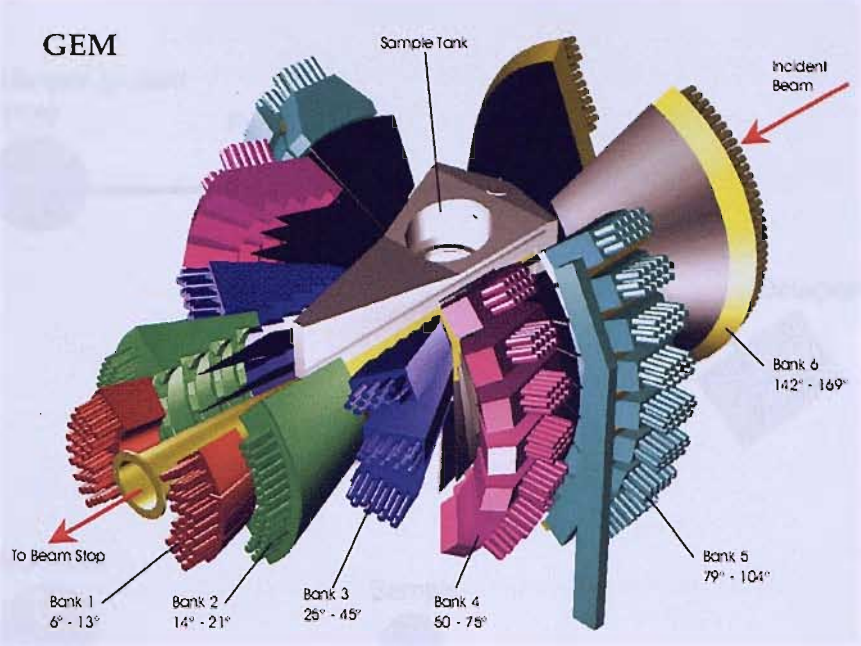

Figure 4.6: the layout of GEM's six scintillator detector banks [14]

4.5. Inelastic Scattering and Dynamical Analysis

The experimental work for this thesis has been carried out using purely time-of-flight instrumentation both at ISIS and the ILL. The time-of-flight (TOF) technique carries a major advantage in that a large detector solid angle may be utilized simultaneously (as opposed to the single-detector triple-axis method).

Direct Geometry TOF Instrumentation

Direct geometry instruments select the neutron energy E_i incident on a sample by use of a crystal or chopper[5], and scattered energy E_f calculated from the total time of flight, while indirect geometry instruments use a crystal or filter to select the final energy.

[5] Although there is not the same need as for a continuous source, some monochromation is required as a pulse still has finite width.

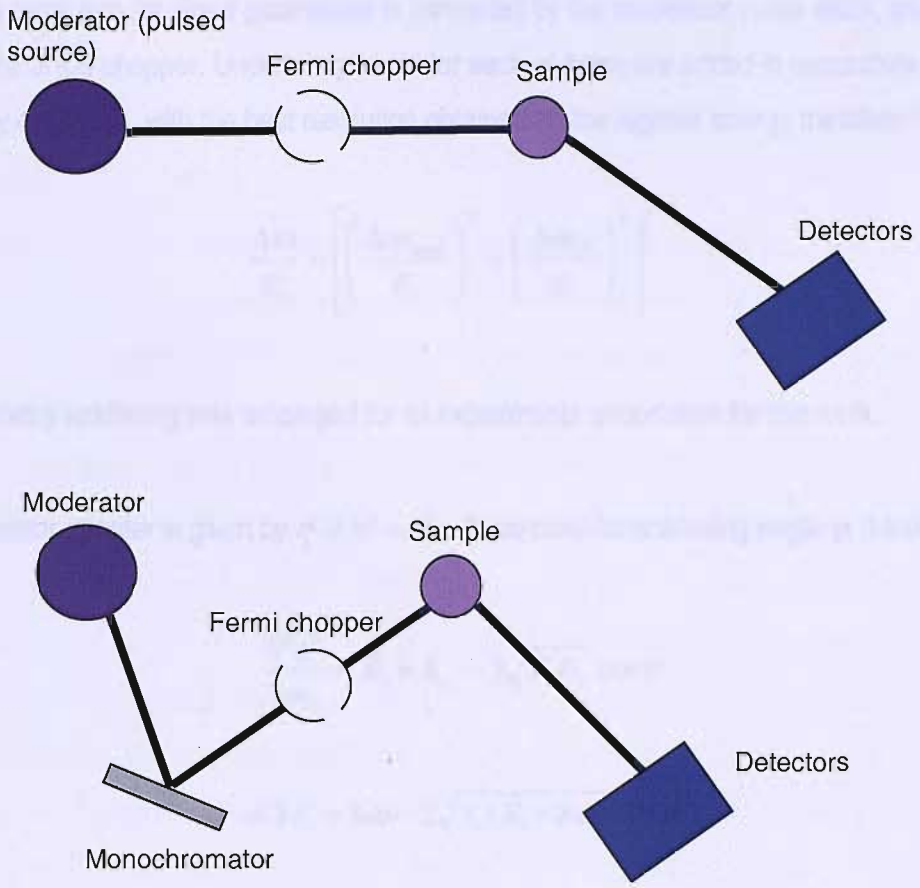

Figure 4.7: layout of a direct-geometry time-of-flight spectrometer at a pulsed source, using a chopper (top) and crystal monochromation (bottom)

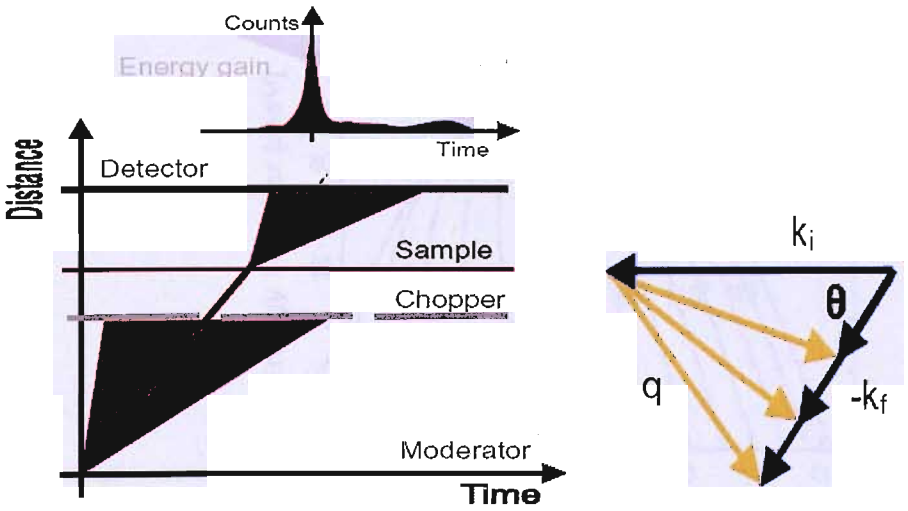

Figure 4.8: time-of-flight diagram for a direct-geometry instrument. "Energy gain" and "energy loss" refer to the neutrons. The scattering triangle for this set-up is also shown [15]

The energy resolution for direct geometries is controlled by the moderator pulse width, and the opening time of the chopper. Uncertainty terms for each of these are added in quadrature to give total energy resolution, with the best resolution obtained for the highest energy transfers [15].

$$\frac{\Delta\omega}{E_i} = \left[\left(\frac{\Delta\omega_{\mathrm{mod}}}{E_i}\right)^2 + \left(\frac{\Delta\omega_{ch}}{E_i}\right)^2\right]^{1/2}$$

Direct geometry scattering was employed for all experiments undertaken for this work.

The wavevector transfer is given by $q^2 = k_i^2 + k_f^2 - 2.k_i k_f \cos\phi$ for scattering angle ϕ. It follows that:

$$\frac{\hbar^2 q^2}{2m_n} = E_i + E_f - 2\sqrt{E_i E_f}\cos\phi$$

$$= 2E_i - \hbar\omega - 2\sqrt{E_i(E_i - \hbar\omega)}\cos\phi$$

Detectors are positioned to cover the maximum solid angle, so that energy and momentum trajectories may be plotted as completely as possible in q-E space.

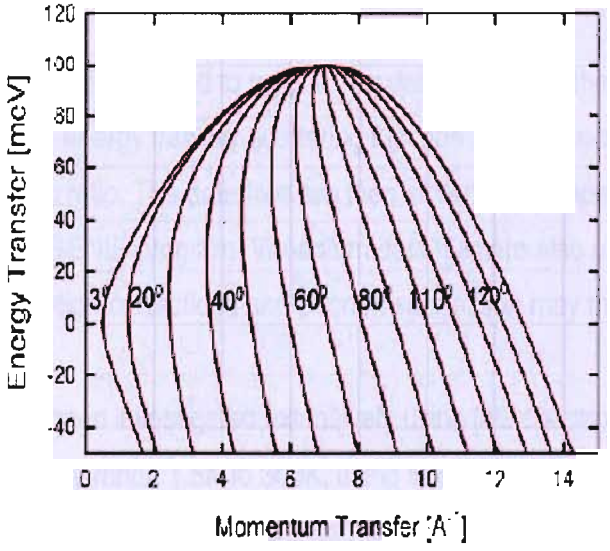

Figure 4.9: the q versus ω detector plot for a direct geometry instrument with E_i = 100meV

Instrumentation

HET

The High Energy Transfer spectrometer at ISIS is optimised for the study of magnetic excitations above 50meV, although the incident neutron energy can be varied between 15 and 2eV. Energy resolution varies between 2 and 6%, depending on the monochromating (Fermi) chopper used. The primary flight path, from moderator to sample, is 12m and there are two secondary flight paths to detector banks at 2.5m and 4m. The low angle detector bank comprises an array of ^{3}He tubes (2.5m) covering angles from 9 - 29°, and a position-sensitive ^{3}He detector array (4m) covering angles from 3 - 7°. Further ^{3}He detector sets cover scattering angles of 110 - 125° (at 4m) and 130 - 140° (2.5m). A nimonic chopper is used to reduce background by closing the spectrometer beam tube as the proton beam hits the spallation target, thus preventing scattering from fast neutrons that thermalise within the spectrometer. The beam tubes and detector tanks are also evacuated to a rough vacuum to minimise air scattering. The internal surfaces of the sample tank are lined with a low-hydrogen B4C resin (also incorporated in shields behind the detectors), again to minimise scattering from high energy neutrons [16].

Four chopper slit packages are available, each optimised to a particular incident energy, and including the "S" ("sloppy") chopper, which gives a relaxed resolution but large flux [16].

The data analysis program HOMER is used to read in raw data and group them into workspaces defined by a mapping file. The energy transfer scattering function is produced, and corrected for detector efficiency and the k_f/k_i ratio. The data files are then stored in an appropriate format to allow subsequent analysis with the GENIE program. Vanadium data files are also used for normalisation at this stage. Subsequent absorption corrections and phonon subtraction may then be carried out.

The β-$Mn_{1-x}M_x$ systems have been investigated extensively using this spectrometer. Spectra have been obtained across the energy range 1.5K to 300K, using incident energies of 40 and 100meV. A study of spin gap formation in the RMn_4Al_8 compounds has also been carried out on HET, using incident energies of 20, 80 and 150 meV, again at temperatures ranging from 1.5K to 300K.

IN4

IN4 is a direct geometry, time-of-flight instrument, at the ILL reactor facility. Two background choppers act as low-pass filters, removing fast neutrons and gamma rays from the beam. The choppers also eliminate higher wavelength orders of $n\lambda$ selected by the monochromator. The monochromator itself is an assembly of 55 pyrolytic graphite crystals and has variable curvature, enabling the incident beam to be focussed onto a suitable small area at the sample. For the experiments described in this thesis, wavelengths of 1.1Å and 2.2Å were selected. A Fermi chopper transmits short pulses of 10 – 50 μs to the sample, and hence sets the resolution. IN4 also uses a ^{3}He detector bank [17].

A study of a $PrMn_4Al_8$ sample was carried out on this instrument, in order to specifically investigate crystal field excitations.

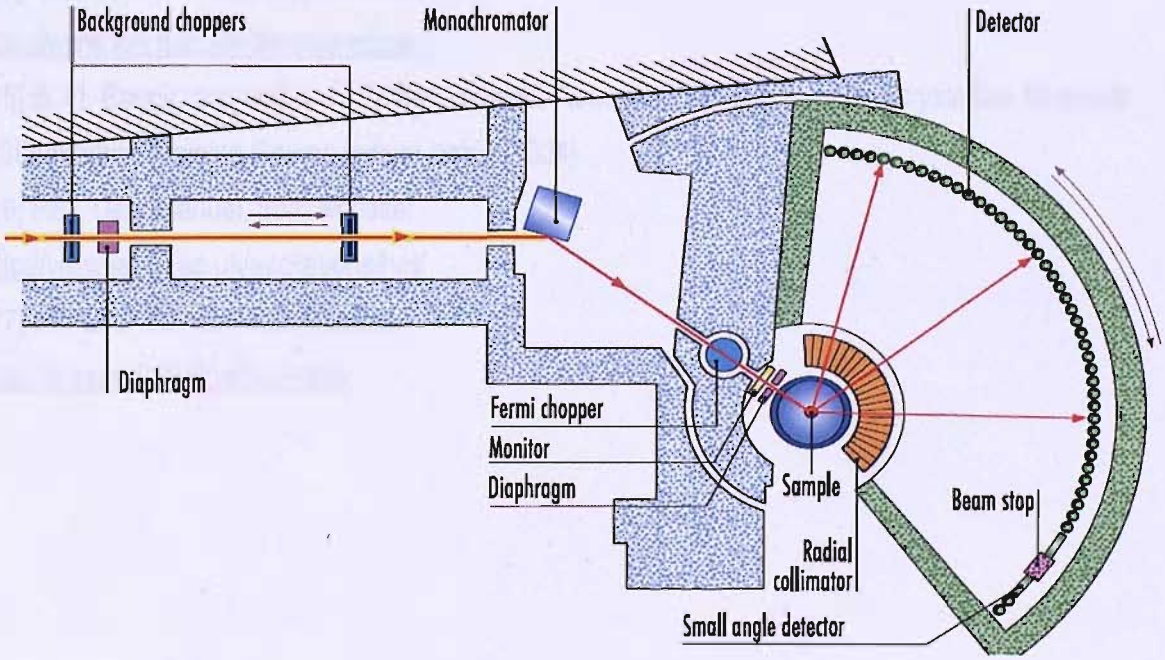

Figure 4.10: layout of the IN4 instrument (ILL) [17]

References

[1] A. C. Hannon, *Neutron Sources* (ISIS Neutron Training Course lecture notes, 2004)

[2] Website of Institut Laue-Langevin

[3] Website of ISIS

[4] Diagram taken from www.missouri.edu/~physwww/neutron_scattering

[5] G. L. Squires, *Introduction to Thermal Neutron Scattering* (1978), Cambridge University Press

[6] S. W. Lovesey, *Theory of Neutron Scattering from Condensed Matter* (1984), Clarendon Press

[7] A. Boothroyd, *Introductory Theory* (9th Oxford School on Neutron Scattering lecture notes, 2005)

[8] C G Windsor, *Pulsed Neutron Scattering*, (Taylor and Francis) 1981

[9] P. J. Brown, International Tables of Crystallography Vol III, p391

[10] B. D. Rainford, *Magnetism and Neutron Scattering*, in "Neutron Scattering on a Pulsed Source" (Eds. B. D. Rainford, R. Cywinski and R. J. Newport p.354)

[11] R. I. Smith, *Powder Diffraction* (ISIS Neutron Training Course lecture notes, 2004)

[12] Polaris User Manual, from website:
http://www.isis.rl.ac.uk/crystallography/polaris/

[13] ROTAX User Manual, from website:
http://www.isis.rl.ac.uk/excitations/rotax/

[14] GEM User Manual, from website:
http://www.isis.rl.ac.uk/disordered/gem

[15] S. M. Bennington and S. F. Parker, *Inelastic Neutron Scattering from Polycrystalline Materials* (ISIS Neutron Training Course lecture notes, 2004)

[16] HET User Manual, from website:
http://www.isis.rl.ac.uk/excitations/het/

[17] IN4 User Manual, from website:
http://www.ill.fr/YellowBook/IN4/

5. Neutron Polarization Analysis

5.1 Introduction

If the incident neutron beam in a scattering experiment can be polarized with respect to spin, subsequent analysis of the *x*, *y* and *z* components of the scattered neutron polarization will allow the extraction of a purely magnetic response. The separation of magnetic and nuclear scattering data has been essential in the studies in this thesis, and polarized neutron measurements have in general facilitated the analysis of magnetic structure, dynamics and short-range correlations.

Polarized neutron techniques make up a small but significant part of the experimental studies reported in this thesis, for example enabling the magnetic structure of β-$Mn_{1-x}Ru_x$ to be determined. As a full description of polarized neutron scattering theory is particularly extensive, the main points will be summarised in this chapter.

5.2 Production of Polarized Neutron Beams

For a scattering experiment in which a single quantisation axis is defined, the polarization of a neutron beam in an applied field may be expressed as [1]

$$P = \frac{F-1}{F+1}$$

where *F* is the *flipping ratio* of neutron spins parallel and antiparallel to the field, denoted N_+ and N_-. There are three principal methods of beam polarization, utilising filters, mirrors and crystals. All measurements reported in this thesis were carried out using the D7 spectrometer at the Institut Laue Langevin, which uses a supermirror polarizer and analyzers [2].

Supermirror polarization

Neutrons have a property analogous to an optical refractive index, which may be defined for a neutron passing between two media and experiencing an energy change equal to a potential $\langle V \rangle$ [1]:

$$n = \frac{k_2}{k_1} = \left[\frac{E_1 - \langle V \rangle}{E_1} \right]^{1/2} \approx 1 - \frac{\langle V \rangle}{2E_1}$$

If $\langle V \rangle$ is of the form of the Fermi pseudopotential, the spin dependent refractive index is given by

$$n_{\pm} = 1 - \left(\frac{N\lambda^2}{2\pi} \right) (\bar{b} \pm \bar{p})$$

where *b* and *p* are the mean coherent nuclear and magnetic scattering lengths, *N* is the number density of scattering centres and λ is the neutron wavelength. Implementing Snell's law of refraction enables the critical incident angle for each neutron state leading to total external reflection to be defined:

$$\theta_{c\pm} = \lambda \left[\frac{N}{\pi} (\bar{b} \pm \bar{p}) \right]^{1/2}$$

between $\theta c+$ and $\theta c-$, the reflected beam is effectively fully polarized.

Multi-bilayer systems of alternating magnetic and nonmagnetic material may be assembled in order to establish an extra Bragg peak at $\sin\theta/\lambda$, in addition to that at $\sin\theta c/\lambda$. Introducing a gradient into the layer spacing leads to a range of effective Bragg angles, and extends the reflectivity from $m = 2$ to $m = 4$ times the θ/λ values expected for normal mirror reflections [3]. This is the principle behind the development of supermirrors, in which several hundred bilayers are typically incorporated: production techniques at the ILL involve sputtering of alternate cobalt and titanium layers onto glass substrate, with around 500 bilayers required for a $m = 3$ supermirror. In this system, consisting of a bilayer of materials A and B, the reflectivity takes the form [1]:

$$R_{\pm} \propto [N_A b_A - N_B (b_B \pm p_B)]^2$$

N and b can be selected so that $R_- = 0$, resulting in a 100% polarized beam for all incident angles. The situation is complicated by the fact that neutrons with polarization P_- must be removed, usually by absorption into a gadolinium layer, at a cost of a reduced polarization due to a non-zero reflectivity. Practical supermirror stacked assemblies are curved to ensure at least one reflection of incident neutrons, and can accommodate an increased angular divergence.

D7 has a focusing, $m = 2.8$ supermirror arrangement consisting of 500 bilayers of Co and Ti sputtered onto glass substrates. Those neutrons that do not correspond to the desired spin state are transmitted by the magnetic layers and absorbed by the substrate.

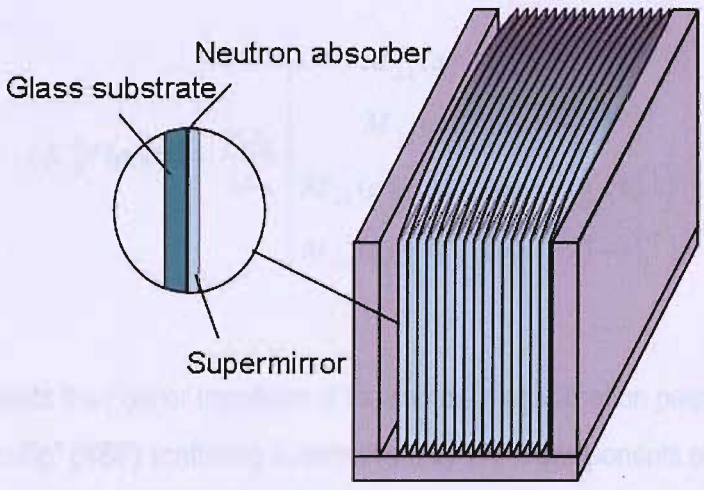

Figure 5.1: supermirror polarizer/analyzer structure on the D7 instrument [2]

5.3 Scattering Theory for Polarized Neutrons

The differential cross-section for elastic neutron scattering may be expressed as

$$\frac{d\sigma}{d\Omega} = \left(\frac{m_n}{2\pi\hbar}\right)\left|\langle k'S'|V|kS\rangle\right|^2$$

For nuclear scattering, where the potential takes the form of the pseudopotential, the matrix elements for processes in which the neutron spin may or may not be flipped are given by:

$$\langle S'|b|S\rangle = b\langle S'|S\rangle = \left\{ \begin{array}{ll} b\left\{ \begin{array}{ll} |\uparrow\rangle \rightarrow & |\uparrow\rangle \\ |\downarrow\rangle \rightarrow & |\downarrow\rangle \end{array} \right\} \\ 0\left\{ \begin{array}{ll} |\uparrow\rangle \rightarrow & |\downarrow\rangle \\ |\downarrow\rangle \rightarrow & |\uparrow\rangle \end{array} \right\} \end{array} \right\}$$

the two upper cases in parentheses represent scattering in which the spins retain their initial polarization, and the two lower cases correspond to processes that cause spin flipping,. Similarly, the matrix elements for magnetic scattering are defined as [1]:

$$\langle S'|V(\boldsymbol{q})|S\rangle = \frac{\gamma_n r_0}{2\mu_B} \left\{ \begin{array}{ll} M_{\perp z}(\boldsymbol{q}) & |\uparrow\rangle \rightarrow |\uparrow\rangle \\ M_{\perp z}(\boldsymbol{q}) & |\downarrow\rangle \rightarrow |\downarrow\rangle \\ M_{\perp x}(\boldsymbol{q}) - M_{\perp y}(\boldsymbol{q}) & |\uparrow\rangle \rightarrow |\downarrow\rangle \\ M_{\perp x}(\boldsymbol{q}) + M_{\perp y}(\boldsymbol{q}) & |\downarrow\rangle \rightarrow |\uparrow\rangle \end{array} \right\}$$

where $\boldsymbol{M}_{\perp}(\boldsymbol{q})$ represents the Fourier transform of the sample magnetisation perpendicular to $\boldsymbol{q}$. Therefore, "non-spin-flip" (NSF) scattering is sensitive only to the components of magnetisation parallel to the neutron spin, while "spin-flip" (SF) scattering is sensitive only to perpendicular components.

A bound state is created between neutron and nucleus during the scattering process, which may correspond to a spin singlet or triplet. As the scattering lengths corresponding to these situations are different, and dependent on nuclear spin, a scattering length operator may be defined [4]:

$$\hat{b} = A + B\boldsymbol{\sigma} \cdot \boldsymbol{I}$$

where *A* & *B* are functions of the different scattering lengths, *I* is the nuclear spin vector and $\boldsymbol{\sigma}$ represents the Pauli spin matrices. The matrix elements are then calculated to be [1]:

$$\langle S'|b|S\rangle = \begin{Bmatrix} A+BI_z & |\uparrow\rangle \rightarrow |\uparrow\rangle \\ A-BI_z & |\downarrow\rangle \rightarrow |\downarrow\rangle \\ B(I_x - iI_y) & |\uparrow\rangle \rightarrow |\downarrow\rangle \\ B(I_x + iI_y) & |\downarrow\rangle \rightarrow |\uparrow\rangle \end{Bmatrix}$$

The scattering matrix elements may then be fully defined for all SF and NSF cases, [5]. From these it is determined that if the polarization vector is parallel to the scattering vector, then the magnetisation in the direction of the polarization will not be observed. As neutrons will only be scattered by components of the magnetization perpendicular to the scattering vector, all magnetic scattering for the case where polarization is parallel to the scattering vector will be spin-flip, since this only sees the component of *M* perpendicular to the neutron spin.

Nuclear incoherent scattering should also be considered, and for an isotropic distribution of I_x, I_y, I_z corresponding to randomly oriented system of nuclei, the *spin-incoherent* and *isotope-incoherent* scattering lengths may also be defined [1]:

$$b_{II} = \sqrt{\left\langle \left(\overline{b}\right)^2 \right\rangle - \overline{b^2}}$$
$$b_{SI} = \sqrt{B^2 I(I+1)}$$

In the case of a ferromagnetic sample aligned in a field perpendicular to the scattering vector, $\boldsymbol{M}_\perp$ has no component in the *xy*-plane, and the spin-flip scattering cross section is zero. The scattering cross sections for neutrons polarized parallel (-) and antiparallel (+) to the field are

$$\frac{d\sigma}{d\Omega} = \left[F_N(\boldsymbol{q}) \mp F_M(\boldsymbol{q})\right]^2$$

where

$$F_N(\boldsymbol{q}) = \sum_i b_i \exp(i\boldsymbol{q}\cdot\boldsymbol{r}_i)$$
$$F_M(\boldsymbol{q}) = \gamma_n r_0 \sum_i g_{J_i} \boldsymbol{J}_i f_i(\boldsymbol{q}) \exp(i\boldsymbol{q}\cdot\boldsymbol{r}_i)$$

The flipping ratio of the parallel and antiparallel cross-sections for a given Bragg reflection may then be determined.

The situation is complicated for 3-directional polarization analysis, referred to as the X-Y-Z difference method. This set-up involves a multidetector covering a range of scattering angles, removing the possibility of parallel scattering and polarization vectors for all detector angles. For a situation utilizing one spin flipper placed before the sample, the observed transitions are $|\uparrow\rangle \rightarrow |\uparrow\rangle$ and $|\downarrow\rangle \rightarrow |\uparrow\rangle$, for which spin- and non-spin-flip cross sections may be defined in terms of a generalised polarization (*x,y,z*) direction, ξ. In the case of a disordered paramagnet, these may be simply expressed as [4]

$$\left(\frac{d\sigma}{d\Omega}\right)^{\xi}_{NSF} = \frac{1}{3}\left(\frac{\gamma r_0}{2}\right)^2 g^2 f^2(\boldsymbol{q})\boldsymbol{J}(\boldsymbol{J}+1)\left[1-\left(\hat{\boldsymbol{P}}\cdot\hat{\boldsymbol{q}}\right)^2\right]$$

$$\left(\frac{d\sigma}{d\Omega}\right)^{\xi}_{SF} = \frac{1}{3}\left(\frac{\gamma r_0}{2}\right)^2 g^2 f^2(\boldsymbol{q})\boldsymbol{J}(\boldsymbol{J}+1)\left[1+\left(\hat{\boldsymbol{P}}\cdot\hat{\boldsymbol{q}}\right)^2\right]$$

Arranging for ξ to coincide with the scattering vector confines all magnetic scattering to the spin-flip cross-section. A unit scattering vector with respect to a detector in the x-y plane is defined in terms of the *Scharpf angle* α, between $\boldsymbol{q}$ and an arbitrary x-axis.

$$\hat{q} = \begin{pmatrix} \cos\alpha \\ \sin\alpha \\ 0 \end{pmatrix}$$

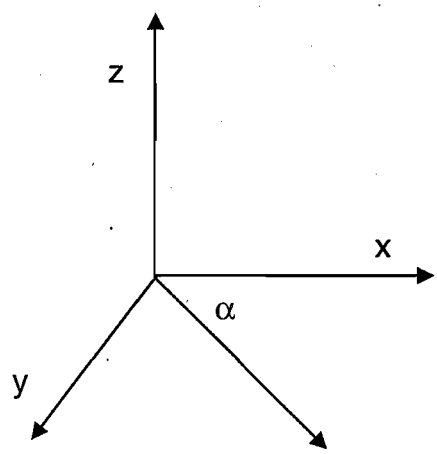

The spin-flip and non-spin-flip cross-sections for each directions may be formulated [6] using this unit scattering vector, including nuclear coherent, isotope incoherent and spin-incoherent terms.

$$\left(\frac{d^2\sigma}{d\Omega dE}\right)^{Z}_{SF} = \frac{2}{3}\left(\frac{d^2\sigma}{d\Omega dE}\right)_{SI} + \frac{1}{2}\left(\frac{d^2\sigma}{d\Omega dE}\right)_{MAG}$$

$$\left(\frac{d^2\sigma}{d\Omega dE}\right)^{Z}_{NSF} = \frac{1}{3}\left(\frac{d^2\sigma}{d\Omega dE}\right)_{SI} + \frac{1}{2}\left(\frac{d^2\sigma}{d\Omega dE}\right)_{MAG} + \left(\frac{d^2\sigma}{d\Omega dE}\right)_{NUC} + \left(\frac{d^2\sigma}{d\Omega dE}\right)_{II}$$

$$\left(\frac{d^2\sigma}{d\Omega dE}\right)^{Y}_{SF} = \frac{2}{3}\left(\frac{d^2\sigma}{d\Omega dE}\right)_{SI} + (1+\sin^2\alpha)\frac{1}{2}\left(\frac{d^2\sigma}{d\Omega dE}\right)_{MAG}$$

$$\left(\frac{d^2\sigma}{d\Omega dE}\right)^{Y}_{NSF} = \frac{1}{3}\left(\frac{d^2\sigma}{d\Omega dE}\right)_{SI} + (\cos^2\alpha)\frac{1}{2}\left(\frac{d^2\sigma}{d\Omega dE}\right)_{MAG} + \left(\frac{d^2\sigma}{d\Omega dE}\right)_{NUC} + \left(\frac{d^2\sigma}{d\Omega dE}\right)_{II}$$

$$\left(\frac{d^2\sigma}{d\Omega dE}\right)^{X}_{SF} = \frac{2}{3}\left(\frac{d^2\sigma}{d\Omega dE}\right)_{SI} + (1+\cos^2\alpha)\frac{1}{2}\left(\frac{d^2\sigma}{d\Omega dE}\right)_{MAG}$$

$$\left(\frac{d^2\sigma}{d\Omega dE}\right)^{X}_{NSF} = \frac{1}{3}\left(\frac{d^2\sigma}{d\Omega dE}\right)_{SI} + (\sin^2\alpha)\frac{1}{2}\left(\frac{d^2\sigma}{d\Omega dE}\right)_{MAG} + \left(\frac{d^2\sigma}{d\Omega dE}\right)_{NUC} + \left(\frac{d^2\sigma}{d\Omega dE}\right)_{II}$$

The principal experimental cross-sections are extracted by combination of these expressions: the magnetic cross-section is obtained via summation of the spin-flip (or non-spin flip) terms in each direction, while the spin-incoherent term involves the difference between total non-spin flip and magnetic scattering. The nuclear and isotope-incoherent terms are combined into a single cross-section, obtained by taking the difference between total non-spin-flip and spin-flip cross-sections [7].

$$\left.\begin{aligned}\left(\frac{d^2\sigma}{d\Omega dE}\right)_{MAG} &= 2\left[\left(\frac{d^2\sigma}{d\Omega dE}\right)^{X}_{SF} + \left(\frac{d^2\sigma}{d\Omega dE}\right)^{Y}_{SF} - 2\left(\frac{d^2\sigma}{d\Omega dE}\right)^{Z}_{SF}\right] \\ \left(\frac{d^2\sigma}{d\Omega dE}\right)_{MAG} &= 2\left[2\left(\frac{d^2\sigma}{d\Omega dE}\right)^{Z}_{NSF} - \left(\frac{d^2\sigma}{d\Omega dE}\right)^{X}_{NSF} - \left(\frac{d^2\sigma}{d\Omega dE}\right)^{Y}_{NSF}\right]\end{aligned}\right\} = \frac{2}{3}\left(\frac{\gamma_n r_0}{2}\right)^2 g_J^2 f^2(q) J(J+1)$$

$$\left(\frac{d^2\sigma}{d\Omega dE}\right)_{SI} = \frac{1}{2}\left(\frac{d^2\sigma}{d\Omega dE}\right)_{total\ SF} - \left(\frac{d^2\sigma}{d\Omega dE}\right)_{MAG} = B^2 I(I+1)$$

$$\left(\frac{d^2\sigma}{d\Omega dE}\right)_{NUC+II} = \frac{1}{6}\left[2\left(\frac{d^2\sigma}{d\Omega dE}\right)_{total\ NSF} - \left(\frac{d^2\sigma}{d\Omega dE}\right)_{total\ SF}\right] = b^2 S(q) + \overline{b^2} - (\bar{b})^2$$

In order to optimize statistics, the magnetic cross-section is usually taken as the weighted average of the spin-flip and non-spin-flip magnetic cross sections [2].

5.4 The D7 Instrument

The general-purpose long wavelength spectrometer D7 (ILL) has been used to obtain a number of spectra for various samples as part of this study. This instrument receives neutrons from the H15 reactor cold source, and utilizes a horizontally and vertically focusing graphite crystal monochromator situated in the neutron guide. Available incident neutron wavelengths are λ = 3.1Å, 4.8Å or 5.7Å, corresponding to E_i = 8.97, 3.49 or 2.35 meV, with higher orders of incident wavelength removed using a beryllium filter [2].

A guide field of ~ 1mT is used to maintain the polarization of the neutron beam in the z-direction after it passes through the supermirror polarizer, until it reaches the sample. This is placed between three orthogonal spin turn coils, which rotate the neutron polarization along the *x*- and *y*- axes prior to the beam falling incident upon the sample, then rotate the scattered neutrons back by the same angle to enable measurement of the scattering cross-section in each direction [2].

The 71 m = 2.8 supermirror analyzers are arranged for transmission of neutrons polarized in the positive *z*-direction. A device must therefore be employed to invert the neutron spin in order to extract the spin-flip cross-section. This function is performed by a Mezei π flipper, in which spin-flipping of the beam is achieved by use of a field $\boldsymbol{H}_{\pi}$ causing Larmor rotation of the neutron spins. The transition from guide to flipper field corresponds to an adiabatic process, with no change in the neutron energy state. The non-spin-flip cross-section is simply measured with an inactive Mezei flipper.

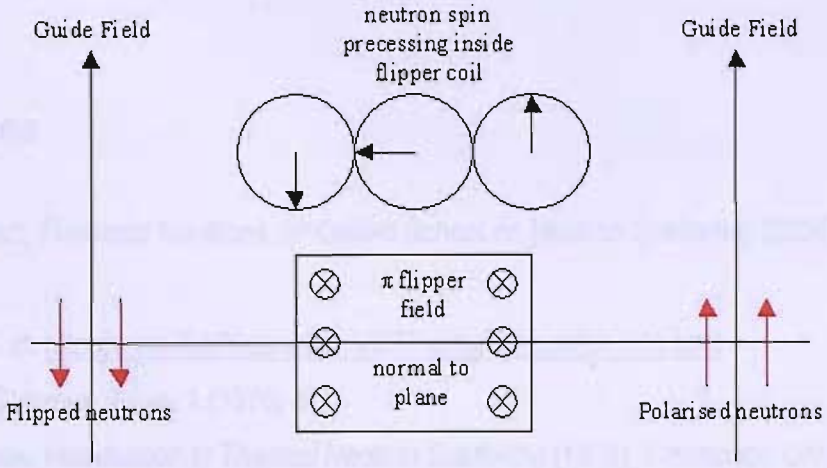

Figure 5.2: spin flipping of polarized neutrons passing through a Mezei flipper (from right to left) [2]

The analyzers are situated in front of 142 ^{3}He detectors, located 1.5m from the sample position. The layout of the spectrometer is shown in Figure 5.3 below.

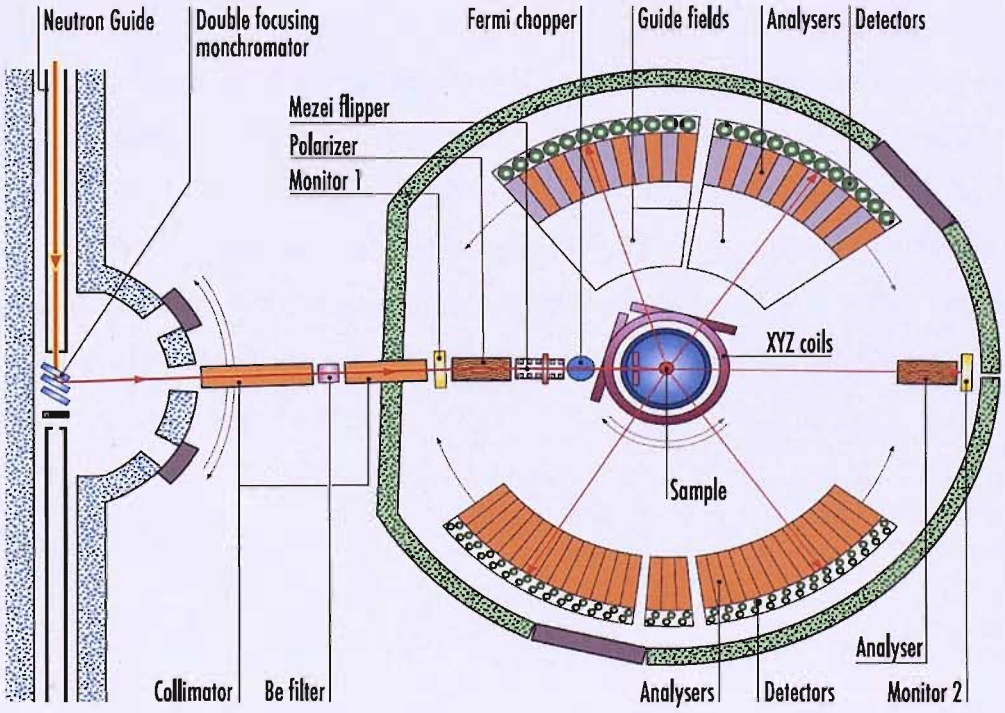

Figure 5.3: layout of the D7 spectrometer (ILL) [2]

References

[1] J. R. Stewart, *Polarized Neutrons*, 9th Oxford School on Neutron Scattering (2005) lecture material

[2] D7 manual at: http://www.ill.fr/YellowBook/D7/home/D7_useful_info.html

[3] F. Mezei, Commun. Phys. **1** (1976) 81

[4] G. L. Squires, *Introduction to Thermal Neutron Scattering* (1978), Cambridge University Press

[5] R. M. Moon, T. Riste and W. C. Koehler, Phys. Rev. **181** (1969) 920

[6] O. Scharpf and H. Capellmann, Phys. Stat. Sol. **A135** (1993) 359

[7] J. R. Stewart, K. H. Andersen, R. Cywinski and A. P. Murani, J. Applied Phys. **87** (2000) 5425

6. Phonon Subtraction Techniques

6.1 Introduction

In studies of magnetic dynamics by inelastic neutron scattering, some method must be employed to remove the lattice dynamics from the total response. There are a number of ways to achieve this: firstly, the technique of neutron polarisation analysis as described in Chapter 5 allows direct separation of magnetic and nuclear scattering as the data is collected. This technique is preferable, and with the current achievable high data collection rates, is the most straightforward way of obtaining the pure magnetic response of a sample. However, with the instrumentation currently available, it is not possible to separate these responses over a wide range of energy transfers.

Where polarised neutron instrumentation is not available, it may also be possible to estimate a sample's lattice vibration spectrum using a so-called "phonon blank". This is an isostructural material whose component elements are of approximately equal mass to those of the system of interest, the response of which is known to be entirely non-magnetic. In studies of RMn_4Al_8 compounds, YMn_4Al_8 has previously been assumed to be nonmagnetic and has consequently been used to estimate the phonon response in other compounds of this series. This has been shown to be an unsuitable choice in the current studies, since it has a small but finite magnetic scattering cross-section. $CeMn_4Al_8$, another potential phonon blank candidate especially suitable for analysis of $LaMn_4Al_8$ due to the close masses of lanthanum and cerium, has also been dismissed as a result of a small magnetic signal. The isostructural (and nonmagnetic) $LaCu_4Al_8$ has made a significant contribution to the estimation of the phonon data in $LaMn_4Al_8$.

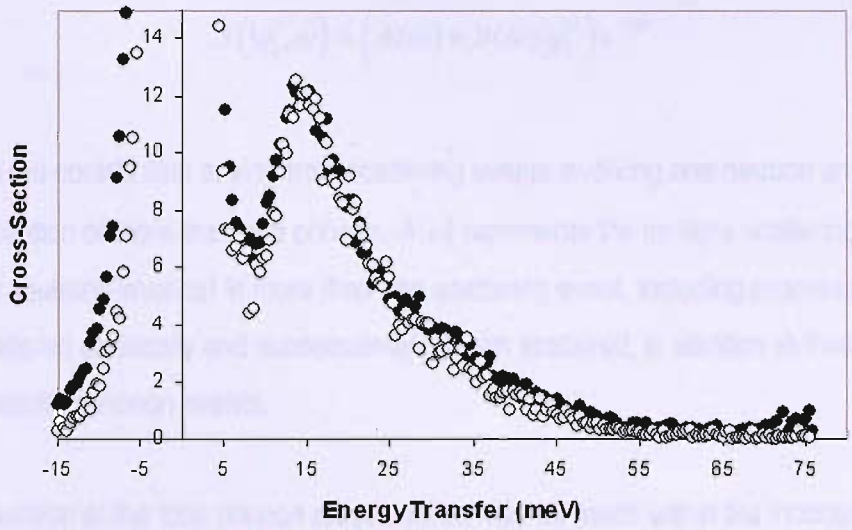

Figure 6.1: high (black circles) and low-angle (open circles) scattering data for $LaCu_4Al_8$, E_i = 80meV (HET). The scaling factor for the low-angle data used here is 3

Simple subtraction of the scattering cross-sections has not been possible, as the opposing scattering lengths of Cu and Mn give a false estimation of magnitude in any phonon features and can lead to oversubtraction. Alternatively, high-angle scattering corresponding to large wavevector transfers can be used to estimate the phonon response if appropriately scaled. In this region the magnetic form factor is anticipated to have fallen to a negligible value while the phonon scattering, which increases as $q^2 e^{-2W}$, dominates the response. The phonon blank sample $LaCu_4Al_8$ has been treated in this way, with a subtraction of high-angle from low-angle data used to obtain a suitable scaling factor for use in subsequent correction processes.

It is also possible to obtain numerical estimates of the phonon spectrum, using a simulation routine as discussed in more detail in the following subsection. This has been used in conjunction with the other techniques listed above, to achieve still more accurate phonon subtractions.

6.2 Monte Carlo Phonon Simulations

The total phonon scattering cross section may be expressed (within the incoherent approximation) simply as [1]

$$S\left(|\boldsymbol{q}|,\omega\right)=\left(A(\omega)+B(\omega)|\boldsymbol{q}|^2\right)\mathrm{e}^{-2W}$$

where $B(\omega)$ is the contribution arising from scattering events involving one neutron and the creation/annihilation of more than one phonon. $A(\omega)$ represents the multiple scattering contribution, resulting from neutrons involved in more than one scattering event, including processes by which a neutron is scattered elastically and subsequently phonon scattered, in addition to those involving two or more consecutive phonon events.

An exact calculation of the total phonon cross-section may be made within the incoherent approximation if the single phonon density of states is known. The phonon scattering cross section may be expressed exactly as [2]:

$$S(|\boldsymbol{q}|,\omega)=\frac{N}{2\pi\hbar}\int_{-\infty}^{\infty}dt\exp[-i\omega t]\exp\left\{\frac{\hbar|\boldsymbol{q}|^2}{2M}[\gamma(t)-\gamma(0)]\right\}$$

for N sites of mass M. $\gamma(t)$ is the displacement correlation function, given by

$$\gamma(t)=\int_{-\infty}^{\infty}d\omega\frac{Z(\omega)}{\omega}n(\omega)\exp[-i\omega t]$$

where $Z(\omega)$ is the single phonon density of states and $n(\omega)$ is a thermal population factor.

$Z(\omega)$ in these analyses has been estimated from high-angle scattering, after removing the high-energy tail which is assumed to heavily feature multi-phonon events. For a given temperature and incident energy, a data sample corresponding to this high-$\boldsymbol{q}$ scattering has been selected using the MATLAB-based MSlice software. This, along with sample mass, density and dimensions forms the input to the DISCUS program[1], containing Monte Carlo phonon simulation algorithms used to calculate the ratio of once-scattered to twice-scattered neutrons. The output is in the form of the total phonon cross-section for the particular spectrum, which may then be simply subtracted from the total scattering cross-section to obtain the magnetic response.

[1] Originally authored by M. W. Johnson

The absolute scale of this simulated phonon contribution has been verified using the scaling of high-angle data as described earlier.

References

[1] R. Osborn (*from private communication with B. D. Rainford and S. J. Dakin*) taken from S. J. Dakin, *Spin Fluctuations in Metallic Magnets* (PhD Thesis), University of Southampton (1992) Chapter 5

[2] S. W. Lovesey, *Theory of Neutron Scattering from Condensed Matter* (1984), Clarendon Press

7. Studies of β-$Mn_{1-x}M_x$ systems (M = Co, Ru)

7.1. Introduction

Of the four[1] allotropes of manganese, the β-phase is unusual in that it is the only phase of that element that fails to display a magnetically ordered state down to the lowest temperatures. This absence of long-range order was confirmed by the very early experimental work: neutron powder diffraction studies gave no indication of either ferromagnetic (from high magnetic field measurements) or antiferromagnetic order, as had been observed in α-Mn [1]. NMR experiments also observed paramagnetic behaviour down to 1.5K [2, 3]. β-Mn does however support large amplitude spin fluctuations, as has been observed via an enhanced Sommerfeld constant γ= 70mJ/mol.K^2 [4] and the temperature dependence of the NMR spin-lattice relaxation rate $1/T_1$, indicative of specifically antiferromagnetic correlations in these fluctuations [5, 6].

β-Mn is not a weakly interacting system, having a large dynamical moment [6]. Magnetic ordering in this case is suppressed by geometrical frustration inherent in the crystallography. The simple cubic crystal structure of space group $P4_132$ comprises a unit cell with lattice parameter a_0 = 6.30Å, containing 20 atoms [7]. These are shared between two inequivalent sites: eight atoms occupying Site I (near-neighbour separation 2.37Å) and 12 atoms on Site II (with interatomic distance 2.52Å). The first near-neighbour atoms of each point in the Site I sublattice form a shell of icosahedral coordination [8] that is the basis of a centre of pseudo five-fold symmetry. The Site II Mn are arranged so as to form a corner-sharing triangular network, of the form of a distorted Kagome lattice known as the "distorted windmill" arrangement. Together the Site I and II atoms form a distorted lattice of corner-sharing tetrahedra.

The coordinates of each of the 20 atoms have been listed according to early crystallographic studies [8]: these are given in Table 4.1 overleaf. If the atomic Site II positions correspond to a critical value of parameter *y*, which has been given as [9]

[1] At ambient pressure

$$y = \frac{9 - \sqrt{33}}{16} \sim 0.2035$$

then the triangular sublattice becomes equilateral, with the triangles of identical size. Reported values of *y* are close to this critical value [8, 10]. In this case the Site II β-Mn sublattice constitutes a prime example of a geometrically frustrated system of antiferromagnetically interacting spins.

The effect of introducing dilute quantities of impurity atoms into the β-Mn structure as a mechanism for lifting this frustration has been the subject of a number of studies. This has involved alloying with various transition and non-transition elements, and generally results in the stabilization of a static magnetic ground state with at least short-range order. Important findings from these investigations are summarized in the following section.

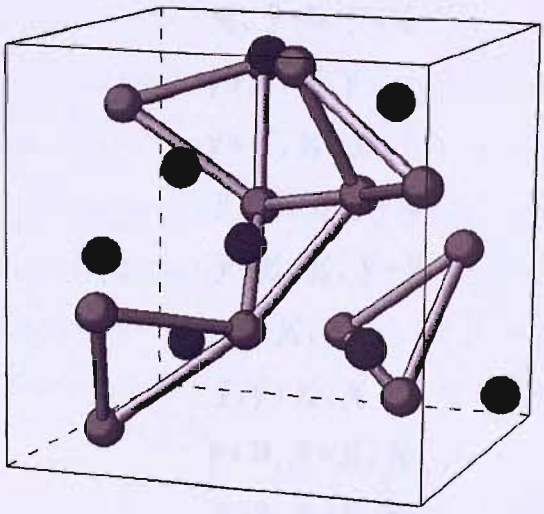

Figure 7.1: the cubic unit cell of β-Mn, showing the corner-sharing triangular network formed by the Site II atoms

Atomic Site	Coordinates	
Site I	x, x, x	$x = 0.061$
	$\bar{x}$ + ½ , $\bar{x}$, x+ ½	
	$\bar{x}$, x+ ½, $\bar{x}$ + ½	
	x+ ½, $\bar{x}$ + ½, $\bar{x}$	
	x+ ¾ , x+ ¼ , $\bar{x}$ + ¼	
	$\bar{x}$ + ¾ , $\bar{x}$ + ¾ , $\bar{x}$ + ¾	
	x+ ¼ , $\bar{x}$ + ¼ , $\bar{x}$ + ¾	
	$\bar{x}$ + ¼ , x+ ¾ , x+ ¼ ,	
Site II	⅛ , y, y + ¼	$y = 0.206$
	⅜ , $\bar{y}$, y + ¾	
	⅞ , y + ½, $\bar{y}$ + ¼	
	⅝ , $\bar{y}$ +½, $\bar{y}$ + ¾	
	y + ¼ , ⅛ , y	
	y + ¾ , ⅜ , $\bar{y}$	
	$\bar{y}$ + ¼ , ⅞ , y + ½	
	$\bar{y}$ + ¾ , ⅝ , $\bar{y}$ + ½	
	y, y + ¼ , ⅛	
	$\bar{y}$, y + ¾ , ⅜	
	y + ½, $\bar{y}$ + ¼ , ⅞	
	$\bar{y}$ +½, $\bar{y}$ + ¾ , ⅝	

Table 7.1: atomic positions of the β-Mn unit cell [8]

7.2. Previous Studies of β-Mn and β-$Mn_{1-x}M_x$

Magnetic Susceptibility

The magnetic susceptibility of β-Mn is nearly constant with temperature and implies Pauli paramagnetism [6] If aluminium is substituted into the lattice, the magnitude of $\chi(T)$ increases and the temperature dependence approaches a Curie-Weiss form [6]. A low temperature maximum occurs for alloys with $x \geq 0.05$, which appears to move to increasingly high temperatures with x. For those alloys with $x \geq 0.1$, the high temperature data is modelled by a modified Curie-Weiss law

$$\chi = \chi_0 + \frac{C}{T - \theta}$$

where χ_0 is a temperature-independent susceptibility term, the contribution of which decreases monotonically with increasing x. In addition, $|\theta|$ increases almost linearly with x (θ is negative for all alloys), and the effective paramagnetic moment μ_{eff}, deduced from C, rises rapidly. This behaviour suggests that the β-$Mn_{1-x}Al_x$ system acquires a localized moment as Al is introduced. The maximum is once again attributed to a spin glass transition, with the almost constant low temperature field-cooled susceptibility (measured for $x = 0.3$ in this study) lending support to this view.

At higher aluminium concentrations ($x \geq 0.1$), a characteristic spin glass-like bifurcation of field cooled and zero-field susceptibilities emerges above a broad peak in the ZFC susceptibility [11] it has been inferred from this data that a change in the magnetic ground state occurs in the vicinity of $x = 0.1$.

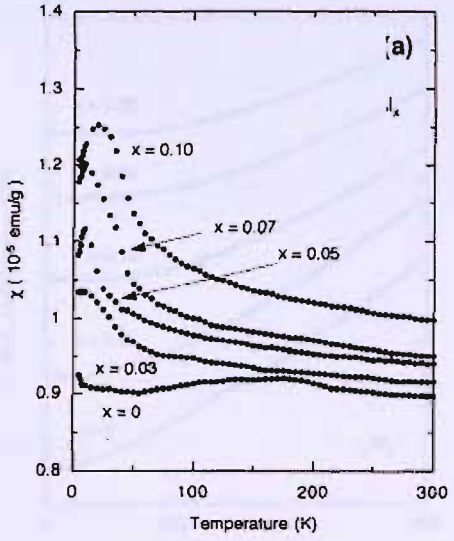

Figure 7.2: magnetic susceptibility $\chi(T)$ for various β-$Mn_{1-x}Al_x$ alloys [6]

Thermal Expansion and Spontaneous Volume Magnetostriction

Thermal expansion effects in β-$Mn_{1-x}Al_x$ have been investigated [6] for Al concentrations up to 20%. In β-$Mn_{1-x}Al_x$ alloys where $x \geq 0.05$, a temperature-independent region in the thermal expansion curve at low temperatures appears (in contrast the unit cell volume of β-Mn increases steadily with increasing temperature). The width of this flat region increases with x, and is attributed to spontaneous volume magnetostriction. The coefficient of linear thermal expansion extracted from this data shows a linear decrease with x, from a large value of $\kappa = 30 \times 10^{-6}\ K^{-1}$ in β-Mn to $\kappa = 18 \times 10^{-6}\ K^{-1}$.

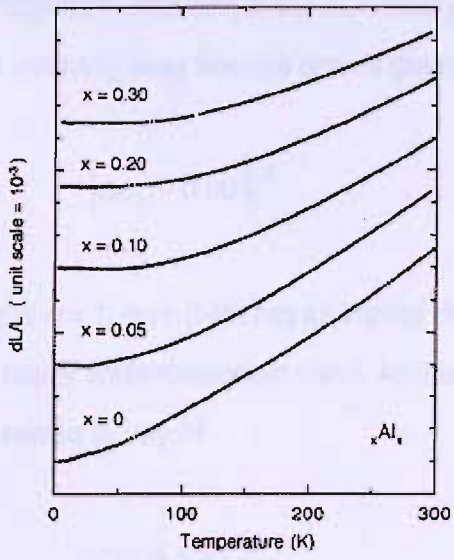

Figure 7.3: thermal expansion curves for various β-$Mn_{1-x}Al_x$ alloys [6]

Specific Heat

The electronic specific heat behaviour of nearly- and weakly-antiferromagnetic metals may be discussed within the framework of the SCR spin fluctuation theory, and in this scenario it is predicted that γ is enhanced considerably by the effect of low-temperature spin fluctuations, especially near a paramagnetic/antiferromagnetic boundary [12].

The low temperature specific heat in a normal metal can usually be expressed as

$$C = \gamma T + \beta T^3$$

with the first term arising from the electronic contribution and the second term corresponding to the lattice. Hence a plot of C/T versus T^2 will yield a value for the Sommerfeld constant γ from the intercept of the temperature axis. An early specific heat study of β-Mn and alloys with Fe, Co, Ni, Cr and V [4] reports an extrapolated value for γ of 70mJ/mol.K² in the pure element.

A plot of γ vs *d*-electron excess (or deficit), Δn_d, produced for these systems [4] yields a single curve irrespective of dopant species, with a peak at $\Delta n_d = 0.005$. The peak in γ corresponds to a critical

point for the onset of antiferromagnetism according to the SCR theory, with the Stoner parameter α = 1. The change (decrease) in γ moving away from the peak is given by

$$\left|\Delta n_d - 0.005\right|^{1/2}$$

For Δn_d = 0.005 corresponding to α = 1, pure β-Mn has an implied Stoner parameter slightly smaller than unity: β-Mn is therefore a nearly antiferromagnetic metal. Additionally, the antiferromagnetic transition temperature may be related to γ by [13]

$$\gamma = A - BT_N^{3/4}$$

where *A* and *B* are constants. In these early studies whereby implied transition temperatures were assumed to correspond to the Neel temperature, γ is shown to be linear in $T_N^{3/4}$ - consistent with this relation - for alloys with Fe, Co and Ni [4].

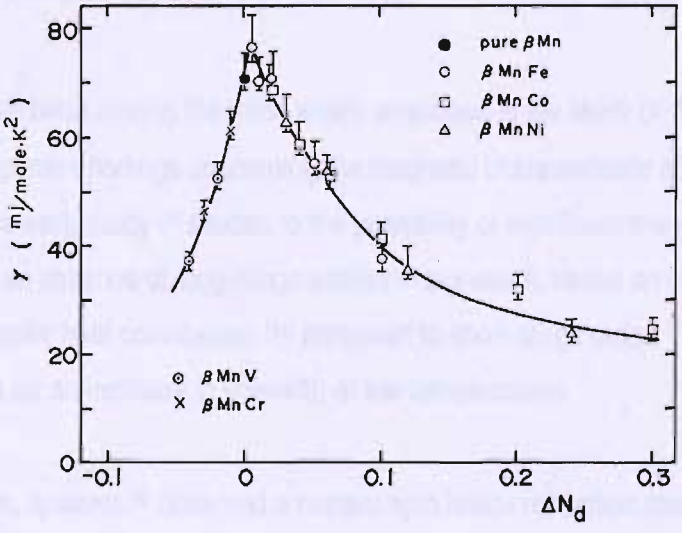

Figure 7.4: the plot of Sommerfeld constant γ versus excess d-electron number for a number of β-Mn alloys using 3d transition element impurities [4]

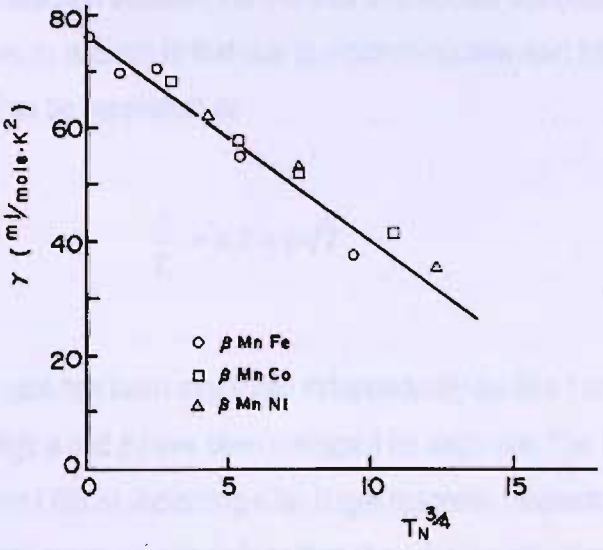

Figure 7.5: the plot of Sommerfeld constant versus $T_N^{3/4}$ for a number of β-Mn alloys using 3d transition element impurities [4]

Nuclear Magnetic Resonance

NMR techniques have been among the most widely employed in the study of β-Mn systems, and have led to many important findings concerning the magnetic characteristics of both the element and its related alloys. One early study [2] alluded to the possibility of significant magnetic interactions in this system, despite an absence of long-range antiferromagnetism, based on contemporary evidence of an anomalous specific heat contribution [14] attributed to short-range order. This, it was reasoned, could be responsible for an increase in linewidth at low temperatures.

A study of β-$Mn_{1-x}Ge_x$ systems [5] observed a nuclear spin lattice relaxation rate in pure β-Mn very close to the predicted $\sqrt{T}$ form for $T >> T_N$ [15]. Weak antiferromagnetism was reported for 1%at. Ge, and a plot of T_N (deduced from the divergent peaks in $1/T_1$) versus x allows an extrapolated value of ~0K for β-Mn to be estimated. In the alloys, $1/T_1$ was shown to decrease rapidly below T_N with the increase in the staggered magnetization, again in line with the behaviour predicted using SCR theory [15].

A relaxation rate due to interaction between the *d*-orbital and nuclear spin exists, which is proportional to temperature, in addition to that due to electron-nuclear spin interaction [16]. The total relaxation rate may therefore be expressed as

$$\frac{1}{T_1} = aT + b\sqrt{T}$$

The spin lattice relaxation rate has been measured independently for Site I and Site II in β-Mn, [17] and from this the coefficients *a* and *b* have been extracted for each site. The *b* value for Site II (800) greatly exceeds that for Site I (35.3), indicating a far larger magnetic moment for the Site II Mn. This has been supported by band structure calculations that show the density of states at the Fermi energy to be minimal for Site I and maximal for Site II, with the Stoner parameter only slightly less than unity for Site II [18].

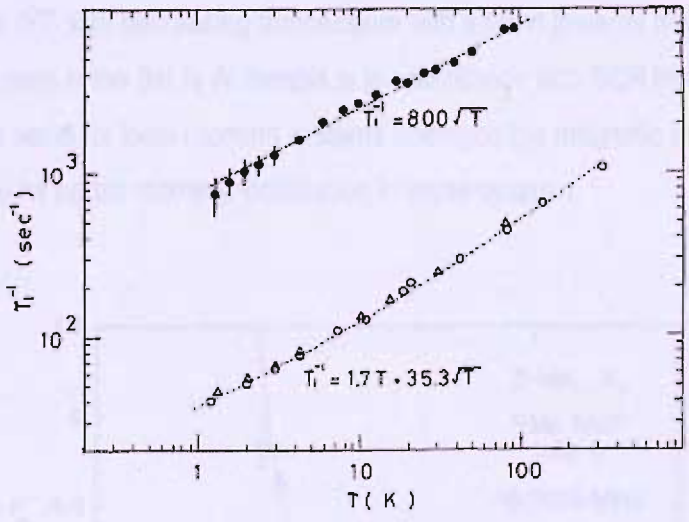

Figure 7.6: nuclear spin-lattice relaxation rates $1/T_1$ measured for the two inequivalent sites in pure β-Mn [17]. Open circles indicate Site I data from a previous study [5].

In one of the earliest studies of hyperfine internal fields [19] involving no less than 18 different impurity systems, antiferromagnetism was inferred in non-transition elements such as aluminium and indium at 4.2K where the interatomic distance is increased by more than 1%. In addition, a static antiferromagnetic ground state was inferred for transition element impurities where the dopant 3*d* electron number exceeds that of Mn. In alloys of iron, $\Delta d/d$ becomes more negative with Fe concentration; this observation led to the consideration of *d*-electron donation as a mechanism for stabilizing the magnetic ground state.

By considering the magnetic properties and lattice expansion characteristics of a number of binary and ternary β-Mn systems, it is possible to construct lines of equivalent internal field in the plane of *d*-electron number and lattice constant. This has been carried out in more than one case [20, 19]. Using this systematic approach it has been established that in non-transition metal alloy systems, expansion of the lattice driving the system towards Mn moment localization plays a key role in stabilizing the static magnetic state. In transition metal systems, the extent of *d*-electron donation is also an important factor, and appears to dominate the effect of lattice expansion where x is small.

A detailed study of the effect of alloying with aluminium has been carried out [6], in which a nonmagnetic ground state has been found for $x \leq 0.03$. For $x \geq 0.05$, a high frequency zero-field signal attributed to Site II Mn appears at 4.2K, indicative of static magnetic ordering in the Site II atoms - consistent with spin glass freezing implied in susceptibility measurements. $1/T_1$ has been shown to increase with increasing temperature for β-$Mn_{0.97}Al_{0.03}$, and has a dependence of the approximate form $60\sqrt{T}s^{-1}$ with a tendency toward saturation above 50K [6] In contrast β-$Mn_{0.9}Al_{0.1}$ shows an increase in $1/T_1$ with decreasing temperature with a trend towards divergence at 50K. While the behaviour seen in the 3at.% Al sample is in accordance with SCR theory, the divergence for 10at.% Al is more usual for local-moment systems undergoing a magnetic transition, and crucially reveals the possibility for partial moment localization in these systems.

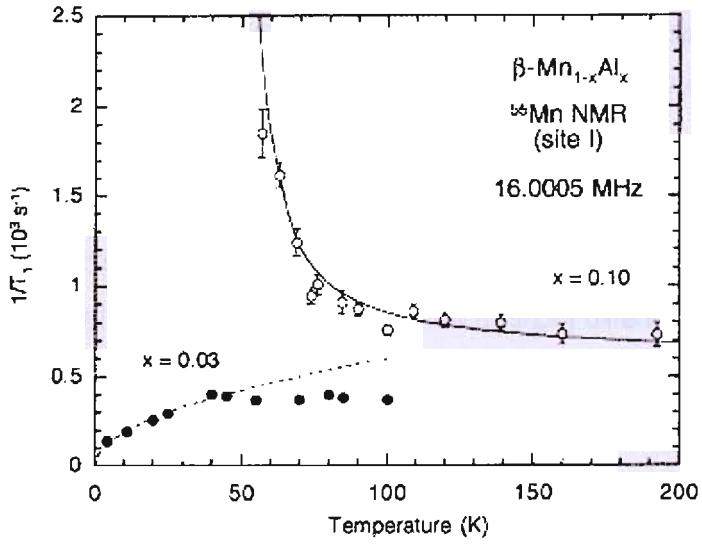

Figure 7.7: $1/T_1$ vs temperature for the β-$Mn_{0.97}Al_{0.03}$ and β-$Mn_{0.9}Al_{0.1}$ alloys, showing typically itinerant nearly-AF and partially localized behaviour respectively [6]

Mossbauer Spectroscopy

Mossbauer spectroscopy can be used to probe the hyperfine field at the impurity nucleus in β-Mn alloy systems, aiding understanding of the mechanism leading to antiferromagnetic ordering. Early investigations showed magnetic ordering at 4.2K for alloys with more than 10at% iron [21]. An extension of this has involved analysis of the hyperfine fields in alloys with Fe (and other 3d transition impurities), as well as the β-$Mn_{1-x}Sn_x$ and β-$Mn_{1-x}Ir_x$ series [22].

The average hyperfine fields at Site I in Fe, Co and Ni alloys appear to depend only on Δn_d. A large negative isomer shift also suggests transfer of electrons from the impurity *d*-band to the *d*-band of Mn is dominant in inducing antiferromagnetism. The value of the hyperfine field increases with lattice expansion where Δn_d is small, and dominates in this case and for non-transition impurities, in confirmation of NMR results [19, 20].

Neutron Polarization Analysis

Polarized neutron scattering measurements on pure β-Mn [23, 6] show a broad peak centred on the elastic line at $\boldsymbol{q} = 1.6\text{Å}^{-1}$, corresponding to around twice the mean interatomic distance and indicating antiferromagnetic correlations in the spin fluctuations. This peak is present at 7K, and infers strong zero-point fluctuations. The energy spectral width of the $\boldsymbol{q} = 1.6\text{Å}^{-1}$ scattering is much larger than the thermal energy (~0.6meV at 7K), and a plot of Γ versus temperature produces a finite (extrapolated) value at 0K, supporting the zero-point fluctuation scenario. In the same study, data for β-$Mn_{0.9}Al_{0.1}$ show the same broad peak at $q = 1.6\text{Å}^{-1}$, but otherwise show distinctly different behaviour. The scattering intensity is found to increase with decreasing temperature, and the energy spectral linewidths become much smaller, approaching zero at 0K. This implies the spin fluctuations become almost static at low temperatures. This change in spin dynamics between the two samples would correspond to a transition from a quantum spin liquid state – in which zero-point fluctuations are capable of moving the system between degenerate states – to a spin glass ground state in β-$Mn_{0.9}Al_{0.1}$. Here, the introduction of a magnetic impurity in the form of Al atoms reduces the magnetic frustration in the β-Mn lattice, and lifts the degeneracy [23].

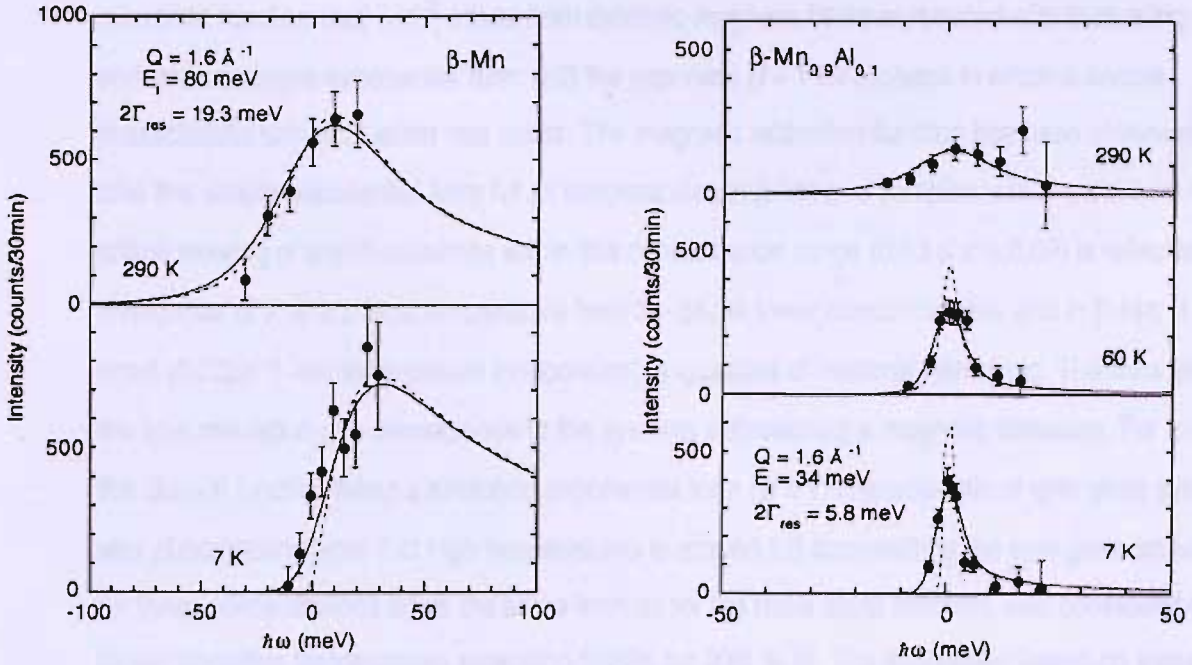

Figure 7.8: Neutron scattering data showing evolution of the $\boldsymbol{q}$ = 1.6 Å^{-1} peak with temperature, in β-Mn (left panel) and β-$Mn_{0.9}Al_{0.1}$ (right panel) [23]

The systems β-$Mn_{1-x}Al_x$ with $0.03 \leq x \leq 0.2$ have been investigated using XYZNPA [24]. A Monte Carlo algorithm was used to simulate a nuclear lattice producing agreement between measured and calculated cross-sections: this was then used in calculations of magnetic correlations. An anticlustering of Al impurity atoms was deduced, with oscillatory behaviour observed in the magnetic correlations in all samples. These correlations were found to be of longer range in the more dilute alloys, with a broadening of magnetic cross-section as x increases. The first three near-neighbour correlations increase in magnitude on increasing the concentration of Al, and the indication is that the frustration in the Site II sublattice is disrupted by the introduction of the impurity.

Muon Spin Relaxation

Zero-field muon spin relaxation in β-$Mn_{1-x}Al_x$ alloys is of the form:

$$A_z(t) = a_0 G_z^{GKT}(t) \times \exp\left[-(\lambda t)^{\beta}\right] + a_b$$

where $G_z^{GKT}(t)$ is the static Gaussian Kubo-Toyabe function as defined in Chapter 3. The magnetic relaxation function $exp[-(\lambda t)^{\beta}]$ arises from dynamic magnetic fields associated with fluctuating spins, and takes a simple-exponential form with the exponent $\beta = 1$ for systems in which a unique characteristic spin fluctuation rate exists. The magnetic relaxation function has been observed to take this simple exponential form for all temperatures in β-Mn and samples with $0 < x \leq 0.09$ [25]. A critical slowing of spin fluctuations within this concentration range ($0.03 \leq x \leq 0.09$) is reflected in the divergence of λ at a critical temperature from 3 – 5K; at lower concentrations, and in β-Mn, λ is very small ($0.02\mu s^{-1}$) and temperature independent, suggestive of motional narrowing. The diverging of the spin relaxation rate corresponds to the systems approaching a magnetic transition. For $x \geq 0.09$, the $G_{MAG}(t)$ function takes a stretched exponential form ($\beta < 1$) characteristic of spin glass systems, with β decreasing from 1 at high temperatures to around 1/3 approaching the spin glass transition. λ for these concentrations takes the same form as for the more dilute systems, with considerably higher transition temperatures extending to 38K for 20at.% Al. The suggestion based on these findings is that Al substitution causes a crossover from the quantum spin liquid to spin glass state.

Inelastic Neutron Scattering: NFL Scaling in β-Mn

A study of quasielastic neutron scattering study in pure β-Mn [26] has determined the limiting low- and high-frequency spin relaxation rates Γ_1 and Γ_2, as well as the "NFL parameter" $(\Gamma_1 - \Gamma_2)/\Gamma_1\Gamma_2$ as defined previously (Chapter 2). All parameters were found to behave in accordance with predictions for a NFL system [27], with the high-frequency end of the relaxation rate distribution $D(\Gamma)$independent of temperature, and the low-frequency end decreasing monotonically with T. The data are consistent with a broad distribution of relaxation times in β-Mn. Resistivity data obtained in this study also show typical NFL behaviour:

$$\rho(T) - \rho_0 \propto T^{3/2}$$

with the 3/2 exponent characteristic of a $T_N = 0$K itinerant electron antiferromagnet, according to SCR theory. This study constitutes the first reported observation of NFL scaling of spin fluctuations in an elemental paramagnet.

Long-range Order in β-Mn Systems

Much attention has recently been focused on the β-$Mn_{1-x}Os_x$ series of alloys. X-ray diffraction and susceptibility measurements [28] for Os concentrations between 6at% and 36at% have confirmed an increase in both lattice constant and the so-called "Neel temperature"[2] with increasing x. The occupation of Site I by the osmium atoms is also confirmed by this X-ray data. Differential scanning calorimetry performed for the same concentrations [28] has revealed a decrease in Sommerfeld constant γ from 44 $mJmol^{-1}K^{-2}$ in β-$Mn_{0.94}Os_{0.06}$ to 14 $mJmol^{-1}K^{-2}$ in β-$Mn_{0.8}Os_{0.2}$. These observations are in agreement with spin fluctuation theory [12]. Interestingly, a change in slope of T_N versus x occurs at around $x = 0.13$, and serves as an indicator of a possible magnetic phase transition.

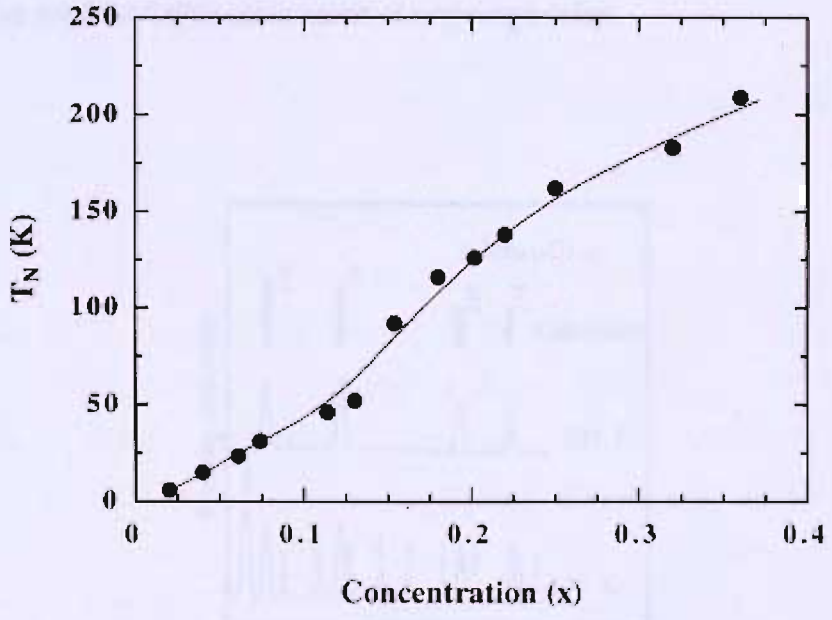

Figure 7.9: Neel temperature (implied from susceptibility measurements) as a function of impurity concentration x in β-$Mn_{1-x}Os_x$ systems [28]

A similar investigation into β-$Mn_{1-x}Ru_x$ systems [29] produced results very similar to those for the Os alloys. The lattice constant was found to increase monotonically with x, as do the temperatures of the susceptibility maxima. A change of gradient in T_N versus x is observed at 15at% Ru. Specific heat

[2] In early work on β-Mn alloys a peak in $\chi(T)$ indicating a transition to a weak antiferromagnetic state was routinely used to define the Neel temperature.

experiments form a significant part of this study, and crucially provide the first *unambiguous* evidence of LRO in β-Mn systems. A decrease in γ with impurity concentration is found, and clear peaks occur in $C(T)$ for concentrations above 18at% Ru, which correspond to the susceptibility maxima. The entropy change due to this magnetic transition, ΔS, has been estimated using this data and its increase with x implies that the magnetic behaviour approaches an intermediate state between the itinerant and localized conditions. In the low Ru concentrations, the results (such as the similar relation between γ and $T_N^{3/4}$ to that observed in other Site I impurity systems) indicate an itinerant, weak antiferromagnetic state. These findings were echoed closely in a subsequent investigation on impurity systems involving iridium [30]. Increases in both the lattice constant and Neel ternperature with x are more significant in the Ir systems than for Ru and Os.

A recent investigation into the thermodynamical properties and neutron diffraction data of palladium-group impurity systems, with the emphasis on the influence of spin fluctuations, has yielded some remarkable results [31]. Firstly, magnetic Bragg peaks in the diffraction spectra of β-$Mn_{0.75}Os_{0.25}$ below 10K have provided further confirmation of long-range order:

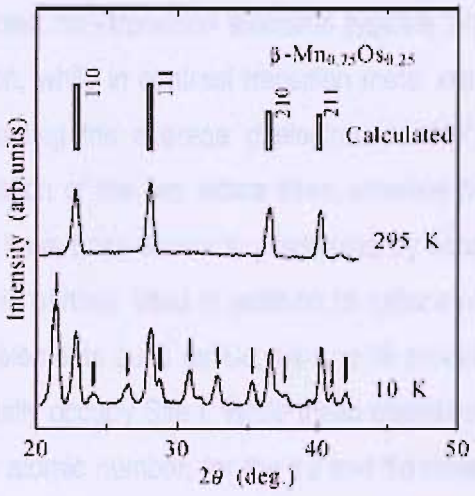

Figure 7.10: powder neutron diffraction patterns for β-$Mn_{0.75}Os_{0.25}$ at 10K and 295K: [31] additional Bragg peaks at 10K are indicated by arrows

In specific heat measurements for Ru, Os and Ir (in addition to Fe and Co) systems, a γ versus $T_N^{3/4}$ plot yields a single line for all impurities at low concentrations. A deviation is observed as x, and consequently T_N, increase. This is taken as corresponding to a transition from weak itinerant antiferromagnet character to an intermediate antiferromagnetic state. For a sample with 33at% Os, γ

is measured as ~ γ_{band} – hence the spin fluctuation effect in this system is weak. A maximum in the universal dT_N/dP versus T_N curve yields a maximum at 70K: those alloys with T_N ~ 70K are those observed to enter the intermediate magnetic state. A significantly large thermal expansion coefficient in a wide range of temperature above T_N was observed in these samples, with a clear spin fluctuation correlation.

In this chapter, the results of further experimental investigation into the nature of the spin dynamics and magnetic ground states of β-$Mn_{1-x}Co_x$ and β-$Mn_{1-x}Ru_x$ alloys are reported and discussed. In the case of the cobalt alloys, the motivation for these studies – which include neutron diffraction, magnetometry, muon spin relaxation, and inelastic neutron scattering – is the need to explore more fully a system in which the solute atom occupies Site I, as for systems of Ru, Ir, and Os, but unlike these systems in which no long range order has so far been observed. For the ruthenium systems, the experimental work has been largely driven by the need to explore further the development of the long-range magnetically ordered state, using alternative experimental techniques.

The issues of site occupancy, the mechanism governing magnetic ordering and their interplay have proven more complicated than originally anticipated. Historically, it has been possible to classify β-$Mn_{1-x}M_x$ systems along two lines: non-transition elements typically bring about moment localization as a result of lattice expansion, while in contrast transition metal impurities tend to generate weak itinerant magnetism by increasing the average *d* electron number. The alternative grouping is according to preferred occupation of the two lattice sites, whereby non-transition elements (with a larger atomic radius than Mn) have been shown to predominantly occupy Site II. The configurational degeneracy in this sublattice is partially lifted in addition to expansion effects, possibly resulting in spin glass states. Transition elements such as Co, Fe and Ni producing weakly antiferromagnetic alloys are shown to preferentially occupy Site I. While these classifications are valid simultaneously for impurities of relatively low atomic number, for the 4*d* and 5*d* transition elements the associated large radii do not accommodate both conventions. Expansion and electron donation are hence both valid scenarios for consideration in explaining the long-range ordered state observed in Ru (4*d*) and Os (5*d*) systems.

7.3. Sample Preparation

Polycrystalline samples were produced for the concentrations 1, 5, 10, 15 and 20% Co. The constituent materials were melted together under an argon atmosphere in an electric arc furnace at the University of Southampton. In each case the quality of the starting materials was at least 0.999% purity, with the manganese etched in a weak nitric acid/methanol solution to remove any surface oxidation.

Prior to the melting procedure the furnace chamber was flushed with pure argon three times with the materials in place. A titanium getter was melted in advance of the sample materials, with the dual purpose of removing any remaining trace impurities and to monitor the purity of the argon atmosphere. After the getter had been allowed to cool and viewed for traces of visible oxidation, sample melting was carried out.

The manganese used was initially in the form of electrolytically produced flake, containing gaseous impurities in addition to surface oxidation. It proved necessary to melt a quantity of this, slightly in excess of that required, several times before the addition of the cobalt. Once an ingot had been produced that did not readily shatter upon melting, the cobalt was added (initially in solid rod form, cut to length corresponding to the required mass). Observation of mass loss during the manganese melts led to a routine addition of 2% excess manganese to the final MnCo composition, with all subsequent mass loss assumed to be due purely to manganese sublimation. Cornpositions have been confirmed by neutron diffraction measurements (see Section 7.3). Each sample was re-melted a minimum of four times after initial combination of the constituents, to ensure maximum homogeneity. A low current and rninimal system coolant were used to reduce thermal shock to the samples.

The resulting ingots were then annealed in sealed quartz ampoules at 900°C for 24 hours before undergoing a rapid quench to below room temperature using an ice/water bath. By this method approximately 20g at each concentration have been produced, in 5g pieces.

7.4. Neutron Powder Diffraction Measurements of β-$Mn_{1-x}Co_x$

A series of neutron powder diffraction measurements on β-$Mn_{1-x}Co_x$ were carried out using the GEM instrument at the ISIS pulsed source facility, for nominal Co concentrations of 10, 15 and 25%.

Room temperature data has been analyzed in order to extract the lattice parameter and atomic coordinates, confirm the sample phase and establish the impurity site occupancy. Rietveld refinement has been performed using the GSAS (General Structure Analysis System) software[3].

The refinement parameters obtained are as follows:

x	Lattice parameter (Å)	X (Å)	Y (Å)	U_{iso} Site I	U_{iso} Site II	R-Factor R_{wp}
0.10	6.3210	0.0641	0.2025	0.424	0.890	0.0547
0.15	6.3233	0.0639	0.2024	0.642	0.989	0.0528
0.25	6.3296	0.0648	0.2027	0.668	0.902	0.0601

Table 7.2: Rietveld refinement parameters from powder diffraction data recorded for β-$Mn_{1-x}Co_x$ samples with the GEM instrument. U_{iso} represents an isotropic thermal factor

x	Site I Occupancy (%)	Corrected Impurity Concentration (%)
0.10	99.3	11.1
0.15	98.9	17.6
0.25	98.1	24.5

Table 7.3: Site I occupation factors and corrected concentrations for cobalt atoms in β-$Mn_{1-x}Co_x$ samples with $0.10 \leq x \leq 0.25$

[3] Authored by R. B. von Dreele and A. C. Larson

These measurements indicate that cobalt impurity atoms substituted into β-Mn preferentially occupy crystallographic Site I, as expected for a transition impurity. The lattice constant *a* as a function of impurity concentration is shown in Figure 7.11:

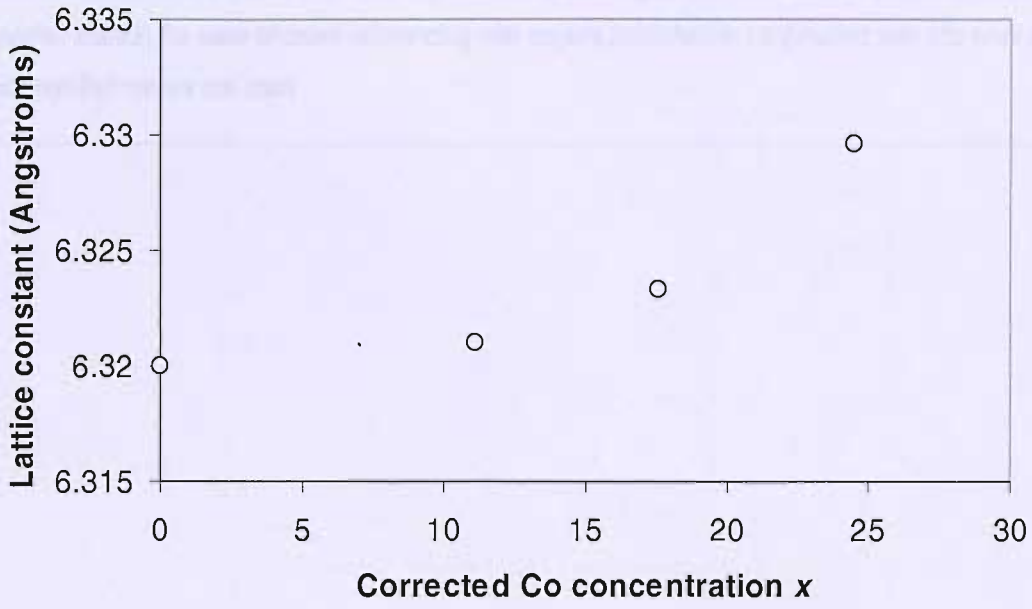

Figure 7.11: impurity concentration dependence of the room temperature lattice parameters in β-$Mn_{1-x}Co_x$

The lattice expansion effect is minimal when compared to Site II impurity systems such as β-$Mn_{1-x}Al_x$, suggesting that this is unimportant in any change in magnetic behaviour observed in cobalt alloys. This is in keeping with previous data, which show that the lattice constant remains below 6.42Å up to 40at.% Co [19, 32]. Electron donation appears to be the dominant mechanism responsible for the weak antiferromagnetism and static ground state previously reported for these systems.

It is noted that the atomic position parameter *y* remains close to, and slightly less than, the critical value of ~ 0.2035 required for the equilateral triangular arrangement of the Site II sublattice.

Note: although corrected values for *x* have been determined as a result of this study, the adopted convention for the remainder of this thesis is to refer the samples according to their nominal compositions (unless otherwise stated), for ease of cross-referencing with papers published in conjunction with this work and in which nominal values are used

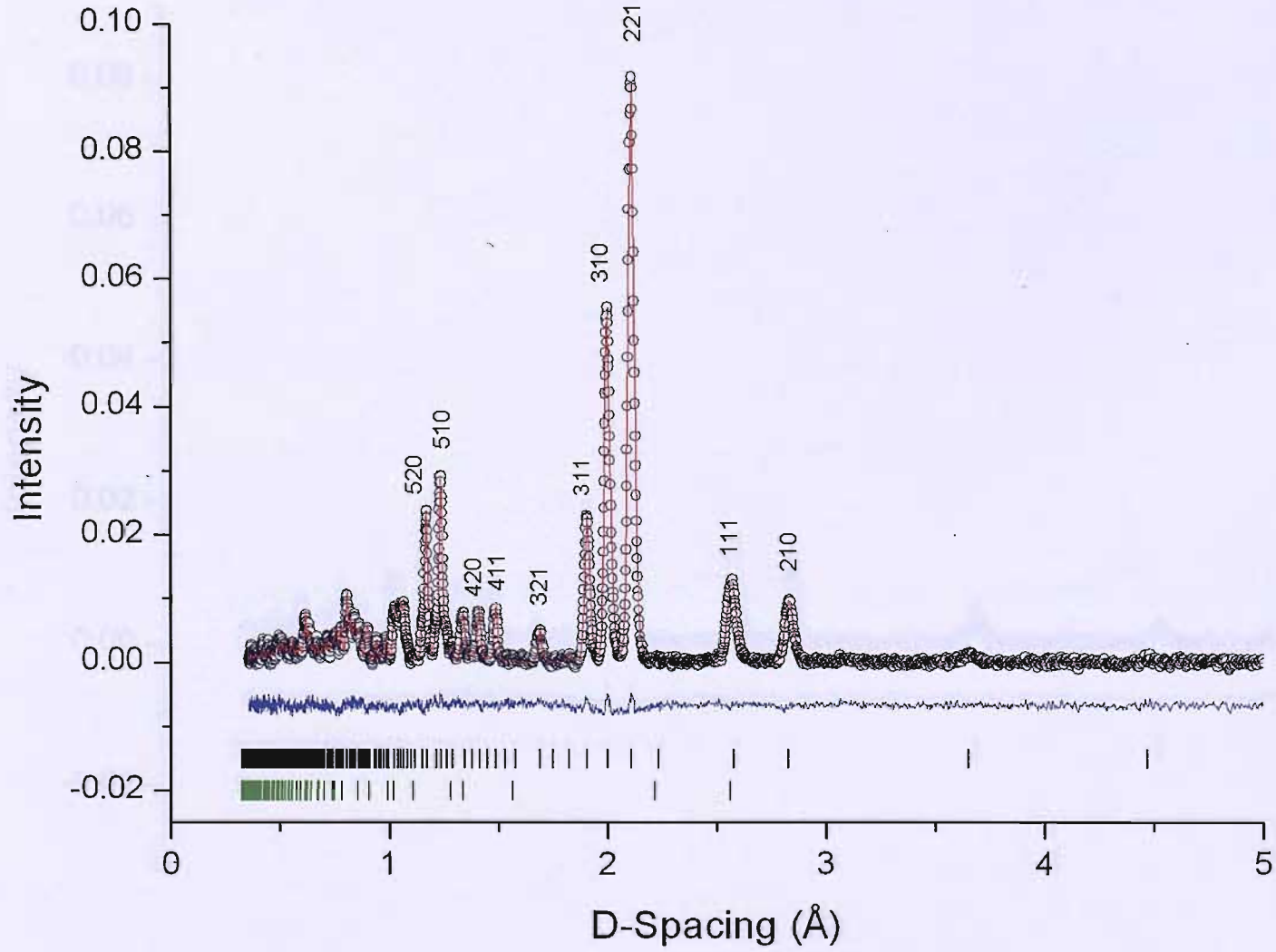

Figure 7.12: room temperature neutron powder diffraction pattern with Rietveld refinement for β-$Mn_{0.9}Co_{0.1}$ (GEM)

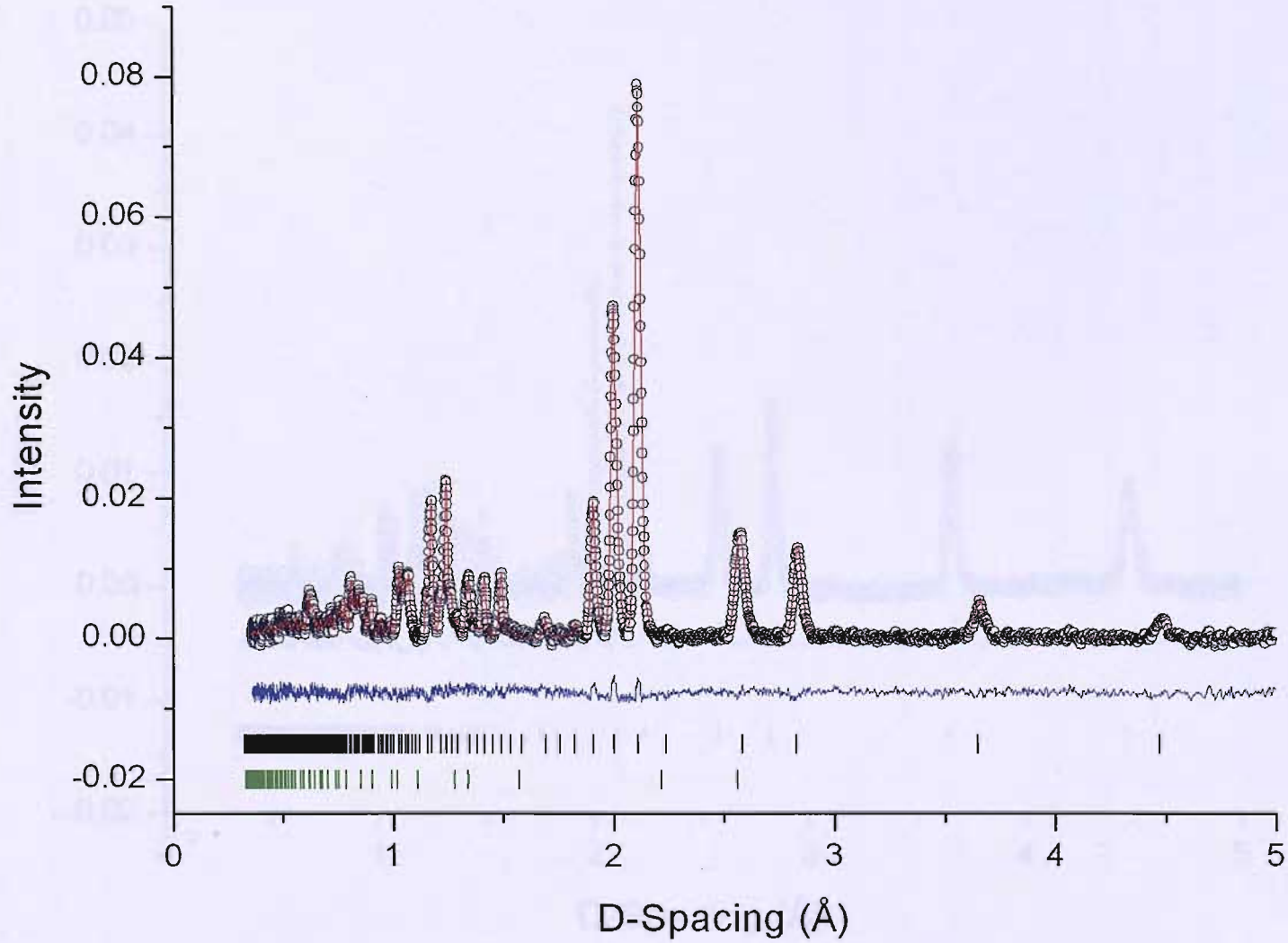

Figure 7.13: room temperature neutron powder diffraction pattern with Rietveld refinement for β-$Mn_{0.85}Co_{0.15}$ (GEM)

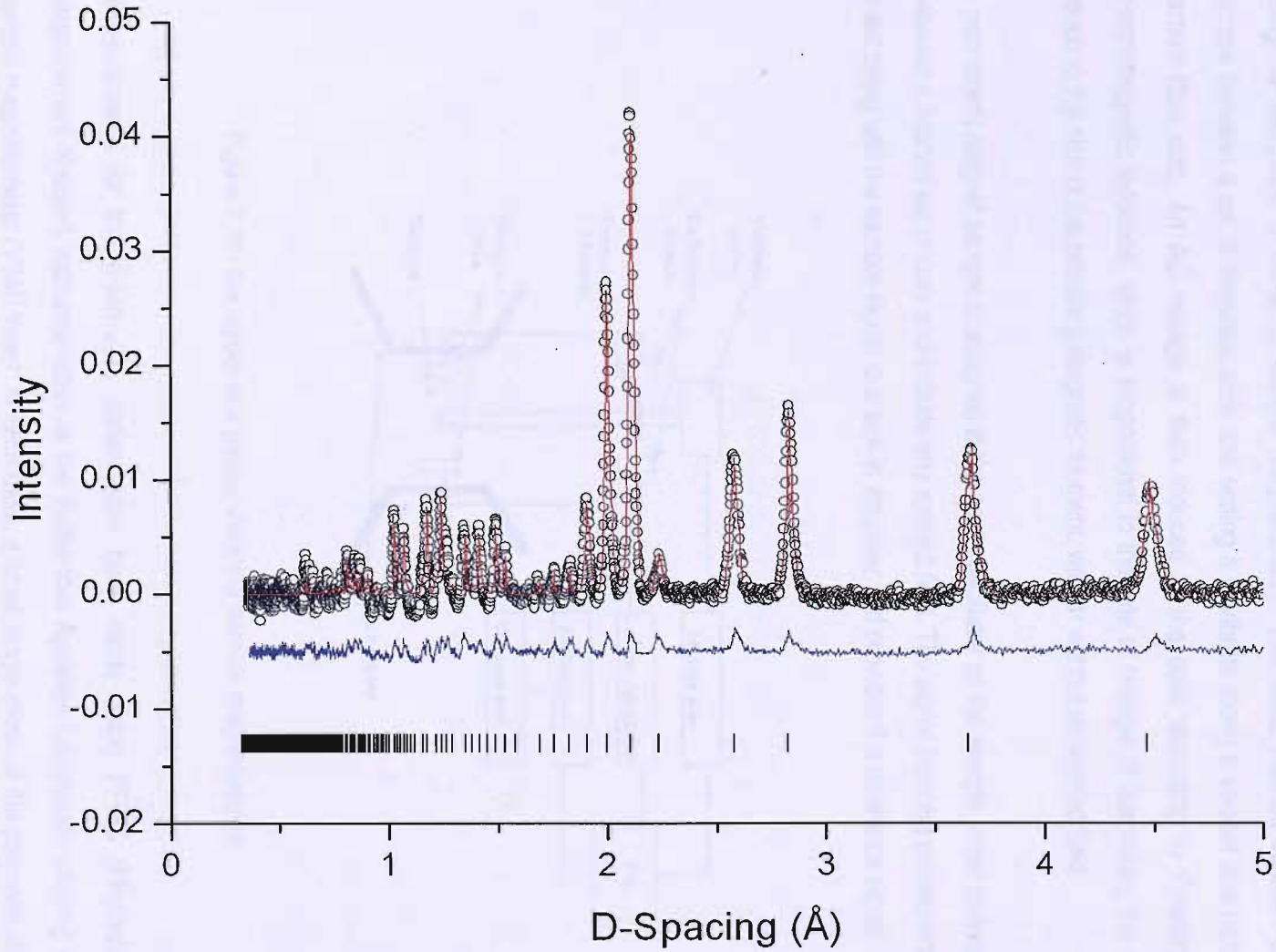

Figure 7.14: room temperature neutron powder diffraction pattern with Rietveld refinement for β-$Mn_{0.75}Co_{0.25}$ (GEM)

7.5. Magnetization Measurements of β-$Mn_{1-x}Co_x$

Sample characterisation has also involved measuring magnetization as a result of an applied field, using the technique of vibrating sample magnetometry. The basic method involves placing the sample between a set of detection coils and setting it to vibrate along a vertical axis (attached to a carbon fibre rod). An AC voltage is then induced in the coils according to Faraday's law of electromagnetic induction, which is proportional to the rate of change of flux linking the circuit and hence to the size of the sample's magnetic moment, with or without an applied field.

A permanent magnet sample is attached to the same oscillator as the sample under investigation, between a second set of coils and outside any applied field. The signal from the permanent magnet is fed along with the sample signal to a lock-in amplifier and provides the reference signal.

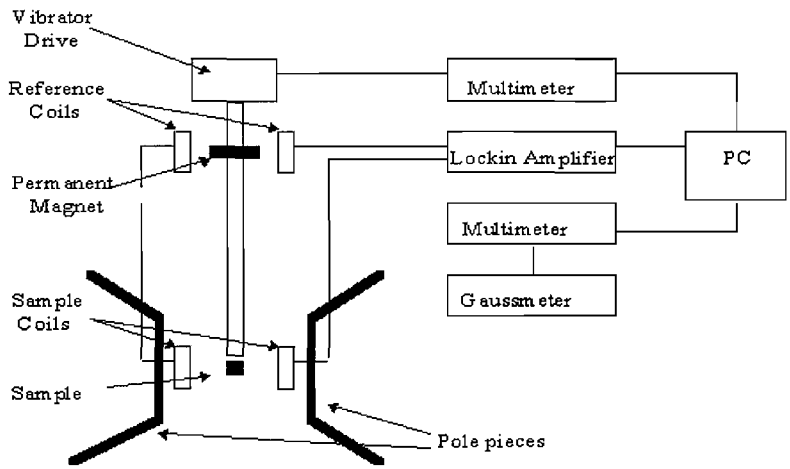

Figure 7.15: the layout of a typical vibrating sample magnetometer

Measurements for the β-$Mn_{1-x}Co_x$ series have been made using PPMS (Physical Property Measurement System) instrumentation at the Rutherford Appleton Laboratory, utilizing a vibrating sample magnetometer (VSM) insert. In each case, a small single piece of the polycrystalline sample was securely affixed to a holder and placed at the end of the vibrating rod. The assembly was inserted into a cryostat between the field coils, and the sample was cooled from room temperature to instrumental base temperature (2.5K). A field of 1000 Gauss was then applied, and the magnetization of the sample recorded as the sample was brought back to room temperature: such a

measurement is referred to as a *zero-field cooled* scan. The sample was then re-cooled to 2.5K, before a further magnetization-temperature scan is performed as the sample is returned to room temperature. This second phase constitutes a *field-cooled* measurement.

In the experiments, the quantity measured is the magnetic moment for the sample induced as a result of the applied dc field. As these quantities are output in cgs units (moments measured in electromagnetic units and applied fields in gauss), it is helpful to first convert these to SI units using the appropriate scaling.

Magnetization may be defined as the magnetic moment of a given material per unit volume; alternatively the specific magnetization, equal to moment per unit mass, may be given. This is related to the *volume susceptibility* by

$$\chi = \left(\frac{\partial M}{\partial H} \right)_{H \to 0}$$

Assuming linearity of the response, susceptibility may be defined as

$$\chi = \frac{M}{H}$$

and is a dimensionless quantity for values in SI units. The volume susceptibility is also related to specific magnetization:

$$\chi = \frac{\sigma \rho}{H} = \frac{\mu_0 \sigma \rho}{B}$$

where σ is the specific magnetization and B the applied field. The *mass susceptibility* is also commonly quoted,

$$\chi_{mass} = \frac{\sigma}{B}$$

having units of $JT^{-2}Kg^{-1}$. Alternatively, the *molar susceptibility* is given by

$$\chi_{mol} = \frac{\sigma M_{mol}}{B}$$

where M_{mol} is the molar mass of the material. The units in this case are $JT^{-2}mole^{-1}$. Susceptibilities generally have to be corrected to take account of demagnetization effects where a component of the magnetic field is perpendicular to the sample surface. The true susceptibility is therefore

$$\chi = \frac{M}{\left(\frac{B_{app}}{\mu_0} - \lambda M\right)}$$

where λ is the *demagnetizing factor.*

For the β-$Mn_{1-x}M_x$ experiments, the sample shape is reasonable well approximated by a flat plate, aligned perpendicular to the applied field. The demagnetizing factor in this situation is 1. Volume susceptibilities for all samples have been obtained along these lines.

In all samples, with concentrations corresponding to x = 0.01, 0.05, 0.10, 0.15 and 0.25, the high-temperature dependence of $\chi(T)$ is weak, and indicative of behaviour close to the itinerant limit. A slight increase with increasing temperature is observed in some samples, particularly β-$Mn_{0.85}Co_{0.15}$.

In previous studies of Al impurity systems, the form of the susceptibility curve becomes increasingly Curie-Weiss-like with increasing x, as a result of a progressive transition towards moment localization. This is not observed in the cobalt systems, and rules out the development of localized moments due to lattice expansion, being consistent with diffraction data reported in the previous section.

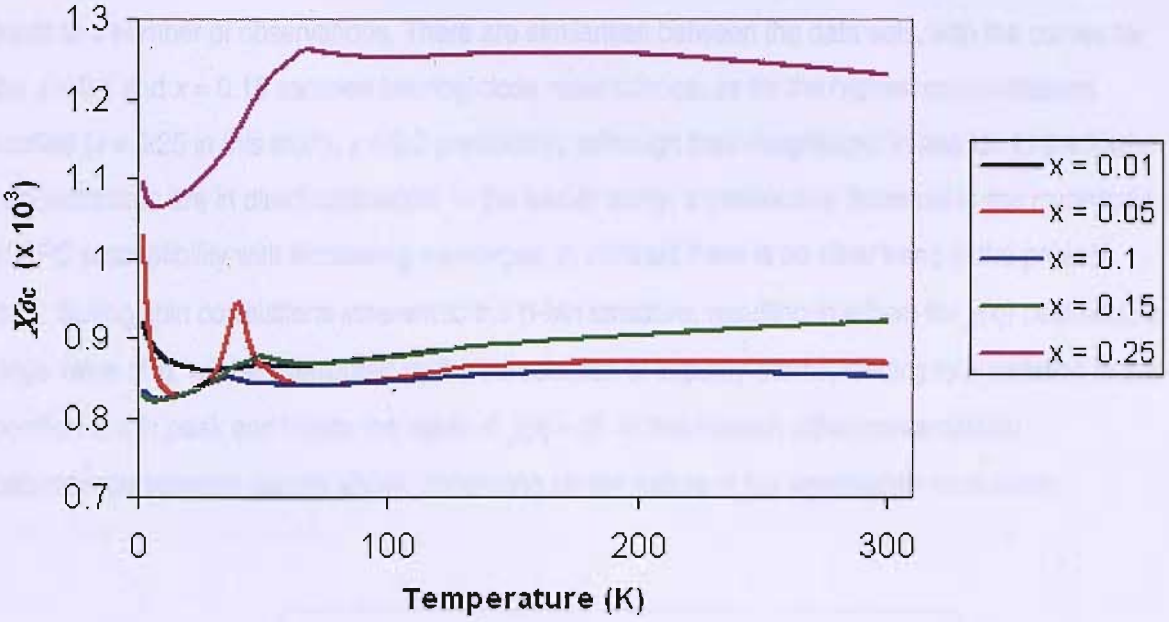

Figure 7.16(a): ZFC susceptibilities for the β-$Mn_{1-x}Co_x$ series, measured in 1000G.

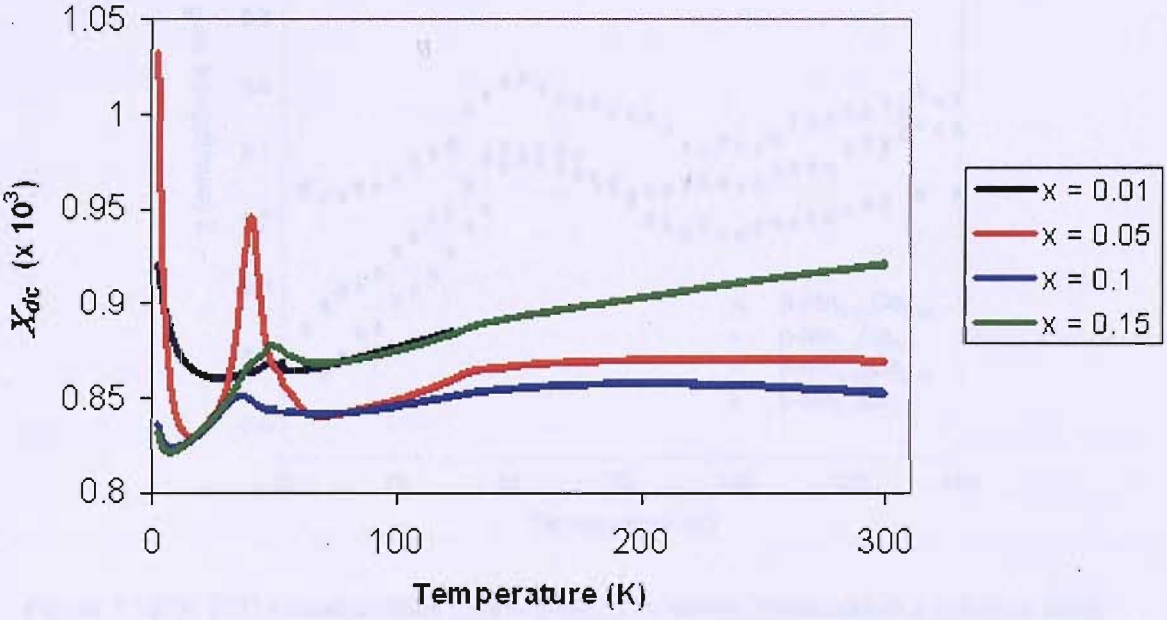

Figure 7.16(b): ZFC susceptibility data for β-$Mn_{1-x}Co_x$ with concentrations $0.01 \leq x \leq 0.15$ on an expanded scale

The magnitude of the ZFC susceptibility, and hence the effective moment, of the $x = 0.25$ sample is much greater than that of the lower concentrations. Of these, the x = 0.15 sample has a slightly larger susceptibility, while below this there appears to be a decrease in the size of the response with

increasing x. A basic comparison to previous susceptibility data[4] for β-$Mn_{1-x}Co_x$ (Figure 7.20(b)) leads to a number of observations. There are similarities between the data sets, with the curves for the $x = 0.1$ and $x = 0.15$ samples bearing close resemblance, as for the highest concentrations studied ($x = 0.25$ in this study, $x = 0.2$ previously), although their magnitudes in relation to the lower concentrations are in direct opposition. In the earlier study, a continuous decrease in the magnitude of ZFC susceptibility with increasing x emerges; in contrast there is no clear trend in the present data. Strong spin correlations inherent to the β-Mn structure, resulting in a form for $\chi(\boldsymbol{q})$ peaked at a large value of $\boldsymbol{q}$, will be interrupted by the introduction of impurity atoms, leading to a variation in the position of this peak and hence the value at $\chi(\boldsymbol{q} = 0)$. In this context either concentration dependence scenario seems viable, depending on the nature of the wavevector modulation.

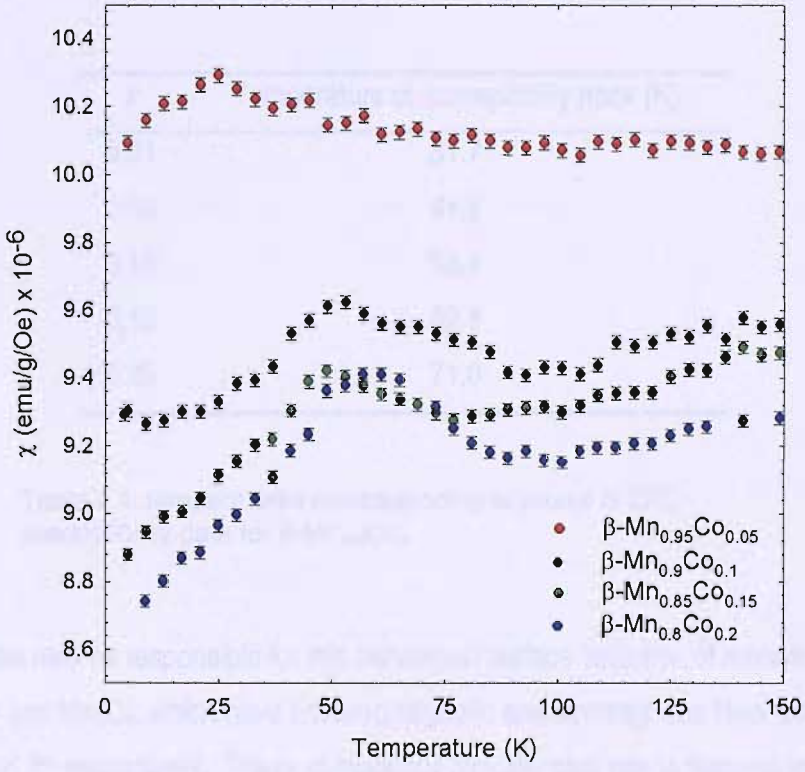

Figure 7.16(b): ZFC susceptibilities for the β-$Mn_{1-x}Co_x$ series, measured in a previous study

All samples exhibit a bifurcation of the field-cooled (FC) and zero-field cooled (ZFC) curves, occurring above a peak in the ZFC susceptibility. Usually, a difference in FC and ZFC responses emerging at a sharp cusp is indicative of entry into a spin glass state, with the freezing transition marked by the peak temperature. Increasing the sample temperature thermally frees the spins, which are eventually re-orientated by a field applied below the freezing temperature. The susceptibility then increases up to a point at which the field-induced order is surpassed by thermal

[4] Unpublished data provided courtesy of J. R. Stewart

fluctuations. If the sample is the re-cooled, the spins will fully align above T_G and freeze in this configuration at T_G.

The addition of impurity atoms may be expected to stabilize a spin glass state where the magnetic frustration has been partially lifted. In this case, the appearance of the susceptibility bifurcation would correspond to the onset of a spin glass transition in the phase diagram at a threshold concentration. The temperature of the peak may also realistically be expected to increase with x. This is not the case with the samples measured in this study. A distinct difference between ZFC and FC responses occurs down to the lowest concentrations, becoming apparent at a temperature between 50 and 100K for $0.01 \leq x \leq 0.15$ and between 100 and 150K for $x = 0.25$. The peaks in the ZFC susceptibility, most noticeable for the 5% Co sample, occur at the following temperatures:

x	Temperature of susceptibility peak (K)
0.01	51.7
0.05	41.5
0.10	38.8
0.15	52.8
0.25	71.0

Table 7.4: temperatures corresponding to peaks in ZFC susceptibility data for β-$Mn_{1-x}Co_x$

Sample impurities may be responsible for this behaviour: surface oxidation of manganese produces the oxides MnO and Mn_3O_4, which have antiferromagnetic and ferrimagnetic Neel temperatures of 120K [33] and 42K [34] respectively. These compounds typically give rise to features in magnetic data of manganese systems, although in this case only the peak in the β-$Mn_{0.95}Co_{0.05}$ sample could be attributed to Mn_3O_4. A less common oxide impurity may give rise to the dominant features for these samples, possibly masking any effect due to intrinsic spin glass behaviour.

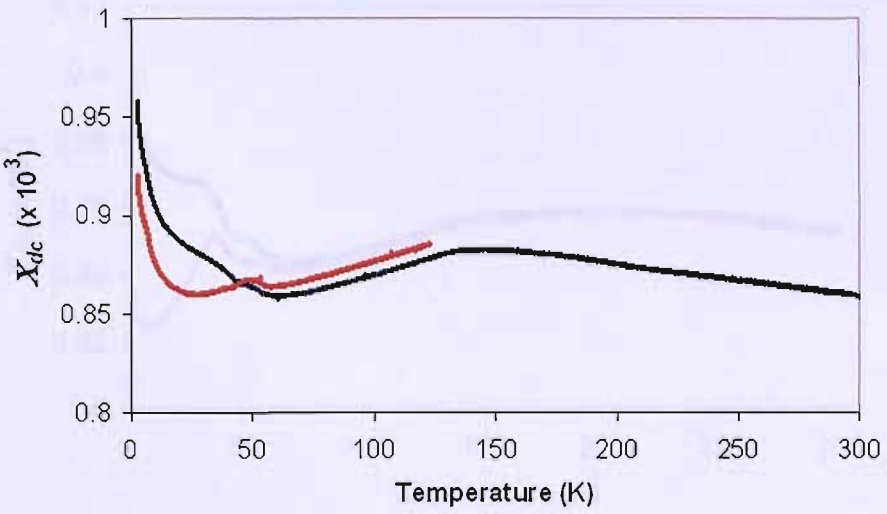

Figure 7.17: ZFC (red) and FC (black) susceptibilities of β-$Mn_{0.99}Co_{0.01}$

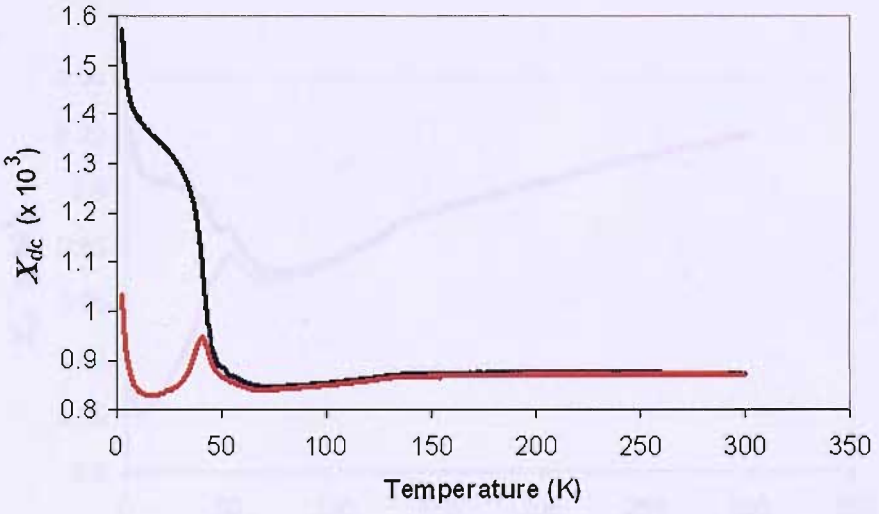

Figure 7.18: ZFC (red) and FC (black) susceptibilities of β-$Mn_{0.95}Co_{0.05}$

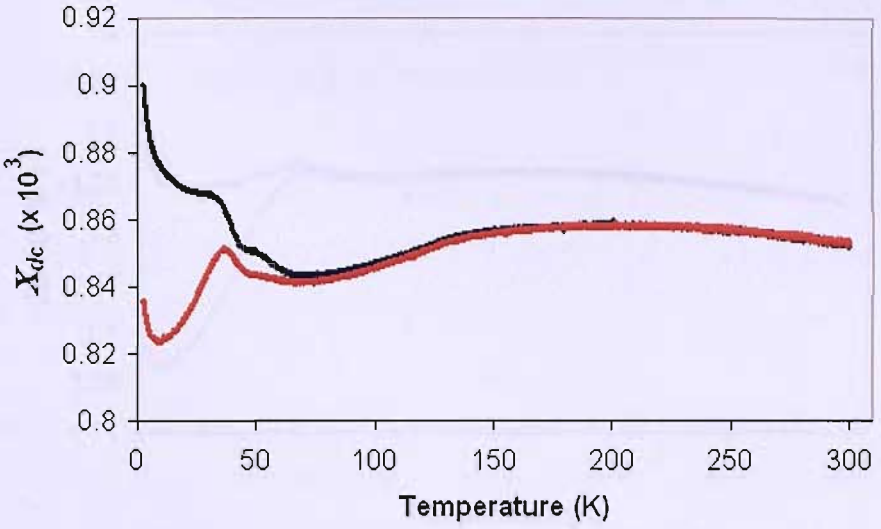

Figure 7.19: ZFC (red) and FC (black) susceptibilities of β-$Mn_{0.9}Co_{0.1}$

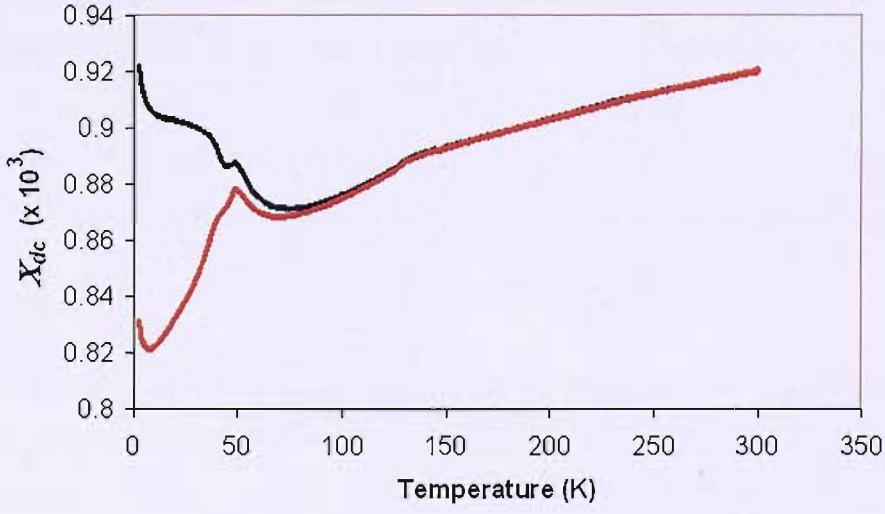

Figure 7.20: ZFC (red) and FC (black) susceptibilities of β-$Mn_{0.85}Co_{0.15}$

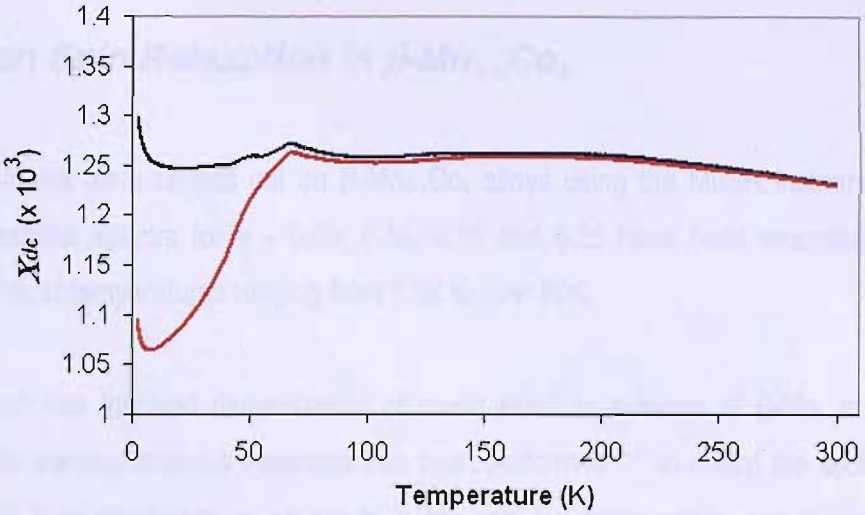

Figure 7.21: ZFC (red) and FC (black) susceptibilities of β-$Mn_{0.75}Co_{0.25}$

7.6. Muon Spin Relaxation in β-$Mn_{1-x}Co_x$

μSR experiments were carried out on β-$Mn_{1-x}Co_x$ alloys using the MuSR instrument at the ISIS facility. Relaxation spectra for x = 0.05, 0.10, 0.15 and 0.25 have been recorded in ZF and LF configurations, at temperatures ranging from 1.5K to over 80K.

Previous work has involved determination of muon sites[5] in systems of β-Mn. In the β-$Mn_{1-x}Al_x$ series a finite element analysis treatment has been performed [11] to obtain the second moment of the Gaussian field distribution at all points in the unit cell, from which σ is extracted. Observed relaxation functions involving a GKT component justify the use of Gaussian field distributions in this model. Calculations for half-integer nuclear spins (as for ^{27}Al and ^{56}Mn) on the β-Mn lattice yield values for σ that exceed the experimental value of 0.37μs^{-1} for all candidate sites. The four octahedrally coordinated sites (3/8,3/8,3/8), (1/8,5/8,7/8), (5/8,7/8,1/8) and (7/8,1/8,5/8) – which are crystallographically equivalent – have the lowest and most acceptable values of σ= 0.40μs^{-1} in each case. The suitability of these sites were confirmed with Monte Carlo simulation procedures carried out for the (3/8,3/8,3/8) site, which seek to determine the nuclear field distribution at this site from multiple iterations using random input nuclear spin directions. Results showed that while the field distributions themselves appeared to be non-Gaussian in nature, the second moment of the field distribution Δ^2 and hence relaxation rate σ are almost identical to those extracted from GKT fits of the data.

The muon spectra were fitted to known relaxation functions using routines within OPENGENIE, a software package designed specifically for the display and analysis of data from ISIS neutron and muon instruments[6].

Zero applied field (ZF) and longitudinal field (LF) spectra have been employed in data analysis, in order to assess independently the total and atomic relaxation. In all cases an applied field of 100G was sufficient to decouple the muon spins from nuclear fields, illustrated in Figure 7.22.

---

[5] Muon diffusion having been ruled out by analysis of observed relaxation.

[6] Authored by F. Akeroyd

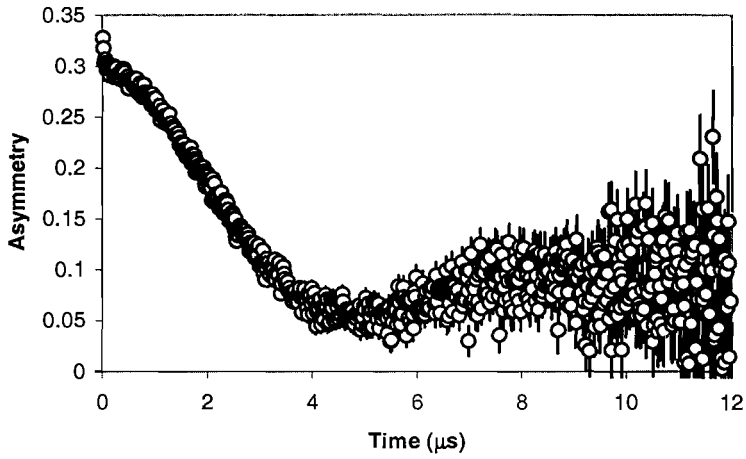

Figure 7.22 80K ZF (above) and 100G LF relaxation (below) in β-$Mn_{0.95}Co_{0.05}$, taking a GKT × exponential and exponential form respectively

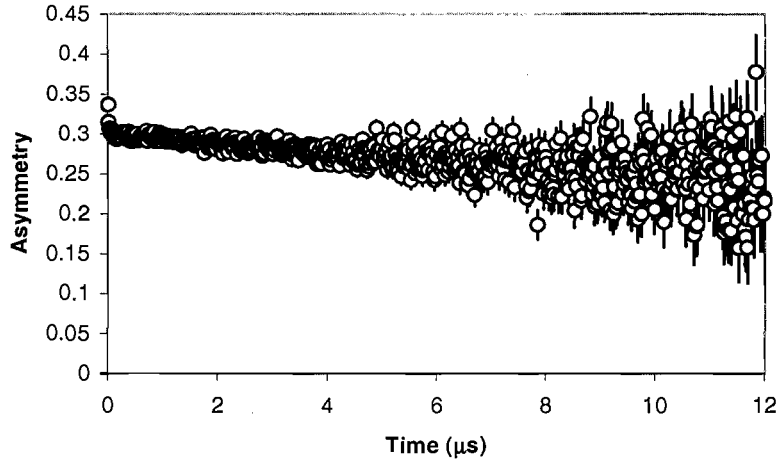

No evidence of muon diffusion was found, with nuclear relaxation taking a Gaussian Kubo-Toyabe form for all samples at all temperatures. The spin dynamics in these systems lead to a similar atomic relaxation form as has been reported for other β-Mn systems such as β-$Mn_{1-x}Alx$, [11] namely the stretched exponential function typical of a concentrated spin glass. The total relaxation is described therefore by

$$A_z(t) = a_0 G_z^{GKT}(t) \exp\left[-(\lambda t)^{\beta}\right] + (background)$$

The nuclear and magnetic relaxation functions are combined in a multiplicative fashion, an assumption that is valid provided that these are associated with independent depolarization channels.

The fitting procedures involve establishing a realistic background and fixing the background parameter at this value of each sample, across the entire temperature range. The remaining parameters - in this case a_0, σ, λ and β - are allowed to vary. Following confirmation of the GKT nature of nuclear relaxation, accurate fitting of the electronic relaxation was carried out using the LF data.

Relaxation for $0.05 \leq x \leq 0.25$

In β-$Mn_{0.95}Co_{0.05}$, the electronic relaxation follows a simple exponential function at high temperatures, with the exponent $\beta \sim 1$. As the temperature decreases this takes a stretched exponential form, whereby β falls to a value of ~ 1/3 at low temperatures. The relaxation rate λ^{β} rises to a peak at around 19.7K, and coincides with a drop in asymmetry from its high temperature value of 0.26 to around 0.12. This fails to reflect any aspect of the ZFC susceptibility data, in which the only visible feature is the peak at 41.5K attributed to the oxide impurity Mn_3O_4.

In β-$Mn_{0.9}Co_{0.1}$ the temperature dependence of the relaxation parameters is qualitatively similar, with a dramatic rise in relaxation rate λ^{β} below 50K, to a peak at 24.7K. The exponent β falls off in the same temperature region, to a value slightly above 1/3. The initial asymmetry drops at a slightly lower temperature. There is also a lack of correspondence with susceptibility data in this sample, with the ZFC susceptibility peak occurring at 38.8K.

For the β-$Mn_{0.75}Co_{0.25}$ sample λ^{β} begins to rise sharply below 80K; at around the same temperature a_0 starts to drop. The relaxation rate peak occurs at 69.8K, close to the peak found in $\chi(T)$ at 71K.

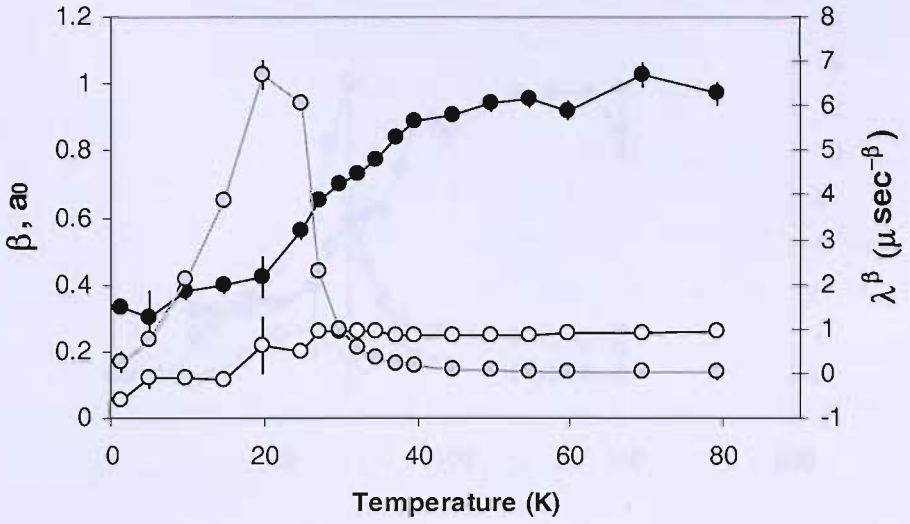

Figure 7.23: muon spin relaxation parameters in LF data recorded for β-$Mn_{0.95}Co_{0.05}$. Initial asymmetry is represented by open circles, while the exponent β is denoted by black circles. The relaxation rate parameter λ^{β} is denoted by grey circles (right-hand scale)

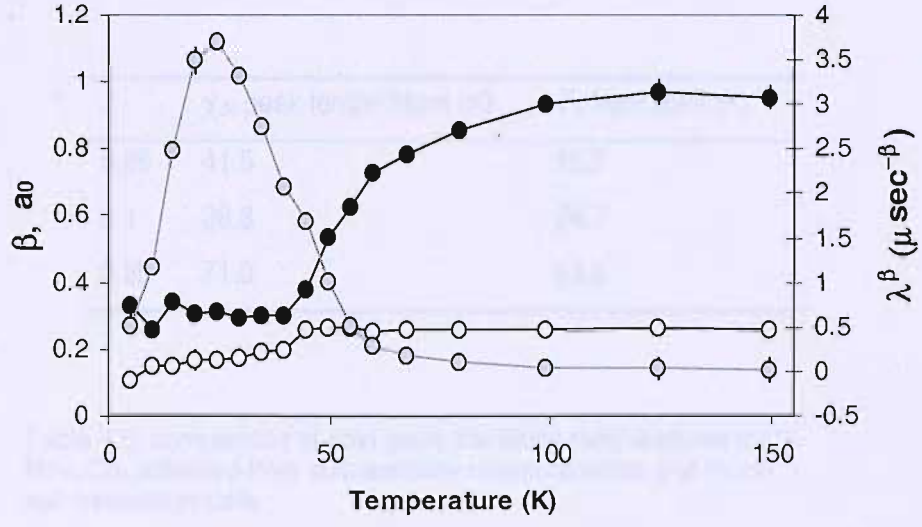

Figure 7.24: muon spin relaxation parameters in LF data recorded for β-$Mn_{0.9}Co_{0.1}$. The symbol key is as for β-$Mn_{0.95}Co_{0.05}$

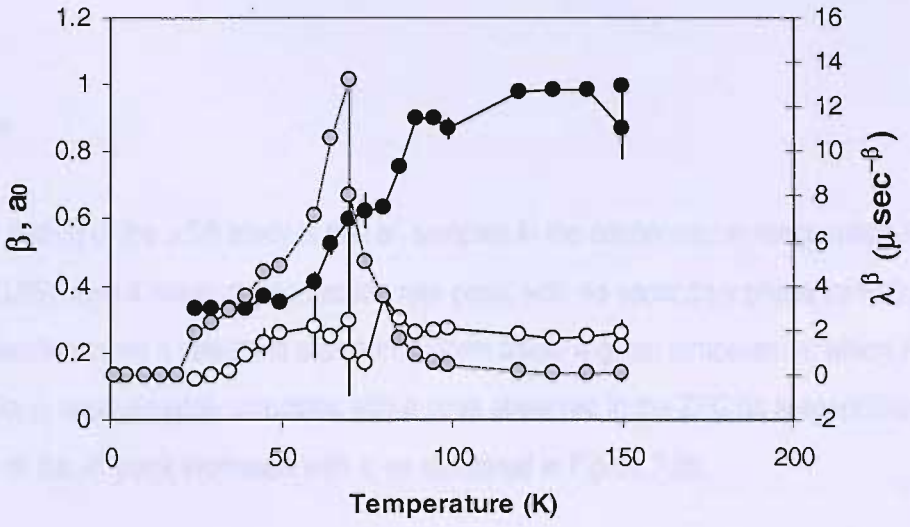

Figure 7.25: muon spin relaxation parameters in LF data recorded for β-$Mn_{0.75}Co_{0.25}$. The symbol key is as given previously

x	χ_{dc} peak temperature (K)	T_G from μSR (K)
0.05	41.5	19.7
0.1	38.8	24.7
0.25	71.0	69.8

Table 7.5: comparison of spin glass transition temperatures for β-$Mn_{1-x}Co_x$ obtained from susceptibility measurements and muon spin relaxation data

Discussion

A significant finding of the μSR study is that all samples in the concentration range measured here ($0.05 \leq x \leq 0.25$) have a single depolarization rate peak, with no secondary phase transition. In each case the relaxation takes a stretched exponential form below a given temperature, which in the case of β-$Mn_{0.75}Co_{0.25}$ approximately coincides with a peak observed in the ZFC dc susceptibility. The temperature of the λ^{β} peak increases with x, as illustrated in Figure 7.26.

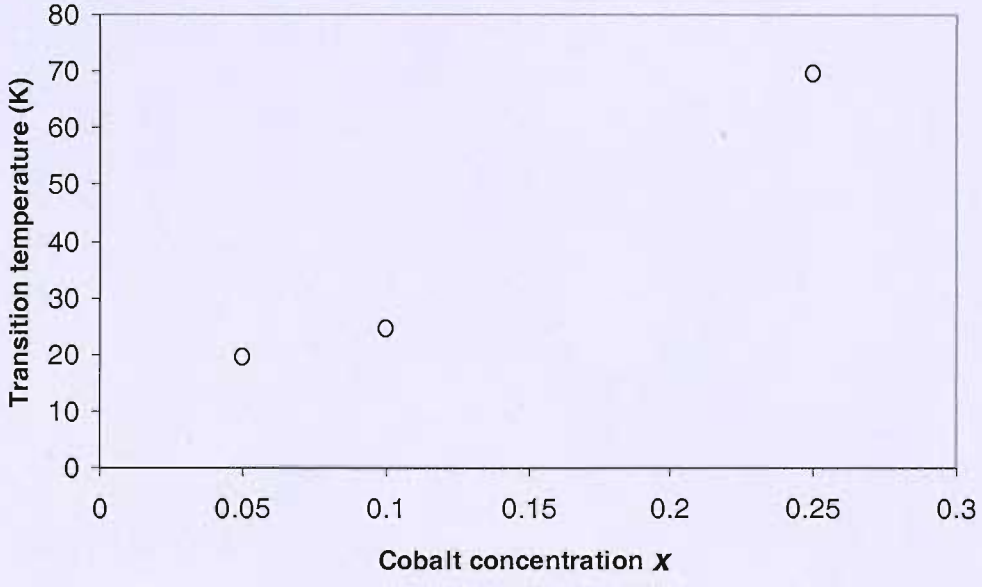

Figure 7.26: transition temperature T_G implied by peaks in the relaxation rate λ^{β} in β-$Mn_{1-x}Cox$ with $0.05 \leq x \leq 0.25$

The single transition would appear to be a spin glass-type freezing transition, as the stretched exponential relaxation function applied to the temperature regime in which the peaks occur is generally associated with spin glass order. The drop in initial asymmetry with temperature does not occur sharply however, as has been observed for other β-$Mn_{1-x}M_x$ systems (such as β-$Mn_{1-x}Al_x$ [35]) on entering a spin glass state. This gradual decrease in a_0 may reflect an inhomogeneous transition, with a steady and continuous growth of strongly depolarizing regions as opposed to a well-defined, critical transition.

As a consequence of the peak in the depolarization rate observed for all samples, it may be stated that a static magnetic ground state is stabilised in β-$Mn_{1-x}Co_x$ systems with $x \geq 0.05$, with an increase in impurity concentration leading to an increase in transition temperature as may be expected. This is of particular interest, in view of the fact that previous muon studies in which spin glass relaxation is evident have involved Site II aluminium impurities. These alloys are seen to undergo a transition from a quantum spin liquid to a spin glass state, whereby substituting onto the Site II sublattice drives both lattice expansion and a partial lifting of geometrical frustration.

β-$Mn_{1-x}Co_x$ is the first system in which a Site I transition impurity has been shown to generate a similar muon response, signalling a static ground state with spin glass-like magnetic correlations.

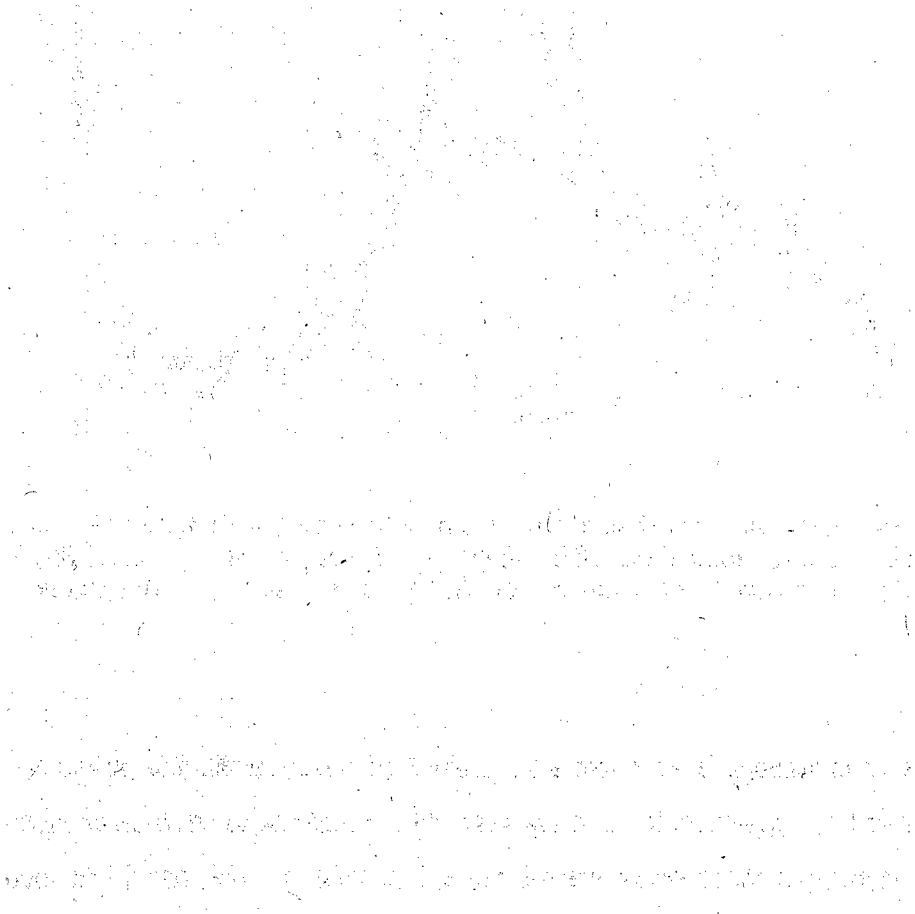

7.7. Polarized Neutron Measurements of β-$Mn_{1-x}Co_x$

A limited number of investigations have been carried out on these alloys using polarized neutron techniques[7]. No long-range order has been reported previously, up to concentrations of 20% Co; however the range of spin correlations is much longer than that found in β-$Mn_{1-x}Al_x$ [36].

No magnetic Bragg peaks are observed at a concentration of 25at.% Co:

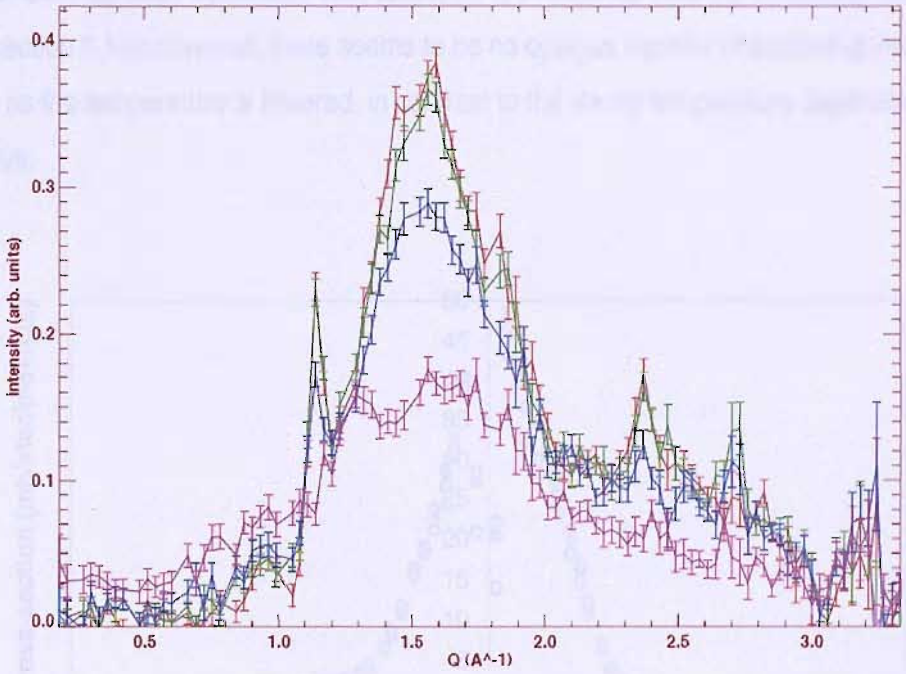

Figure 7.27: magnetic diffuse scattering data from polarized neutron measurements (D7) in β-$Mn_{0.75}Co_{0.25}$, for temperatures 2K (cerise), 100K (blue), 200K (green) and room temperature (red). The peak at $\boldsymbol{q}$ ~ 1.15Å^{-1} is attributable to a MnO impurity phase

There is considerable diffuse scattering evident in this response, suggestive of a disordered component as would be expected for a spin glass system. Unfortunately, insufficient measurements have been performed using this technique to explore any concentration dependence on the range of magnetic correlations.

[7] Measurements carried out by J.R. Stewart

7.8. Inelastic Neutron Scattering Measurements of β-$Mn_{1-x}Co_x$

Inelastic spectra have been obtained for samples with x = 0.01, 0.1, 0.15 and 0.25 using the HET spectrometer (ISIS). Incident energies of 40 and 100meV were used, and the temperature was varied between 7K and room temperature. The magnetic scattering has been extracted by simulating and subtracting the phonon cross-section, estimated using the DISCUS program.

For β-$Mn_{0.75}Co_{0.25}$, an intense quasielastic component appears peaked above 3.0Å^{-1}, revealing the presence of low-frequency dynamics. This response is in common with the scattering data for β-$Mn_{1-x}Ru_x$ (see section 7.15); however, there seems to be no obvious transfer of scattering intensity to the elastic line as the temperature is lowered, in contrast to the strong temperature dependence noted in the Ru alloys.

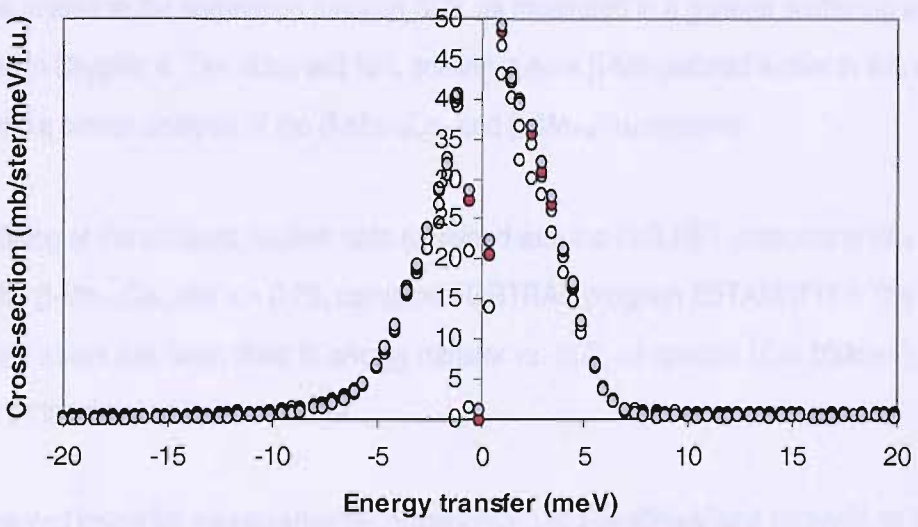

Figure 7.28: magnetic inelastic neutron cross-sections for β-$Mn_{0.75}Co_{0.25}$ at 300K (open circles), 150K (black circles) 50K (red circles) and 7K (grey circles). Scattering corresponds to q = 3.4Å^{-1}

Non-Fermi Liquid Scaling

In the Fermi liquid state, inelastic neutron lineshapes can usually be fitted to the form of a simple Lorentzian function. For materials entering the NFL state, where the spin fluctuation distribution function follows the Bernhoeft "top hat" form, it has been demonstrated [27] that the imaginary part of the dynamical susceptibility can be modelled by:

$$\chi''(\omega) = \frac{\chi\sqrt{\Gamma_1\Gamma_2}}{\Gamma_2 - \Gamma_1}\left[\tan^{-1}\left(\frac{\omega}{\Gamma_1}\right) - \tan^{-1}\left(\frac{\omega}{\Gamma_2}\right)\right]$$

This may be related to the correlation function $S(Q, \omega)$ measured in a general scattering experiment as described in Chapter 4. The observed NFL scaling in pure β-Mn outlined earlier in this chapter has prompted a similar analysis of the β-$Mn_{1-x}Co_x$ and β-$Mn_{1-x}Ru_x$ systems.

Lineshape fitting of the inelastic neutron data (obtained with the ISIS HET instrument) has been performed for β-$Mn_{1-x}Co_x$ with x = 0.25, using the FORTRAN program BETAMNFIT [8]. The Bernhoeft function given above has been fitted to energy transfer vs. $S(Q, \omega)$ spectra (E_i = 100meV), and is normalized by the detailed balance factor.

This is presented below for measurements corresponding to E_i= 40meV and 100meV, at 300K. More detailed analyses of non-Fermi liquid scaling have been carried out for the β-$Mn_{1-x}Ru_x$ series: these are reported in Section 7.15.

[8] BETAMNFIT subroutines developed by B. D. Rainford

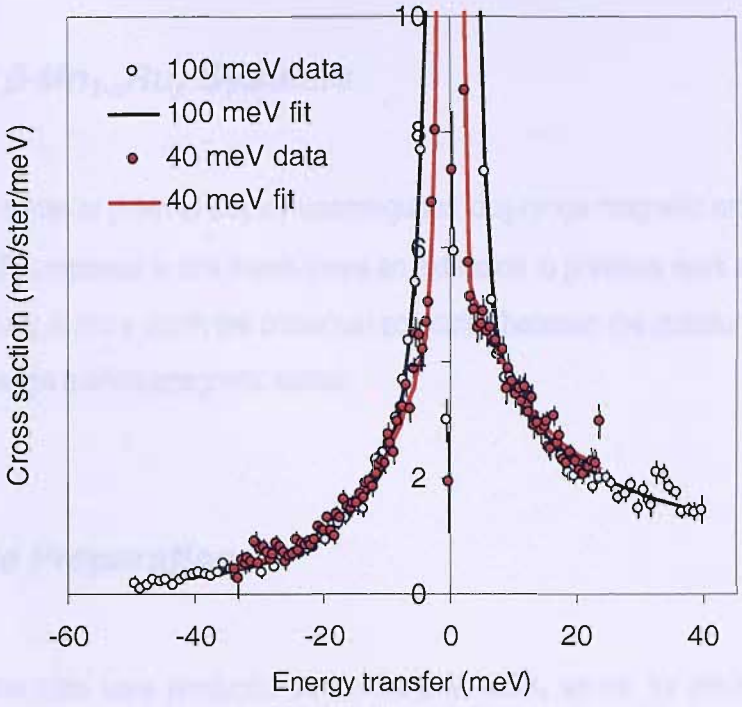

Figure 7.29: magnetic cross-section for β-$Mn_{0.75}Co_{0.25}$ at 300K, corresponding to a wavevector transfer of 1.5 $Å^{-1}$. Fits of both 40meV and 100meV data are shown as given in the key, with data denoted by circles and the Bernhoeft fitting function shown by solid lines

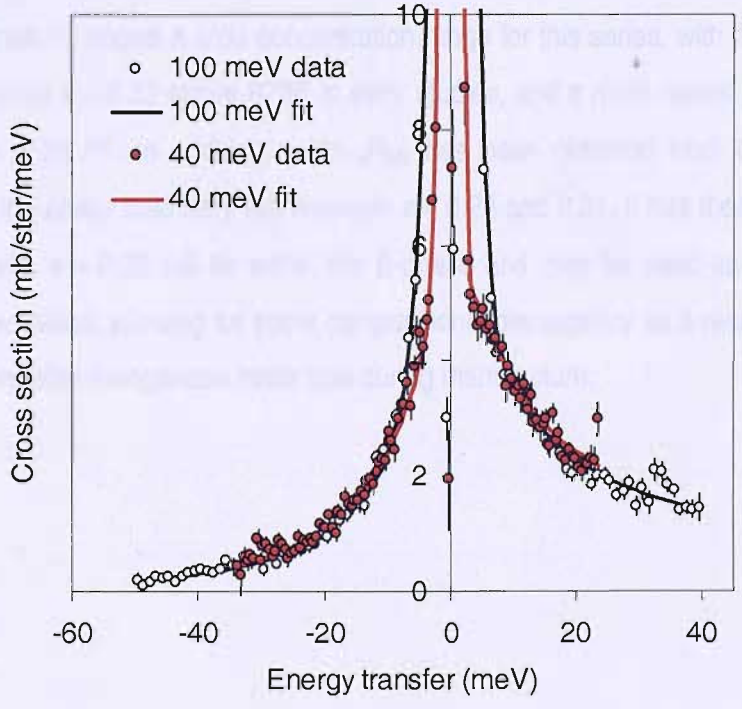

Figure 7.30: magnetic cross-section for β-$Mn_{0.75}Co_{0.25}$ at 200K, corresponding to a wavevector transfer of 1.5 $Å^{-1}$. Fits of 40meV and 100meV data to the Bernhoeft function are shown as above

Studies of β-$Mn_{1-x}Ru_x$ Systems

As the first alloy series of β-Mn to display unambiguous long-range magnetic order, the experimental study of β-$Mn_{1-x}Ru_x$ reported in this thesis forms an extension to previous work and provides an opportunity to study in more depth the crossover scenarios between the quantum spin liquid, spin glass and long-range antiferromagnetic states.

7.9. Sample Preparation

Polycrystalline samples were produced as for the β-$Mn_{1-x}Co_x$ series, by electric arc melting in an argon atmosphere. Concentrations of 3, 6, 9, 12, 19 and 23at.% Ru have been prepared, using constituent starting materials of at least 0.999% purity. The ruthenium used was obtained in sponge form.

The phase diagram [37] shows a wide concentration range for this series, with the β-$Mn_{1-x}Ru_x$ phase shown to exist up to $x = 0.22$ above 873K in early studies, and a more recent single-phase sample obtained at $x = 0.28$ [29]. In addition, γ-$Mn_{1-x}Ru_x$ has been obtained from $0.31 \leq x \leq 0.37$ [38] suggesting that the phase boundary lies between $x = 0.28$ and 0.31. It has therefore been assumed that a sample with $x = 0.23$ will lie within the β-phase and may be used as a reliable maximum ruthenium concentration, allowing for some compositional discrepancy as a result of the high vapour pressure and inevitable manganese mass loss during manufacture.

7.10. Neutron Powder Diffraction Measurements of β-$Mn_{1-x}Ru_x$

Room temperature powder diffraction patterns were obtained for β-$Mn_{1-x}Ru_x$ samples at concentrations in the range $0.03 \leq x \leq 0.19$, using the POLARIS instrument at the ISIS facility, RAL. Rietveld refinement was carried out using the GSAS software.

The refinement parameters obtained are as follows:

x	Lattice parameter (Å)	X (Å)	Y (Å)	U_{iso} Site I	U_{iso} Site II	R-Factor R_{wp}
0.03	6.3342	0.0635	0.2029	0.581	0.676	0.0856
0.06	6.3743	0.0645	0.2036	0.510	1.054	0.0327
0.09	6.3905	0.0651	0.2028	0.802	0.912	0.0395
0.19	6.4621	0.0630	0.2040	0.617	1.369	0.0106

Table 7.6: Rietveld refinement parameters from powder diffraction data recorded for β-$Mn_{1-x}Ru_x$ samples with the POLARIS instrument. U_{iso} represents an isotropic thermal factor

x	Site I Occupancy (%)	Corrected Impurity Concentration (%)
0.03	98.0	1.37%
0.06	97.7	5.86%
0.09	98.2	7.7%
0.19	97.4	14.7%

Table 7.7: Site I occupation percentages and corrected impurity concentrations for ruthenium atoms in β-$Mn_{1-x}Ru_x$ samples with $0.03 \leq x \leq 0.19$

In addition, a room temperature diffraction spectrum was obtained for the β-$Mn_{0.77}Ru_{0.23}$ sample using the D1A diffractometer at the Institut Laue Langevin. Rietveld analysis using GSAS yields a value for the lattice parameter a = 6.4835Å, with a corrected concentration of 17.4at.% Ru. All measurements indicate a strong preference for occupation of lattice Site I by the ruthenium. In this case, the accuracy with which the sample compositions have been determined has been improved considerably by the contrasting scattering lengths of manganese and ruthenium.

The lattice parameter values produced in these refinements agree closely with previous diffraction data [29]. The expansion effect with increasing impurity concentration is particularly noticeable, with an increment of 0.1493Å over the range $0.03 \leq x \leq 0.23$. In contrast, the β-$Mn_{1-x}Al_x$ series exhibits a change in a of 0.0499Å over a similar range in x [39].

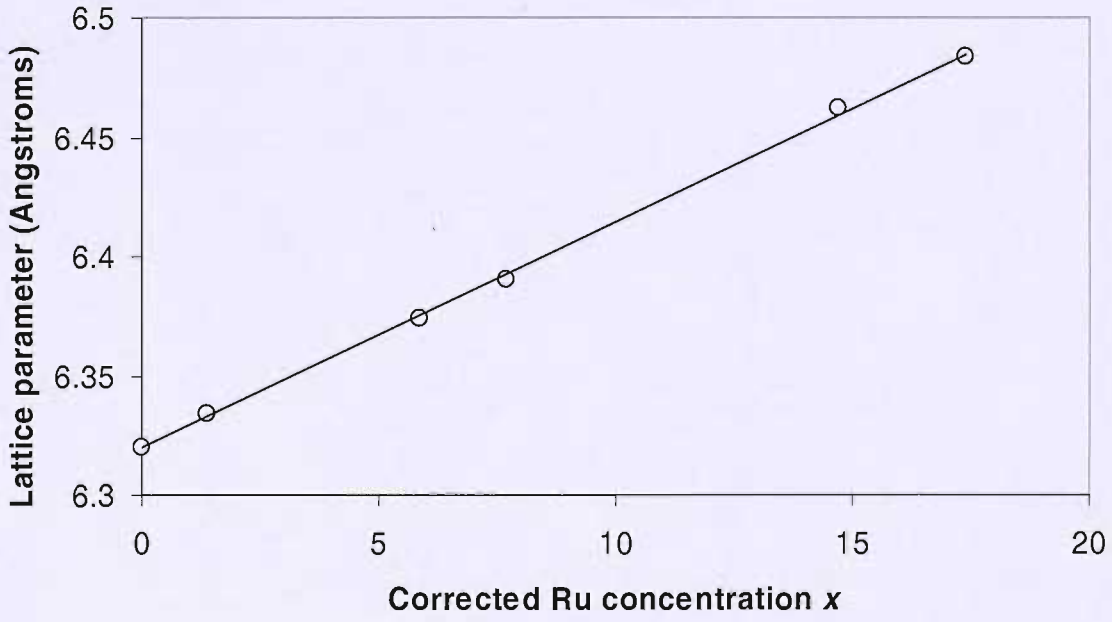

Figure 7.31: impurity concentration dependence of the room temperature lattice parameters in β-$Mn_{1-x}Ru_x$

Lattice parameters for these concentrations appear to be consistent with Vegard's law, with a monotonic increase for increasing x. Structural analysis in these ruthenium alloys has provided further confirmation that the atomic radius of the site preference is not determined strictly by impurity element atomic radius, and highlights the suitability of the β-$Mn_{1-x}Ru_x$ for investigating the effects of lattice expansion in transition-doped β-Mn samples.

A further point of interest is that the values of atomic positional parameter *y* are particularly close to the ~ 0.2035 value required for an equilateral triangular Site II sublattice, in comparison with other Site I impurity systems (such as β-$Mn_{1-x}Co_x$) and Site II alloys.

Additional Bragg peaks occur in the low temperature spectra recorded for β-$Mn_{1-x}Ru_x$ with $x \geq 0.12$, which are not indexable on the crystal cell. These data have been used to elucidate the magnetic structure of these alloys, and will be reported in Section 7.14.

Note: nominal compositions will be used in subsequent discussion of β-$Mn_{1-x}Ru_x$ data, as for the β-$Mn_{1-x}Co_x$, unless otherwise stated

---

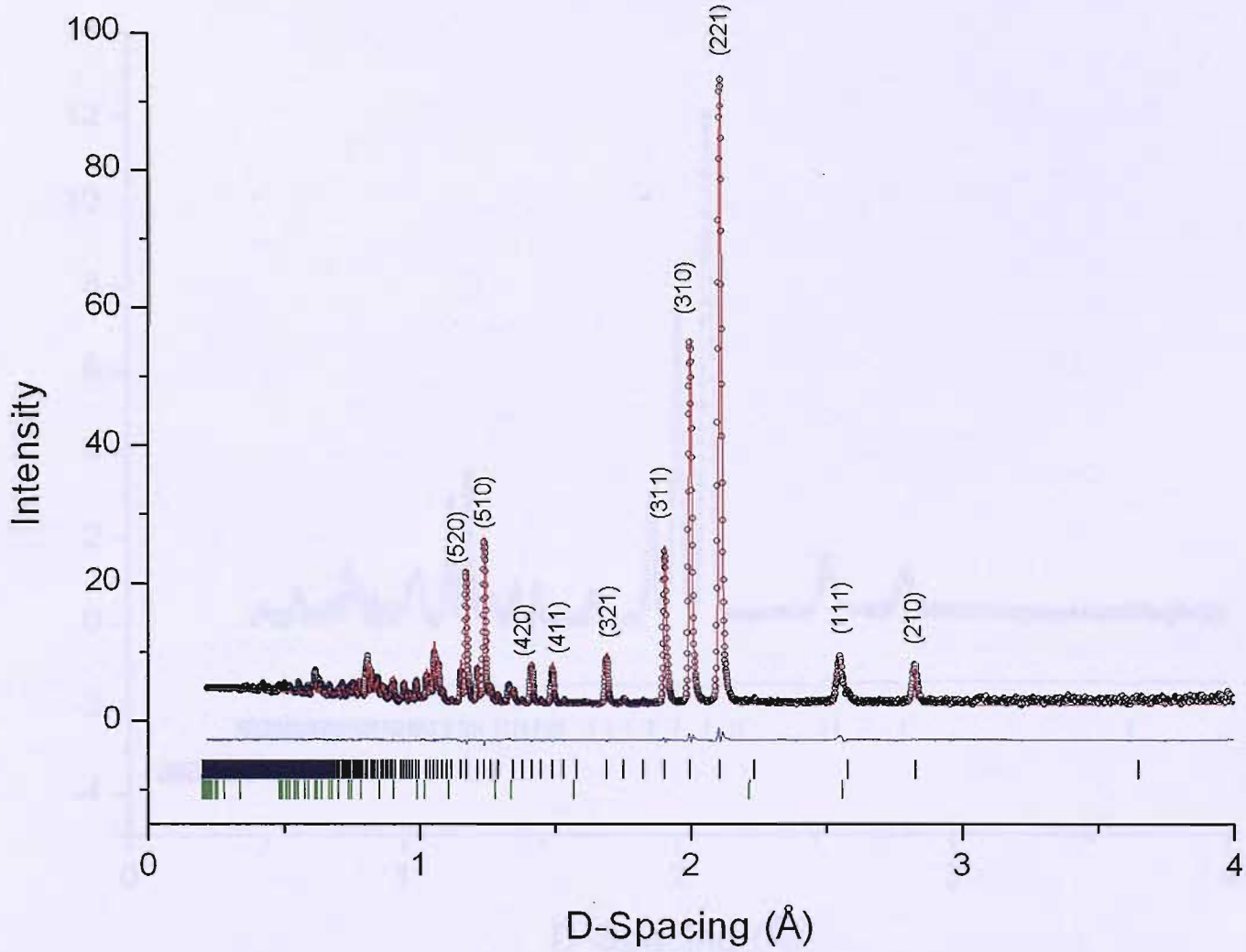

Figure 7.32: room temperature neutron powder diffraction pattern and Rietveld refinement for β-$Mn_{0.97}Ru_{0.03}$ (POLARIS)

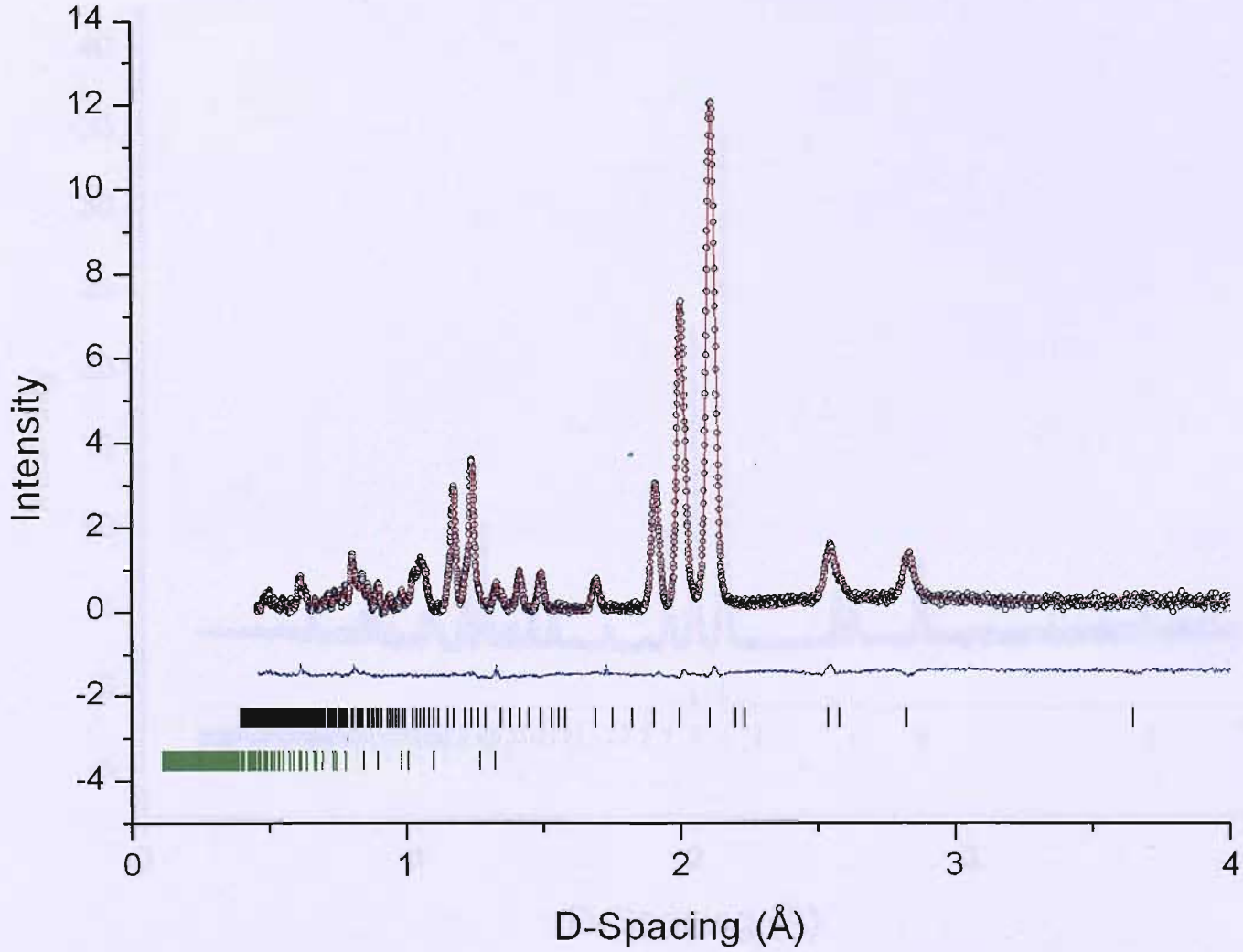

Figure 7.33: room temperature neutron powder diffraction pattern and Rietveld refinement for β-$Mn_{0.94}Ru_{0.06}$ (POLARIS)

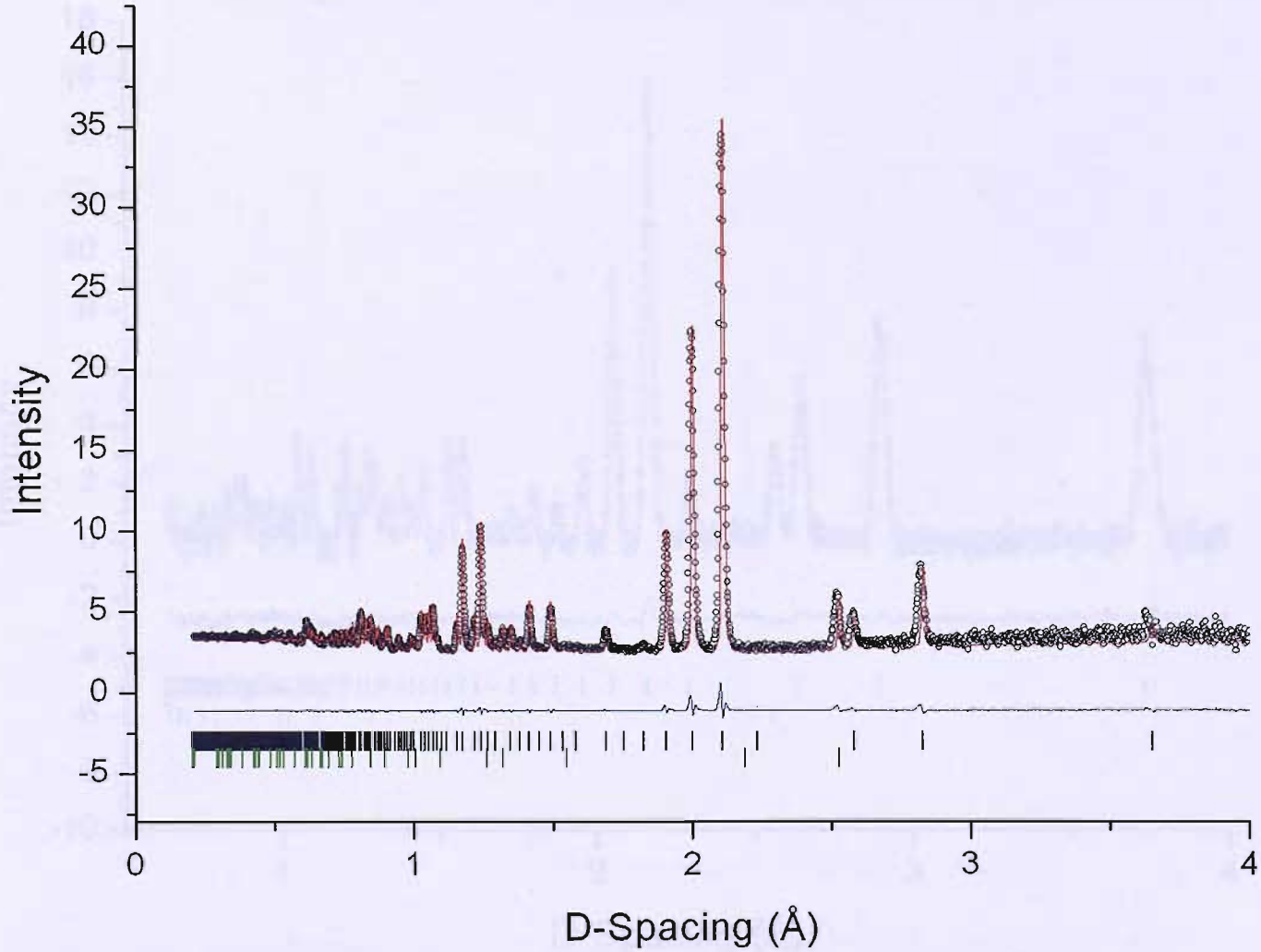

Figure 7.34: room temperature neutron powder diffraction pattern and Rietveld refinement for β-$Mn_{0.91}Ru_{0.09}$ (POLARIS)

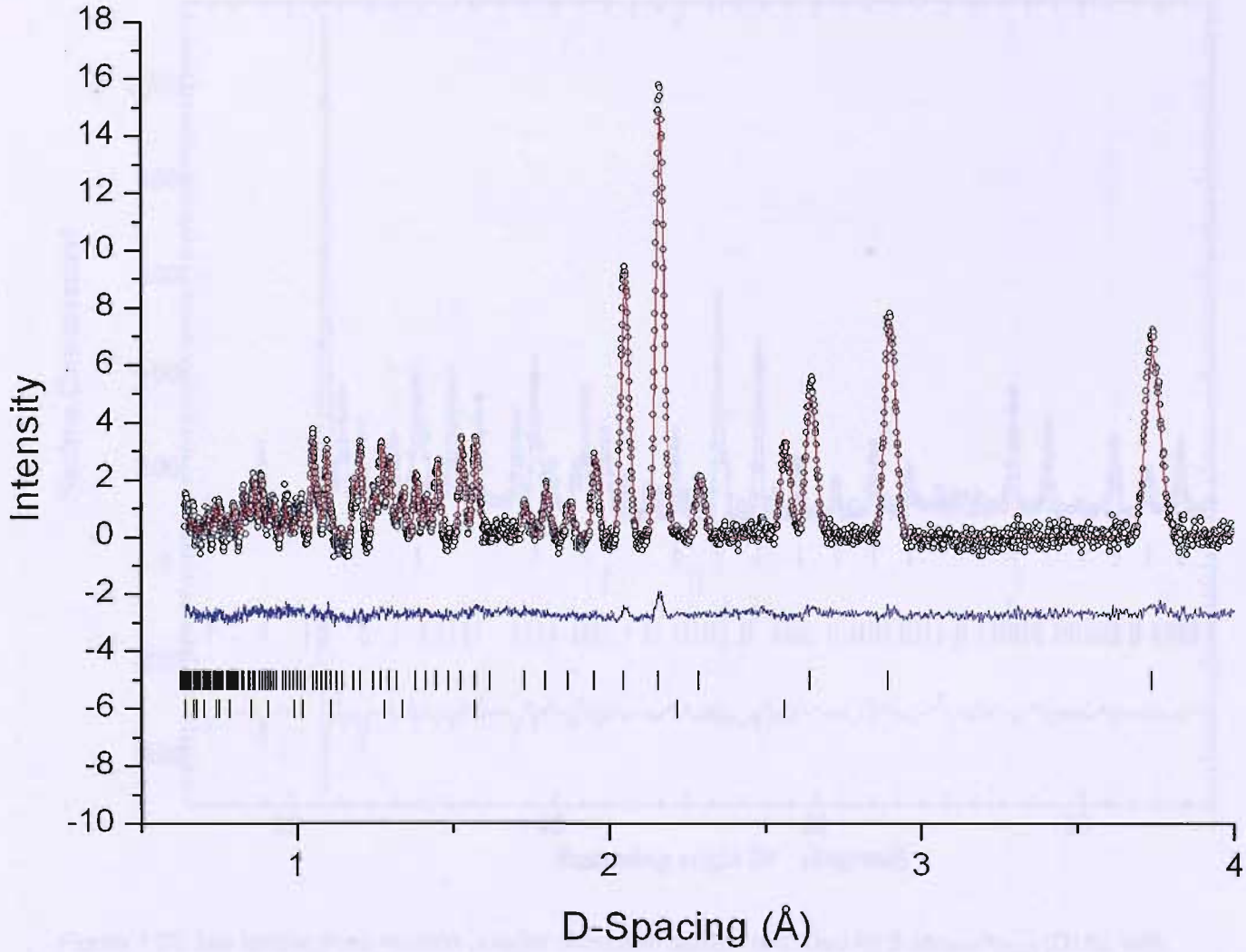

Figure 7.35: room temperature neutron powder diffraction pattern and Rietveld refinement for β-$Mn_{0.81}Ru_{0.19}$ (POLARIS)

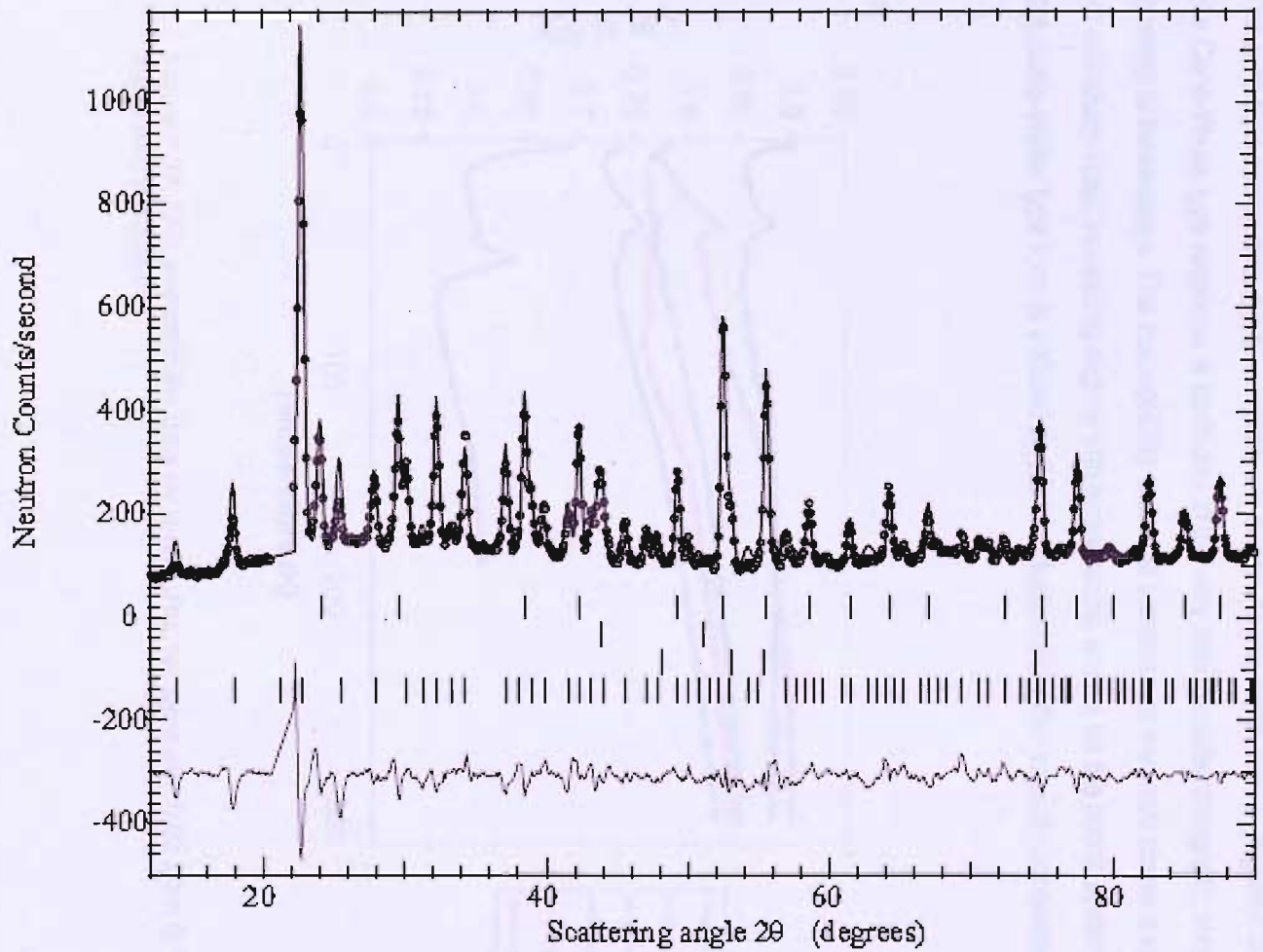

Figure 7.36: low temperature neutron powder diffraction pattern recorded for β-$Mn_{0.77}Ru_{0.23}$ (D1A), with tickmarks corresponding to (from the top) nuclear scattering from the β-$Mn_{0.77}Ru_{0.23}$ phase, low levels of MnO and Ru scattering, and the incommensurate magnetic β-$Mn_{0.77}Ru_{0.23}$ structure - see Section 7.14

7.11. Magnetization Measurements of β-$Mn_{1-x}Ru_x$

Measurements were performed for the β-$Mn_{1-x}Ru_x$ series with $0.03 \leq x \leq 0.23$, as for the β-$Mn_{1-x}Co_x$ samples.

The zero-field cooled data for all samples are shown on the same axes in Figure 7.37. The absence of a Curie-Weiss type response is attributed to the very strong antiferromagnetic short-range order inherent to these alloys. The susceptibility is almost temperature-invariant above a significant Curie tail and sharp cusp, increasing slightly with temperature, and as for the cobalt systems no transition to a Curie-Weiss type form is initiated by the introduction of higher impurity concentrations.

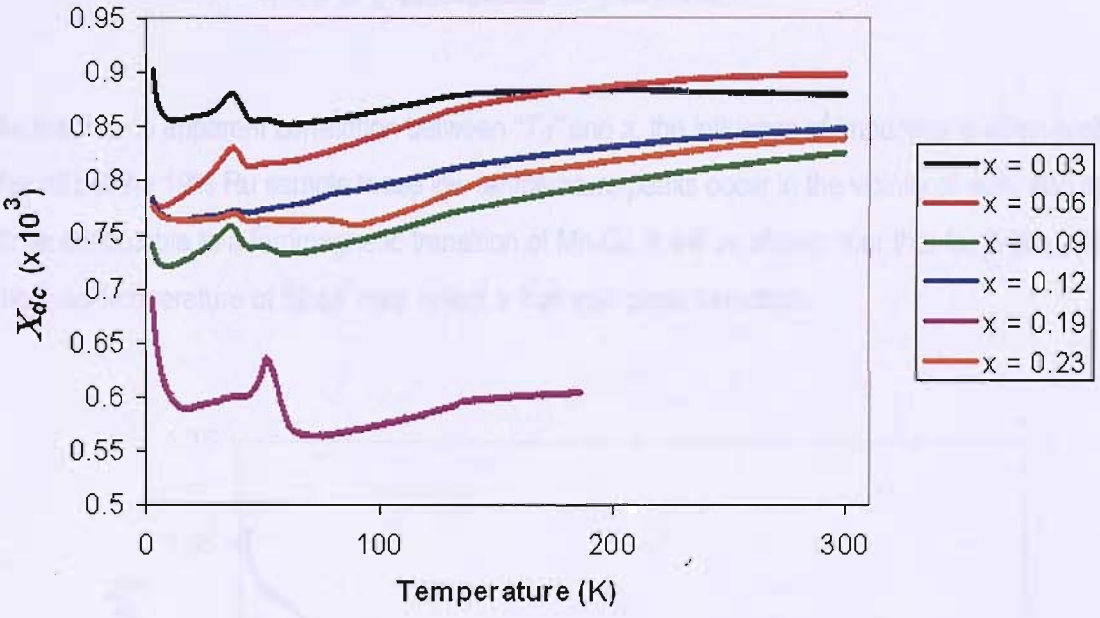

Figure 7.37: ZFC susceptibility data for β-$Mn_{1-x}Ru_x$ samples with $0.03 \leq x \leq 0.19$, measured in 1000G

In light of the expansion effects brought about by the substitution of Ru into the β-Mn lattice, it may be argued that the temperature dependence of the susceptibility would be expected to follow a form similar to that observed in the β-$Mn_{1-x}Al_x$ alloys. These show a Curie-Weiss type decrease in χ_{dc} with increasing temperature above a low-temperature peak, for concentrations greater than 10at.% Al [40].

As with the β-$Mn_{1-x}Co_x$ series, all samples show bifurcation of the FC and ZFC data, which may be construed as typically spin glass-like. The history dependences emerges above, at or below the ZFC cusps in different samples, with the latter occurring at the following temperatures:

x	Temperature of susceptibility peak (K)
0.03	39.4
0.06	39.2
0.09	37.7
0.12	41.5
0.19	52.5
0.23	39.5

Table 7.8: temperatures corresponding to peaks in the ZFC susceptibility for β-$Mn_{1-x}Ru_x$

As there is no apparent correlation between "T_G" and *x*, the influence of impurities is again probable. For all but the 19% Ru sample these low temperature peaks occur in the vicinity of 40K, and appear to be attributable to a ferrimagnetic transition of Mn_3O_4. It will be shown later that for β-$Mn_{0.81}Ru_{0.19}$, the cusp temperature of 52.5K may reflect a true spin glass transition.

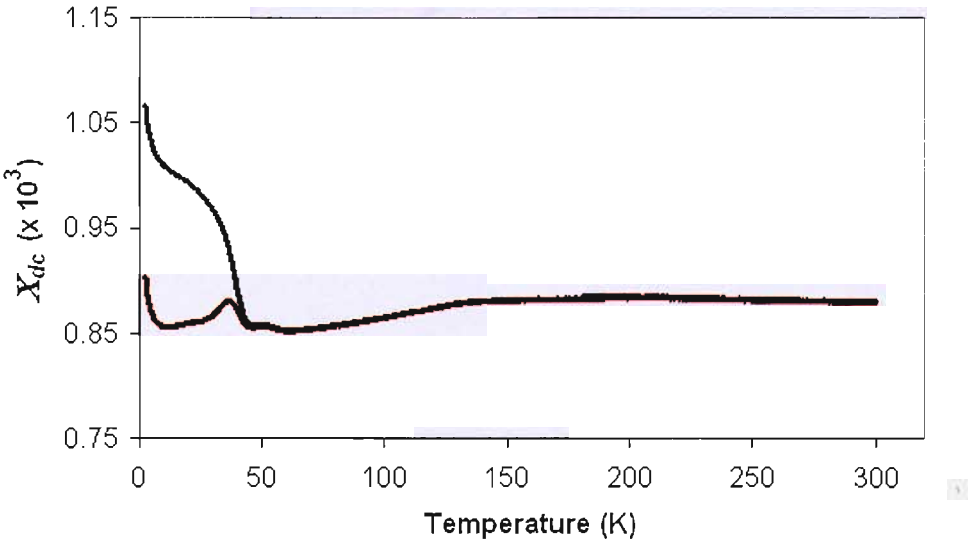

Figure 7.38: ZFC (red) and FC (black) susceptibilities of β-$Mn_{0.97}Ru_{0.03}$

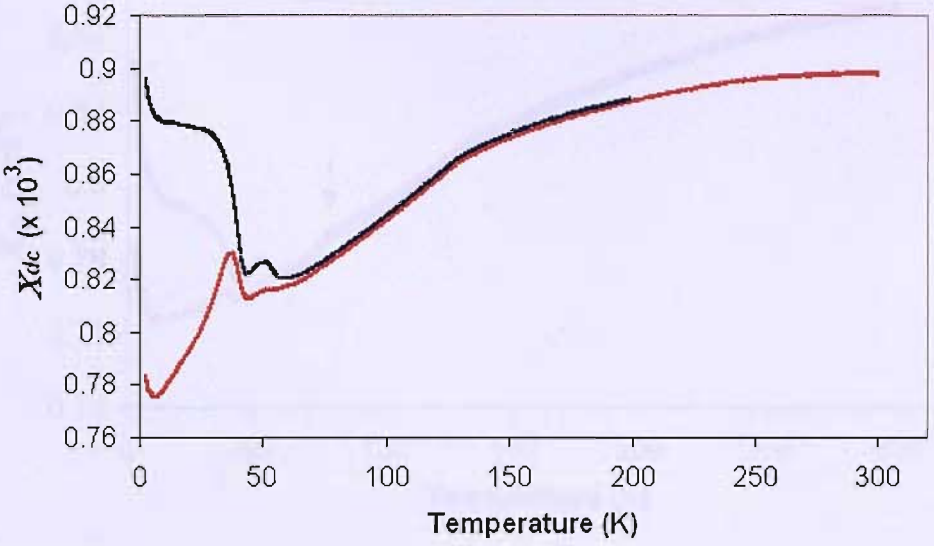

Figure 7.39: ZFC (red) and FC (black) susceptibilities of β-$Mn_{0.94}Ru_{0.06}$

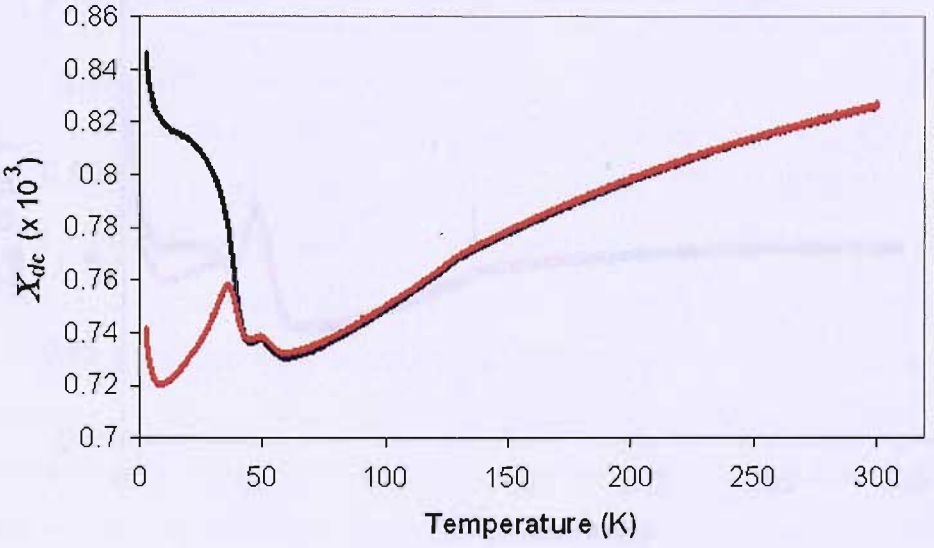

Figure 7.40: ZFC (red) and FC (black) susceptibilities of β-$Mn_{0.91}Ru_{0.09}$

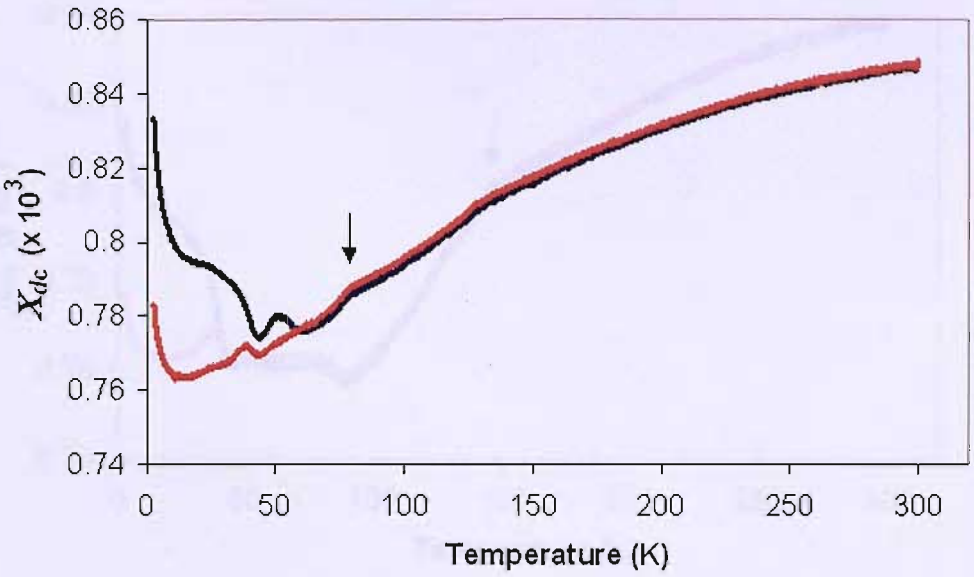

Figure 7.41: ZFC (red) and FC (black) susceptibilities of β-$Mn_{0.88}Ru_{0.12}$. T_N is indicated by an arrow

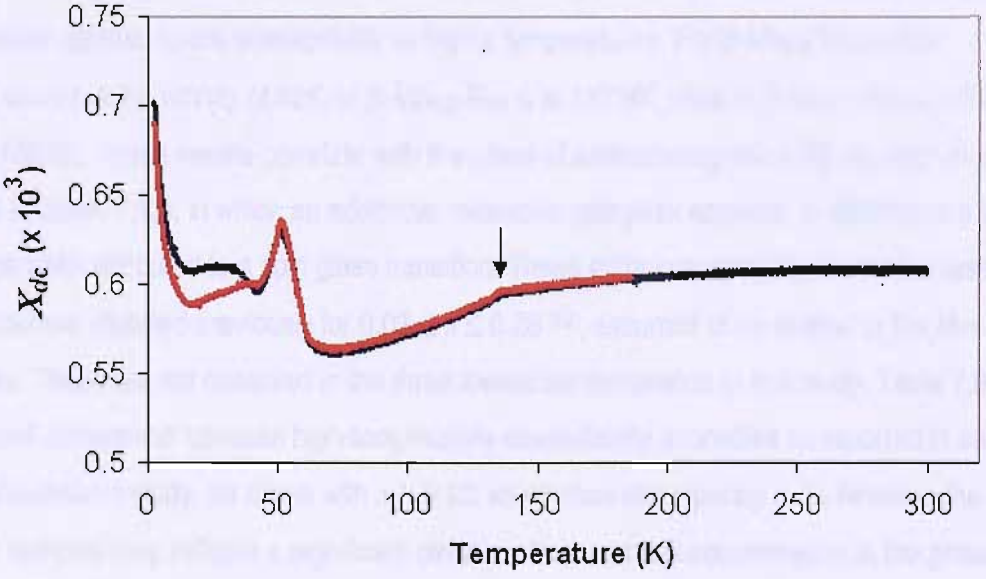

Figure 7.42: ZFC (red) and FC (black) susceptibilities of β-$Mn_{0.81}Ru_{0.19}$. T_N is indicated by an arrow

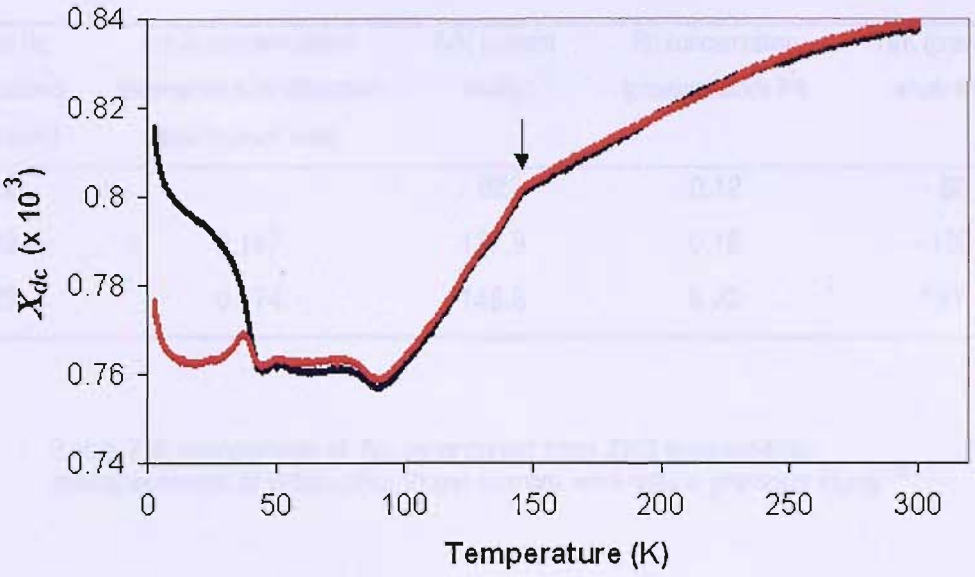

Figure 7.43: ZFC (red) and FC (black) susceptibilities of β-$Mn_{0.77}Ru_{0.23}$. T_N is indicated by an arrow

A significant finding established by the magnetometry data is that for concentrations $x \geq 0.12$, a second feature appears in the susceptibility at higher temperatures. For β-$Mn_{0.81}Ru_{0.12}$ this "shoulder" occurs in the vicinity of 82K, in β-$Mn_{0.81}Ru_{0.19}$ at 137.9K, while in β-$Mn_{0.77}Ru_{0.23}$ a feature is seen at 148.8K. These results correlate with the onset of antiferromagnetic LRO as seen in the muon data (Section 7.13), in which an additional relaxation rate peak appears, in addition to a low-temperature peak attributed to a spin glass transition. These extra susceptibility anomalies resemble the weak maxima reported previously for $0.03 \leq x \leq 0.28$ [29], assumed to be related to the Neel temperature. These are not observed in the three lowest concentrations in this study. Table 7.9 makes a brief comparison between high-temperature susceptibility anomalies as reported in earlier work and the present study, for alloys with $x \geq 0.12$: an obvious discrepancy in T_N between the 12at.% Ru samples may indicate a significant deviation from nominal concentration in the present sample, while for 23at.% Ru a seemingly close agreement in T_N on first inspection cannot be held as meaningful, due to the somewhat reduced concentration in sample used for this study.

Nominal Ru concentration x (current work)	Actual concentration x determined from diffraction data (current work)	T_N/K (current work)	Ru concentration (previous study [29])	T_N/K (previous study [29])
0.12	-	82	0.12	~ 60
0.19	0.147	137.9	0.18	~120
0.23	0.174	148.8	0.23	151

Table 7.9: comparison of T_N, determined from ZFC susceptibility measurements of β-$Mn_{1-x}Ru_x$ in the current work and a previous study [29]

7.12. Specific Heat Measurements of β-$Mn_{1-x}Ru_x$

Specific heat measurements for β-$Mn_{0.88}Ru_{0.12}$ and β-$Mn_{0.81}Ru_{0.19}$ have been made using PPMS instrumentation at RAL.

In the 12at.% sample, there is a change in the slope of C/T versus T at around 78K, coinciding with a secondary μSR feature (see Chapter 7.13) and in the vicinity of a cusp observed in the magnetic susceptibility (82K). While there is an absence of a clear, well-defined peak as occurs in β-$Mn_{0.81}Ru_{0.19}$, it is probable that this relates to the onset of magnetic ordering, corresponding to the approximate temperature at which weak Bragg peaks appear in diffraction and polarized neutron data.

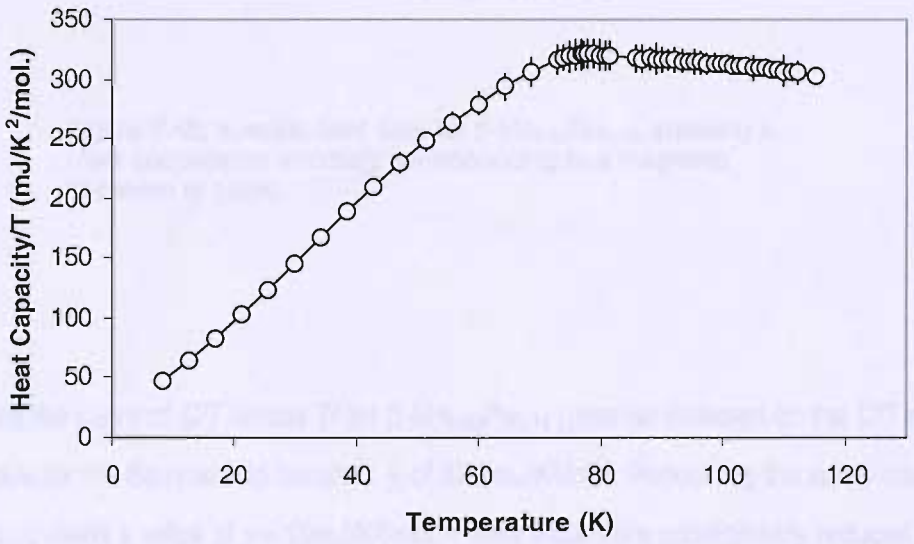

Figure 7.44: specific heat data for β-$Mn_{0.88}Ru_{0.12}$, showing a weak peak at 77K

In contrast, the 19at.% Ru sample shows a clear cooperative anomaly at 133K, coinciding with the high-temperature cusp in the magnetic susceptibility (137.9K), and agreeing closely with a μSR peak at 131.3K.

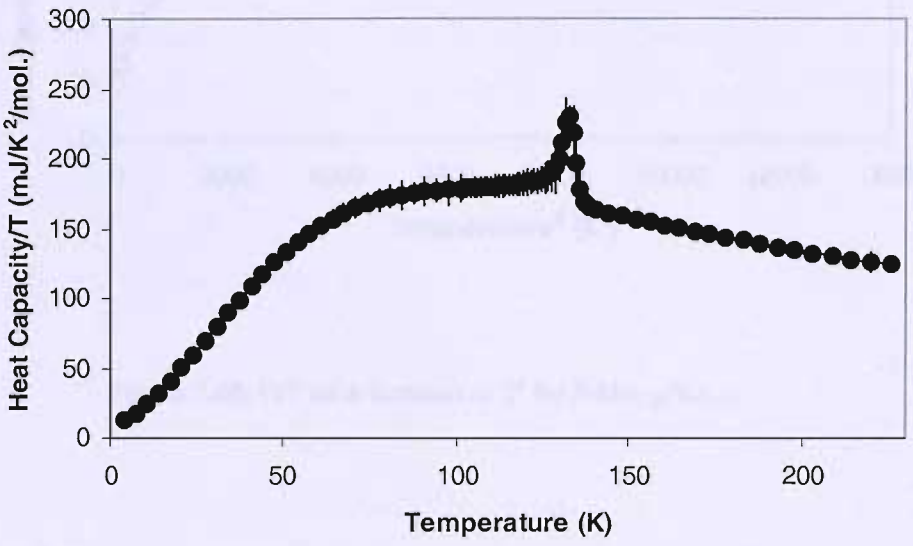

Figure 7.45: specific heat data for β-$Mn_{0.81}Ru_{0.19}$, showing a clear cooperative anomaly corresponding to a magnetic transition at 133K

Extrapolating the curve of *C/T* versus T^2 for β-$Mn_{0.88}Ru_{0.12}$ gives an intercept on the *C/T* axis, and hence a value for the Sommerfeld constant γ, of 37.5mJ/K²/mol. Performing the same treatment for β-$Mn_{0.81}Ru_{0.19}$ yields a value of γ= 10mJ/K²/mol. These values are considerably reduced from the pure element value of 70 mJ/K²/mol.

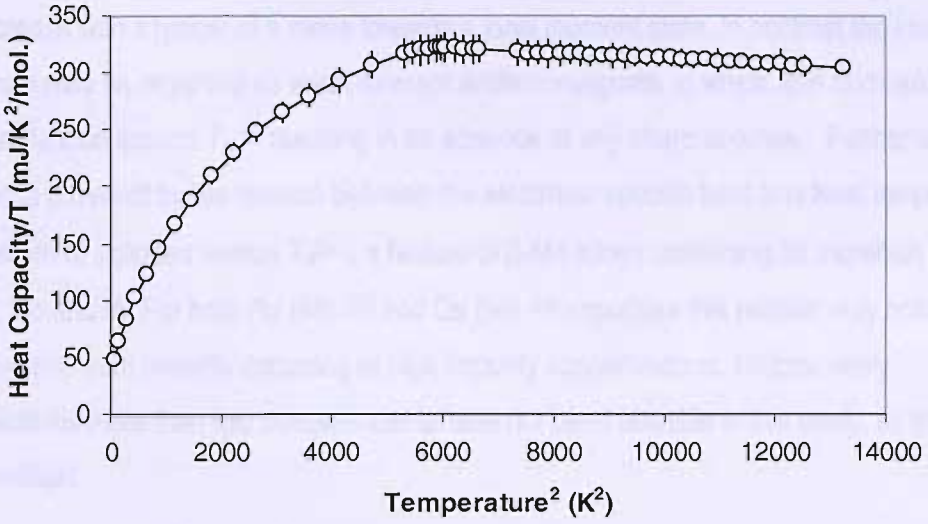

Figure 7.46: C/T as a function of T^2 for β-$Mn_{0.88}Ru_{0.12}$.

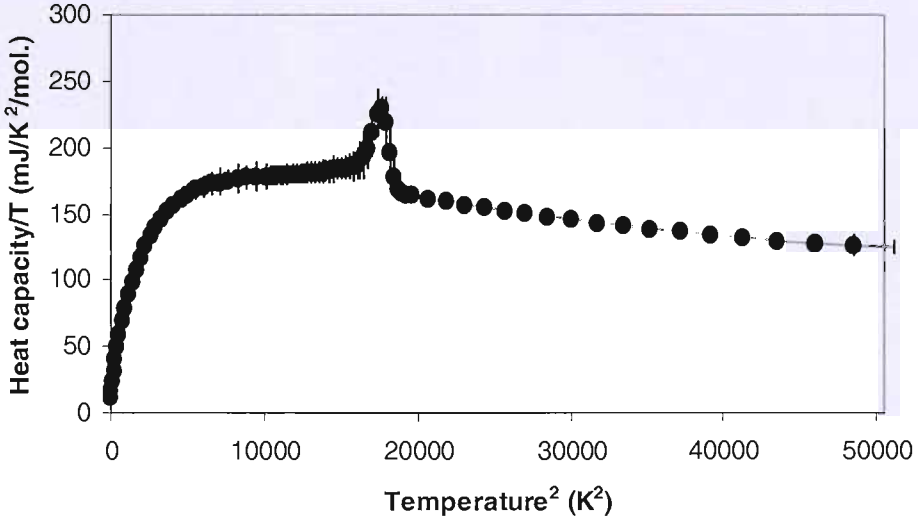

Figure 7.47: C/T as a function of T^2 for β-$Mn_{0.81}Ru_{0.19}$

These results are in agreement with previous specific heat data [29], in which clear, sharp peaks are observed in $C(T)$ in the concentration range $0.18 \leq x \leq 0.28$. At $x = 0.12$, the peak diminishes dramatically.

It has been suggested that the magnetic character of β-$Mn_{1-x}Ru_x$ approaches an intermediate state between the weak itinerant magnetism expected for a Site I impurity system and a localized regime.

This is supported by previous heat capacity measurements, in which magnetic entropy estimates [29] show an increase with x typical of a move towards a local moment state. In contrast the lower concentrations may be regarded as weak itinerant antiferromagnets, in which spin fluctuation effects are widely enhanced around T_N [4] resulting in an absence of any sharp anomaly. Further support for this scenario is provided by the relation between the electronic specific heat and Neel temperature: the linear nature of γ plotted versus $T_N^{3/4}$ is a feature of β-Mn alloys containing 3d transition additives such as Fe, Co and Ni. For both Ru (4d) [29] and Os (5d) [28] impurities this relation only holds for low x, with a deviation from linearity occurring at high impurity concentrations. Unfortunately, measurements for more than two concentrations have not been possible in this study, so this scaling cannot be verified.

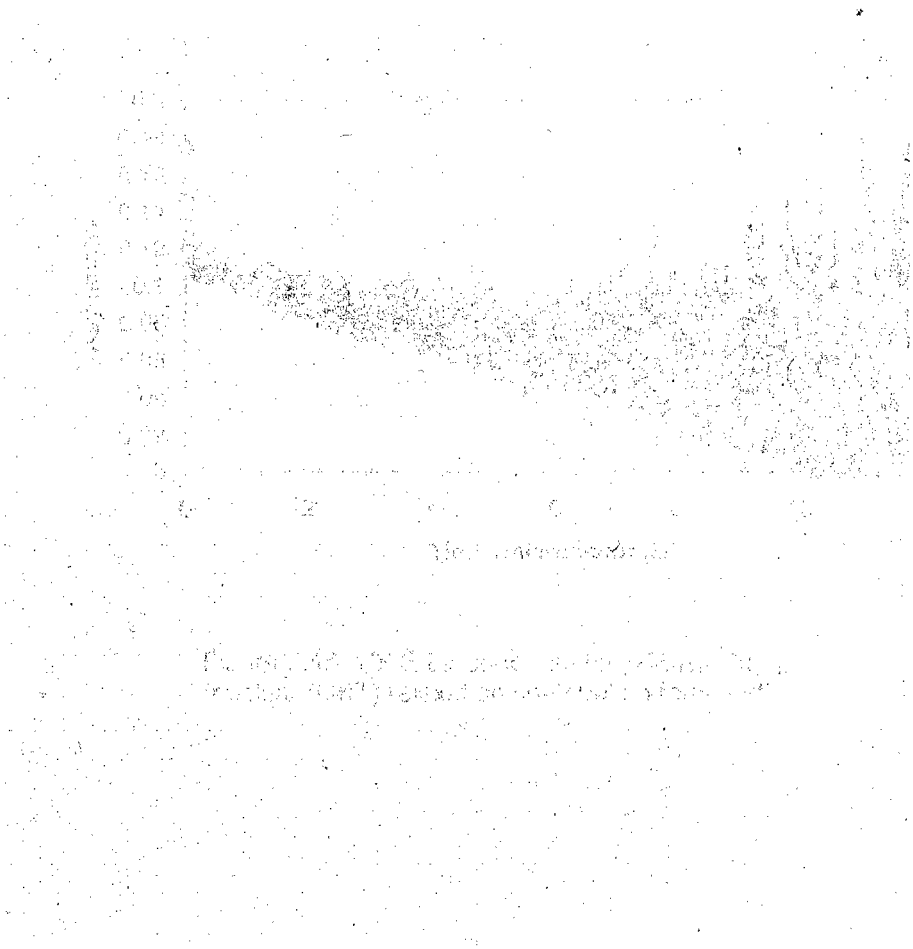

7.13. Muon Spin Relaxation in β-$Mn_{1-x}Ru_x$

Muon spin relaxation spectra were obtained for samples with nominal concentrations of 3, 6, 9, 12, 19 and 23at.% Ru, using the MuSR instrument at ISIS.

Data fitting has shown a similar response to the β-$Mn_{1-x}Co_x$ samples, with a ZF function composed of GKT and stretched exponential components. At high temperatures the exponent β becomes ~ 1, corresponding to simple exponential relaxation from spin fluctuations.

In all cases an applied field of 100G was sufficient to decouple the muon spins from nuclear fields, illustrated by the following spectrum recorded for β-$Mn_{0.81}Ru_{0.19}$ at ~ 115K

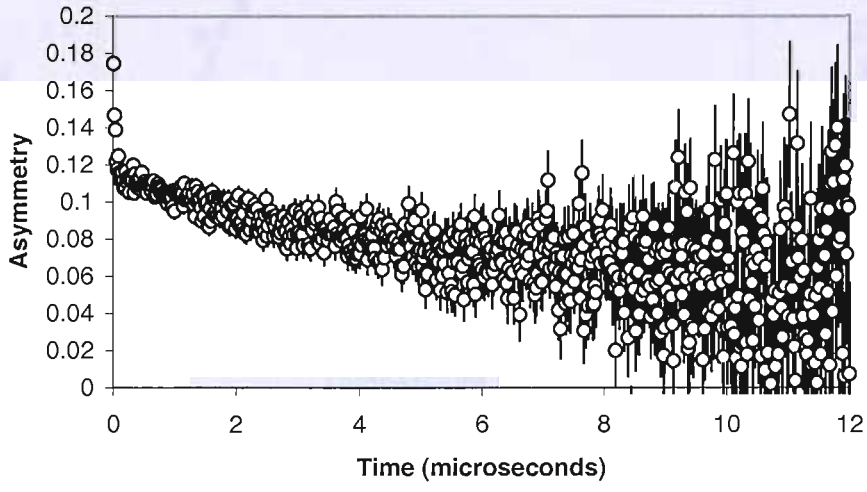

Figure 7.48: 100G LF spectrum for β-$Mn_{0.81}Ru_{0.19}$ (nuclear (GKT) relaxation contribution removed)

Relaxation for $0.03 \leq x \leq 0.09$

For samples with $x < 0.12$ (3, 6 and 9at.% Ru), the stretched exponential relaxation function is established below a characteristic temperature. Peaks in the relaxation rate λ (or λ^{β}) occur at temperatures slightly below those of the susceptibility cusps for $x = 0.03$ and 0.06, and at a slightly higher temperature in $x = 0.09$. The exponent β falls to around 1/3 of its initial value at the transition, from a value of ~1 at high temperatures (the high temperature magnetic relaxation is simple Lorentzian). The initial asymmetry falls to around half of its initial value at the same temperature. The results of this analysis are shown below:

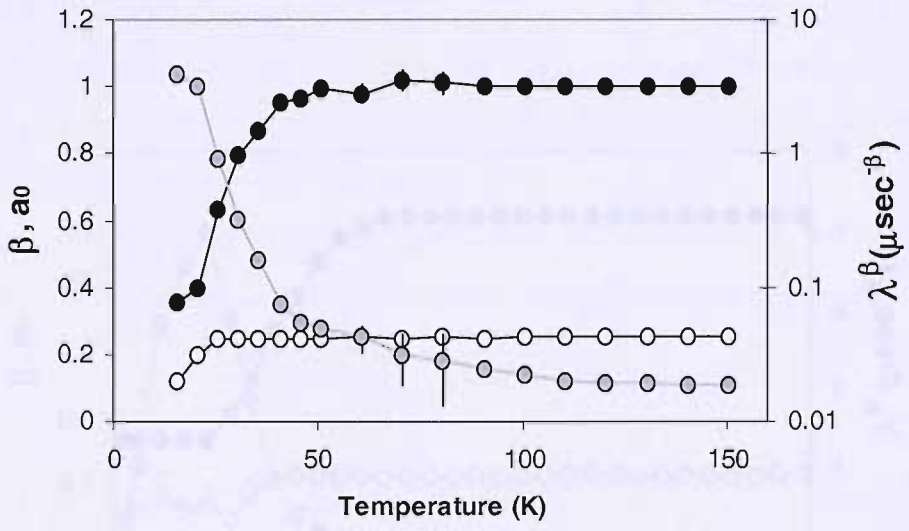

Figure 7.49: temperature dependence of the μSR fitting parameters in β-$Mn_{0.97}Ru_{0.0.3}$, measured in a 100G LF
Key: Grey circles = rate parameter λ^{β}, black circles = exponent β, open circles = initial asymmetry a_0

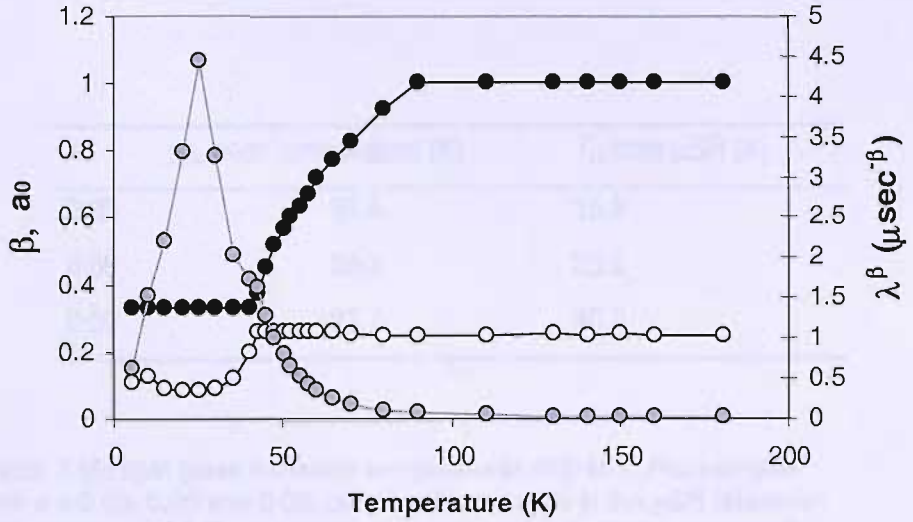

Figure 7.50: temperature dependence of the μSR fitting parameters in β-$Mn_{0.94}Ru_{0.0.6,}$ measured in a 100G LF (Key as for Figure 7.49)

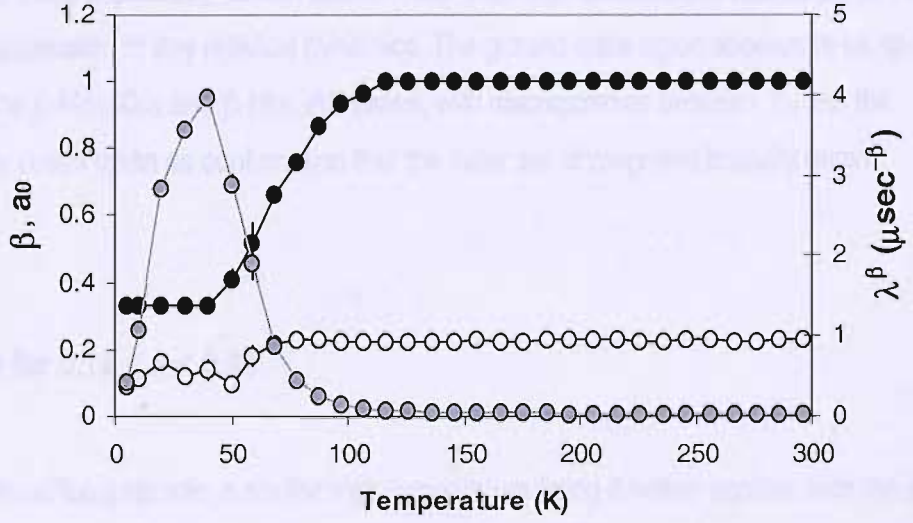

Figure 7.51: temperature dependence of the μSR fitting parameters in β-$Mn_{0.91}Ru_{0.0.9,}$ measured in a 100G LF (Key as given previously)

x	χ_{dc} peak temperature (K)	T_G from μSR (K)
0.03	39.4	15.9
0.06	39.2	25.2
0.09	37.7	40.2

Table 7.10: spin glass transition temperatures of β-$Mn_{1-x}Ru_x$ samples with x = 0.03, 0.06 and 0.09, obtained from peaks in the μSR relaxation rate parameter λ^{β}. Temperatures of peaks in the dc ZFC susceptibility are given for comparison

The divergence of λ^{β} for all samples, accompanied by a decrease in a_0 that is far sharper than for the cobalt alloys, indicate a well-defined transition to a static ground state. The base temperature values of the initial asymmetry remain above 1/3 of their high temperature counterparts, implying complete suppression of any residual dynamics. The ground state again appears to be spin glass-like, as for the β-$Mn_{1-x}Co_x$ and β-$Mn_{1-x}Al_x$ series, with discrepancies between T_G and the susceptibility cusps taken as confirmation that the latter are of magnetic impurity origin.

Relaxation for $0.12 \leq x \leq 0.23$

For the β-$Mn_{0.88}Ru_{0.12}$ sample, a similar high-temperature fitting function applies, with the simple Lorentzian relaxation ($\beta = 1$) again observed in the LF data. This persists down to around 100K, below which the asymmetry a_0 drops suddenly to around 1/3 of its high temperature value, and stretched exponential relaxation is observed with a peak in λ^{β} occurring in the vicinity of T_N. The exponent β does not reduce to 1/3 its initial value as in the lower Ru concentrations, and decreases slowly to an eventual value of 0.6. A further peak occurs in λ^{β} at 40.1K, close to the susceptibility peak at 41K. The x = 0.19 and x = 0.23 samples follow a similar pattern: in β-$Mn_{0.81}Ru_{0.19}$ the high temperature depolarization peak occurs at 131.3K and coincides with a loss of asymmetry. This may be compared with the high temperature peak in $\chi(T)$, at 137.9K. Further peaks at 52.K (χ_{dc}) and 44.8K (μSR) are less well correlated. Meanwhile in β-$Mn_{0.77}Ru_{0.23}$ the initial λ^{β} divergence is in good

agreement with the Neel temperature susceptibility cusp, although as for the $x = 0.19$ alloy a second feature at 50.1K does not correspond to the lower susceptibility peak (39.5K).

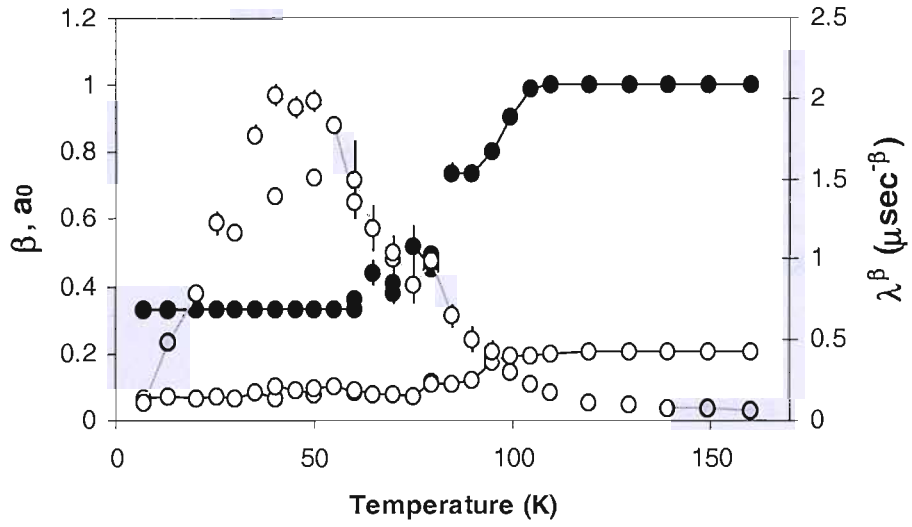

Figure 7.52: temperature dependence of the μSR fitting parameters in β-$Mn_{0.88}Ru_{0.12}$, measured in a 100G LF (Key is as given previously)

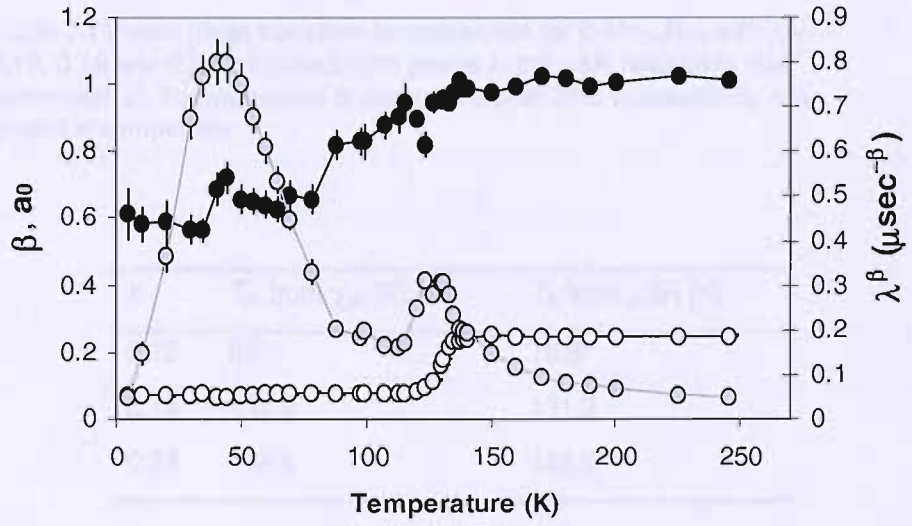

Figure 7.53: temperature dependence of the μSR fitting parameters in β-$Mn_{0.81}Ru_{0.19}$, measured in a 100G LF(Key is as given previously)

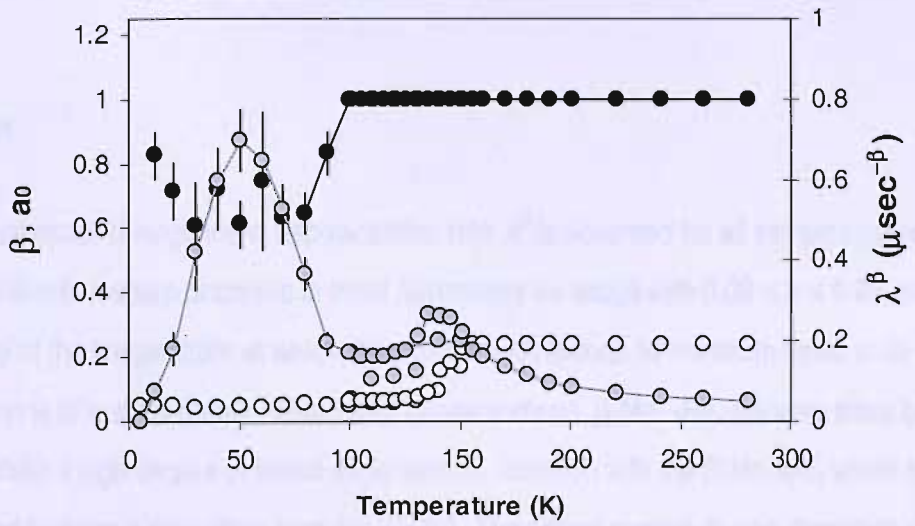

Figure 7.54: temperature dependence of the μSR fitting parameters in β-$Mn_{0.77}Ru_{0.23}$, measured in a 100G LF (Key is as given previously)

x	χ_{dc} peak temperature (K)	T_G from μSR (K)
0.12	41.5	40.1
0.19	52.5	44.8
0.23	39.5	50.1

Table 7.11: spin glass transition temperatures for β-$Mn_{1-x}Ru_x$ with x = 0.12, 0.19 and 0.23, obtained from peaks in the μSR relaxation rate parameter λ^{β}. Temperatures of peaks in the dc ZFC susceptibility are given for comparison

x	T_N from χ_{dc} (K)	T_N from μSR (K)
0.12	82	79.8
0.19	137.9	131.3
0.23	148.8	145.9

Table 7.12: AF transition temperatures for β-$Mn_{1-x}Ru_x$ with x = 0.12, 0.19 and 0.23, obtained from high-temperature peaks in the μSR relaxation rate parameter λ^{β}. Temperatures of peaks in the dc ZFC susceptibility are given for comparison

Discussion

The low temperature divergence in depolarization rate λ^{β} is observed for all samples investigated. This coincides with a sharp decrease in initial asymmetry for alloys with $0.03 \leq x \leq 0.09$, and occurs in the vicinity of the temperature at which the exponent β reaches its minimum value in all cases. The indication is of a static ground state for all concentrations. β-$Mn_{1-x}Ru_x$ systems have been shown to exhibit a high degree of lattice expansion, in common with the β-$Mn_{1-x}Al_x$ which have been demonstrated to enter a spin glass state for $x \geq 0.1$. The abrupt change in spin dynamics occurring in the aluminium alloys can be attributed not only to lattice expansion, leading to narrowing of the spin fluctuation spectral width, but is also due to the introduction of local disorder and lifting of configurational degeneracy in the magnetic sublattice. In fact, since no discontinuity is seen in the lattice constant of these compounds at the critical concentration [39], it has been suggested that disruption of magnetic Site II exchange and a reduction in the degree of geometrical frustration is largely responsible for the quantum spin liquid – spin glass transition. This highlights the significance of the results reported for this μSR study, as for β-$Mn_{1-x}Co_{1-x}$ providing new evidence of spin glass dynamics in Site I impurity systems.

A further remarkable finding lies in the observation of secondary, higher-temperature relaxation peaks for the alloys with $x \geq 0.12$, coinciding approximately with Neel temperature maxima in the $\chi(T)$ curves. These features seem to provide further evidence of a long-range antiferromagnetically ordered state, and correspond to a drop in a_0 for the higher concentrations. A residual dynamical component appears to persist in these systems, with a_0 falling to below 1/3 of the high temperature value. The co-existence of the long-range ordered and spin glass regimes is suggested by the polarized neutron data, which show no loss of AF order parameter within the spin glass state.

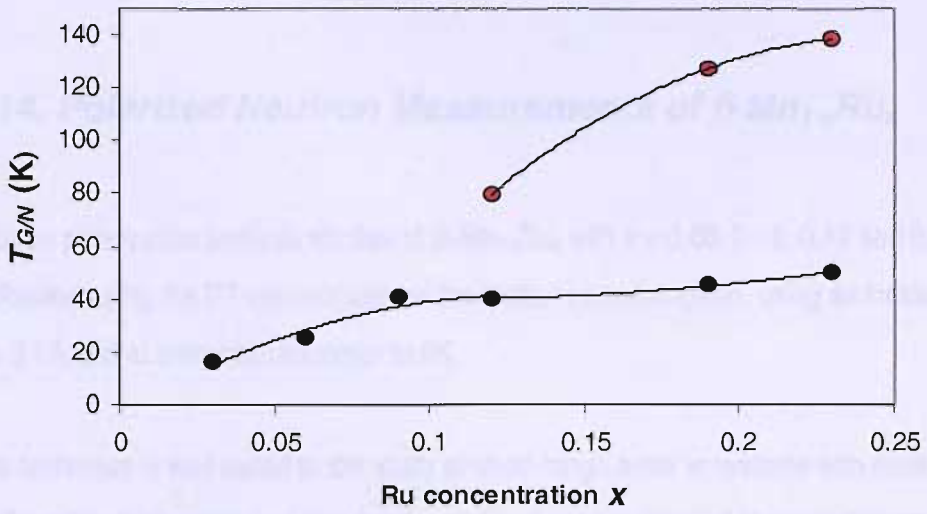

Figure 7.55: spin glass transition temperatures T_G (black circles) and Neel temperatures T_N (red circles) for β-$Mn_{1-x}Ru_x$ as a function of ruthenium concentration x, as determined by μSR experiments. There is an apparent change of gradient in T_G around $x = 0.12$

The experimental work and analysis discussed in this section is due for publication in:

- B. D. Rainford, J. R. Stewart, C. J. Leavey and A. D. Hillier, J. Magn. Magn. Mater. **310 2** (2007) 1314
- C. J. Leavey, J. R. Stewart, B. D. Rainford and A. D. Hillier, J. Phys.: Condens. Matter **19** (2007) 145288

7.14. Polarized Neutron Measurements of β-$Mn_{1-x}Ru_x$

Neutron polarization analysis studies of β-$Mn_{1-x}Ru_x$ with x = 0.06, 0.12, 0.19 and 0.23 have been performed using the D7 spectrometer at the Institut Laue-Langevin, using an incident wavelength of λ = 3.1Å and at temperatures down to 2K.

This technique is well suited to the study of short-range order in systems with nuclear and magnetic configurational disorder, and has previously been used in detailed characterisation of β-$Mn_{1-x}Al_x$ samples [24]. Diffuse magnetic scattering is generally of small amplitude and would normally coexist with nuclear diffuse and spin-incoherent scattering, and so separation of these contributions is essential.

Separated nuclear and magnetic responses for the β-$Mn_{0.81}Ru_{0.19}$ sample, measured at 2K, are shown below (Figure 7.58). A number of magnetic Bragg peaks are evident, which do not coincide with those of the crystal cell as reported in Section 7.10. There is in addition a considerable level of diffuse scattering in both nuclear and magnetic contributions:

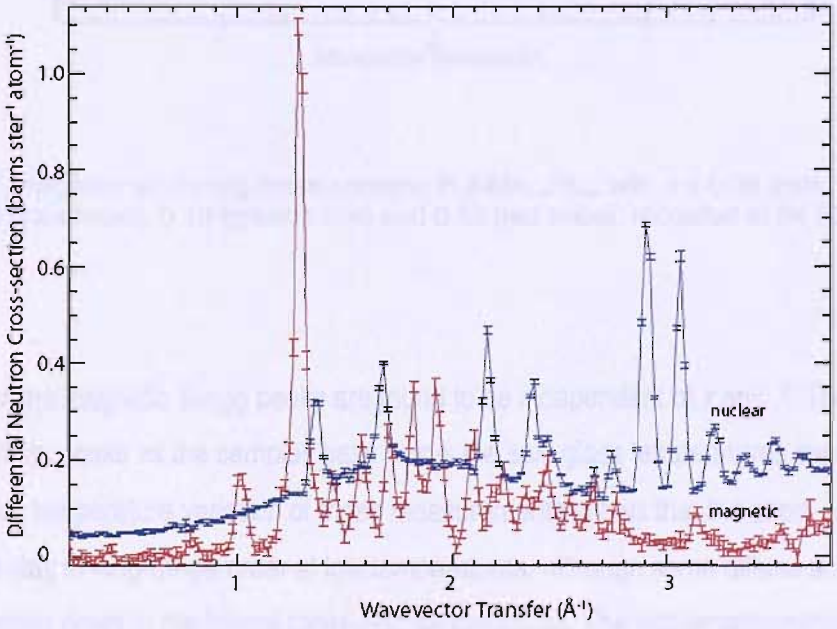

Figure 7.56: separated nuclear (blue trace) and magnetic (red trace) scattering cross-sections in β-$Mn_{0.81}Ru_{0.19}$, recorded at 2K (D7)

This diffuse response indicates the presence of magnetic disorder, which appears to be co-existent with the long-range order observed below ~140K. Previous studies of diffuse nuclear scattering in β-Mn alloys [24] have deduced the existence of non-random concentration fluctuations in the solute atoms, and in this case appear to support the idea of anti-clustering of ruthenium.

The diffuse scattering is observed in all samples with $0.06 \leq x \leq 0.23$, with magnetic Bragg peaks appearing at low temperatures for $x \geq 0.12$.

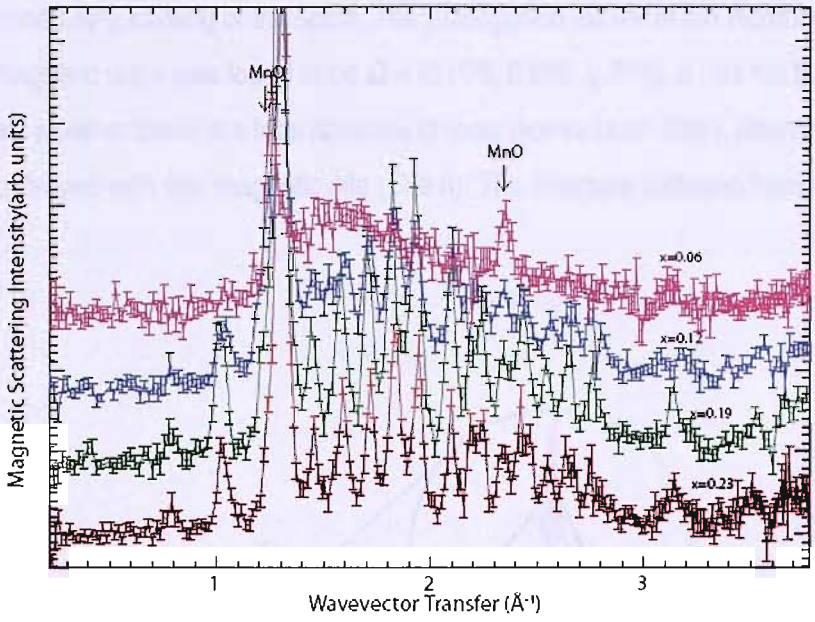

Figure 7.57: magnetic scattering cross-sections in β-$Mn_{1-x}Ru_x$, with $x = 0.06$ (pink trace), 0.12 (blue trace), 0.19 (green trace) and 0.23 (red trace), recorded at 2K (D7)

The positions of the magnetic Bragg peaks are found to be independent of x and T. There is no loss of intensity in these peaks as the samples pass below the spin glass temperatures implied in the μSR data; in fact temperature variation of these measurements shows that the short-range order gradually gives way to long-range order at low temperatures, although some diffuse scattering component persists down to the lowest measured temperatures. The antiferromagnetically ordered and spin glass phases therefore seem to be co-existent for all samples with $x \geq 0.12$.

Magnetic Structural Refinement

A full assessment of the magnetic structure of β-$Mn_{1-x}Ru_x$ alloys has been undertaken in a parallel investigation to this work[1]. A number of trial incommensurate wavevectors have been investigated, for which the magnetic structure factors for equal moments on the magnetic sites have been refined, using a reverse Monte Carlo technique. Rietveld refinement of diffraction data for β-$Mn_{0.77}Ru_{0.23}$ has been carried out using jointly the SARAh[2] and FullProf[3] software suites.

The structure has been found to assume the form of a complex helix, exhibiting a high degree of frustration evidenced by a canting of the spins. The propagation vector of the incommensurate long-range antiferromagnetic state was found to be $\boldsymbol{Q}$ = (0.278, 0.278, 0.278). It has not been possible to state conclusively whether there is a total absence of local moments on Site I, despite a good fit to the data being achieved with one magnetic site (Site II). The structure deduced from this study is shown below.

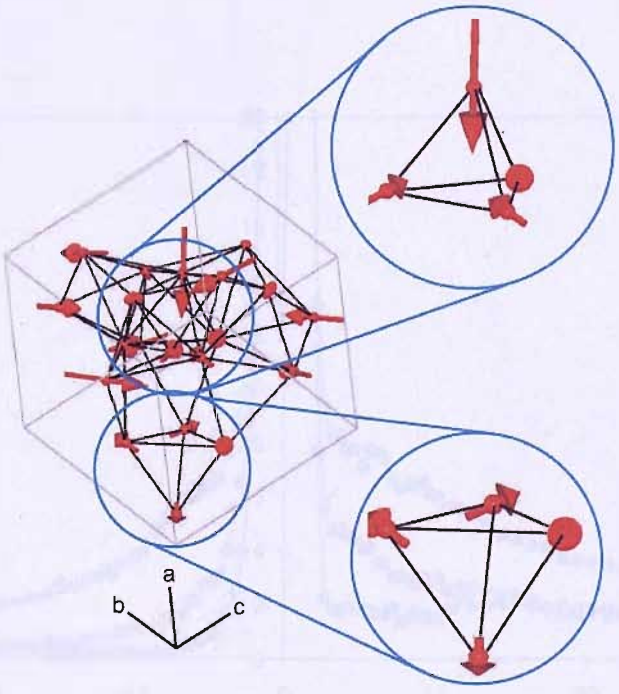

Figure 7.58: the magnetic structure of β-$Mn_{0.77}Ru_{0.23}$ with all spins on Site II

[1] Magnetic structural refinements, analysis and interpretation carried out by J. R. Stewart and A. S. Wills, reported in: *J. R. Stewart, A. S. Wills, C. J. Leavey, B. D. Rainford and C. Ritter, J. Phys.: Condens. Matter* ***19*** *(2007) 145291*

[2] *A. S. Wills, Physica B* ***276*** *(2000) 680*

[3] *J. Rodriguez-Carvajal, Physica B* ***192*** *(1993) 55*

7.15. Inelastic Neutron Scattering Measurements of β-$Mn_{1-x}Ru_x$

Inelastic spectra have been obtained for the $x = 0.03$, 0.06 and 0.19 samples, using the HET spectrometer (ISIS). As for the β-$Mn_{1-x}Co_x$ samples, data has been obtained for incident neutron energies of 40 and 100meV and temperatures from 7 to 300K.

All alloys display a broad response with a linewidth of order 30meV, peaked near $|q| = 1.5$. Closer observation of the $x = 0.19$ sample shows a high temperature magnetic response peaked at zero energy transfer. Below 100K there is a dramatic change in the dynamical character with the quasielastic width decreasing, accompanied by a transfer of spectral weight to the elastic line. There is a further reduction of quasielastic intensity below approximately 50K as the sample enters the spin glass state. Unfortunately, it has not been possible to accurately assess the temperature dependence of this quasielastic width, due to a limited energy resolution in these measurements (of the order of 2.5meV). The existence of such a magnetic scattering component does however suggest the presence of low frequency dynamics that are likely to be connected with the onset of spin glass ordering.

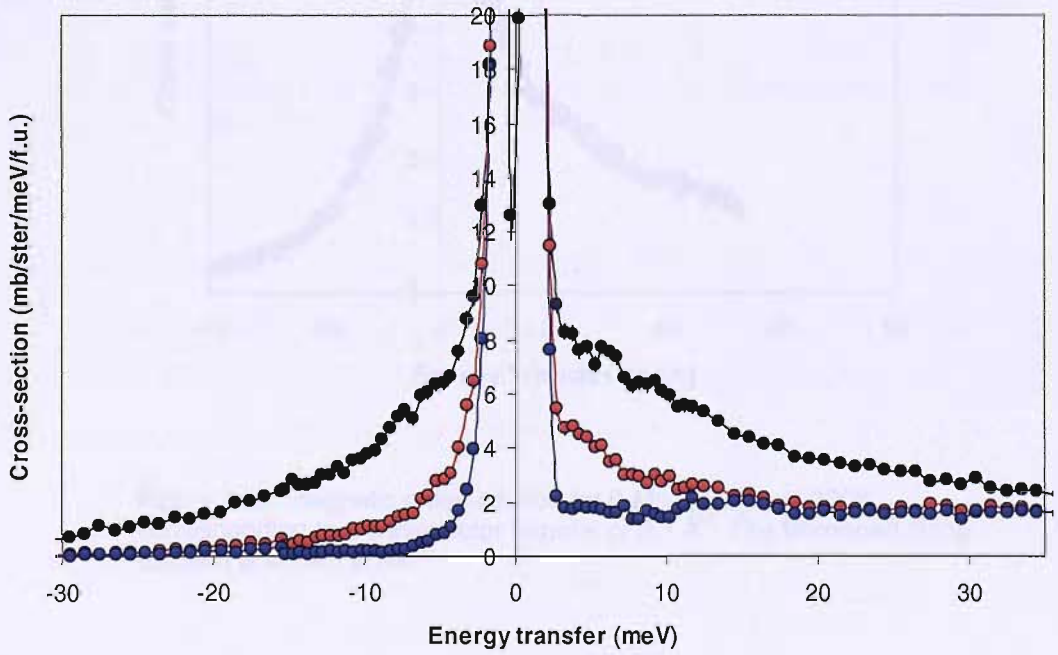

Figure 7.59: The magnetic response in β-$Mn_{0.81}Ru_{0.19}$, measured at 300K (black circles), 100K (red circles) and 7K (blue circles). The scattering here corresponds to $q = 1.5\text{Å}^{-1}$

Non-Fermi Liquid Scaling

Lineshape fitting of HET data for β-$Mn_{1-x}Ru_x$ has been performed as for the β-$Mn_{1-x}Co_x$ alloys, using the FORTRAN program BETAMNFIT. The Bernhoeft function has been fitted to energy transfer vs. $S(\boldsymbol{q},\omega)$ spectra (corresponding to E_i = 100meV and 40meV merged data), and is normalised with the detailed balance factor.

A good fit indicating possible NFL scaling emerges in β-$Mn_{0.81}Ru_{0.19}$, as shown below for 300K, $\boldsymbol{q}$ = 2.1Å^{-1}:

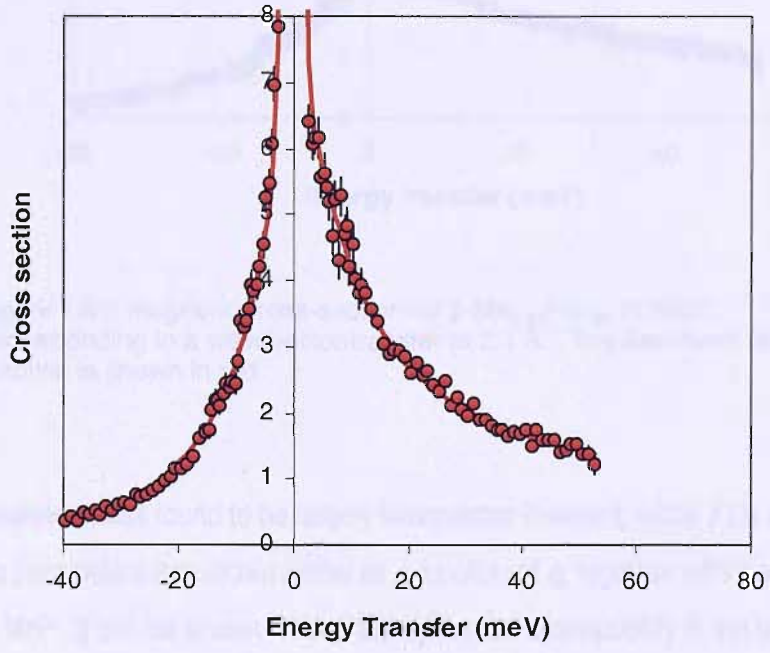

Figure 7.60: magnetic cross-section for β-$Mn_{0.81}Ru_{0.19}$ at 300K, corresponding to a wavevector transfer of 2.1 Å^{-1}. The Bernhoeft fitting function is shown in red

A similar response is observed in β-$Mn_{0.94}Ru_{0.06}$:

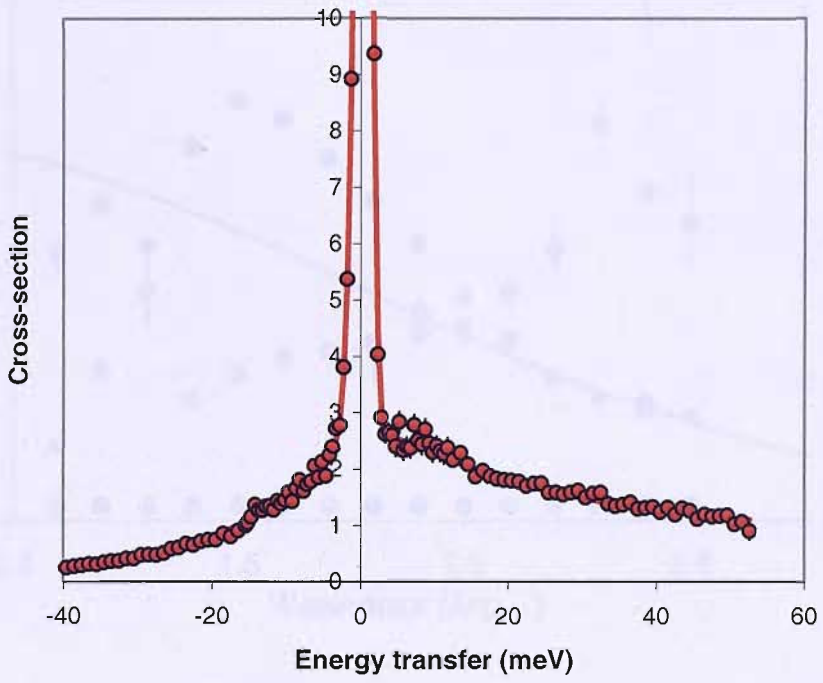

Figure 7.61: magnetic cross-section for β-$Mn_{0.94}Ru_{0.06}$ at 300K, corresponding to a wavevector transfer of 2.1 $Å^{-1}$. The Bernhoeft fitting function is shown in red

The NFL parameter Γ_1 has found to be largely wavevector-invariant, while Γ_2 is ***q***-dependent in both samples. Both parameters are shown below as a function of ***q***, together with the squared magnetic form-factor for Mn^{2+}. It can be shown [41] that the dynamical susceptibility in the limit $\omega \rightarrow 0$ (the static wavevector-dependent susceptibility) is given by:

$$\chi(\ ) = \frac{u}{\Gamma_2 - \Gamma_1} \log\left(\frac{\Gamma_2}{\Gamma_1}\right)$$

where u is defined in terms of a scaling factor of the relaxation rate with the susceptibility:

$$\Gamma(\ ,\omega) = u(\ ,\omega)\chi^{-1}(\ ,\omega)$$

In the lineshape fitting procedures used here, the fitting parameter H_1 (the inelastic Lorentzian lineshape area parameter) may be used to represent u.

$\chi(\boldsymbol{q})$ has been extracted accordingly and plotted along with the NFL fitting parameters, in each case.

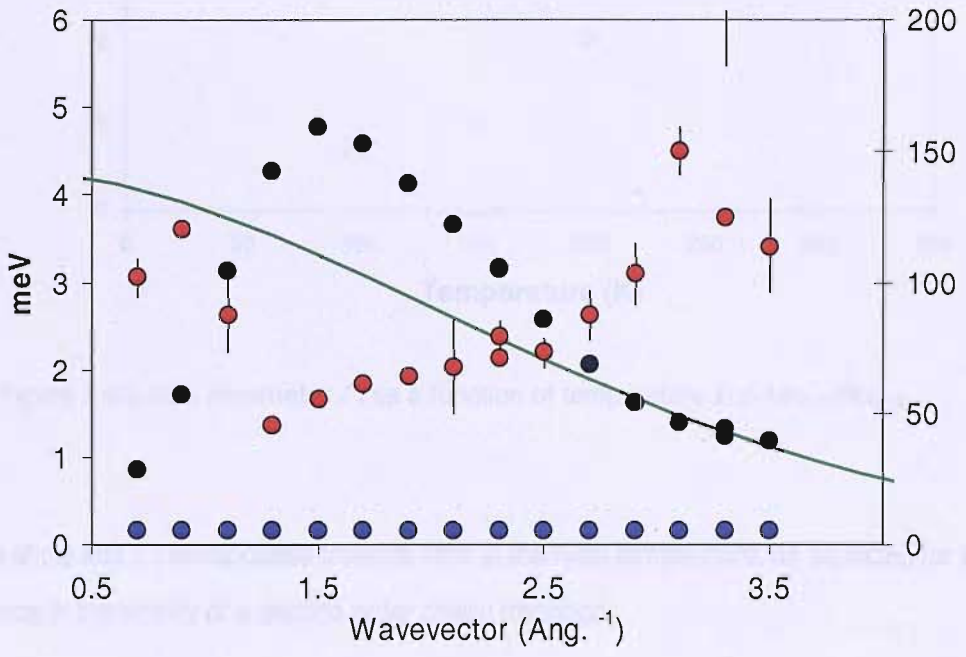

Figure 7.62: NFL parameters Γ_1 (blue circles) and Γ_2 (red circles) (right hand scale) as a function of wavevector in β-$Mn_{0.81}Ru_{0.19}$ at 300K. Black circles indicate the susceptibility, while the Mn^{2+} squared form factor is represented by the green trace (left hand scale).

For the 300K data, a minimum is observed in parameter Γ_2 for a wavevector of 1.3Å^{-1}. This approximately corresponds to a peak in the susceptibility. The susceptibility itself is shown to coincide with the squared magnetic form factor beyond the region of this low-$\boldsymbol{q}$ peak.

Good fits to the data have been achieved using a fixed value of 5.2 meV for Γ_1, across the entire range of $\boldsymbol{q}$. Applying the same procedure across the measured temperature range produces the following Γ_1 versus T curve (for $\boldsymbol{q}$ = 1.5Å^{-1}):

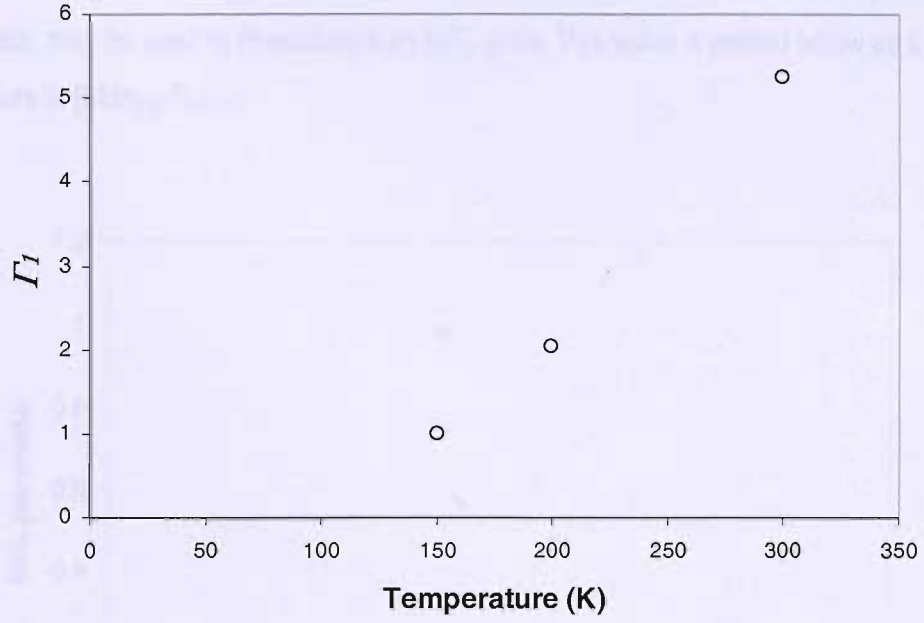

Figure 7.63: NFL parameter Γ_1 as a function of temperature in β-$Mn_{0.81}Ru_{0.19}$

The data show that Γ_1 extrapolates towards zero at the Neel temperature, as expected for a slowing of dynamics in the vicinity of a second order phase transition.

There is little temperature dependence in the Γ_2 parameter:

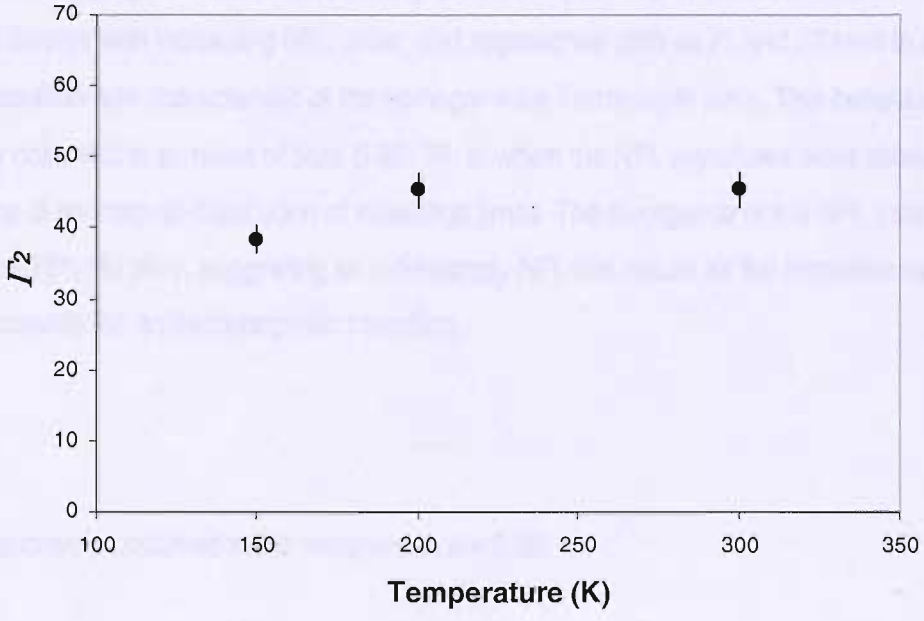

Figure 7.64: NFL parameter Γ_2 as a function of temperature in β-$Mn_{0.81}Ru_{0.19}$

The NFL parameter, defined as the ratio of the relaxation rate distribution width to the paramagnetic relaxation rate, may be used to characterize an NFL state. This value is plotted below as a function of temperature in β-$Mn_{0.81}Ru_{0.19}$:

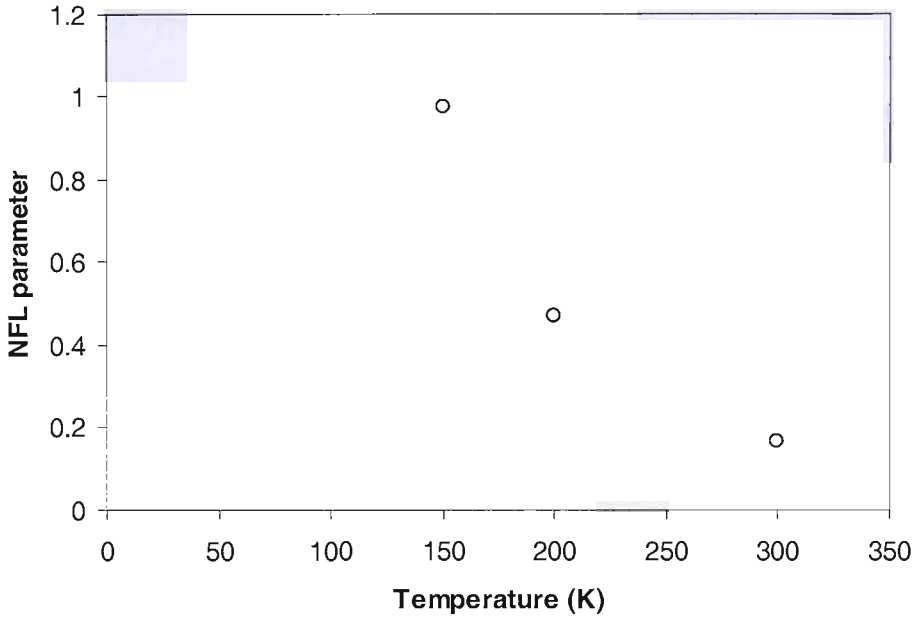

Figure 7.65: NFL parameter ($\Gamma_2 - \Gamma_1$)/ $\Gamma_1\Gamma_2$) as a function of temperature in β-$Mn_{0.81}Ru_{0.19}$

For a system displaying non-Fermi liquid scaling of thermodynamic properties, this parameter is expected to diverge with increasing NFL order, and approaches zero as Γ_1 and Γ_2 tend to a common relaxation rate characteristic of the homogeneous Fermi-liquid state. This behaviour has been clearly observed in samples of pure β-Mn [26], in which the NFL signatures were shown to be a consequence of an intrinsic distribution of relaxation times. The divergence of the NFL parameter is echoed in the 19% Ru alloy, suggesting an increasingly NFL-like nature as the temperature decreases towards the antiferromagnetic transition.

A similar response is observed in the sample with $x = 0.06$:

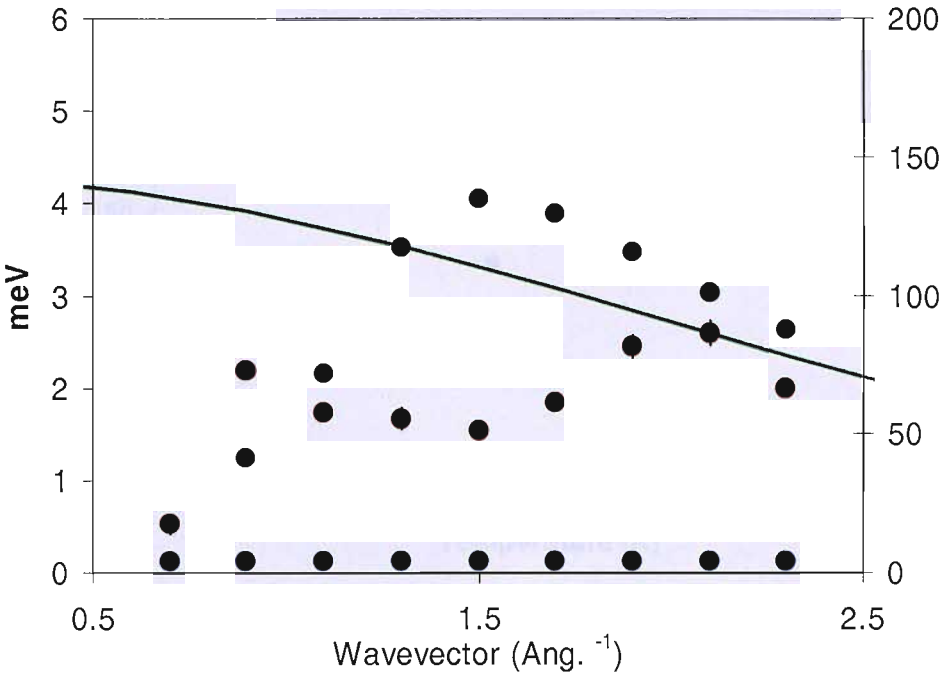

Figure 7.66: NFL parameters Γ_1 and Γ_2 as a function of wavevector in β-$Mn_{0.94}Ru_{0.06}$ at 200K. The susceptibility and Mn^{2+} magnetic form factor are also given
(Key as for β-$Mn_{0.81}Ru_{0.19}$)

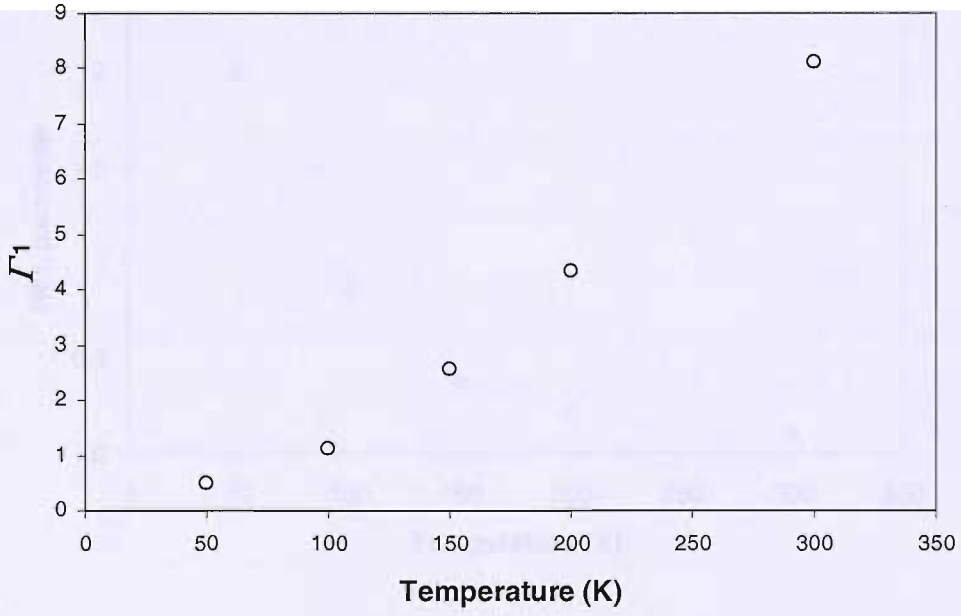

Figure 7.67: NFL parameter Γ_1 as a function of temperature in β-$Mn_{0.81}Ru_{0.06}$

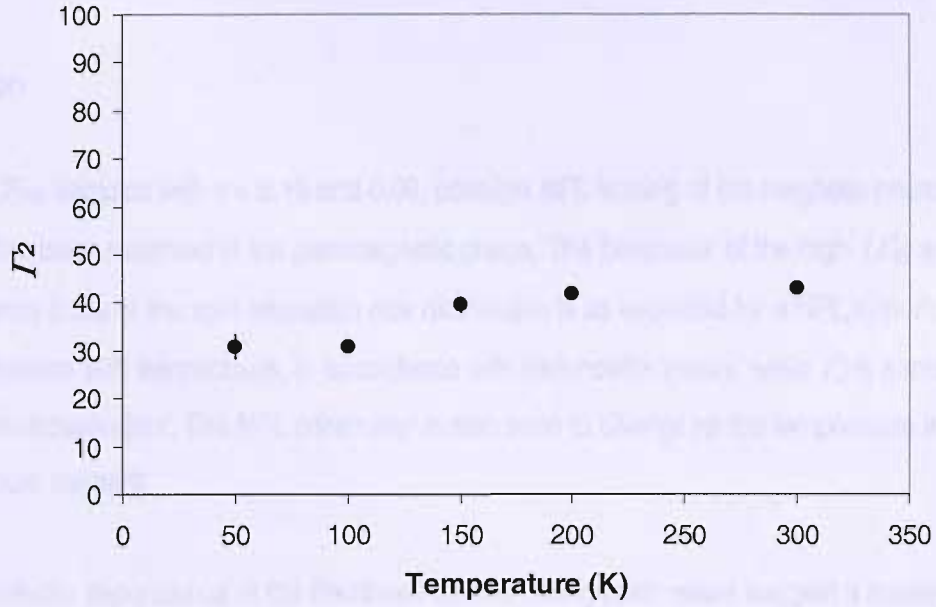

Figure 7.68: NFL parameter Γ_2 as a function of temperature in β-$Mn_{0.81}Ru_{0.06}$

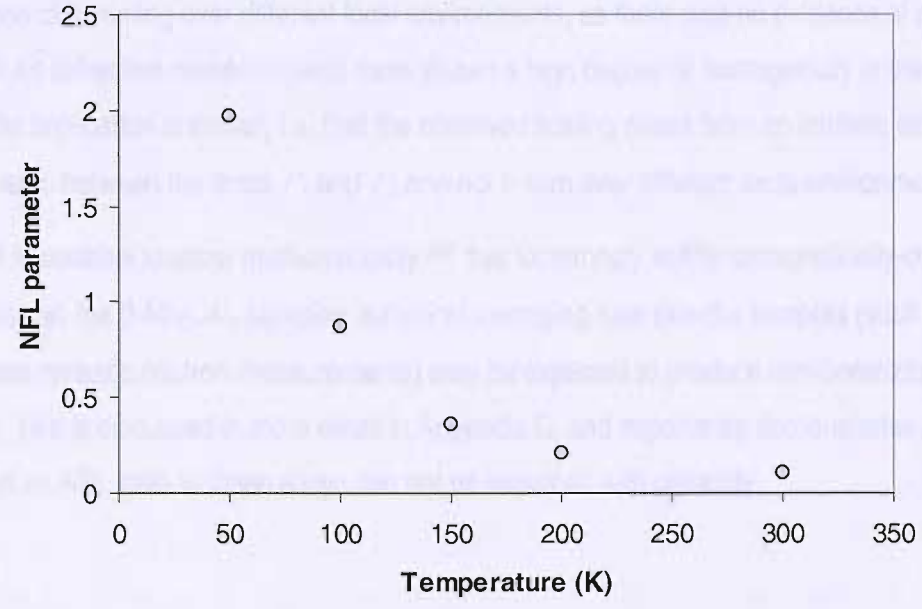

Figure 7.69: NFL parameter $(\Gamma_2 - \Gamma_1)/\ \Gamma_1\Gamma_2)$ as a function of temperature in β-$Mn_{0.81}Ru_{0.06}$

Discussion

For β-$Mn_{1-x}Ru_x$ samples with $x = 0.19$ and 0.06, possible NFL scaling of the magnetic neutron response has been observed in the paramagnetic phase. The behaviour of the high- (Γ_2) and low- (Γ_1) frequency limits of the spin relaxation rate distribution is as expected for a NFL system: Γ_1 is seen to decrease with temperature, in accordance with Bernhoeft's theory, while Γ_2 is almost temperature-independent. The NFL parameter is also seen to diverge as the temperature is lowered, as for the pure element.

Clear wavevector dependence of the Bernhoeft function fitting parameters suggest a spatially correlated state; in addition, minima in the wavevector dependence of the high frequency limit of the relaxation rate distribution are seen to coincide with peaks in the wavevector-dependent susceptibility extracted from the neutron data.

NFL behaviour in pure β-Mn has been shown to be of a fundamental nature, rather than a consequence of summing over different local environments, as there was no evidence of any site disorder [26] As diffraction measurements have shown a high degree of homogeneity in these alloy samples, the implication is similar, i.e. that the observed scaling arises from an intrinsic distribution of relaxation rates between the limits Γ_1 and Γ_2 and not a sum over different local environments.

However, it is possible to show mathematically [42] that for strongly antiferromagnetically-correlated systems such as the β-$Mn_{1-x}Al_x$ samples, spherical averaging over powder samples (such as those used in these inelastic neutron measurements) may be expected to produce non-Lorenztian lineshapes. This is discussed in more detail in Appendix C, and importantly demonstrates that the existence of an NFL state in these alloys can not be assumed with certainty.

References

[1] J. S. Kasper and B. W. Roberts, Phys. Rev. **101** (1956) 537

[2] V. Jaccarino, M. Peter and J. H. Wernick, Phys. Rev. Lett. **5** (1960) 53

[3] Y. Masuda, K. Asayama, S. Kobayashi and J. Itoh, J. Phys. Soc. Japan **19** (1964) 460

[4] T. Shinkoda, K. Kumagai and K. Asayama, J. Phys. Soc. Japan **46** (1979) 1754

[5] M. Katayama, S. Akimoto and K. Asayama, J. Phys. Soc. Japan **42** (1977) 97

[6] H. Nakamura, K. Yoshimoto, M. Shiga and K. Kakurai, J. Phys. Cond. Matt. **9** (1997) 4701

[7] G. D. Preston, Phil. Mag. **5** (1928) 1198

[8] P. I. Kripyakevich, Sov. Phys.-Crystal. **5** (1960) 253, *referenced from*: Y. Nakai, H. Oyamatsu and N. Kunitomi, J. Phys. Soc. Japan **58** (1989) 2805 (*forms an extension of the original work*)

[9] M. O'Keefe and S. Andersson, Acta Cryst. **A33** (1977) 914

[10] C. B. Shoemaker, D. P. Shoemaker, T. E. Hopkins and S. Yindepit, Acta Cryst. **B34** 3573

[11] J.R. Stewart and R. Cywinski, Phys. Rev. B **59** (1999) 4305

[12] H. Hasegawa, J. Phys. Soc. Japan **38** (1975) 107

[13] H. Hasegawa and T. Moriya, J. Phys. Soc. Japan **38** (1975) 107

[14] R. J. Weiss and K. J. Tauer, J. Phys. Chem. Solids **4** (1958) 135

[15] T. Moriya and K. Ueda, Solid State Commun. **15** (1974) 169: K. Ueda and T. Moriya, J. Phys. Soc. Japan **38** (1975) 32

[16] U. El-Hannany and W. W. Warren, Phys. Rev. B **12** (1975) 861

[17] Y. Kohori, Y. Noguchi and T. Kohara, J. Phys. Soc. Japan **62** (1993) 447

[18] V. Sliwko, P. Hohn and K. Schwarz, J. Phys. Cond. Matter **6** (1994) 6557

[19] T. Kohara and K. Asayama, J. Phys. Soc. Japan **37** (1974) 401

[20] M. Katayama and K. Asayama, J. Phys. Soc. Japan **44** (1978) 425

[21] C.W. Kimball, J.K. Tison and M.V. Nevitt, J. Appl. Phys. **38** (1967) 1153

[22] Y. Nishihara, S. Ogawa and S. Waki, J. Phys. Soc. Japan **42** (1977) 845

[23] M. Shiga, H. Nakamura, M. Nishi and K. Kakurai, J. Phys. Soc. Japan **63** (1994) 1656

[24] J.R. Stewart and R. Cywinski, J. Magn. Magn. Materials **676** (2004) 272

[25] J.R. Stewart and R. Cywinski, Phys. Rev. B **59** (1999) 4305

[26] J.R. Stewart, B.D. Rainford, R.S. Eccleston and R. Cywinski, Phys. Rev. Lett. **89** (2002) 186403

[27] N. Bernhoeft, J. Phys. Cond. Mat. **13** (2001) R771

[28] Yamauchi, Miyakawa, K. Sasao and K. Fukamichi, J. Alloys. Comp. **311** (2000) 124

[29] K. Sasao, R.Y. Umetsu and K. Fukamichi, J. Alloys. Comp. **325** (2001) 24

[30] M. Miyakawa, R.Y. Umetsu, K. Sasao and K. Fukamichi, J. Phys. Cond. Matt. **15** (2003) 4605

[31] Miyakawa, Umetsu, Ohta, Fujita, K. Fukamichi and Hori, Phys. Rev. B **72** (2005) 054420

[32] T. Hori, J. Phys. Soc. Japan **38** (1975) 1780

[33] C. G. Shull, W. A. Strauser and E. O. Wollan, Phys. Rev. **76** (1949) 1256

[34] G. B. Jensen and O. V. Nielsen, J. Phys. **C 7** (1974) 409

[35] J. R. Stewart, *Moment Localization in β-$Mn_{1-x}Al_x$* (PhD Thesis), University of St Andrews (1998) Chapter 6

[36] J. R. Stewart, *private communication*

[37] E. Raub and W. Mahler, Z. Metallkde **46** (1955) 282

[38] K. Sasao, R. Yamauchi, K. Fukamichi, H. Yamauchi, IEEE Trans. Magn. **35** (1999) 3910

[39] J. R. Stewart, *Moment Localization in β-$Mn_{1-x}Al_x$* (PhD Thesis), Chapter 5

[40] J. R. Stewart, *Moment Localization in β-$Mn_{1-x}Al_x$* (PhD Thesis), Chapter 4

[41] N. Bernhoeft, *private communication with B. D. Rainford*

[42] B. D. Rainford, *private communication*

8. Studies of RMn_4Al_8 Systems

8.1. Introduction

The RMn_4Al_8 intermetallics crystallize in a body-centred tetragonal structure of $ThMn_{12}$ type, with space group I_4/mmm [1]. While studies have historically largely failed to show evidence of magnetic ordering [2, 3, 4], interest in these compounds has been revived recently due to the suggestion that $LaMn_4Al_8$ is a nearly antiferromagnetic metal [5]. It is suggested that in this particular system, moment formation is inhibited by a quasi-one dimensional arrangement of the manganese sublattice: the manganese atoms, occupying the 8f Wyckoff position, form linear chains along the crystal c-axis with near neighbour separation of 2.58Å and inter-chain separation of 4.53Å.

The crystal structure of the RMn_4Al_8 and its implications introduces the concept of low-dimensional magnetism to these studies in analogy to the geometrical frustration of the β-$Mn_{1-x}M_x$ alloys. The aim of this work and of many prior experimental studies has been to observe the effect of substituting various elements of the lanthanide series, along with yttrium and scandium, on stabilising a long-range ordered state associated with local manganese moments.

More recently, certain intermetallics of this series - namely, those involving yttrium, yttrium/lanthanum alloys, lutetium and scandium - have been identified as spin gap compounds [6, 7, 8]. The effect of varying the impurity species on spin gap size has therefore also been opened up as an area of interest, with the objective of establishing the mechanism of gap formation and any links to reduced dimensionality.

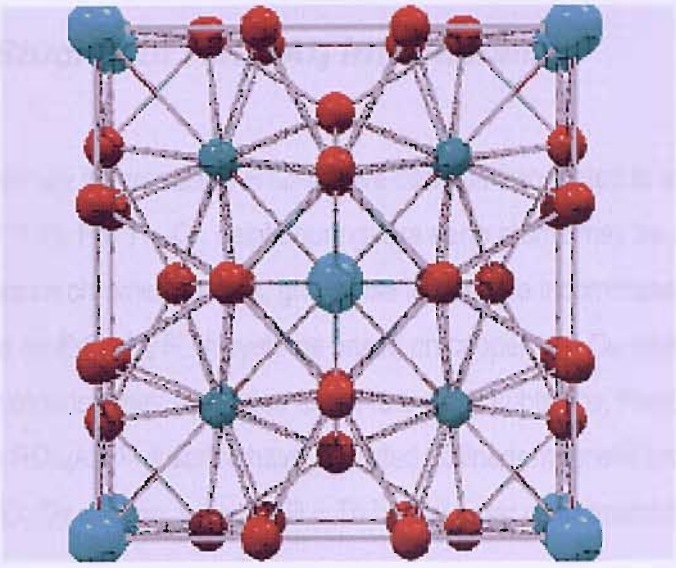

Figure 8.1: the tetragonal structure of RMn_4Al_8 as viewed along the c-axis, with a single rare-earth (large blue atoms) at site 2a, Mn (small blue atoms) at positions 8f and Al (red atoms) at positions 8i and 8j.

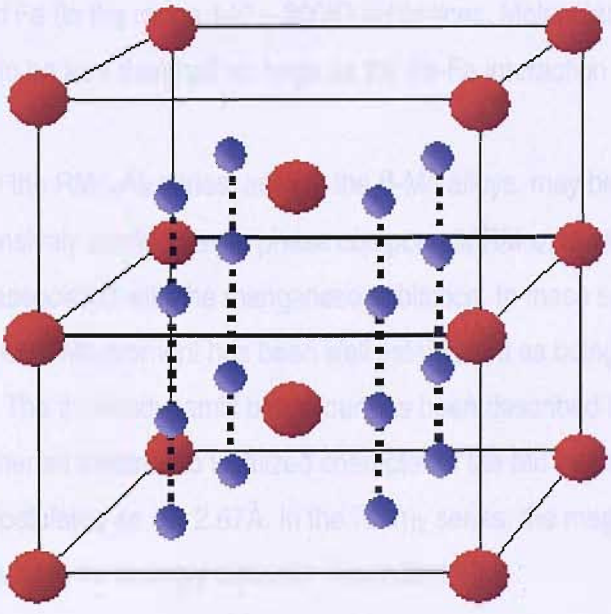

Figure 8.2: the linear Mn (shown in blue) chains of RMn_4Al_8, illustrated with two adjacent unit cells along the *c*-axis. Al atoms are omitted for clarity.

8.2. Previous Studies of RMn_4Al_8 Intermetallics

The general class of ternary intermetallics RT_4Al_8 have been demonstrated to show a range of magnetic behaviour [9, 10, 11]. For T = Cr, neighbouring rare earth atoms may be responsible for inducing local moments on chromium atoms, giving rise to possible incommensurate magnetic structures, as reported for $ErCr_4Al_8$ [4]. In systems based on copper, the Cu atoms are nonmagnetic and antiferromagnetic ordering may occur due to the rare earth sublattice. Powder diffraction measurements on the RCu_4Al_8 [12, 4] series have indicated collinear magnetic order at low temperatures for R = Er, Dy and Ho, while for R = Tb helical order was reported [12].

In studies of RFe_4Al_8 systems investigated using magnetometry and Mossbauer techniques [13, 2], magnetic ordering has been observed both in compounds in which only the Fe atoms carry a moment (La, Ce, Y, Lu, Th), as well as in those where a rare earth moment is also established (Gd, Tb, Dy, Ho, Er). Two transitions are observed, indicating independent ordering of rare earth (at very low temperatures) and Fe (in the range 140 – 200K) sublattices. Molecular field calculations show the R –Fe interaction to be less than half as large as the Fe-Fe interaction.

Magnetic behaviour in the RMn_4Al_8 series, as with the β-Mn alloys, may be expected to have some parallels with the extensively studied Laves phase compounds RMn_2, in which the onset of local moment formation is associated with the manganese sublattice. In these systems and related alloys, the development of a local Mn moment has been well established as being strongly correlated with Mn-Mn separation [14]. The thermodynamic behaviour has been described in terms of the SCR theory as a transition from itinerant electron to localized character of the Mn moment, with the critical distance for stability postulated as $d = 2.67$Å. In the RMn_{12} series, the magnetic interactions of the Mn have also been found to be strongly distance-dependent [15].

Early studies reported evidence for magnetic ordering in the RMn_4Al_8, with Mossbauer data suggesting relatively high Neel temperatures [10]:

Compound	T_N (K)
$PrMn_4Al_8$	11
$NdMn_4Al_8$	7
$SmMn_4Al_8$	12
$EuMn_4Al_8$	20
$GdMn_4Al_8$	28
$TbMn_4Al_8$	21
$DyMn_4Al_8$	19
$HoMn_4Al_8$	14
$ErMn_4Al_8$	15
$TmMn_4Al_8$	13

Table 8.1: antiferromagnetic ordering temperatures in RMn_4Al_8 reported from early Mossbauer experiments [10]

These finding have generally not, however, been duplicated in subsequent experimental work.

Magnetic Susceptibility

The relation between atomic separation and magnetic interactions has been studied closely, via comparisons of magnetic susceptibility within the YMn_xAl_{12-x} series [16]. The manganese occupy predominantly the 8f sites in YMn_4Al_8, both 8f and 8j in YMn_6Al_6, and are divided randomly between the 8f, 8i and 8j sites in YMn_5Al_7 [17, 18, 19]. Susceptibility data for YMn_4Al_8 show a broad maximum around 340K, and above 500K follow a modified Curie-Weiss law:

$$\chi = \frac{C}{T-\theta} + \chi_0$$

where the term χ_0 corresponds to a temperature-independent contribution [16].

An effective moment deduced from the Curie constant, μ_{eff} = 3.93μ_B is close to the Mn^{4+} ion value of 3.87μ_B [16]. Below 300K, the susceptibility decreases monotonically, before rising in a sharp Curie tail at very low temperatures [2].

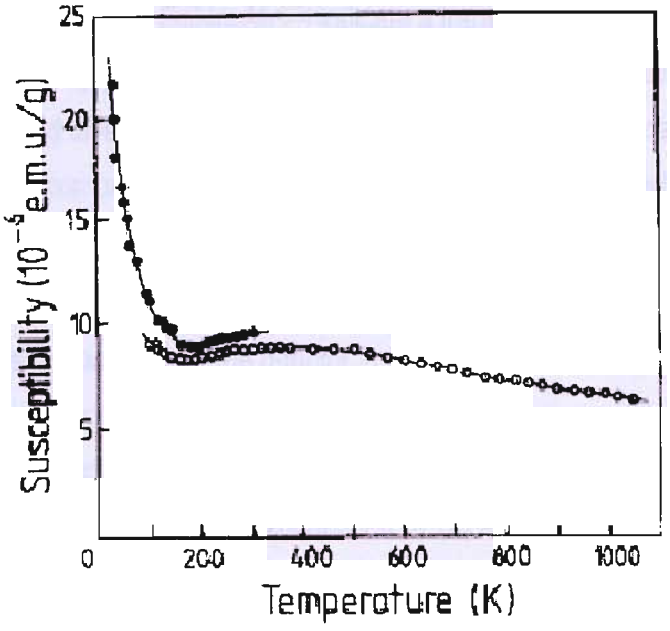

Figure 8.3: susceptibility peak for YMn_4Al_8, with high-temperature data shown by open circles [16]. Additional low-temperature data from an earlier study [2] is represented by closed circles

At low temperatures, 7.3% of the manganese atoms were calculated as having a local moment [16]: this corresponds closely to the site occupancy deviation for 8f Mn extracted from neutron diffraction [17]. The 7% manganese atoms distributed over sites 8i and 8j occupy a relatively expanded sublattice in which the Mn-Mn distances are greater than the estimated critical value d = 2.6Å (compared with d_{ff} = 2.56Å), in addition to which the 8i and 8j Al atoms cut the 3d Mn bonds, narrowing the local 3d bandwidth. Using SCR theory [20] it was suggested that the 8f susceptibility contribution retains itinerant character, with longitudinal spin fluctuations increasing in amplitude with temperature until a saturation point T^*, beyond which local moment behaviour governs the response. The contribution from the 8i and 8j sites decreases rapidly with temperature.

A deviation from linearity in$1/\chi(T)$ is noted at T^* = 520K, as predicted using SCR theory. This saturation temperature decreases to 310K in YMn_6Al_6, where substantial suppression of spin fluctuations occurs as a result of the higher 8j occupancy. The high temperature moments on the 8f and 8j sites in this compound correspond to the Mn^{4+} (3.87μ_B) and Mn^{3+} (4.90μ_B) ion values

respectively [16]. The susceptibility for YMn_5Al_7 shows an anomaly near 220K, and the high-temperature response infers the existence of Mn^{3+} and Mn^{2+} ions. The partial occupation of all three sites in this alloy leads to the formation of a spin glass state at low temperatures [16].

Susceptibility measurements for $GdMn_4Al_8$ [21] indicate a transition from itinerant to local moment character at sufficiently high temperatures as for YMn_4Al_8, with a spin fluctuation saturation temperature established at 490K. The contribution of Mn moments to the measured susceptibility has been extracted by comparison to data for $GdCu_4Al_8$. Fits to the modified Curie-Weiss function have produced values of $\mu_{Gd} = 7.92\mu_B$, $\mu_{Mn} = 3.81\mu_B$, $\theta = -232K$ and $\chi_0 = 2.1 \times 10^{-6}$ emu/g above 500K (compared to $7.92\mu_B$, $\theta = 11K$ and $\chi_0 = 1.9 \times 10^{-6}$ emu/g in $GdCu_4Al_8$). ESR experiments have shown a temperature dependence of the g-factor in $GdMn_4Al_8$ [21] in contrast to a constant value for $GdCu_4Al_8$, reflecting the increasing influence of Mn moments with temperature. The indication is that Mn atoms in this compound constitute an extra relaxation channel for conduction electron relaxation, and provide an effective fluctuating field experienced by Gd spins.

A similar study for $CeMn_4Al_8$ [22] has shown a susceptibility maximum at 270K, with a longitudinal spin fluctuation saturation temperature of 440K. The effective moment per Ce ion above this temperature is close to the free Ce^{3+} ion value. A tendency for the Ce contribution to the measured susceptibility to increase towards very low temperatures, noted in $CeMn_4Al_8$, is a common feature of Ce compounds in a mixed valent state [23], and XPS spectra [22] have confirmed a progressive change from a Ce^{4+} state at very low temperatures to an intermediate valence state at room temperature. The decrease in spin fluctuation saturation temperature from 520K in YMn_4Al_8 to 440K in $CeMn_4Al_8$ is attributed to a partial quenching of spin fluctuations caused by 4f-5d and 3d-5d hybridizations.

Compound	Temperature of χ(T) peak (K)	Saturation temperature T* (K)
YMn_4Al_8	340	520
$GdMn_4Al_8$	-	490
$CeMn_4Al_8$	270	440

Table 8.2: temperatures corresponding to susceptibility parameters in RMn_4Al_8, R = Y, Gd and Ce [16, 21, 22]

A further study [24] has identified low-temperature features in the susceptibilities of a number of RMn_4Al8 compounds, summarized in the following table:

Compound	T_N
$ScMn_4Al_8$	No order to 4.2K
$SmMn_4Al_8$	9.2K
$TbMn_4Al_8$	6.6K
$DyMn_4Al_8$	3.5K
$HoMn_4Al_8$	2K

Table 8.3: temperatures corresponding to susceptibility anomalies in RMn_4Al_8 compounds [24]

Neutron Diffraction

A study of RMn_4Al_8 compounds with R = Nd, Dy, Ho and Er [4] has given no indication of long-range magnetic order down to 1.6K. Structural determination has confirmed [17] the preferential site occupancies of Mn on site 8f, and Al on sites 8i and 8j, with a small residual disorder of Mn and Al on all three sites. An identical result has been reported for $TbMn_4Al_8$ [3]. In comparison, the isotopic compound $ErCr_4Al_8$ has shown weak magnetic reflections below 4K that are not indexable on the unit cell, and suggest a possible incommensurate magnetic structure [4]. A diffraction pattern for $ErCu_4Al_8$ has revealed an antiferromagnetic structure below 5.5K with moments aligned along the c-axis, with ordering due to the Er^{3+} sublattice. This result is in agreement with early Mossbauer data [10].

Specific Heat

A specific heat study carried out for compounds with R = Y, La, Pr, Nd, Dy and Er [25] has produced values for the Sommerfeld constant γ of 265 mJ/K^2 = 66 mJ/K^2 mol.Mn, and 83 mJ/K^2 = 21 mJ/K^2 mol.Mn for $LaMn_4Al_8$ and YMn_4Al_8 respectively. These values are enhanced (the corresponding values for the isostructural compounds YCu_4Al_8 and YFe_4Al_8 are 20 mJ/K^2 [26] and 60 mJ/K^2 [27]), and

in the case of the lanthanum alloy is comparable to those found for frustrated Mn systems such as β-Mn (~ 70 mJ/K² mol.Mn) [28] and Y(Sc)Mn2 (~80 mJ/K² mol.Mn) [29]. This indicates heavy fermion character due to large longitudinal spin fluctuation amplitudes of the Mn 3d electrons. The C/T versus T^2 relation for these compounds is linear down to 1.5K, with no indication of anomalies corresponding to a phase transition.

The magnetic contribution to the specific heat has been extracted for the systems with R = Pr, Nd, Dy and Er [25]. A plot of C_{mag}/T shows a sharp peak at 14K for $PrMn_4Al_8$ attributed to a magnetic phase transition, occurring very close to but slightly higher than a previously reported value of 11K [10]. No such anomalies are reported for the Nd and Dy compounds down to 1.5K, or in the Er compound down to 0.5K, in contrast with previous studies reporting magnetic ordering transitions at 7K in $NdMn_4Al_8$ [10], 15K in $ErMn_4Al_8$ [10] and 19K in $DyMn_4Al_8$ [3]. Schottky anomalies are reported for these alloys at 38K, 35K and 8K respectively [25].

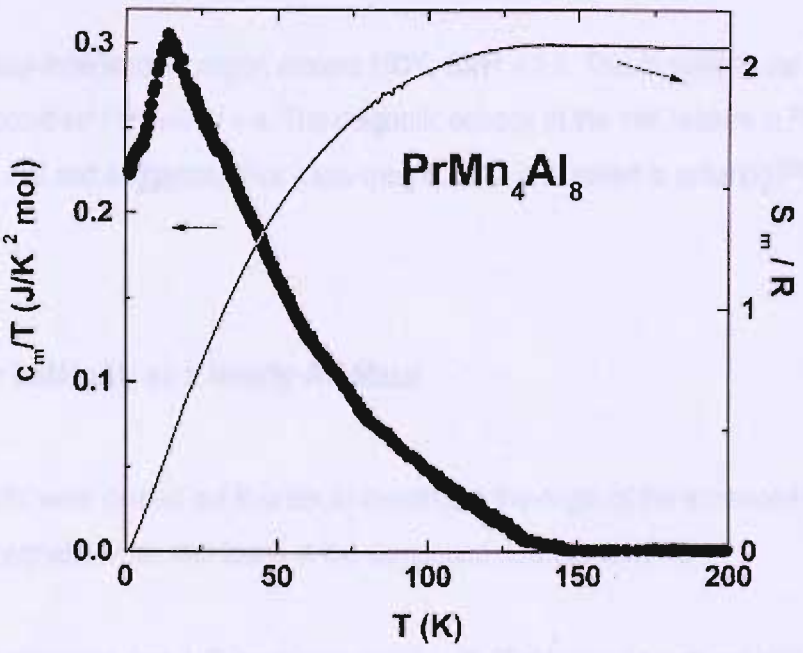

Figure 8.4: temperature dependence of the magnetic specific heat C_m/T for $PrMn_4Al_8$ (left scale), showing the 14K anomaly. The temperature dependence of the magnetic entropy is also given (solid curve, right scale) [25]

The temperature dependence of the magnetic entropy has also been obtained for these systems, by integration of C_{mag}/T [25]. The entropy curves tend to saturate at temperatures between 50K and 150K, at which the thermal populations of the CF states appear almost complete, suggesting small

overall splittings not in excess of 200K. High-temperature values for magnetic entropy per rare earth S_m/R have been extracted[1], and are compared with calculated values for the R^{3+} ions in the table below. The values agree closely in the first three cases, although the experimental value is slightly lower than expected for $ErMn_4Al_8$.

R	S_m/R	$\ln(2J+1)$	J state
Pr	2.1	2.19	4
Nd	2.5	2.30	9/2
Dy	2.9	2.77	15/2
Er	2.3	2.77	15/2

Table 8.4: experimental and calculated values of magnetic entropy for rare earth ions in RMn_4Al_8 [25]

In the temperature-independent region around 150K, $S_m/R = 2.1$. This is close to the $ln\,(2J+1) = 2.19$ value expected for Pr^{3+} with $J = 4$. The magnetic entropy at the 14K feature in $PrMn_4Al_8$ is 0.7 per Pr, close to $ln\,2$ and suggesting that a low-lying doublet is involved in ordering [25].

NMR Studies: $LaMn_4Al_8$ as a Nearly-AF Metal

NMR experiments were carried out in order to investigate the origin of the enhanced specific heat of $LaMn_4Al_8$. No magnetic order was found in the compound down to 1.4K [5].

The spin-lattice relaxation rate $1/T_1$ increases rapidly with T at low temperatures and tends to saturate at high temperatures, in line with expected behaviour for a nearly-antiferromagnetic metal, in which longitudinal antiferromagnetically-correlated spin fluctuations grow rapidly with temperature. This result is similar to the behaviour observed in β-Mn systems [30, 31], $Y(Sc)Mn_2$ [32, 33] and $Y(Lu)Mn_2$ [34]. In the same study, the high temperature magnetic susceptibility was found to obey a modified Curie-Weiss law as reported elsewhere for YMn_4Al_8 [16], with a dominant temperature-independent

[1] This treatment involved the incorrect assumption that the YMn_4Al_8 data represents purely a lattice contribution, used in subsequent subtractions to obtain C_{mag}/T for the other samples. Additionally, any very low temperature contribution has been neglected.

contribution $\chi_0 \sim 8.8 \times 10\text{-}3$ emu/mol. An effective moment per formula unit of $\mu_{eff} \sim 2.34\mu_B$ was obtained, with a value of $0.59\mu_B$ per manganese, indicating the nature of this alloy as a typical itinerant electron magnet. A broad maximum is observed in the low temperature susceptibility for $LaMn_4Al_8$, occurring at approximately 5K

SCR theory predicts that for a nearly antiferromagnetic metal, the spin-lattice relaxation rate $1/T_1$ is proportional to $T\chi(\mathbf{Q})^{1/2}$ for isotropic spin fluctuations around the antiferromagnetic wavevector $\mathbf{Q}$ [36]. A fit of the experimental data to the relation

$$\frac{1}{T_1} = \frac{\alpha T}{(T-\theta)^{1/2}}$$

produces good agreement:

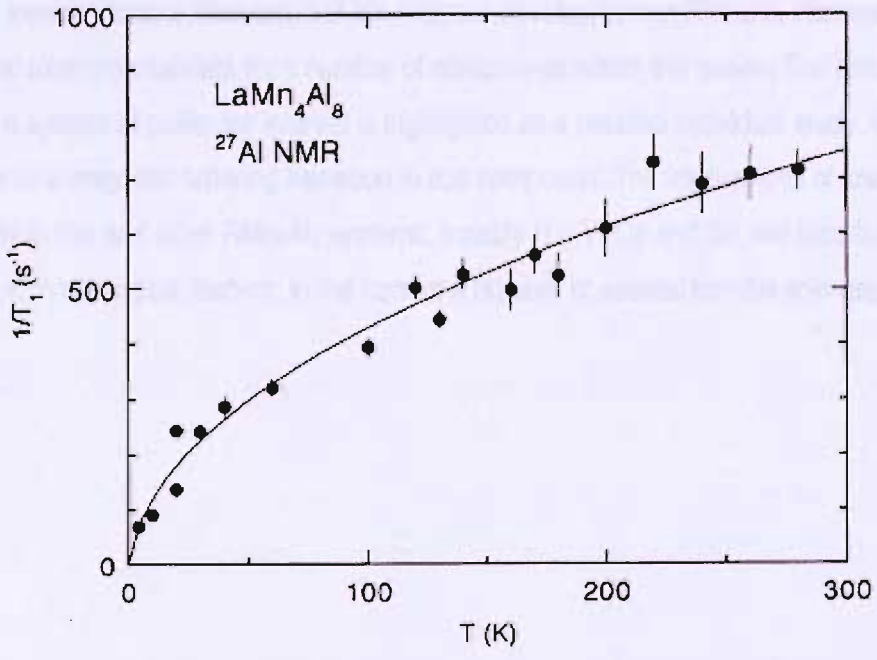

Figure 8.5: temperature dependence of the ^{27}Al spin lattice relaxation rate $1/T_1$ in $LaMn_4Al_8$ at 74MHz. The solid curve shows the best fit to the relation $1/T_1 = \alpha T/(T - \theta)^{1/2}$ [5]

Since the Mn-Mn distance in $LaMn_4Al_8$ is only slightly less than the value of 2.6Å regarded as necessary for local moment formation, it would appear that this system is on the cusp of moment stability and long range order. In light of the similarities between $LaMn_4Al_8$ and the $Y(Sc)Mn_2$ and β-Mn systems, in which 3D geometrical frustration of the antiferromagnetic interaction stabilizes the

spin liquid, high-entropy ground state, it is suggested that the 1D-arrangement of the Mn chains in $LaMn_4Al_8$ is responsible for the disordered ground state and large residual spin entropy (large γ).

The interaction of sublattices in the RT_4Al_8 class is a complicated subject. Ordering of systems with T = Cu has implied that the rare earth species is dominant in this respect, influencing moment development (T = Cr) and ordering transitions (T = Mn) in the transition element [10]. On the other hand, there have been indications that R-R coupling is weak – for example in $GdMn_4Al_8$ [2]. In RMn_4Al_8, the role of the Mn sublattice appears to be of crucial importance, with magnetism seemingly highly dependent on manganese interatomic separation. The influence of Mn spin fluctuations can account for key characteristics in these compounds, such as the nearly-antiferromagnetic type behaviour reported for $LaMn_4Al_8$ [5]. A nearly-critical Mn-Mn spacing suggests a system on the verge of long range order, with the linear chain arrangement accounting for the absence of any transitions in experimental observations to date.

This chapter involves further discussion of Mn moment development in RMn_4Al_8 intermetallics, in line with additional experimental data for a number of compounds within this series. The emergence of $LaMn_4Al_8$ as a system of particular interest is highlighted as a detailed individual study, including the first evidence of a magnetic ordering transition in this compound. The implications of low dimensionality in this and other RMn_4Al_8 systems, notably R = Y, Ce and Sc, are introduced and presented in a chronological fashion, in the form of a number of several parallel spin gap studies.

8.3. Sample Preparation

As with the β-Mn alloys, each of the RMn_4Al_8 samples was prepared by argon arc melting the constituent elements together (starting materials 99.99% purity). These samples required annealing at 1000°C for 1 –2 weeks to ensure homogeneity. It has been reported previously that site disorder among the 8f, 8i and 8j sites of the $ThMn_{12}$ structure occurs readily [5], and coupled with the high vapour pressure of manganese, it can consequently prove difficult to synthesize compounds with the correct stoichiometric concentrations. For this reason extra care was taken when melting the constituent materials with each ingot turned and melted no less than five times. A small percentage of Mn was added to the starting concentration as with the β-Mn alloys, to compensate for mass loss. The concentrations have subsequently been confirmed satisfactorily using powder neutron diffraction techniques, with only small deviations from the expected site occupancies.

These polycrystalline samples have been used for all subsequent experiments either as whole ingots or in powdered form: attempts to produce single $LaMn_4Al_8$ crystals have so far proven unsuccessful.

8.4. Neutron Powder Diffraction Measurements of RMn_4Al_8

Diffraction patterns have been obtained for the RMn_4Al_8 systems with R = La, Y, Pr, Ho and Ce at room temperature and instrumental base temperature (1.3K) using the ISIS ROTAX diffractometer.

Rietveld refinement has subsequently been carried out using the GSAS software suite, in which the body-centred tetragonal structure described earlier has been assumed, with the rare earth/yttrium atoms occupying the 2a positions, the manganese initially assumed to occupy solely the 8f positions, and the aluminium distributed over the 8i and 8j positions. The fractional atomic coordinates for each element are then:

Atom	Fractional coordinates for unit cell
R	0, 0, 0
Mn	¼, ¼, ¼
Al (8i)	*x*, 0, 0
Al (8j)	*y*, ½, 0

Table 8.5: unit cell coordinates in RMn_4Al_8

The values for *x* and *y* are generally given as approximately 0.34 and 0.28 respectively.

The fitting parameters corresponding to this model are given in the following tables:

R	Lattice parameter *a* (Å)	Lattice parameter *c* (Å)	*X*	*Y*
La	9.0288	5.1636	0.3479	0.2739
Ce	8.9941	5.1661	0.3442	0.2775
Pr	8.9571	5.1432	0.3439	0.2765
Y	8.8746	5.1051	0.3417	0.2793
Ho	8.8509	5.0973	0.3409	0.2798

Table 8.6: unit cell parameters and atomic coordinates established in Rietveld refinement of room temperature powder neutron diffraction in RMn_4Al_8 (ROTAX)

	U_{iso} (Site 2a)	U_{iso} (Site 8f)	U_{iso} (Site 8i)	U_{iso} (Site 8j)	R-factor R_{wp}
La	0.539	0.814	0.510	0.737	0.0772
Ce	0.454	0.526	0.617	0.598	0.0624
Pr	0.724	0.779	0.739	0.835	0.0332
Y	0.725	0.690	0.750	0.645	0.0553
Ho	0.619	0.623	0.722	0.759	0.0444

Table 8.7: isotropic thermal factors for each atomic site, together with the R-factors established in Rietveld refinement of room temperature powder neutron diffraction in RMn_4Al_8 (ROTAX)

R	Occupancy of site 2a by R (%)	Occupancy of site 8f by Mn(%)	Occupancy of site 8i/8j by Al (%)
La	100	93.31	96.56
Ce	100	93.56	98.47
Pr	100	97.51	98.76
Y	100	94.59	96.88
Ho	100	95.79	97.89

Table 8.8: percentage occupancies of each atomic site in RMn_4Al_8, determined by Rietveld analysis. Identical behaviour for the 8i and 8j sites has been assumed

The lattice parameters *a* and *c* obtained as a result of these measurements are in good agreement with previously-determined values as given in the following table:

Compound	*a* (Å)	*c* (Å)
$LaMn_4Al_8$ [11]	9.031	5.166
$CeMn_4Al_8$ [10]	8.910	5.150
$PrMn_4Al_8$ [10]	8.952	5.142
YMn_4Al_8 [11]	8.856	5.103
$HoMn_4Al_8$ [10]	8.845	5.097

Table 8.9: lattice parameters for RMn_4Al_8 previously reported in the literature

Values of *a* generated by these refinements are found to decrease across the rare earth series as expected, with the value obtained for the yttrium compound lying between the light rare earth compounds and that for $HoMn_4Al_8$, the heavy rare earth example used in these measurements. Lattice parameter *c* follows the same approximate trend, but with an apparent slight increase going from La – Ce. Previous measurements show a continuous decrease in *c*, and an anomalous increase in *a* going from Ce - Pr. The implication is of a larger than expected increase in the ratio *c/a* in the vicinity of the cerium compound. This is shown in the following plots of the two lattice parameters and the ratio *c/a* versus R:

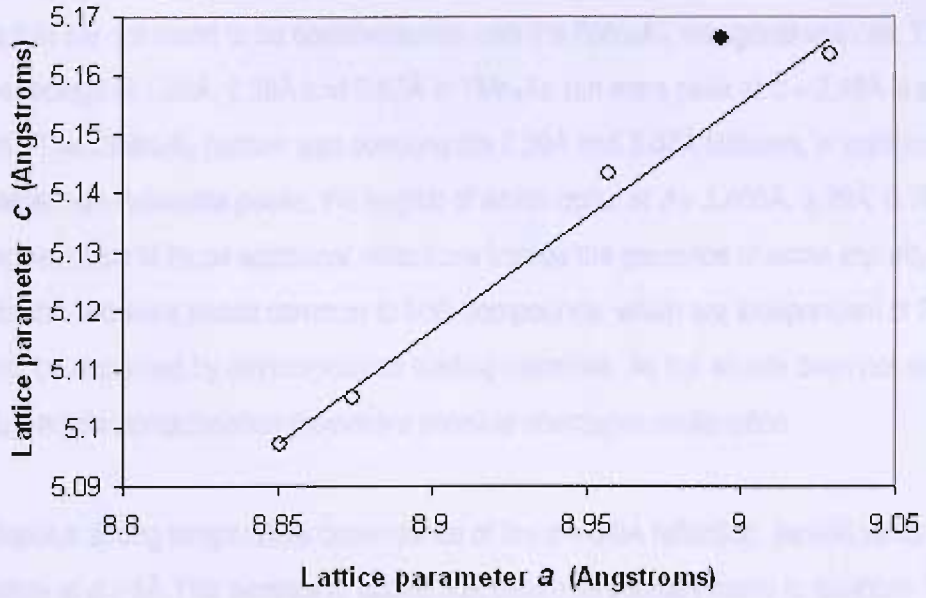

Figure 8.6: changes in lattice parameters for the RMn_4Al_8 series. $CeMn_4Al_8$, denoted by the closed circle, lies outside the linear relation found to hold for the rest of the series

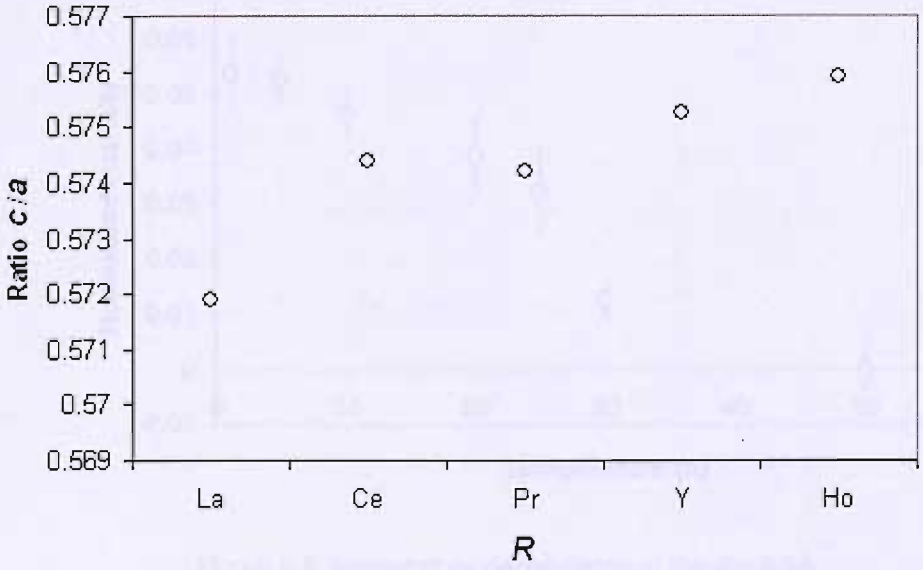

Figure 8.7: ratio of lattice parameters for the RMn_4Al_8 series, showing a general increase in *c/a* going toward the holmium end of the rare earth series. A deviation from linearity occurs for $CeMn_4Al_8$

For RMn_4Al_8 with R = Pr, Ho and Ce, refinement of room temperature diffraction data shows the samples to be single phase. No extra peaks are seen in diffraction patterns recorded at the ROTAX base temperature of 1.3K.

For the $LaMn_4Al_8$ and YMn_4Al_8 samples, room temperature diffraction indicates a number of weak extra peaks that are not found to be commensurate with the RMn_4Al_8 tetragonal unit cell. These occur for *d*-spacings of 1.88Å, 2.39Å and 3.67Å in YMn_4Al_8 (an extra peak at $d = 2.13$Å is attributable to vanadium). The $LaMn_4Al_8$ pattern also contains the 2.39Å and 3.67Å features, in addition to a number of other non-indexable peaks, the largest of which occur at $d = 3.405$Å, 3.79Å, 6.78Å and 8.0Å. The appearance of these additional reflections implies the presence of some impurity phase, especially for the two extra peaks common to both compounds, which are independent of R and hence cannot be explained by unincorporated starting materials. As the source does not seem to be MnO/Mn_3O_4, sample contamination provides a possible alternative explanation.

$LaMn_4Al_8$ displays strong temperature dependence of the $d = 8.0$Å reflection, as well as for a smaller impurity feature at $d = 5$Å.This persists to above 30K before its intensity starts to diminish. This peak has been echoed in the elastic line of preliminary inelastic neutron scattering measurements (IN4) as a feature observed at a wavevector transfer of $\boldsymbol{q} = 0.8$Å^{-1}, with $d = 2\pi/\boldsymbol{q}$ giving a corresponding *d*-spacing of 7.85Å.

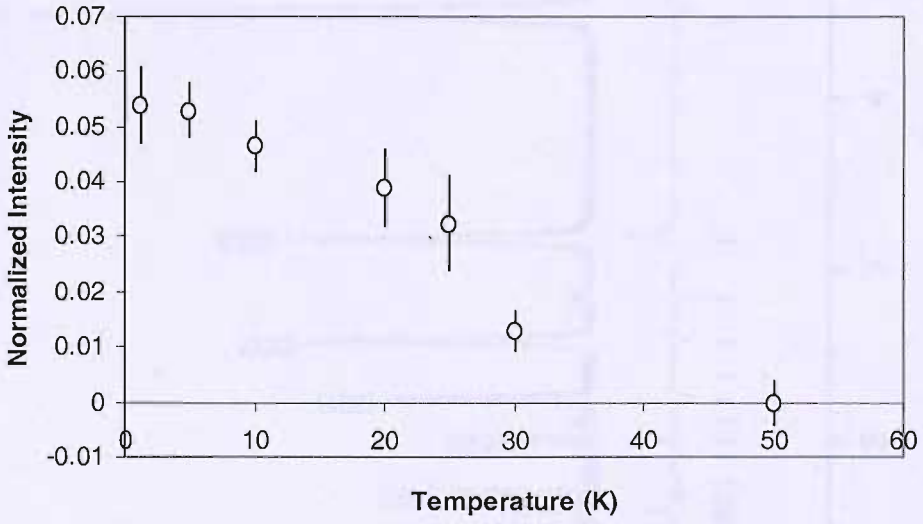

Figure 8.8: temperature dependence of the $d = 8.0$Å magnetic peak in the $LaMn_4Al_8$ sample

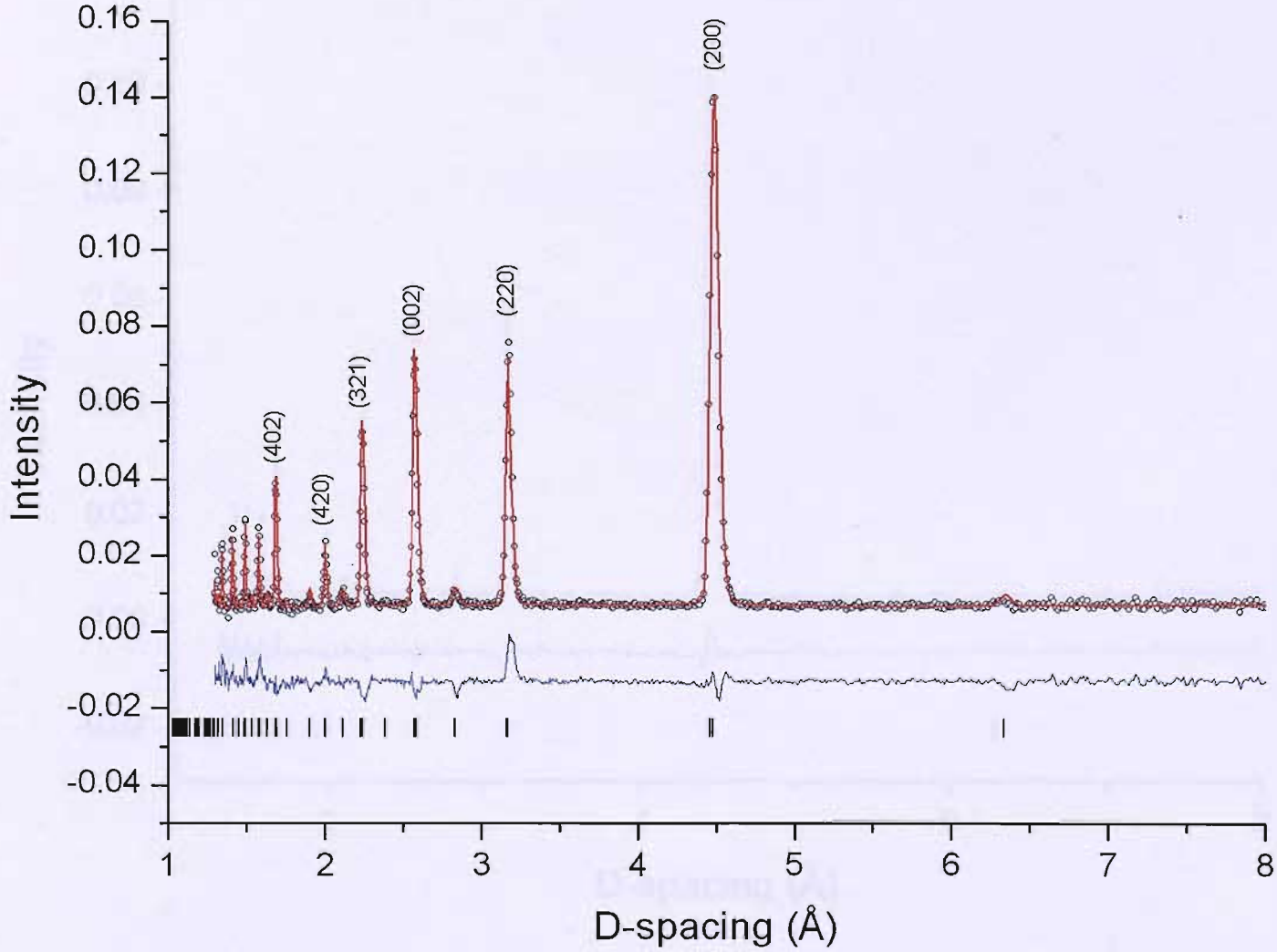

Figure 8.9: Room temperature neutron powder diffraction pattern recorded for $PrMn_4Al_8$. The Rietveld refinement fit line generated by GSAS is shown in red. Residual values and calculated reflection positions are also shown

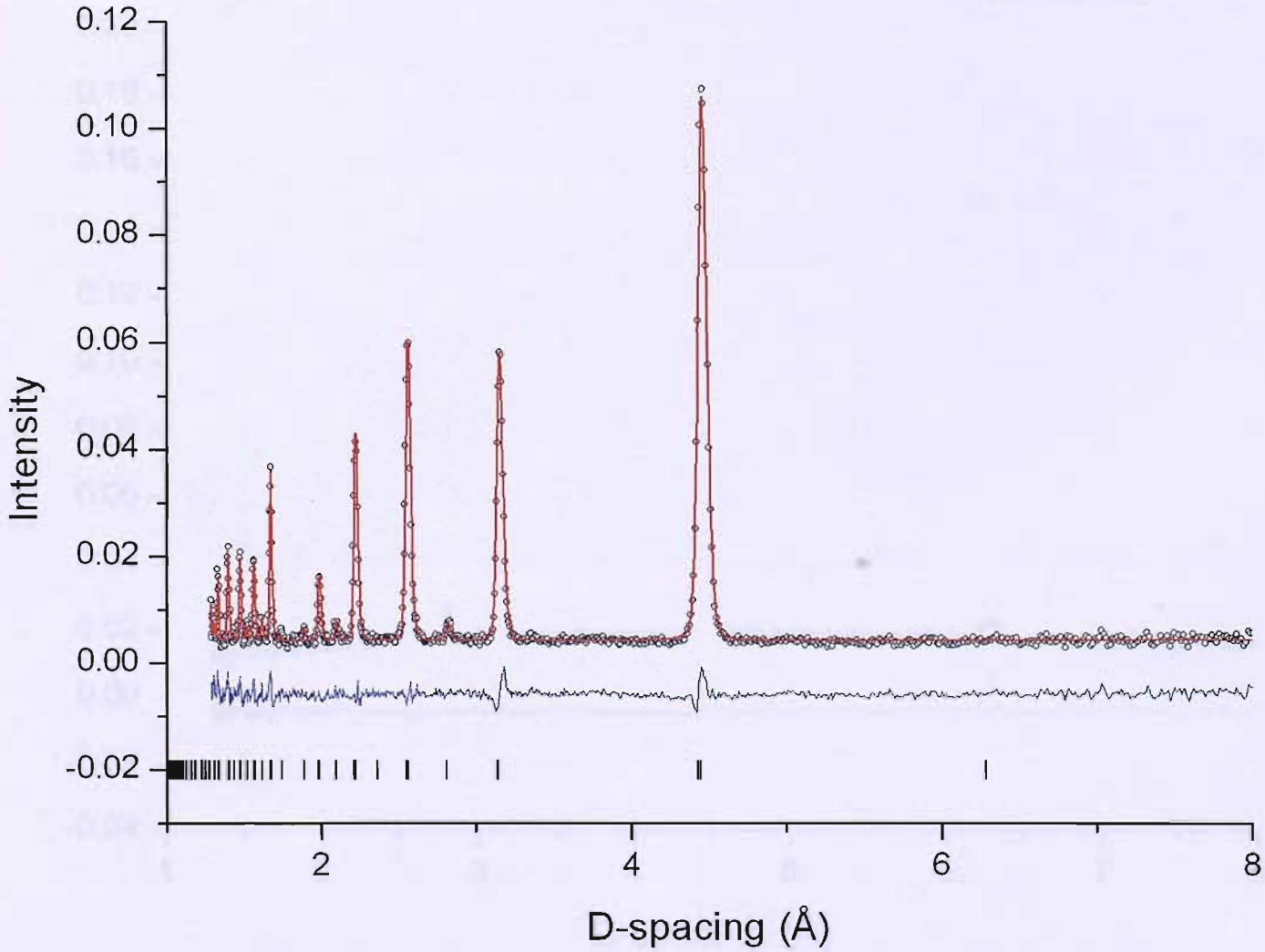

Figure 8.10: Room temperature neutron powder diffraction pattern and Rietveld refinement for $CeMn_4Al_8$ (ROTAX)

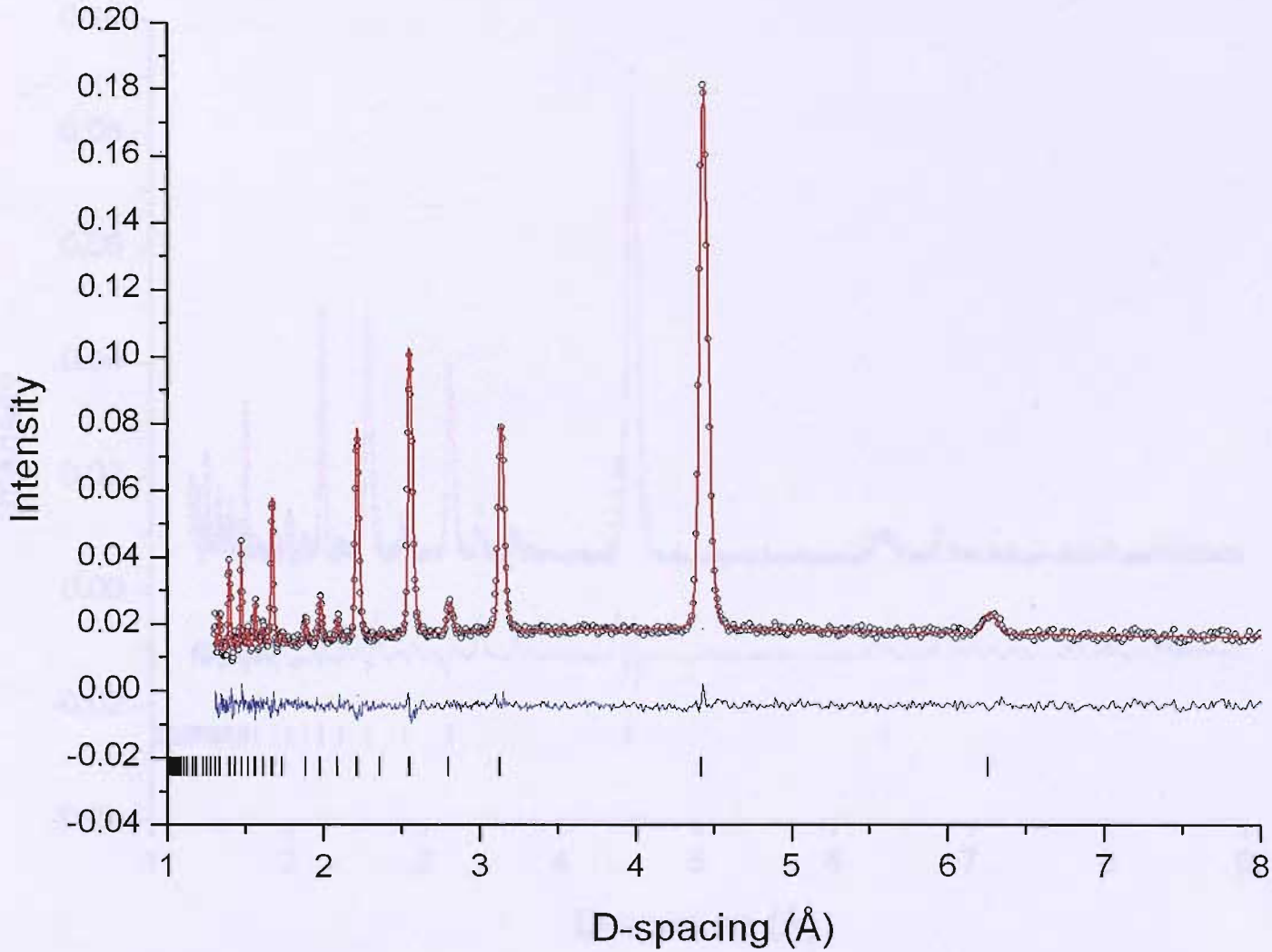

Figure 8.11: Room temperature neutron powder diffraction pattern and Rietveld refinement for $HoMn_4Al_8$ (ROTAX)

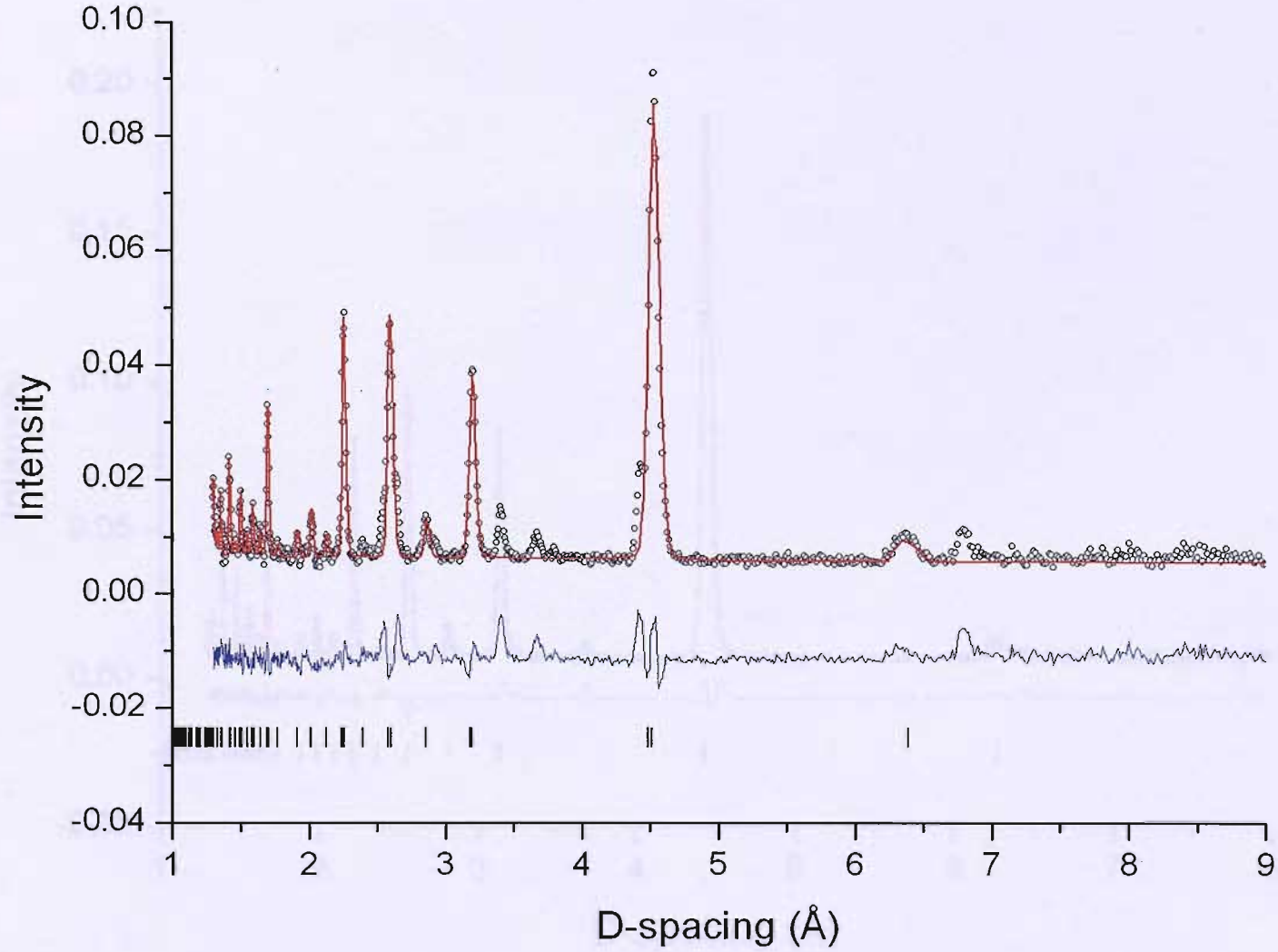

Figure 8.12: Room temperature neutron powder diffraction pattern and Rietveld refinement for $LaMn_4Al_8$ (ROTAX)

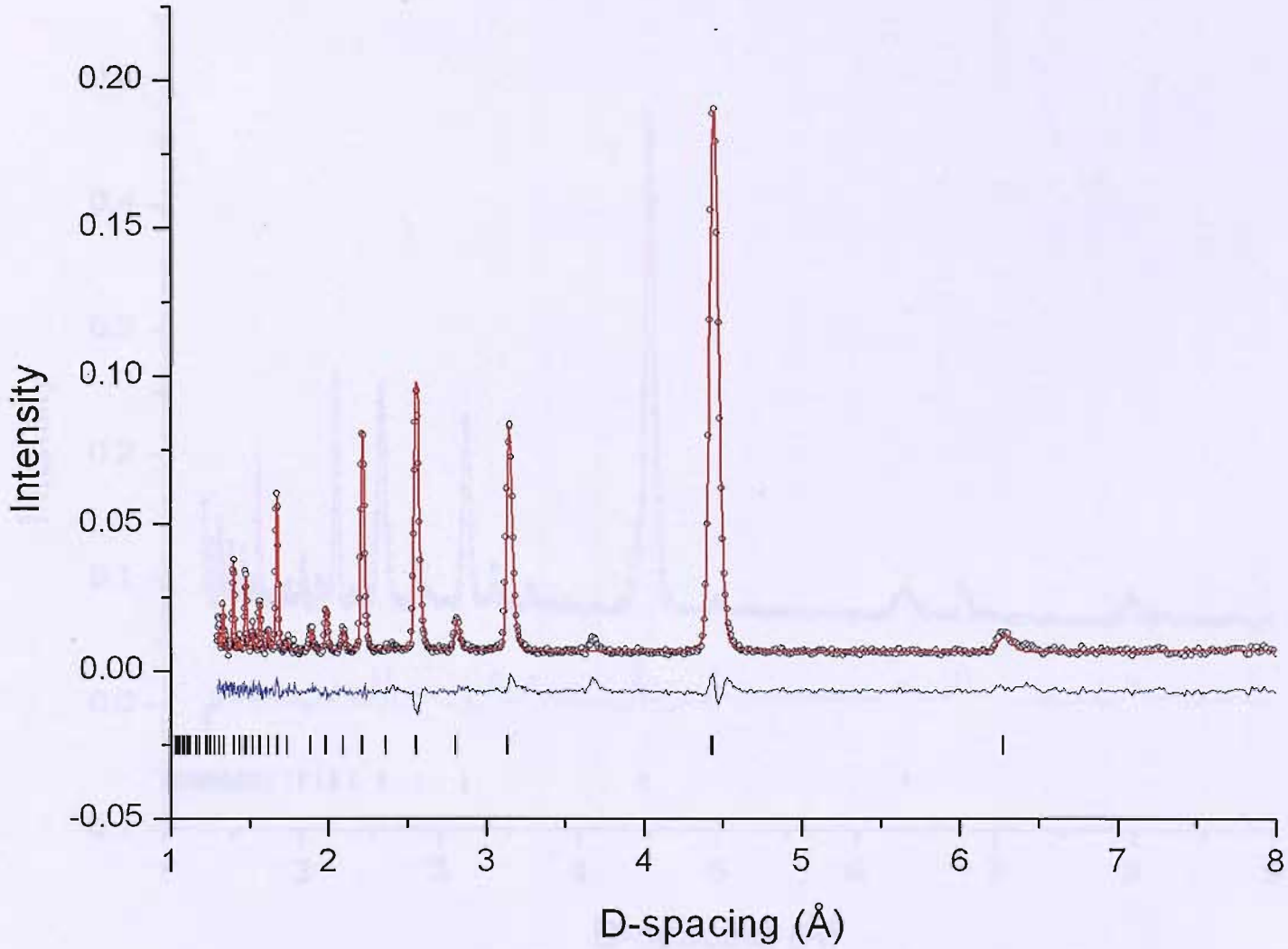

Figure 8.13: Room temperature neutron powder diffraction pattern and Rietveld refinement recorded for YMn_4Al_8 (ROTAX)

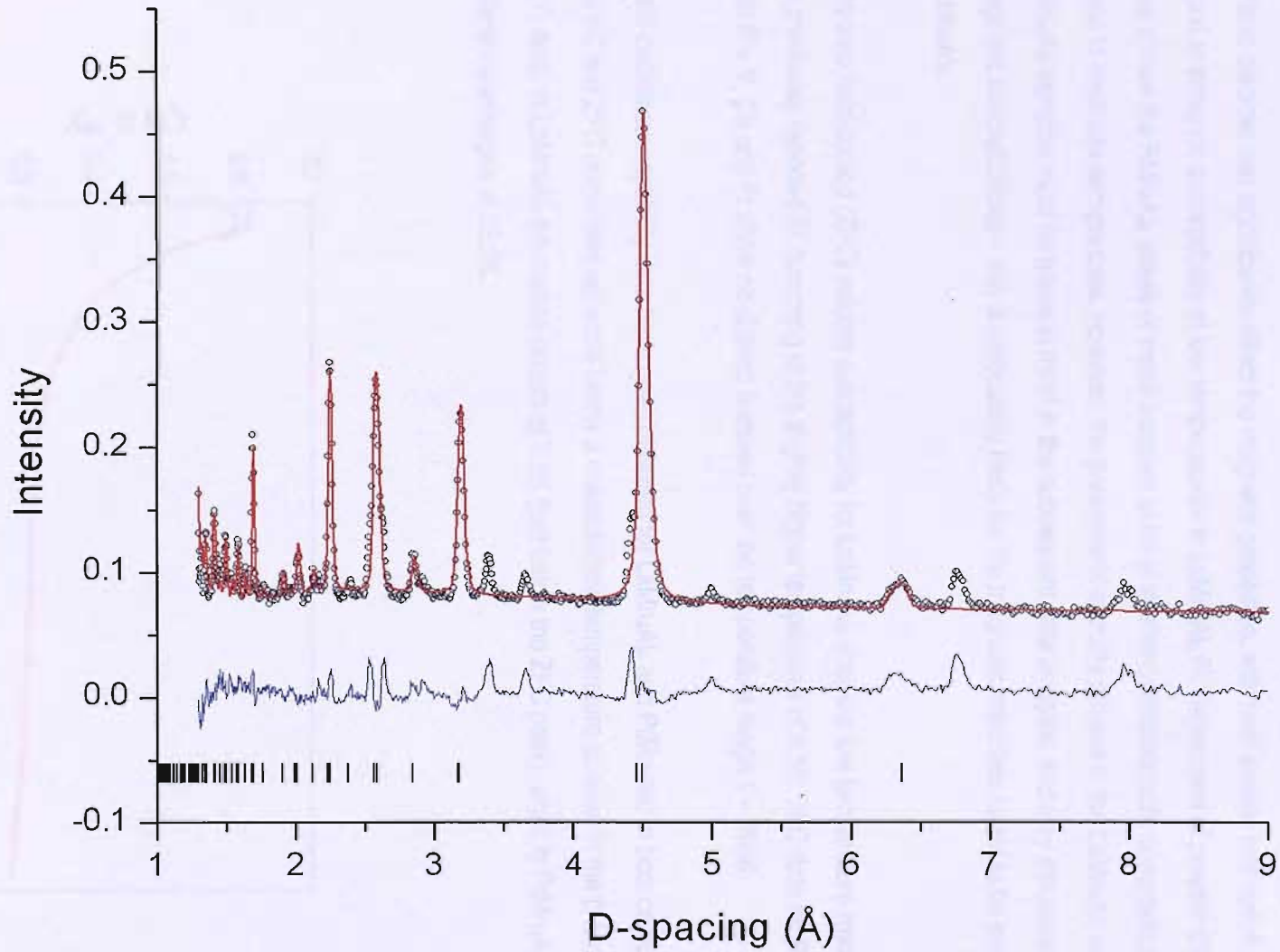

Figure 8.14: Neutron powder diffraction pattern and Rietveld refinement for $LaMn_4Al_8$ at 1.3K (ROTAX)

8.5. Magnetization Measurements of RMn_4Al_8

Light Rare-Earth Compounds (R = La, Ce, Pr) and YMn_4Al_8

Atomic disorder can significantly affect the magnetic properties, with both excess and deficit of Mn found to enhance susceptibility at low temperatures in $LaMn_4Al_8$ [5]. Refinement of powder diffraction data shows the RMn_4Al_8 phase of these samples to be of intended stoichiometric composition, with close to ideal site occupancies. However, the presence of impurity phases in the $LaMn_4Al_8$ and YMn_4Al_8 samples must be borne in mind in the subsequent data analysis, and may influence magnetic susceptibilities – this is particularly likely for the magnetic impurities found to be present in $LaMn_4Al_8$.

The zero field-cooled (ZFC) volume susceptibility for $LaMn_4Al_8$ shows a low temperature maximum as previously reported [5], occurring at the slightly higher temperature of 8.5K. ZFC data for RMn_4Al_8 with R = Y, Ce and Pr show no distinct features over the temperature range 1 – 300K.

Field-cooled susceptibility data have been obtained for $LaMn_4Al_8$ and $PrMn_4Al_8$: in both compounds the FC and ZFC responses separate below a characteristic temperature as seen in the β-$Mn_{1-x}M_x$ $\chi(T)$ data. In $LaMn_4Al_8$ bifurcation occurs at 7.3K (just below the ZFC peak), while in $PrMn_4Al_8$ the difference emerges at 33.2K.

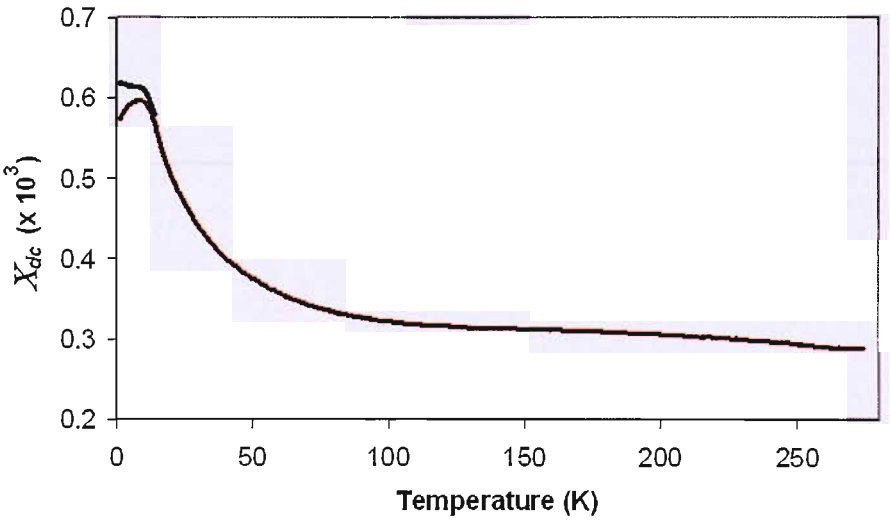

Figure 8.15: temperature dependence of the magnetic susceptibility in $LaMn_4Al_8$, measured in 1000G (ZFC data represented by the red curve, FC by the black curve)

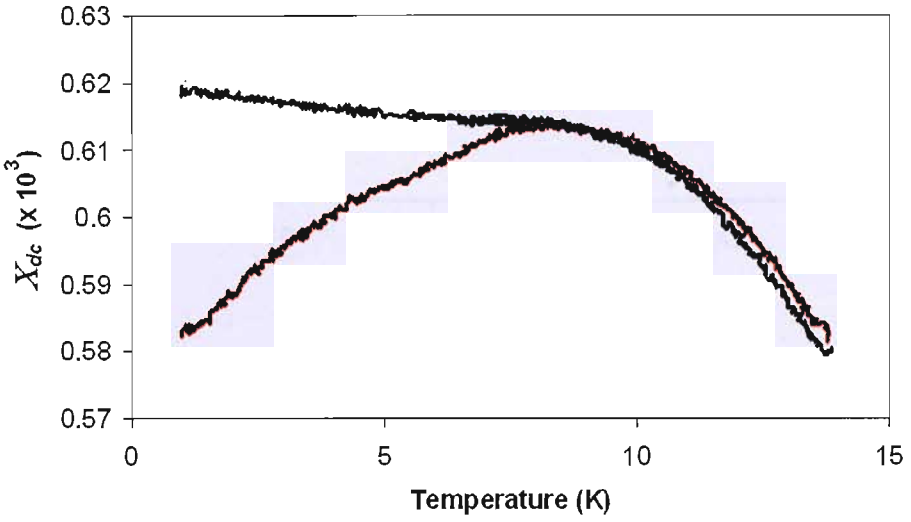

Figure 8.16: the bifurcation of FC (black curve) and ZFC (red curve) susceptibilities in $LaMn_4Al_8$, on an expanded scale

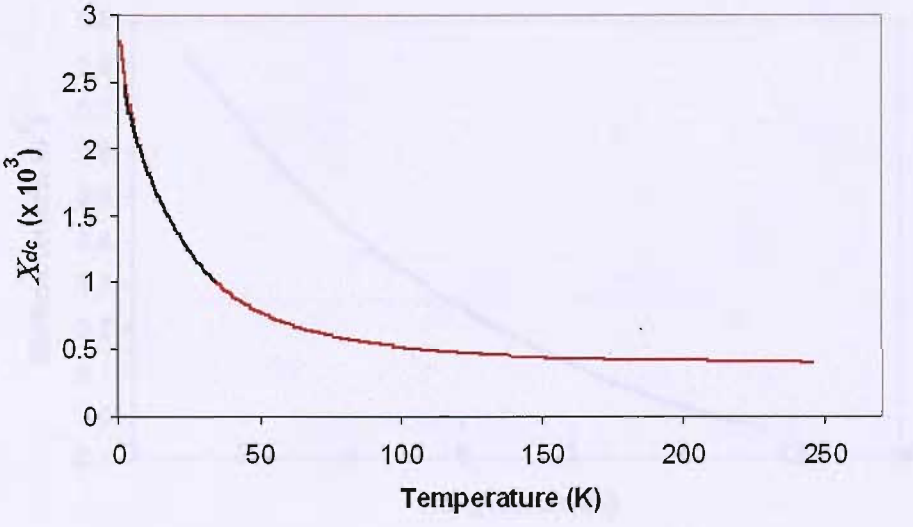

Figure 8.17: temperature dependence of the magnetic susceptibility in $PrMn_4Al_8$, measured in 1000G (ZFC data represented by the red curve, FC by the black curve)

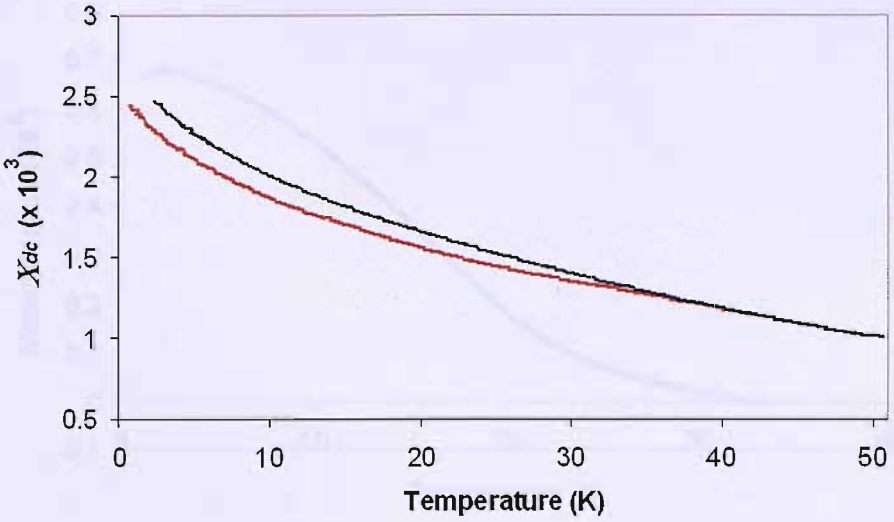

Figure 8.18: the bifurcation of FC (black curve) and ZFC (red curve) susceptibilities in $PrMn_4Al_8$, on an expanded scale

Thermoremanent magnetization also occurs in $LaMn_4Al_8$ below 10.5K, and in $PrMn_4Al_8$ below 32.5K for samples cooled in an applied field of 1T:

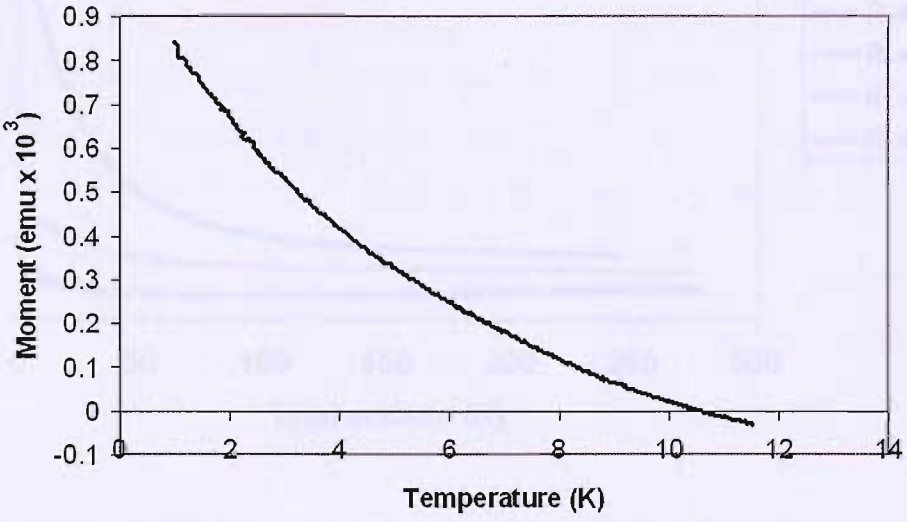

Figure 8.19: thermoremanent magnetization in a sample of $LaMn_4Al_8$ cooled in 1T

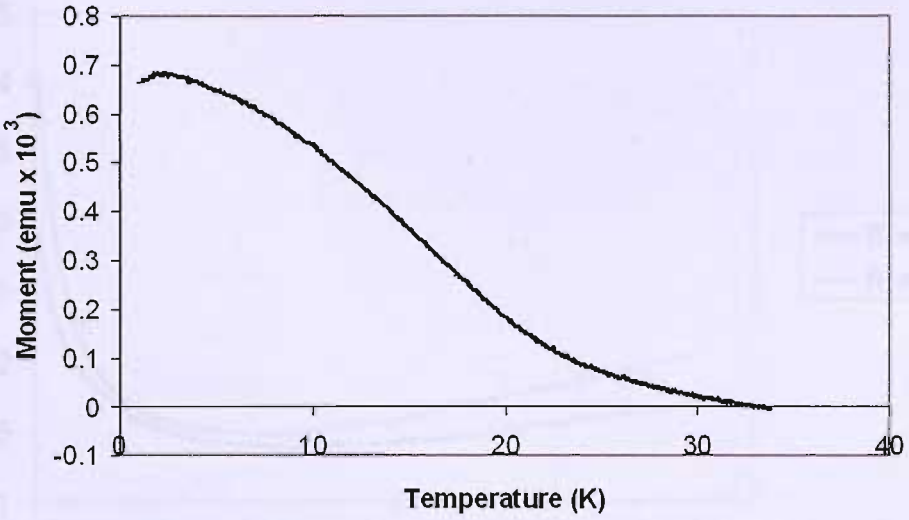

Figure 8.20: thermoremanent magnetization in a sample of $PrMn_4Al_8$ cooled in 1T

The ZFC responses of all light RMn_4Al_8 samples are shown below on the same axes:

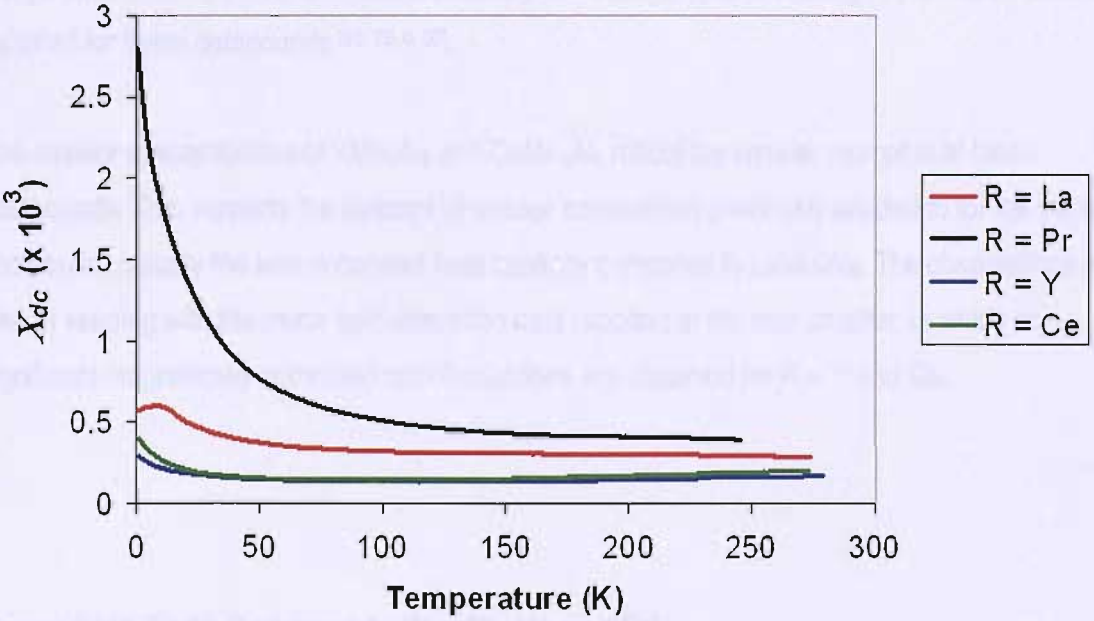

Figure 8.21: ZFC $\chi(T)$ data for the light RMn_4Al_8. The data for YMn_4Al_8 and $CeMn_4Al_8$ are shown below on an expanded scale

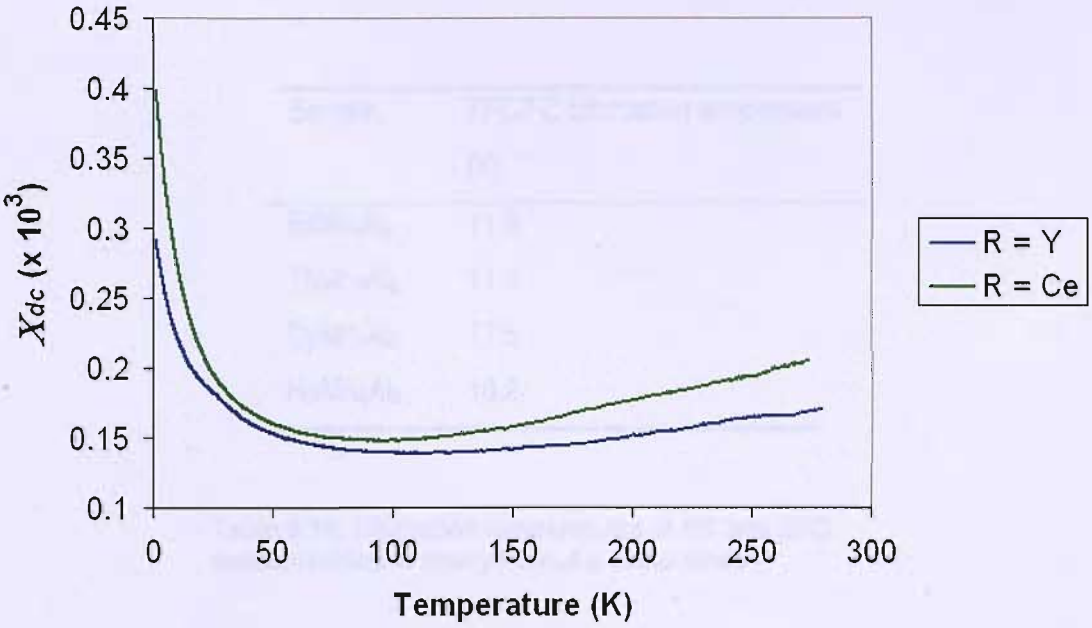

$\chi(T)$ is largely temperature-independent at high temperatures in $LaMn_4Al_8$ and $PrMn_4Al_8$. In YMn_4Al_8 and $CeMn_4Al_8$ there is a slight upturn at high temperatures, visible when the data for these compounds is viewed on a finer scale, probably corresponding to broad high temperature peaks reported for these compounds [16, 22, 6, 37].

The smaller susceptibilities of YMn_4Al_8 and $CeMn_4Al_8$ reflect the smaller moments of these compounds. This supports the concept of weaker correlations previously alluded to for the yttrium compound, notably the less enhanced heat capacity compared to $LaMn_4Al_8$. The observations are also in keeping with the muon spin relaxation data reported in the next chapter, in which no significant magnetically correlated spin fluctuations are observed for R = Y and Ce.

Heavy Rare-Earth Compounds (R = Tb, Ho and Er)

Low-temperature magnetic susceptibilities have been measured for the samples with heavy rare earths elements, where R = Er, Tb and Ho. As with the lighter compounds, these show bifurcation of ZFC and FC responses at temperatures given in the following table:

Sample	ZFC/FC bifurcation temperature (K)
$ErMn_4Al_8$	11.8
$TbMn_4Al_8$	11.4
$DyMn_4Al_8$	17.5
$HoMn_4Al_8$	10.2

Table 8.10: bifurcation temperatures of FC and ZFC susceptibilities in heavy RMn_4Al_8 compounds

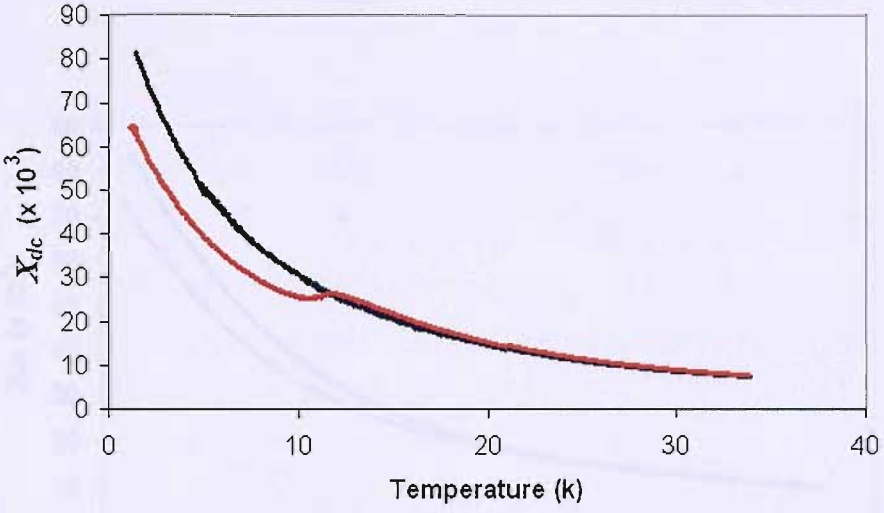

Figure 8.22: FC (black) and ZFC (red) susceptibilities of $ErMn_4Al_8$, measured in 1000G

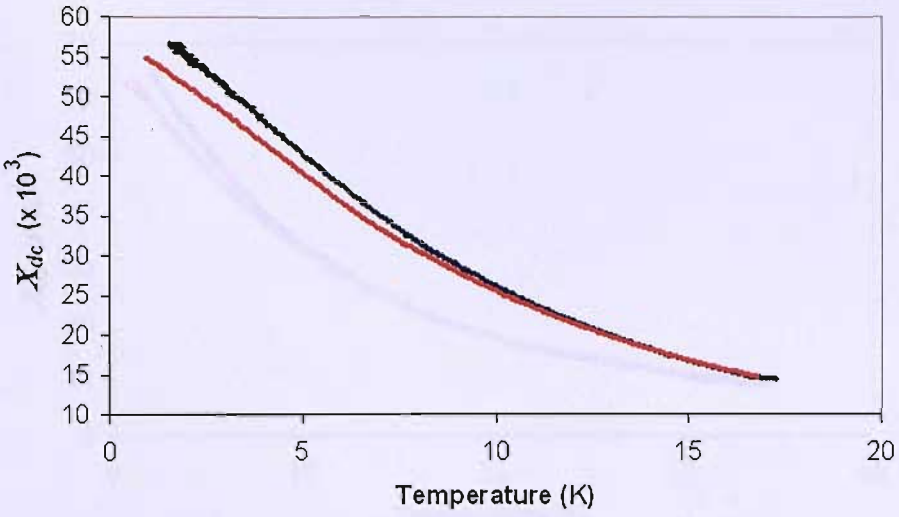

Figure 8.23: FC and ZFC susceptibilities of $TbMn_4Al_8$, measured in 1000G

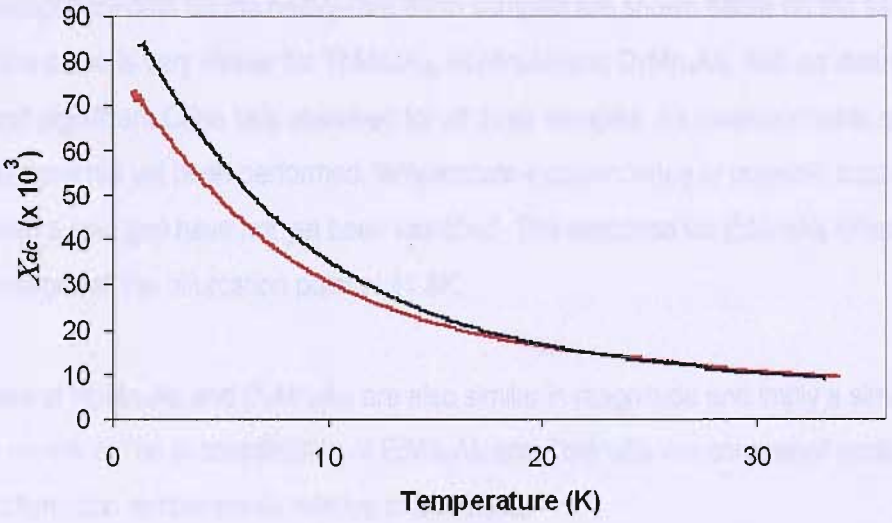

Figure 8.24: FC and ZFC susceptibilities of $DyMn_4Al_8$, measured in 1000G

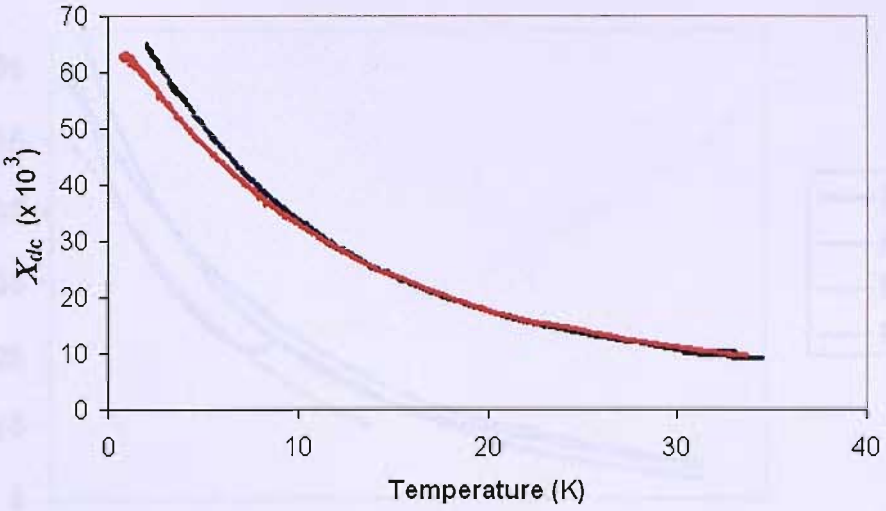

Figure 8.25: FC and ZFC susceptibilities of $HoMn_4Al_8$, measured in 1000G

The ZFC susceptibility data for the heavy-rare earth samples are shown below on the same axes. The form of the curve is very similar for $TbMn_4Al_8$, $HoMn_4Al_8$ and $DyMn_4Al_8$, with no distinct anomalies and significant Curie tails observed for all three samples. As measurements at higher temperatures have not yet been performed, temperature-independence or possible broad peaks associated with a spin gap have not yet been identified. The response for $ErMn_4Al_8$ differs in that a ZFC peak emerges at the bifurcation point of 11.8K.

The responses of $HoMn_4Al_8$ and $DyMn_4Al_8$ are also similar in magnitude and imply a similar value of the effective moment. The susceptibilities of $ErMn_4Al_8$ and $TbMn_4Al_8$ are somewhat smaller, despite their higher bifurcation temperatures relative to $DyMn_4Al_8$.

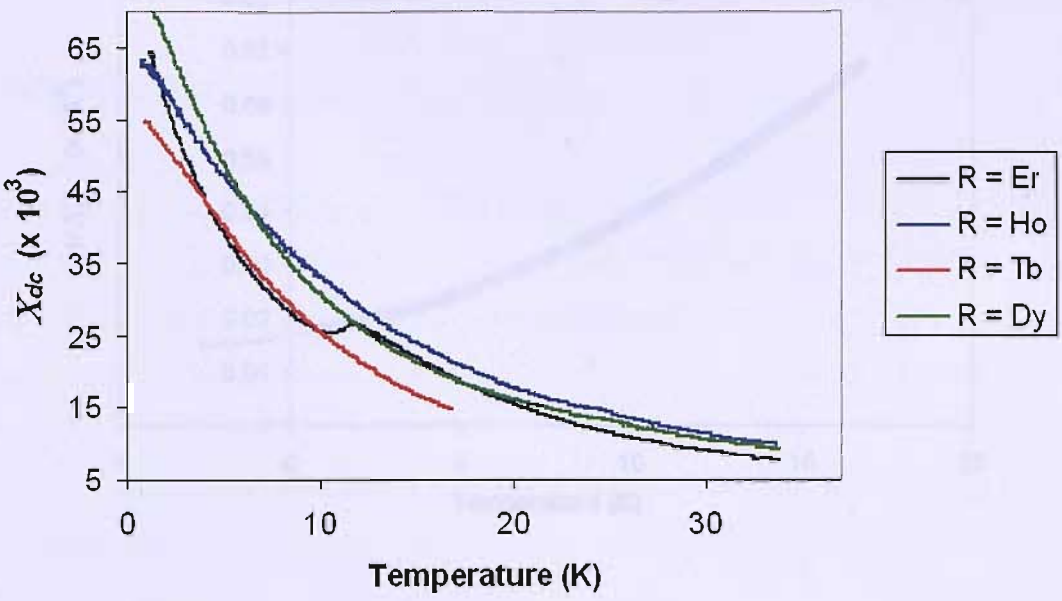

Figure 8.26: ZFC susceptibilities of the heavy rare earth RMn_4Al_8 compounds

The reciprocal volume susceptibility of $TbMn_4Al_8$ is shown below. A positive intercept in $1/\chi(T)$ indicating $\theta > 0$ has been previously reported [10] for $TbMn_4Al_8$, suggesting that a ferromagnetic phase may exist in this compound at very low temperatures. The current response is dominated in the low-temperature regime by a temperature-independent Van-Vleck contribution, which gives rise to a misleading, negative intercept which may be interpreted as corresponding to $\theta < 0$. An extrapolation of the high-temperature data would give rise to a positive, $\theta > 0$ intercept in accord with previous measurements. However, some consideration must be given to a possible superposition of anisotropic susceptibilities, as a result of using a powder sample: if the exchange interactions associated with correlations along the *a* and *c* axes are of different sign, there may be some compensation effect from a powder sample with random crystal orientation, which in certain circumstances can result in an apparent Weiss parameter of 0. Single crystal studies, allowing independent measurement of $\chi(T)$ parallel and perpendicular to the crystal c-axis, would be required in this event. Hence any estimation of the value of θ from these data would not necessarily be accurate.

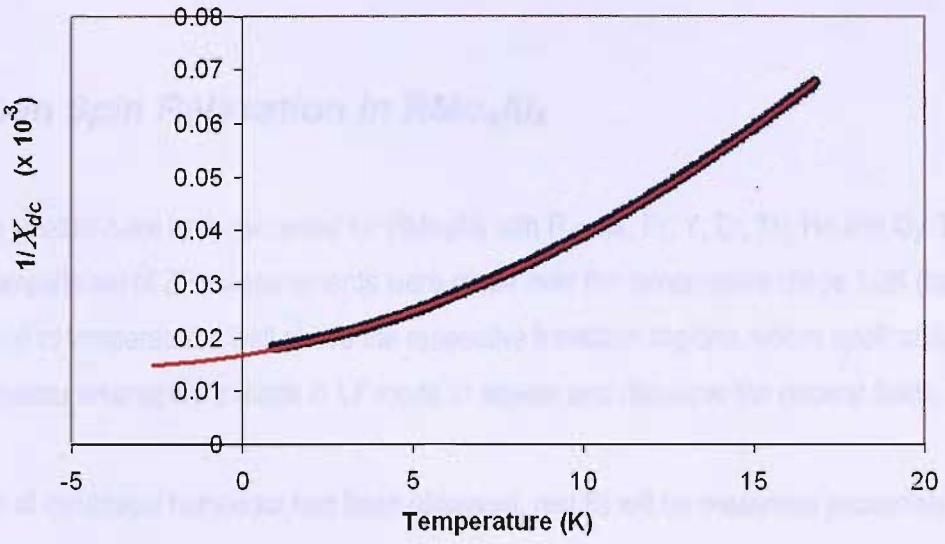

Figure 8.27: reciprocal susceptibility in $TbMn_4Al_8$.
The line of extrapolation to $T = 0$ is shown in red

8.6. Muon Spin Relaxation in RMn_4Al_8

Relaxation spectra have been recorded for RMn_4Al_8 with R = La, Pr, Y, Er, Tb, Ho and Dy. In all cases a complete set of ZF measurements were made over the temperature range 1.2K (base temperature) to temperatures well above the respective transition regions, where applicable. Selected measurements were made in LF mode to assess and decouple the nuclear fields.

As a range of dynamical behaviour has been observed, results will be presented separately for each of these compounds.

$LaMn_4Al_8$

Measurements have been performed over the temperature range 1.2 – 70K in the absence of an applied field, with LF data recorded in 100G showing complete decoupling from nuclear fields.

The high-temperature ZF response is modelled by a pure Gaussian Kubo-Toyabe (GKT) function (plus a small temperature-independent background), associated with relaxation due entirely to static nuclear moments, with no muon diffusion. Below 20K, evidence for dynamical processes begins to emerge, with the relaxation taking the form of a GKT function multiplied by a stretched exponential (SE) component

$$A_z(t) = a_0 G_z^{GKT}(t)\exp\left[-(\lambda t)^{\beta}\right] + (background)$$

as observed in the β-$Mn_{1-x}Ru_x$ and β-$Mn_{1-x}Co_x$ spin glass systems.

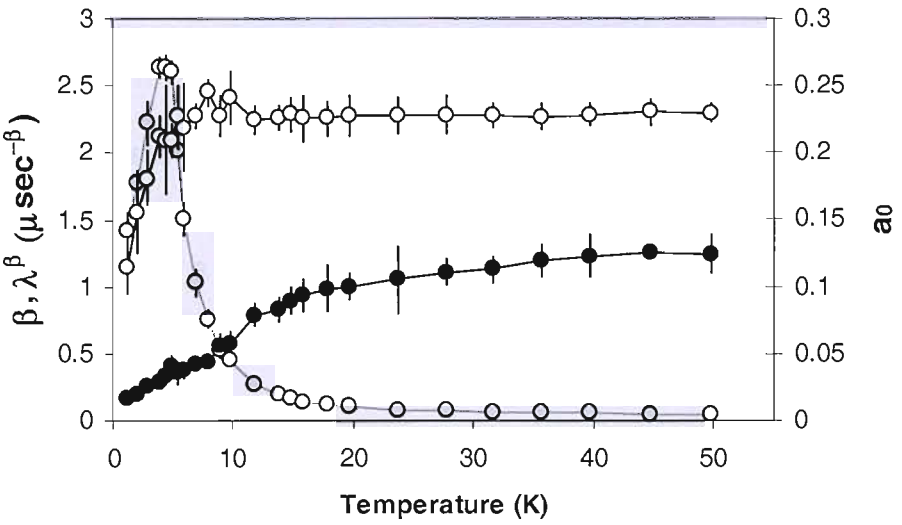

Figure 8.28: temperature dependence of the ZF μSR fitting parameters in $LaMn_4Al_8$.
Key: closed circles indicate exponent β, open circles represent initial asymmetry a_0, and grey circles indicate relaxation rate λ^β

The temperature dependence of the GKT × SE fitting parameters is as shown above. The exponent β falls from a value greater than 1 at high temperatures (consistent with dynamical modification to the GKT function) to a value of 0.5 at around 10K: this coincides with a rapid increase in the relaxation rate parameter λ^β, which peaks at 4.5K. Below this temperature the asymmetry a_0 decreases smoothly. A value of 0.285 was obtained for the Gaussian field distribution parameter σ.

YMn_4Al_8, $CeMn_4Al_8$

Relaxation measurements were carried out with the YMn_4Al_8 sample as for $LaMn_4Al_8$, with an applied longitudinal field of 100G again found to be sufficient in decoupling the muons from the nuclear fields.

In this sample GKT relaxation persists down to 1.2K, with no obvious dynamical component. Fluctuations in the Mn moments must occur on a timescale so rapid that the muons spins are unable to couple to them, giving rise to a motionally-narrowed response as described in section 3.4. It may therefore be assumed that no significant dynamical processes occur in this sample within the muon

time window. The absence of slow spin fluctuations in this compound is consistent with its smaller Sommerfeld constant when compared to $LaMn_4Al_8$ [25].

Spectra recorded for $CeMn_4Al_8$ between 1.2 and 30K showed a similar response, with the GKT function again emerging, this time modified by a very small dynamical (Lorentzian) component. The relaxation rate parameter ν is small at approximately 0.05, leading to only minimal suppression of the 1/3 tail and indicating that dynamics do not play a large part in this system.

$PrMn_4Al_8$

ZF and LF spectra recorded between 1.2 and 70K again show GKT nuclear relaxation in the high temperature region, with a small dynamical component suppressing the GKT tail. Below 35K, a distinctly different response to that observed in any other sample emerges. An oscillatory component develops in this temperature region, which increases in amplitude and frequency with decreasing temperature. The form of the oscillation is best fit with a Bessel function, $j_0(\gamma_\mu H_{max} t)$, carried out using the FORTRAN program MUFIT2[1]. This type of relaxation function has been found to apply to systems in which there is a spread of internal fields, such as those with incommensurate spin density waves [38]. Hence the total fitting function for the ZF data below 35K is

$$A_z(t) = \left[a_0 G_z^{GKT}(t)\, j_0(\omega,t)\right]\exp[-\lambda t] + (background)$$

where

$$j_0 = \frac{\sin(\omega t)}{\omega t}$$

[1] MUFIT2 subroutines initially developed by B. D. Rainford and modified by the author

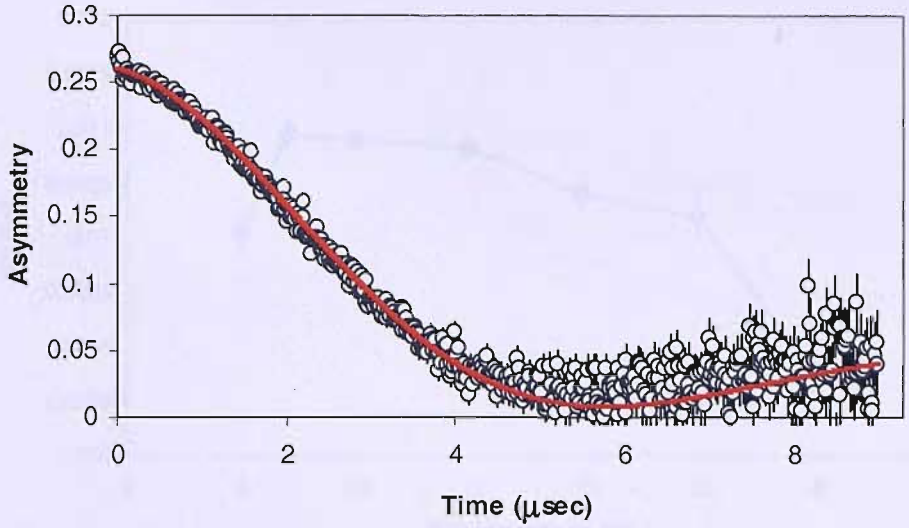

Figure 8.29: 70K relaxation in $PrMn_4Al_8$, fitted to a GKT function with a small dynamical modification (shown by red curve)

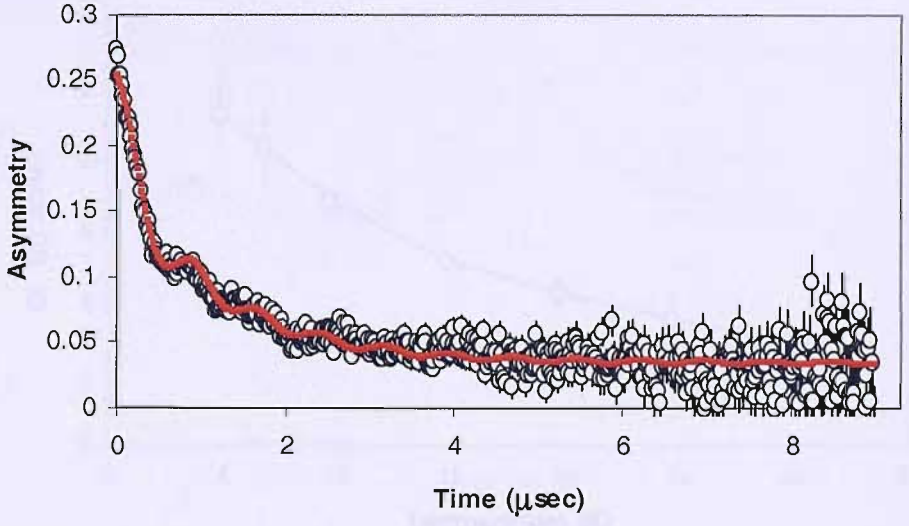

Figure 8.30: 7K relaxation in $PrMn_4Al_8$, fitted to a dynamical GKT function multiplied by the Bessel function $j_0(\gamma_\mu H_{max} t)$. The fitting function is represented by the red curve

The oscillatory relaxation component increases in amplitude with decreasing temperature below 35K, reaching a maximum around 10K and dying away at very low temperatures. The frequency increases with decreasing temperature, with the gradient of ω versus T increasing slightly at approximately 10K.

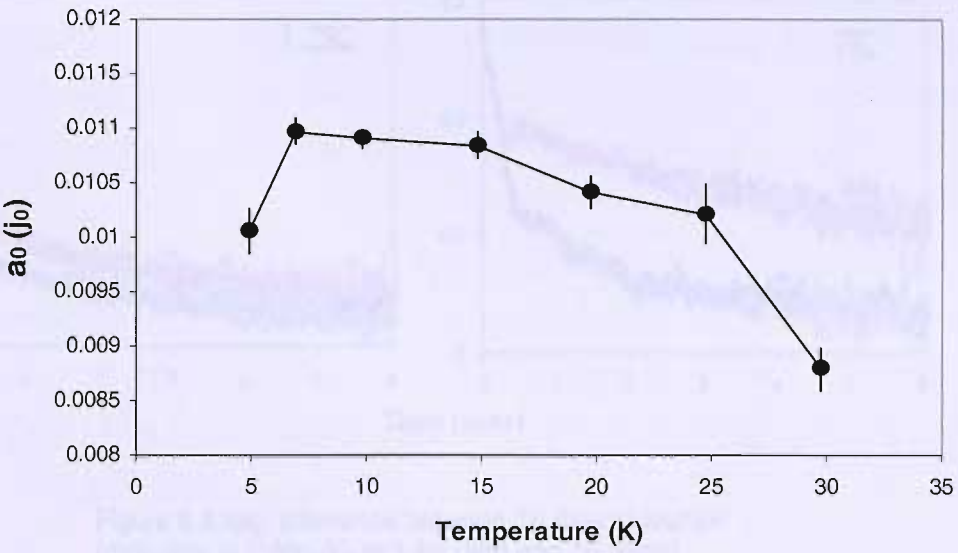

Figure 8.31: amplitude of the oscillatory asymmetry component in $PrMn_4Al_8$ as a function of temperature

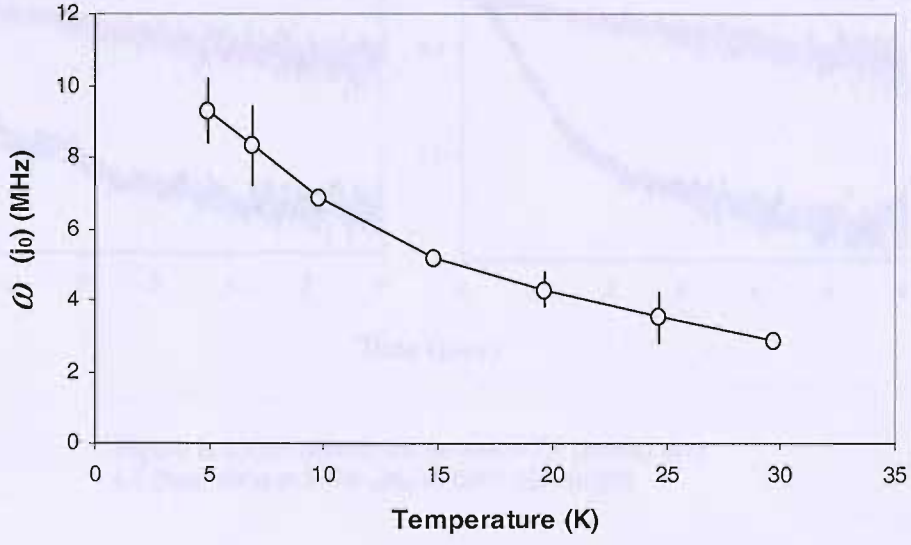

Figure 8.32: frequency of the oscillatory asymmetry component in $PrMn_4Al_8$ as a function of temperature

At high temperatures, an applied longitudinal field of 100G leads to a recovery of asymmetry. As the temperature is lowered, this field is unable to decouple the muon spins from rapidly varying internal fields of comparatively large magnitude, as seen from the small difference between ZF and LF data at the lowest temperatures:

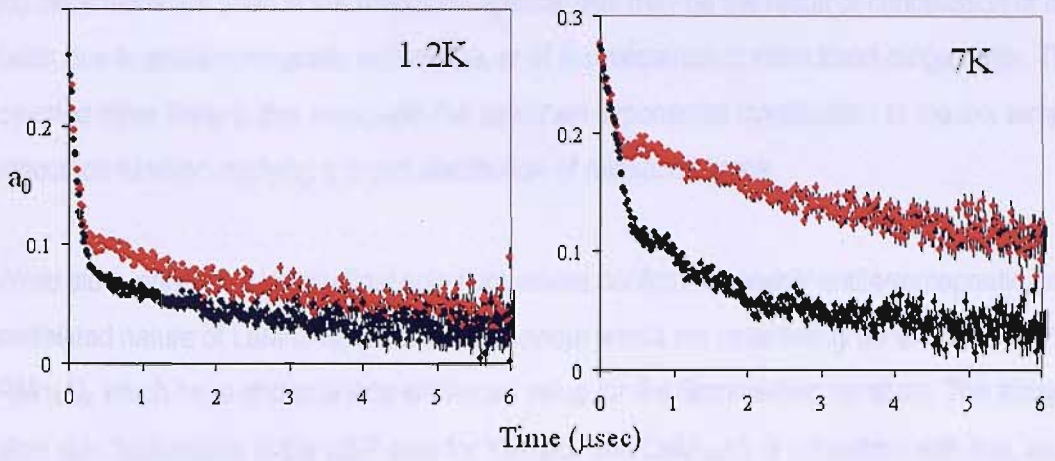

Figure 8.33(a): difference between ZF (black) and LF (red) data in $PrMn_4Al_8$ at 1.2K (left) and 7K (right)

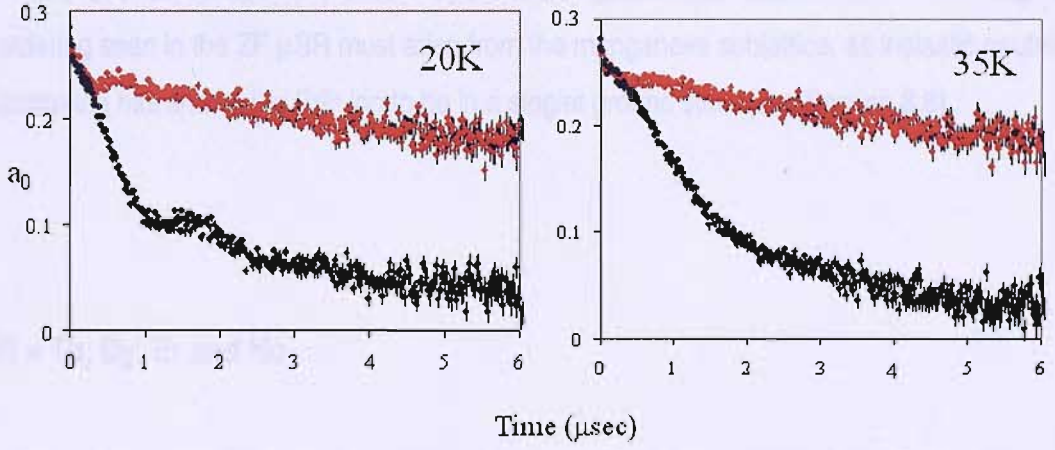

Figure 8.33(b): difference between ZF (black) and LF (red) data in $PrMn_4Al_8$ at (left) 35K (right)

This behaviour corresponds to the ZFC/FC bifurcation seen in the susceptibility below 35K.

Discussion

The low temperature peak in the relaxation rate for $LaMn_4Al_8$ is indicative of a magnetic phase transition, coinciding with susceptibility features in this region and presenting the first evidence that a static magnetic low-temperature phase exists in this compound.

No oscillations are seen in the relaxation spectra; this may be the result of cancellation of internal fields due to antiferromagnetic sublattices, or of the existence of more short-range order. The latter is deemed more likely in this case, with the stretched exponential modification to the low temperature relaxation function implying a broad distribution of relaxation times.

While slow, enhanced longitudinal spin fluctuations confirm the nearly-antiferromagnetic, strongly-correlated nature of $LaMn_4Al_8$, the same behaviour would not necessarily be expected in those RMn_4Al_8 which have shown a less enhanced value for the Sommerfeld constant. The absence of slow spin fluctuations in the μSR data for YMn_4Al_8 and $CeMn_4Al_8$ is consistent with this, and is also in line with the reduced susceptibilities measured for these systems.

The oscillatory signal observed below 35K is not the first reported evidence of magnetic long-range order in $PrMn_4Al_8$. In addition to the early Mossbauer work that found an apparent transition at 11K [10], more recent studies have shown a peak in the specific heat data at 14K [25]. The magnetic ordering seen in the ZF μSR must arise from the manganese sublattice, as inelastic neutron scattering has shown the Pr^{3+} ion to be in a singlet ground state (see Section 8.8).

R = Tb, Dy, Er and Ho

Zero field measurements were carried out on the MuSR spectrometer at the ISIS facility, RAL, between 1.2K and 200K.

In all four of these samples the relaxation consists of two distinguishable components, which for R = Dy, Tb and Er have approximately equal asymmetry above 50K. The polarization function is found to take the form of a sum of two Lorentzian $G_z(t)$ terms plus a small time-independent background contribution:

$$A_z(t) = a_1 \exp[-\lambda_1 t] + a_2 \exp[-\lambda_2 t] + (background)$$

The second component is slowly relaxing when compared to the first term, with λ_2 an order of magnitude smaller than λ_1. For $ErMn_4Al_8$ λ_2 rises to a maximum at 25K, just above the temperature

(17K) at which the ZFC susceptibility displays a cusp. The asymmetry a_2 corresponding to this component drops below 25K; in the same region the component with a_1 rises. The rapid relaxation rate λ_1 displays more unusual behaviour, rising to a peak at 50K then decreasing to a minimum at 20K, close to the λ_2 peak but considerably higher in temperature than the ZFC susceptibility peak (11.8K). Below 15K, λ_1 increases very rapidly.

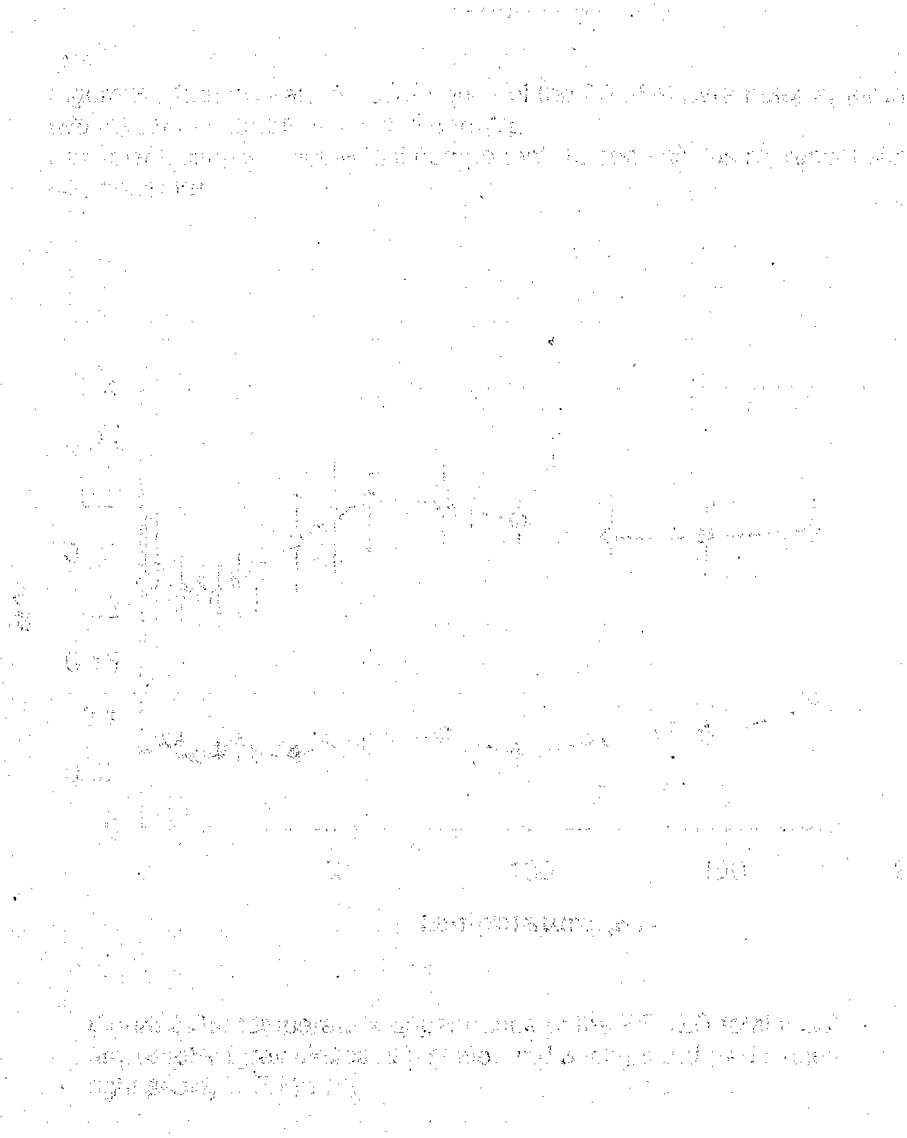

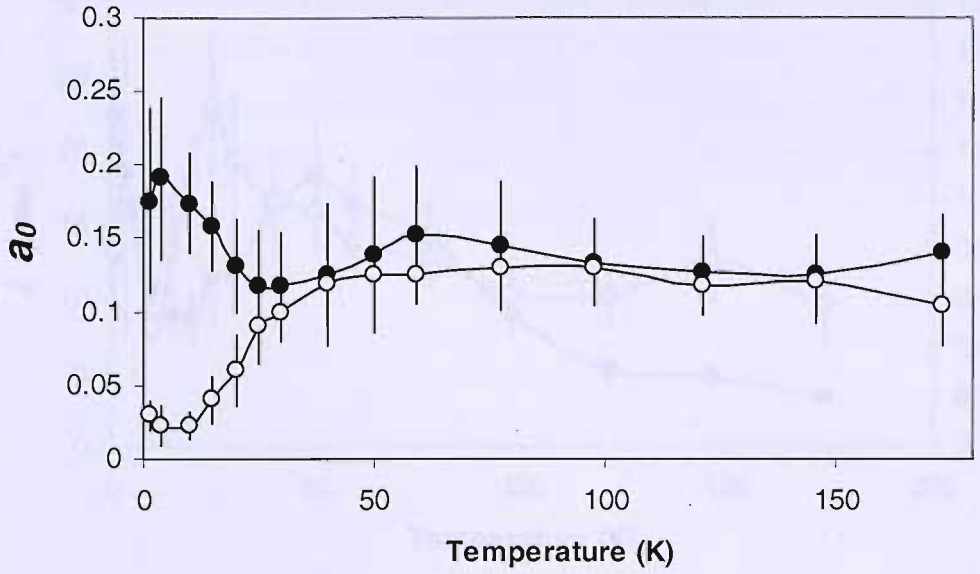

Figure 8.34: temperature dependence of the ZF μSR parameter a_0 for the two relaxation contributions in $ErMn_4Al_8$.
Key: black circles indicate fast component a_1, open circles represent slow component a_2

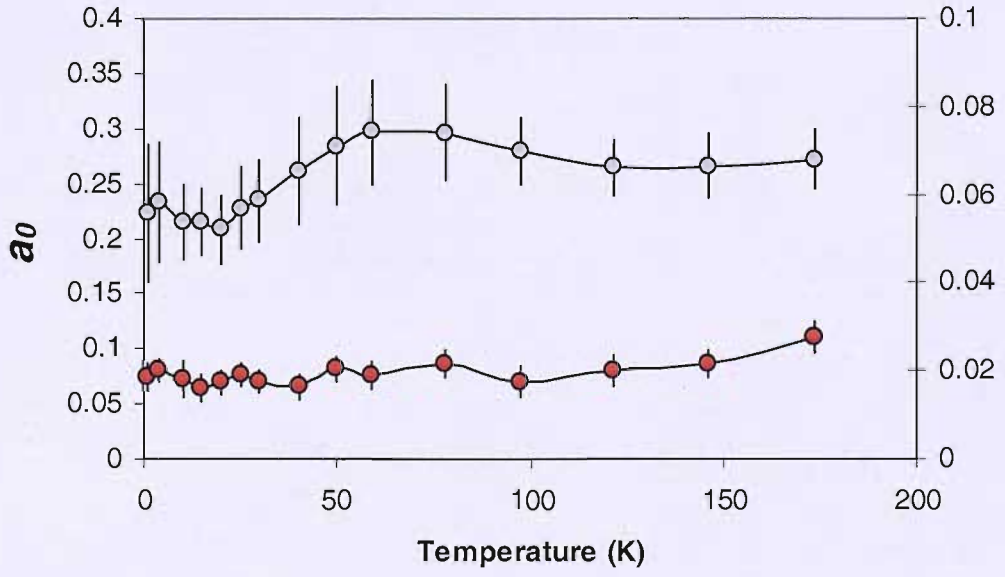

Figure 8.35: temperature dependence of the ZF μSR total initial asymmetry (grey circles, left scale) and background (red circles, right scale) in $ErMn_4Al_8$

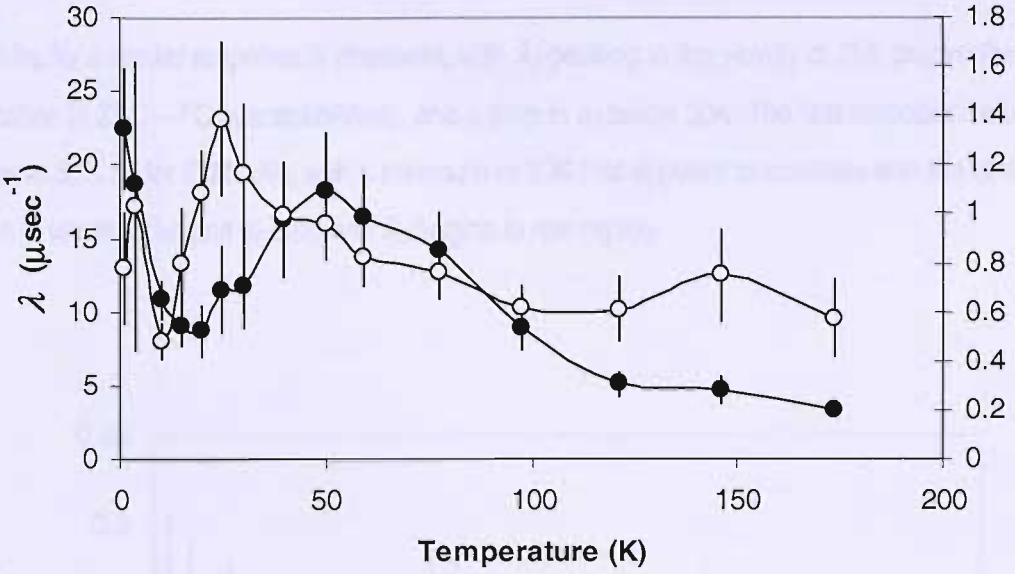

Figure 8.36: temperature dependence of the ZF μSR relaxation rates λ_1 (black circles, left scale) and λ_2 (open circles, right scale) in $ErMn_4Al_8$

In $TbMn_4Al_8$ a similar response is observed, with λ_2 peaking in the vicinity of 25K (above the 11.4K bifurcation in ZFC – FC susceptibilities), and a drop in a_2 below 30K. The fast relaxation rate λ_1 has a peak at 50K as for $ErMn_4Al_8$, with a minimum at 30K that appears to correlate with the temperature region in which a_2 begins to drop and λ_2 begins to rise rapidly.

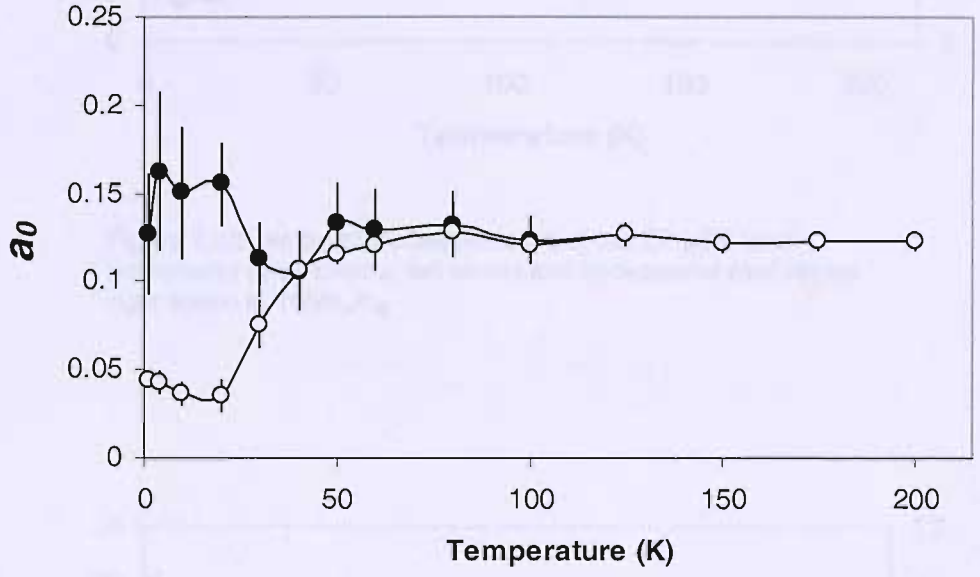

Figure 8.37: temperature dependence of the ZF μSR parameter a_0 for the two relaxation contributions in $TbMn_4Al_8$
Key: closed circles indicate fast component a_1, open circles represent slow component a_2

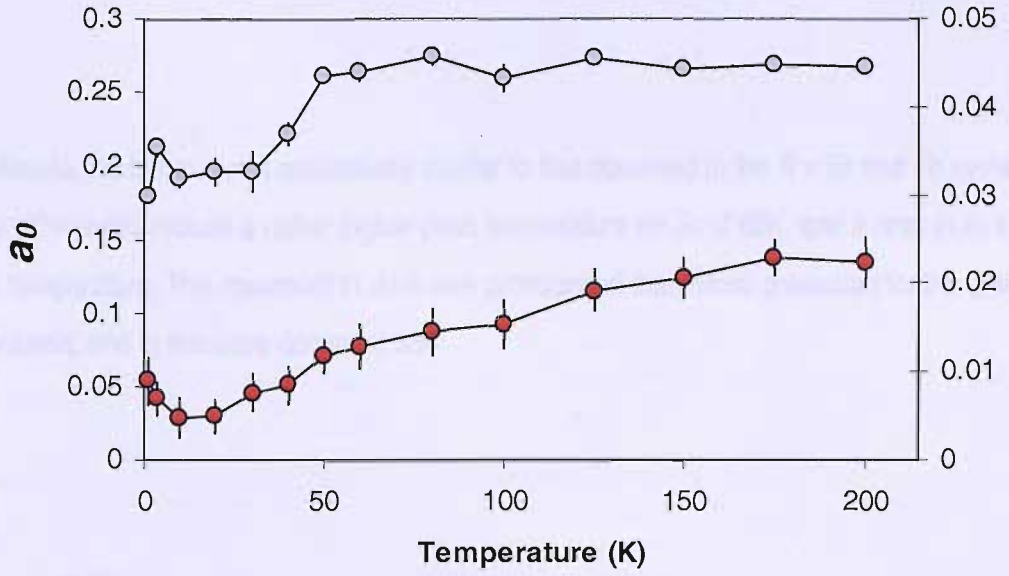

Figure 8.38: temperature dependence of the ZF μSR total asymmetry (grey circles, left scale) and background (red circles, right scale) in $TbMn_4Al_8$

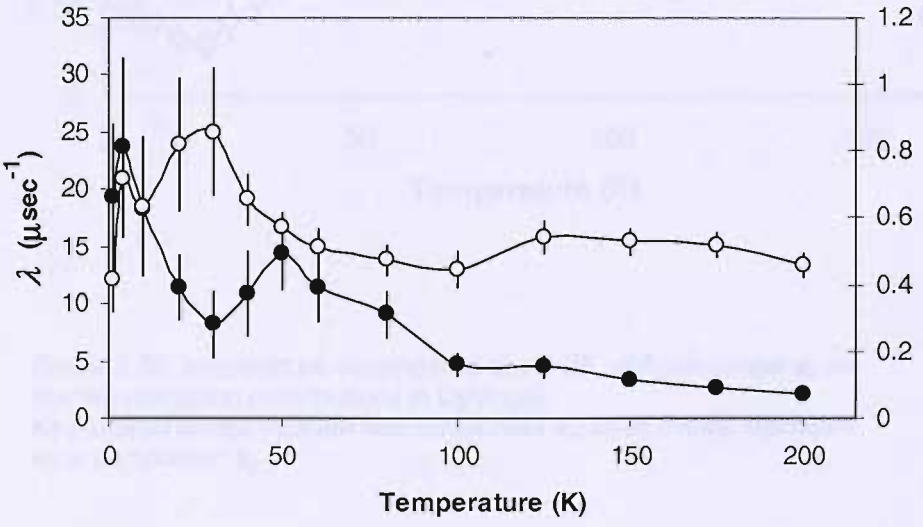

Figure 8.39: temperature dependence of the ZF μSR relaxation rates λ_1 (black circles, left scale) and λ_2 (open circles, right scale) in $TbMn_4Al_8$

In $DyMn_4Al_8$ the behaviour is qualitatively similar to that observed in the R = Er and Tb systems: the subtle differences include a rather higher peak temperature for λ_1 of 60K, and a drop in a_2 at the same temperature. The maximum in λ_2 is less pronounced than those presented for the previous compounds, and in this case occurs at 35K.

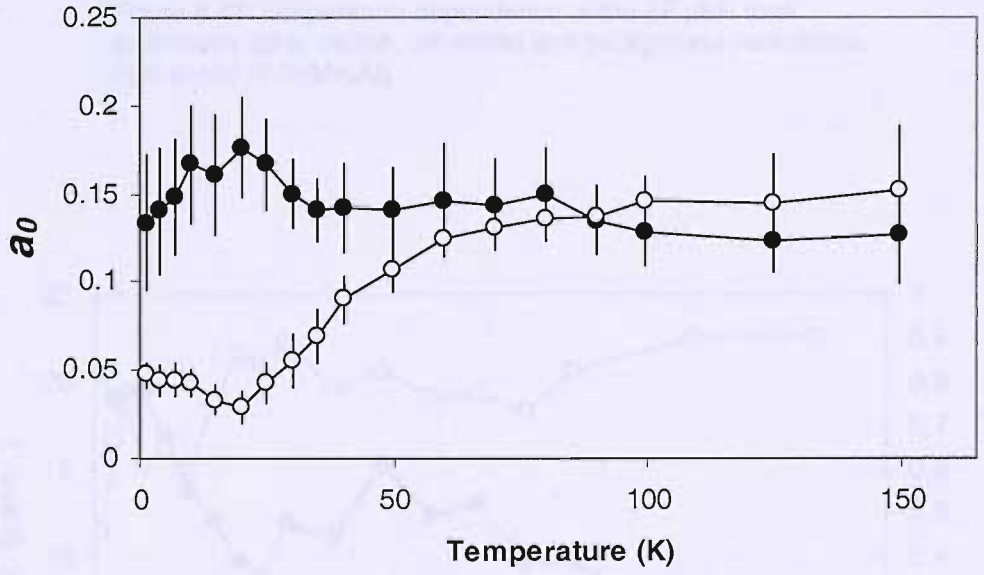

Figure 8.40: temperature dependence of the ZF μSR parameter a_0 for the two relaxation contributions in $DyMn_4Al_8$
Key: closed circles indicate fast component a_1, open circles represent slow component a_2

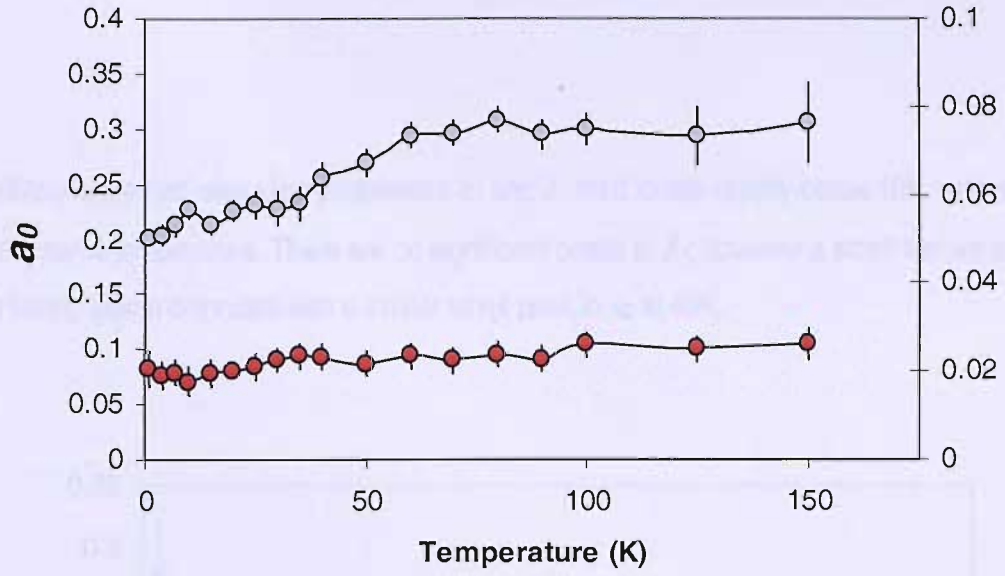

Figure 8.41: temperature dependence of the ZF μSR total asymmetry (grey circles, left scale) and background (red circles, right scale) in $DyMn_4Al_8$

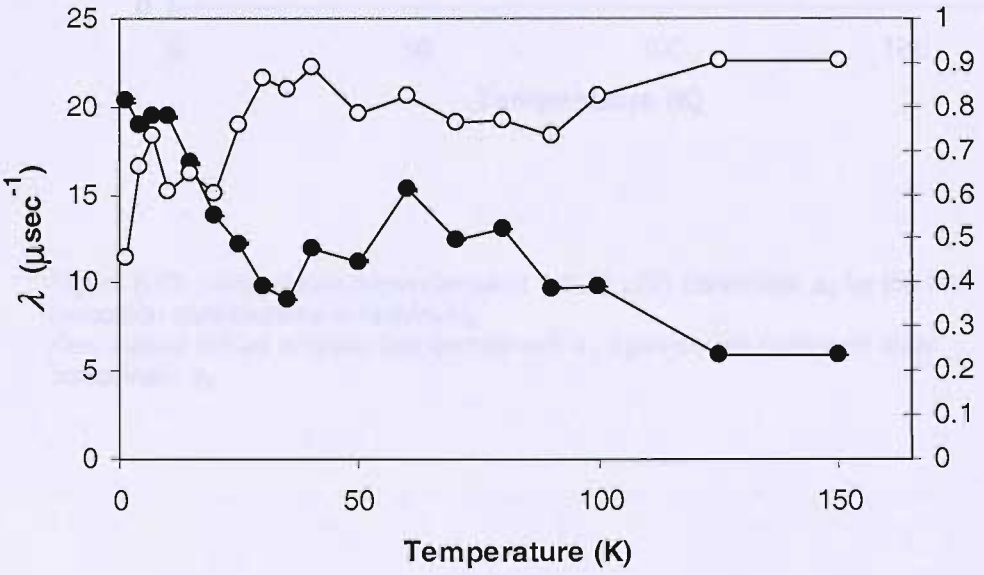

Figure 8.42: temperature dependence of the ZF μSR relaxation rates λ_1 (black circles, left scale) and λ_2 (open circles, right scale) in $DyMn_4Al_8$

For $GdMn_4Al_8$ the fast relaxation parameters a_1 and λ_1 start to rise rapidly below 10K, with a_2 falling off at the same temperature. There are no significant peaks in λ_1; however a small feature at 40K that is barely visible coincides with a similar small peak in a_2 at 40K.

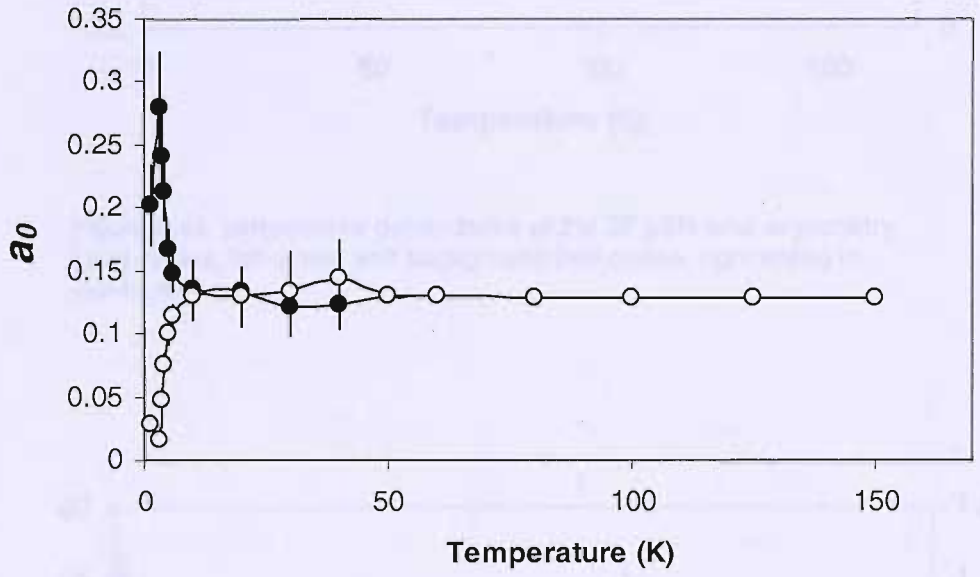

Figure 8.43: temperature dependence of the ZF μSR parameter a_0 for the two relaxation contributions in $GdMn_4Al_8$
Key: closed circles indicate fast component a_1, open circles represent slow component a_2

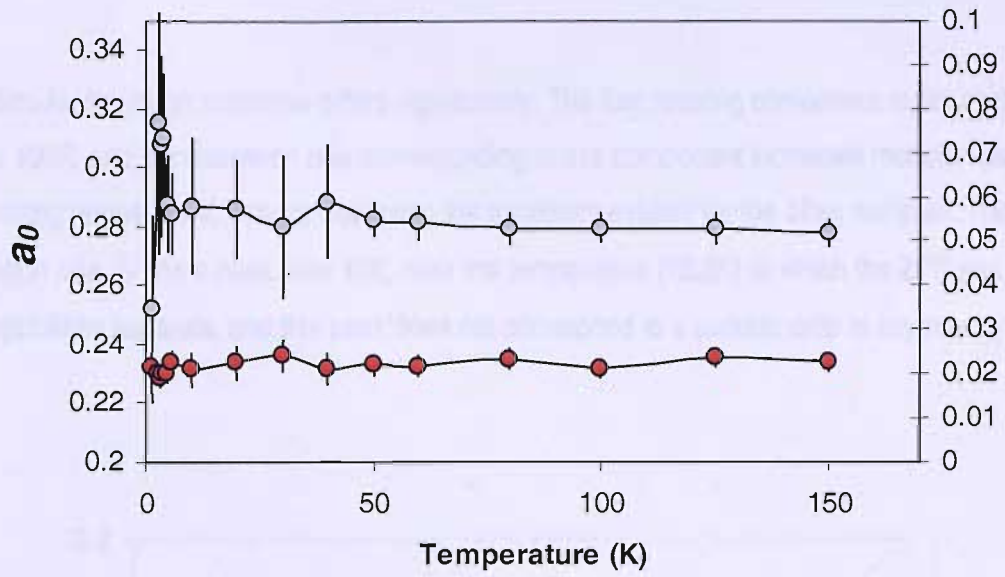

Figure 8.44: temperature dependence of the ZF μSR total asymmetry (grey circles, left scale) and background (red circles, right scale) in $GdMn_4Al_8$

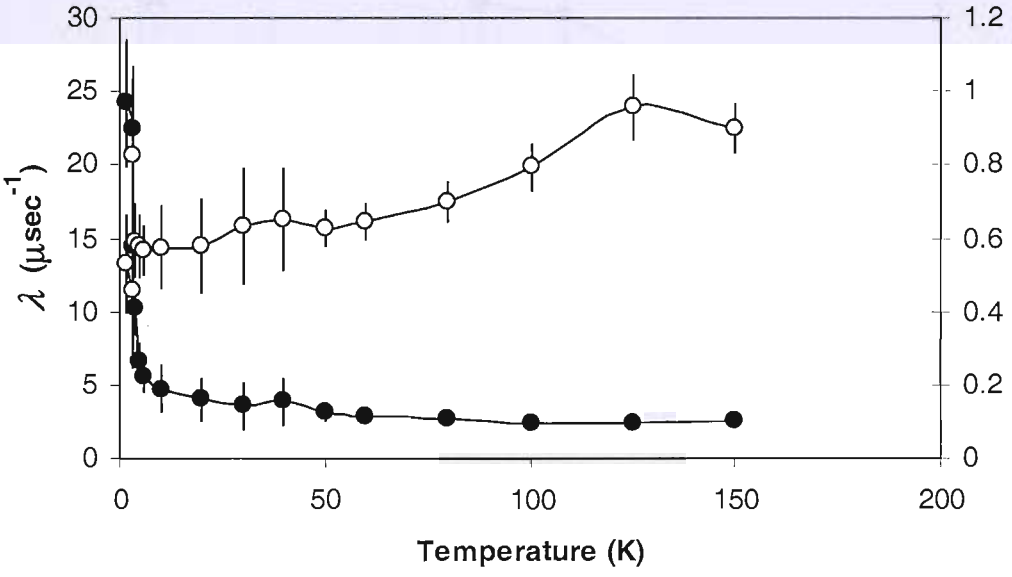

Figure 8.45: temperature dependence of the ZF μSR relaxation rates λ_1 (black circles, left scale) and λ_2 (open circles, right scale) in $GdMn_4Al_8$

In $HoMn_4Al_8$ the muon response differs significantly. The fast relaxing component is not evident above 100K, and the relaxation rate corresponding to this component increases monotonically with decreasing temperature, without displaying the maximum evident for the other samples. The slow relaxation rate λ_2 has a peak near 10K, near the temperature (10.2K) at which the ZFC and FC susceptibilities separate, and this peak does not correspond to a sudden drop in asymmetry a_2.

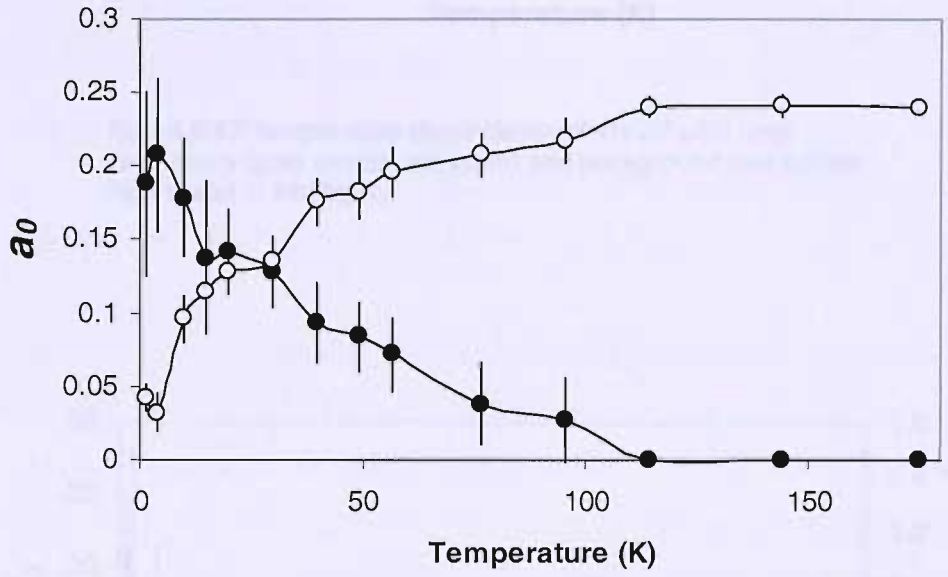

Figure 8.46: temperature dependence of the ZF μSR parameter a_0 for the two relaxation contributions in $HoMn_4Al_8$
Key: closed circles indicate fast component a_1, open circles represent slow component a_2

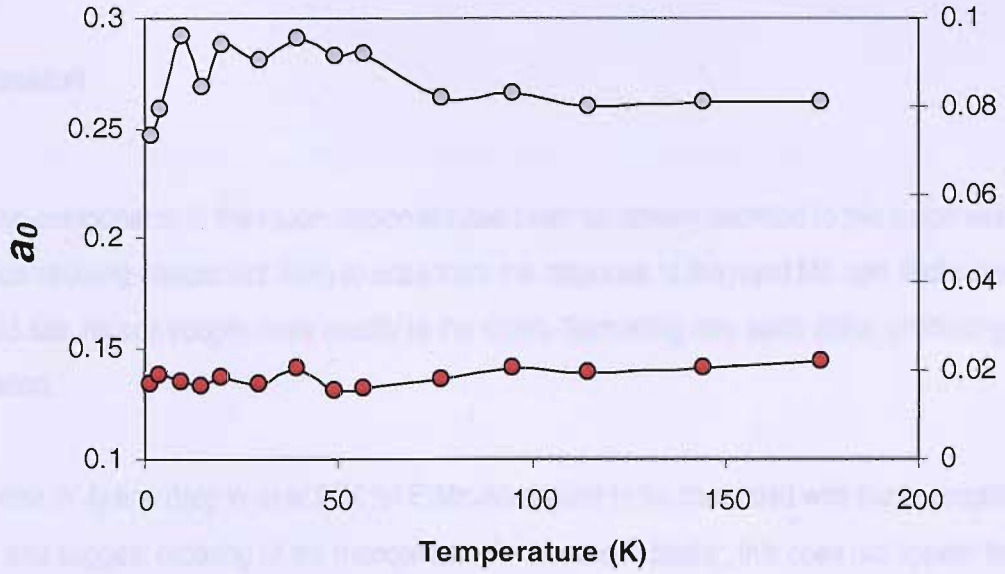

Figure 8.47: temperature dependence of the ZF μSR total asymmetry (grey circles, left scale) and background (red circles, right scale) in $HoMn_4Al_8$

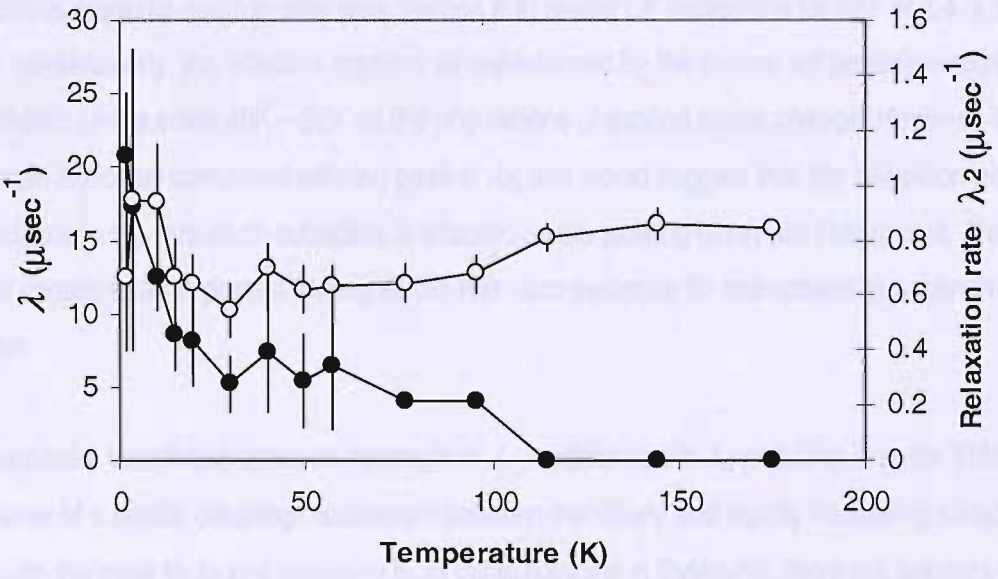

Figure 8.48: temperature dependence of the ZF μSR relaxation rates λ_1 (black circles, left scale) and λ_2 (open circles, right scale) in $HoMn_4Al_8$

Discussion

The two components in the muon response have been tentatively ascribed to two muon sites, with the slow relaxing component likely to arise from the response to the rapid Mn spin fluctuations. At the second site, muons couple more readily to the slowly-fluctuating rare earth spins, producing fast relaxation.

The peak in λ_2 and drop in a_2 at 25K for $ErMn_4Al_8$ appear to be correlated with the susceptibility cusp, and suggest ordering of the manganese. As discussed earlier, this does not appear to be a transition to a long range ordered state, but is more likely to correspond to freezing of short range, spin glass-like order. It is then possible that the low temperature, rapid rise in λ_1 represents a critical slowing of rare earth spin fluctuations. Experimental evidence suggests that the Er sublattice orders magnetically at very low temperatures, indicated by a sharp upturn in the specific heat C/T [25].

The peak in λ_1 at 50K together with the minimum at 20K could have its origins in crystal field transitions. Inelastic neutron data (see Section 8.8) reveal CF excitations for Er^{3+} at 2.4, 4.1 and 6.7 meV: consequently, the effective moment as experienced by the muons will be temperature dependent on the scale 40K – 50K as the populations of excited states change. However, the 20K minimum is closely correlated with the peak in λ_2, and would suggest that the relaxation rate attributable to the rare earth sublattice is affected by the slowing of the Mn fluctuations. This result would constitute an important finding as the first clear evidence for interactions between the Mn and R sites.

The apparent correlation between minimum in λ_1, sudden rise in λ_2 and drop in a_2 for $TbMn_4Al_8$ is indicative of a similar coupling mechanism between the slowly and rapidly fluctuating components. Although the peak in λ_2 and minimum in λ_1 fail to coincide in $DyMn_4Al_8$, there still appears to be some interaction between the two relaxation components with a drop in a_2 occurring at the same temperature as the peak in λ_1. This is also true for $GdMn_4Al_8$. The differences in behaviour between these samples and $HoMn_4Al_8$ are not understood at present.

The experimental work and analysis discussed in this section has been published in:

- B. D. Rainford, C. J. Leavey, A. D. Hillier and J. R. Stewart, Physica B **359-361** (2005) 929 (μSR studies of RMn_4Al_8 with R = La, Y and Pr);
- C. J. Leavey, B. D. Rainford and A. D. Hillier, Physica B **374 – 375** (2006) 106 (μSR studies of RMn_4Al_8 with R = Er, Tb, Dy and Ho)

8.7. Polarized neutron measurements of $LaMn_4Al_8$

A limited amount of diffraction data has been recorded for $LaMn_4Al_8$ using the polarized neutron spectrometer D7 (ILL).

The magnetic response shows weak Bragg peaks below 15K, on top of a diffuse background. This indicates the presence of a small component of 3d antiferromagnetic order. The diffuse background may arise as a result of static correlations reflecting a powder average of 1d order, or an integral over dynamical correlations.

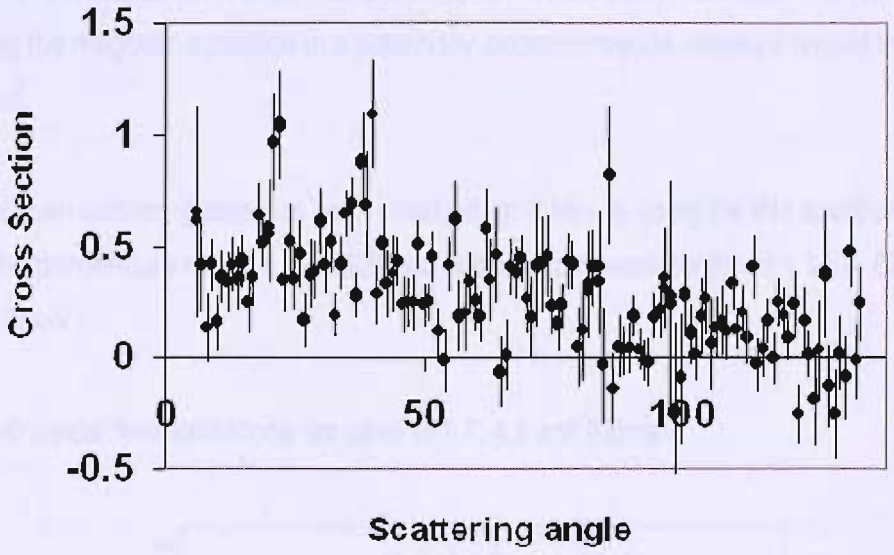

Figure 8.49: weak Bragg peaks in $LaMn_4Al_8$, superimposed on a diffuse signal in polarized neutron data

8.8 Inelastic Neutron Scattering Measurements of RMn_4Al_8 with R = Pr, Er

Crystal Field Analyses of $PrMn_4Al_8$ and $ErMn_4Al_8$

As discussed in Section 5.7, the zero-field μSR data for $PrMn_4Al_8$ shows an oscillatory relaxation component below 35K, corresponding to long-range magnetic order. In the event that this observed muon behaviour is of incommensurate spin density wave origin, a complicated magnetic structure would be anticipated; in $ErCr_4Al_8$, for which a possible incommensurate magnetic structure has been reported [4], local rare earth moments are thought to induce moments on the Cr sublattice. Helical order apparent in $TbCu_4Al_8$ [12] is attributed entirely to the rare earth moments. The importance of establishing the magnetic sublattice in a potentially incommensurate structure should therefore be emphasised.

Inelastic neutron scattering data has been obtained for $PrMn_4Al_8$ using the IN4 spectrometer at the ILL, over the temperature range 1.2 – 150K and with incident wavelengths of 1.1Å (~ 67.5meV) and 2.2Å (~16.9meV).

Three sharp crystal field excitations are seen at 1.7, 4.5 and 8.6meV:

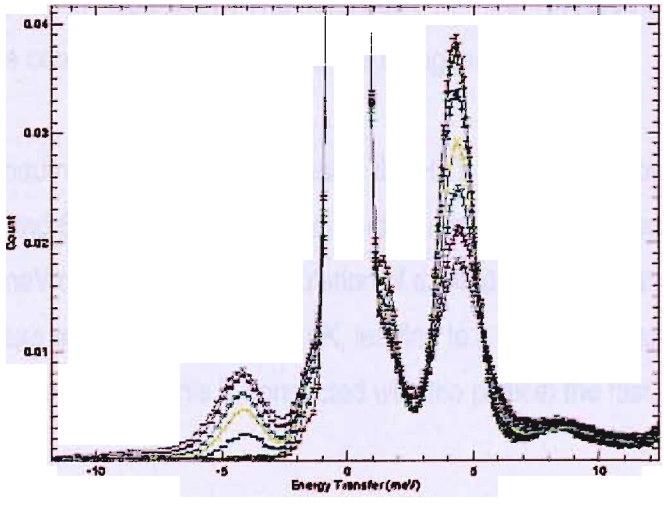

Figure 8.50: crystal field excitations observed in inelastic neutron scattering data for $PrMn_4Al_8$, at 1.7meV, 4.5meV and 8.6meV. A further transition at 6.9meV is not clear in the data. Coloured traces at different amplitudes correspond to data obtained at temperature intervals between 1.2 and 150K.

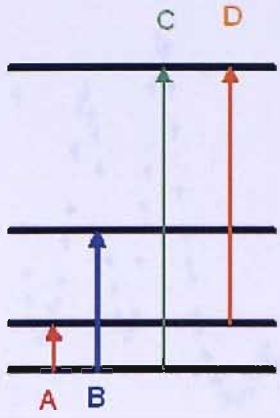

Figure 8.51: CF level diagram representing excitations in $PrMn_4Al_8$ at 1.7meV (A), 4.5meV(B) and 8.6meV (C). Transition (D) at 6.9meV is not clearly observed

For the $J = 4$ Pr^{3+} ion, the tetragonal crystal field splits the electronic states into 7 non-degenerate states, for which allowed transitions may be determined using the selection rule $\Delta m = 0, \pm 1$. The results obtained are consistent with this scheme, with the three transitions from the ground state to the three excited states shown on the above diagram clearly visible. No evidence has emerged of the excited state transition between the second and third levels. There may be a feature in the above spectrum corresponding to the transition between second and fourth levels at 6.9meV, but this is possibly masked by the peaks at 4.5 and 8.6meV.

These measurements indicate that the Pr^{3+} ion has a singlet ground state: further details of crystal field calculations are given in Appendix B. The magnetic behaviour revealed in the μSR measurements may be consequently attributed to the manganese sublattice.

In $ErMn_4Al_8$, inelastic neutron spectra obtained using the HET instrument show well-defined excitations at 2.4, 4.1 and 6.7meV. Overall crystal field splitting in this compound has previously been estimated at 12meV or 140K [25]. The population of excited states may therefore be expected to change on a temperature scale of the order of 50K, leading to a significant variation in the size of the effective moment. It is possible that this is connected with the peak in the fast relaxation rate seen in the muon response.

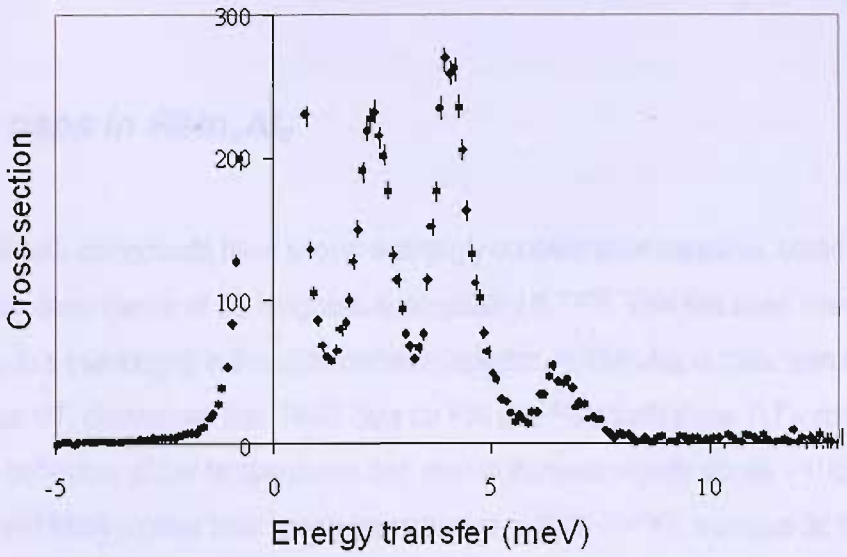

Figure 8.52: Crystal field excitations in $ErMn_4Al_8$ occurring in inelastic neutron scattering data (HET)

Discussion

The Pr^{3+} ion in $PrMn_4Al_8$ was shown by inelastic neutron scattering to have a singlet ground state. This is in contrast to earlier suggestions made on the basis of magnetic entropy analysis [25], that a low-lying doublet state was involved in ordering. These findings are of interest, having considerable relevance to the process of determining the origin of the magnetic state due to Mn. In $PrMn_4Al_8$, the low temperature magnetically ordered state revealed through muon spin rotation measurements has been shown to be entirely associated with the manganese sublattice. It is curious then that this compound could be considered as having a more stable Mn moment than the isostructural $LaMn_4Al_8$, despite its more contracted lattice parameter. Although $LaMn_4Al_8$ was found to have a low temperature phase transition, demonstrated by a critical slowing of spin fluctuations in the region, no oscillations corresponding to a uniform sample field were observed of the type seen in the $PrMn_4Al_8$ spectra.

8.9. Spin gaps in RMn_4Al_8

The $(La_{1-x}Y_x)Mn_4Al_8$ compounds have shown a strongly concentration-sensitive, broad maximum in the temperature dependence of the magnetic susceptibility [6, 7, 37][2]. This has been interpreted as corresponding to a pseudogap in the spin excitation spectra. In YMn_4Al_8, nuclear spin lattice relaxation rates $1/T_1$ determined from NMR data for ^{27}Al and ^{55}Mn both show T_1T = constant, Korringa-type behaviour at low temperatures and start to increase rapidly above ~ 100K [6]. These susceptibility and NMR profiles bear strong resemblance to FeSi [39,40,41], a unique 3d transition metal, correlated-gap compound. A simple model for the effective density of states, similar to that used to describe FeSi, has been used in subsequent data analysis. The assumed model has simple, square bands separated by a narrow, partially filled gap:

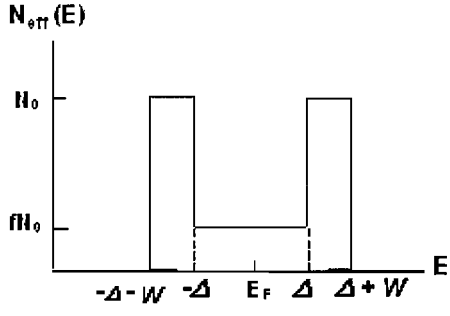

Figure 8.53: Density of states model assumed in interpretation of spin gap features in RMn_4Al_8 [6]

The experimental susceptibility is reproduced as:

$$\chi(T) = -2\mu_B^2 \int N_{eff}(E) \frac{\partial f(E,T)}{\partial E} dE + \frac{C}{T-\theta}$$

[2] Note that the peak temperature value recorded for YMn_4Al_8 is considerably higher than that obtained previously [16]

where the second term represents the low temperature Curie tail and $f(E,T)$ is the Fermi distribution function. The Curie-Weiss parameters, bandwidth W, gap width Δ (roughly corresponding to the temperature of the susceptibility maximum), filled gap fraction f and maximal density of states N_0 are the fitting parameters used in a least-squares refinement of the experimental data. The experimental susceptibility data (along with NMR data for YMn_4Al_8) has been well reproduced within this model, with the relation $W \sim 2\Delta$ and $f \sim 25\%$ holds for all samples. This suggests a common mechanism for gap formation in these systems, with the gap width controlled continuously by chemical pressure effects [7].

The concentration dependence of the tetragonal lattice parameters on the yttrium concentration in these systems shows higher sensitivity in c than in a; the fact that this anisotropic shrinkage leads to a nearly uniform expansion of effective bands suggests that the DOS near the Fermi energy is dominated by an anisotropic interaction, such as the Mn-Mn intrachain interaction [7]. To confirm the sensitivity of gap width to volume effects, measurements have been extended to compounds with R = Lu and Sc, both of which have smaller lattice volumes than the $(La_{1-x}Y_x)Mn_4Al_8$ [42]. The DOS model was also found to apply to these systems in fits to susceptibility data, while further anisotropies are reported for all compounds in thermal expansions measurements, with expansion along the c axis 2-4 times greater than that along the a axis. The c-axis expansion coefficient is correlated with gap width Δ, reflecting near-saturation of longitudinal spin fluctuations (characteristic of itinerant systems) for $LaMn_4Al_8$ around room temperature.

	$d_{Mn\text{-}Mn}$(Å)	Δ (K)
$LaMn_4Al_8$	2.583	250
YMn_4Al_8	2.552	500
$LuMn_4Al_8$	2.542	610
$ScMn_4Al_8$	2.523	700

Table 8.11: intrachain Mn-Mn distances and pseudogap widths in RMn_4Al_8 [7, 42]

The strong correlation between Δ and intrachain Mn-Mn distance $d_{Mn\text{-}Mn}$ is explored further: for classical 3d bands a volume effect equal to d^{-5} is expected, where d is the $3d$ interatomic distance [43]. Fits of the data to the relation $\Delta \propto (d_{Mn\text{-}Mn})^{-\Gamma}$ has given $\Gamma = -\ln\Delta/\ln(d_{Mn\text{-}Mn}) = 48 \pm 3$ [42], which suggests that the electronic structure around E_F is not dominated by classical interactions.

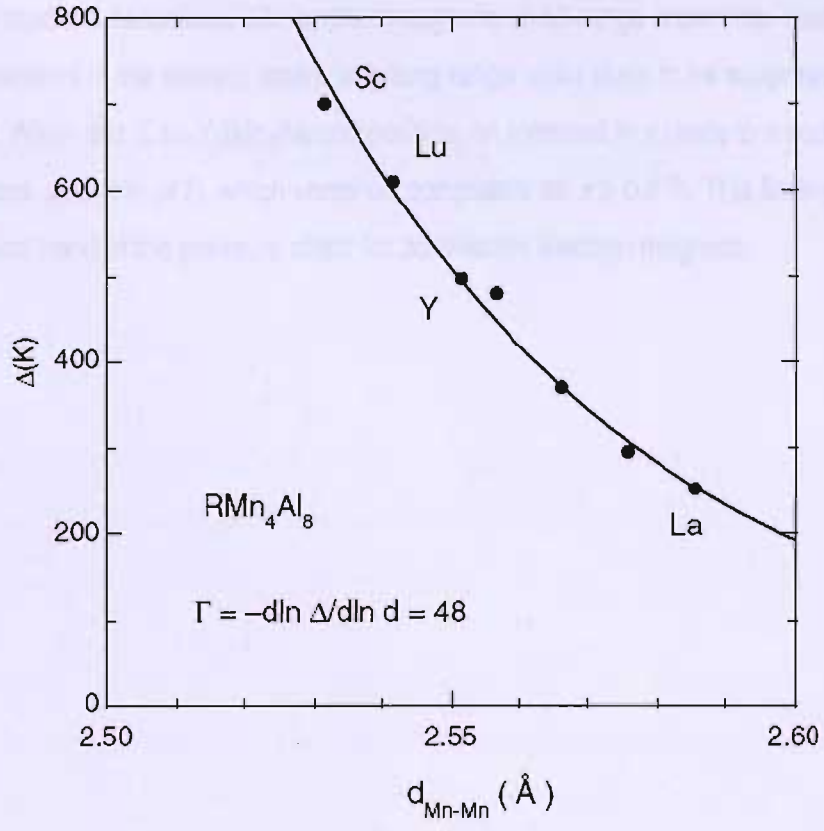

Figure 8.54: width of pseudogap Δ in the RMn_4Al_8 compounds, plotted as a function of intrachain Mn-Mn distance $d_{Mn\text{-}Mn}$ [7, 42]

The strong dependence of pseudogap width on the intrachain Mn separation supports the conjecture of gap formation as a consequence of the linear chain arrangement of manganese atoms. Small intrachain interatomic distances, compared to the interchain separations, across the RMn_4Al_8 series indicate a quasi-1D nature of the magnetic interaction as inferred for $LaMn_4Al_8$ [5]. There is then a possibility of a Spin-Peierls type instability occurring as expected generally for a 1D Heisenberg antiferromagnet.

It does in fact appear from these studies that $LaMn_4Al_8$ exhibits a degree of localized character, with number of anomalies occurring in the data below 50K. A resistivity minimum is observed at 45K [37], above which $\rho(T)$ increases monotonically with temperature and saturates at higher temperatures. This behaviour is one again in common with the strongly correlated Mn compounds $Y(Sc)Mn_2$ [44] and β-Mn [45] in which longitudinal spin fluctuations are expected to be thermally induced and eventually saturate. Magnetoresistance in this compound shows a rapid increase with decreasing temperature, while negative thermal expansion occurs below 40K, indicating growth of local spin with decreasing temperature [37]. While no direct observations of a magnetic phase transition exist in these measurements, the indication is of recovery of spin and development of magnetic correlation in the low temperature range. The peak in the magnetic susceptibility at 5K [37, 5] may then correspond to a

slowing of fluctuations associated with antiferromagnetic short-range order (this idea is supported by μSR measurements in the present work), with long range order likely to be suppressed by the 1D arrangement. Within the $(La_{1-x}Y_x)Mn_4Al_8$ compounds, an increase in x leads to a suppression of the low-temperature upturn in $\rho(T)$, which vanishes completely for $x \geq 0.2$ [7]. This finding is consistent with the general trend of the pressure effect for 3d itinerant electron magnets.

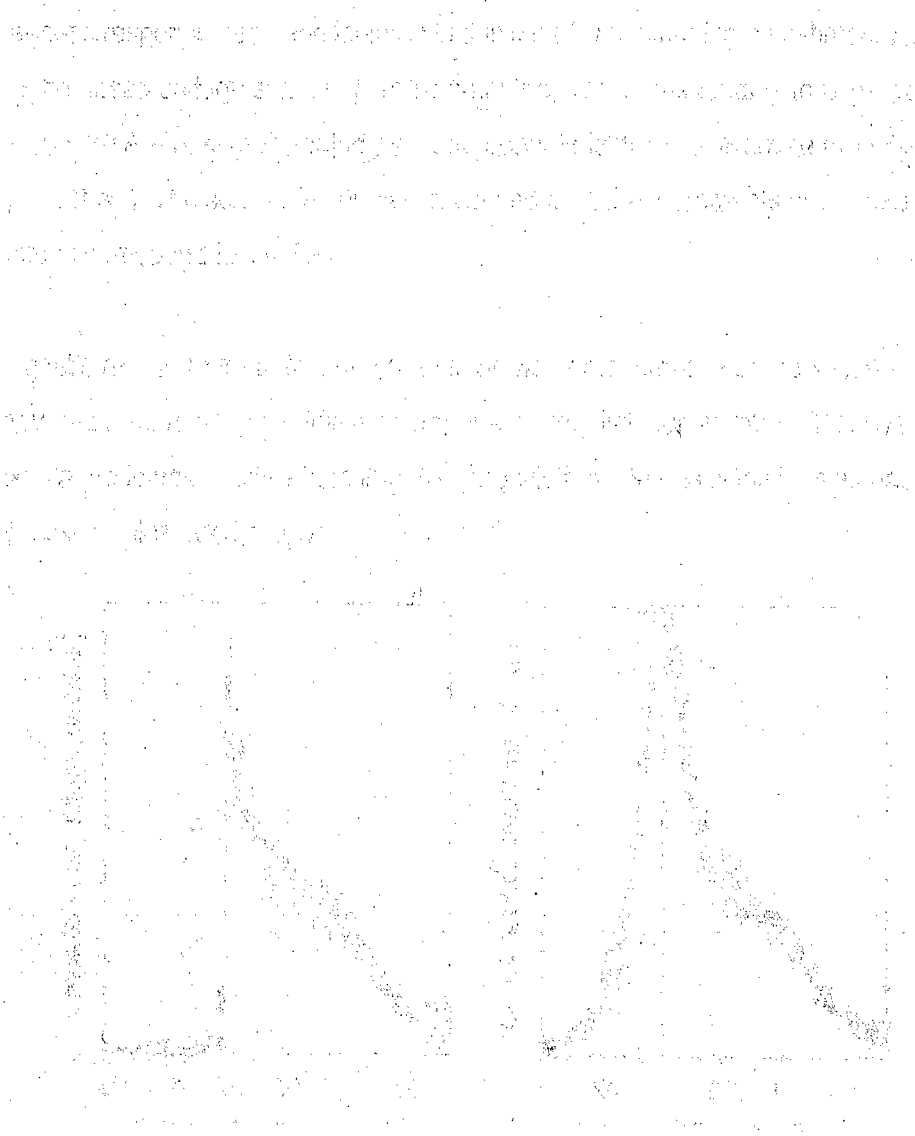

8.10. Inelastic Neutron Scattering Measurements of RMn_4Al_8

Spin dynamics in $LaMn_4Al_8$

Inelastic neutron spectra have been obtained for $LaMn_4Al_8$ using the HET spectrometer at the ISIS facility, over the temperature range 2 – 300K and with incident neutron energies of 20, 80 and 150meV. The data were normalized to absolute cross-section using a standard vanadium sample

The magnetic response has been isolated in this case by subtracting an estimated phonon contribution based on high scattering angle data: the data corresponding to large wavevector transfer ($q > 10$ Å^{-1}) has been scaled by an appropriate factor and removed from the low-q data (0.3 Å^{-1} > q > 3.2 Å^{-1}). The scaling factor was estimated from measurements performed on the isostructural compound $LaCu_4Al_8$.

The magnetic response for $LaMn_4Al_8$ consists of two components, a broad inelastic feature centred at 30meV and a narrower, quasielastic component. Very little temperature dependence of the inelastic feature is noted, while both intensity and width of the quasielastic response vary with temperature, as illustrated below:

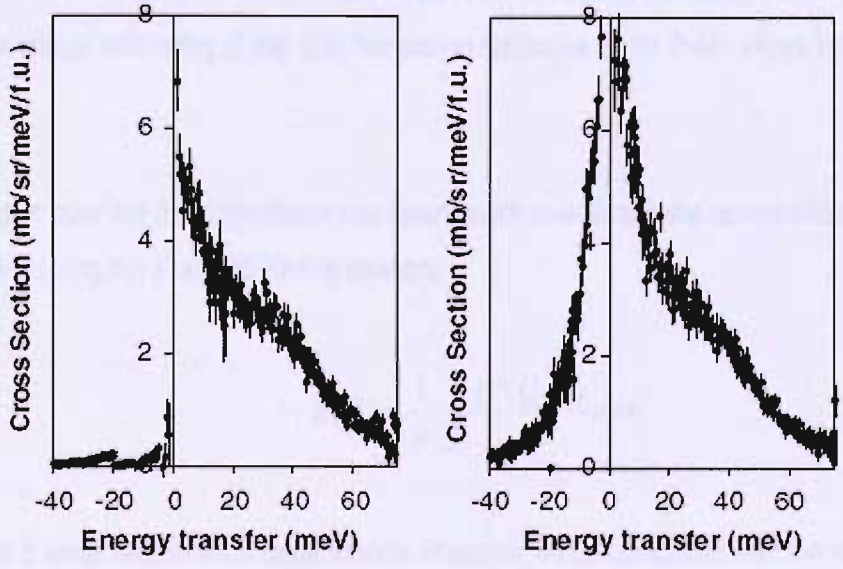

Figure 8.55: inelastic neutron scattering data for $LaMn_4Al_8$ at 7K (left) and 225K (right), consisting of a broad 30meV response and a narrow QE feature. The temperature dependence of the latter is clearly visible

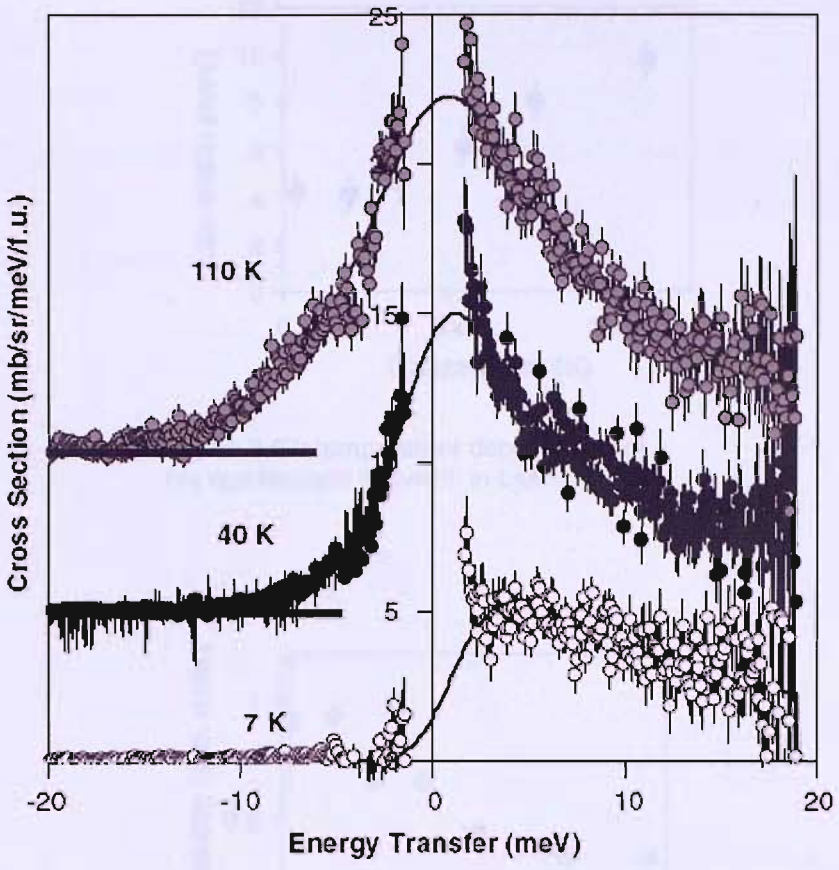

Figure 8.56: temperature evolution of the quasielastic neutron feature in $LaMn_4Al_8$. Solid lines show fits to Lorentzian lineshape functions

The quasielastic feature fits well to a Lorentzian lineshape multiplied by the detailed balance factor. The Lorentzian linewidth (half-width at half maximum) decreases smoothly with temperature, and suggests a critical narrowing of the spin fluctuation response as for β-Mn alloys in the spin glass state.

An integration over the fitted lineshape has been used[3] to estimate the contribution to static susceptibility using the Kramers-Kronig relation:

$$\chi(Q) = \frac{1}{\pi}\int_{-\infty}^{\infty}\frac{\chi''(Q,\omega)}{\omega}d\omega$$

This shows a weak temperature dependence. However, to be compared with the measured bulk susceptibility (Section 5.6) this would need to additionally incorporate the data at higher energies.

[3] Analysis carried out by B. D. Rainford

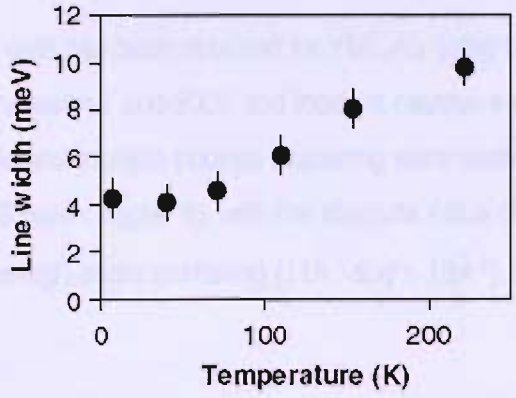

Figure 8.57: temperature dependence of the quasielastic linewidth in $LaMn_4Al_8$

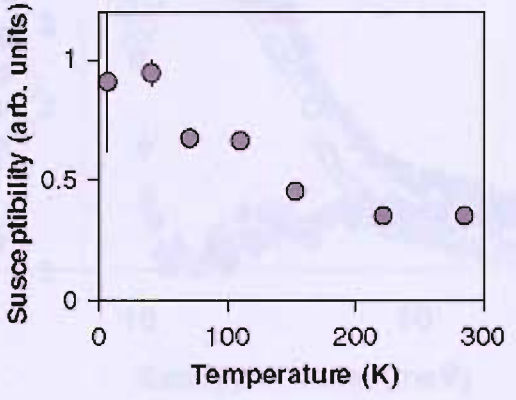

Figure 8.58: temperature dependence of the static susceptibility extracted from QE neutron data in $LaMn_4Al_8$

There appears to be very little dependence in this magnetic response on wavevector transfer: in fact the data presented are the result of summation over a broad range of ***q***.

Spin gap features in RMn_4Al_8 with R = Y, Ce and Sc

In YMn_4Al_8 a weak but significant magnetic response has been found, in contrast to previous studies that have not only concluded this compound to be nonmagnetic, but which have used data from YMn_4Al_8 as a phonon blank sample [25]. This magnetic scattering is observed despite the small susceptibility (compared to $LaMn_4Al_8$, Section 5.6) and absence of low frequency spin fluctuations (Section 5.7).

Inelastic neutron scattering data has been obtained for YMn_4Al_8 using the HET spectrometer (ISIS), with sample temperatures between 7 and 300K and incident neutron energies between 20 and 150meV. Estimates of single and multiple phonon scattering were made using the Monte Carlo simulation program DISCUS (see Chapter 6), with the absolute value of total phonon scattering determined by scaling of the high-angle scattering ($11Å^{-1} \leq q \leq 16Å^{-1}$).

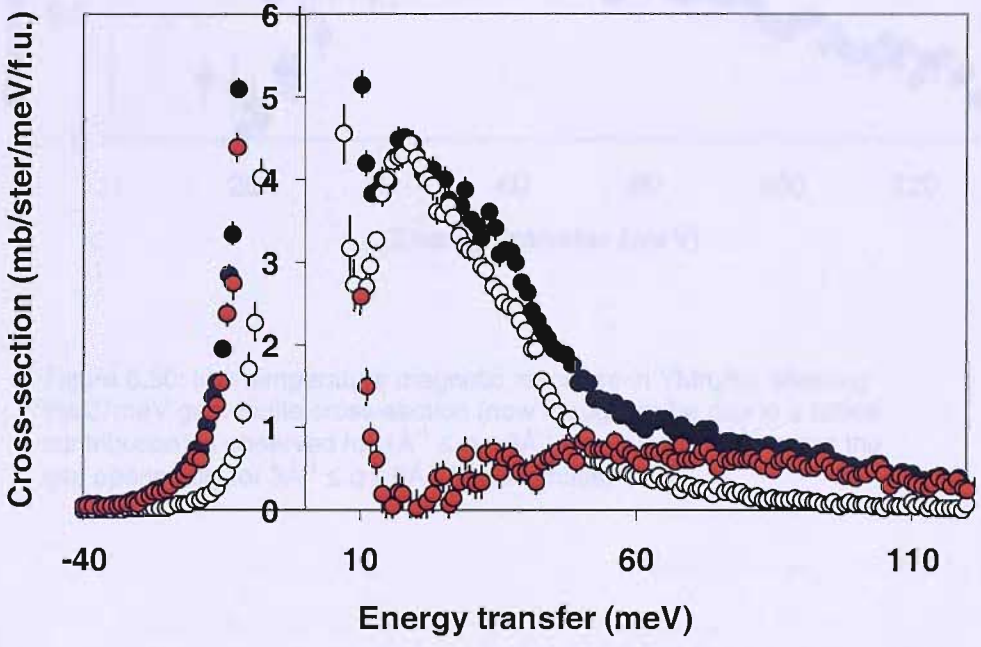

Figure 8.59: low-temperature inelastic neutron data measured in YMn_4Al_8. Black circles correspond to total cross-section, open circles represent phonon scattering, and red circles represent magnetic (total – phonon) scattering

Clear evidence of a gap exists in the magnetic response, below approximately 27meV. A strong q-dependence is immediately obvious, with the gap opening fully only above $q = 3Å^{-1}$. For scattering corresponding to smaller wavevectors, while a maximum is clearly visible at 50meV, there is a finite cross-section below 25meV. While this was originally anticipated as being associated with the magnetic response, a very recent supplementary study has shown that a significant phonon response over this low-wavevector range is responsible for filling the gap (see Chapter 9).

The 50meV maximum is no longer visible above 100K, where it is masked by an increasing quasielastic contribution. The value of 27meV obtained for the magnitude of the gap in this compound is around half of that obtained from NMR and susceptibility measurements [6].

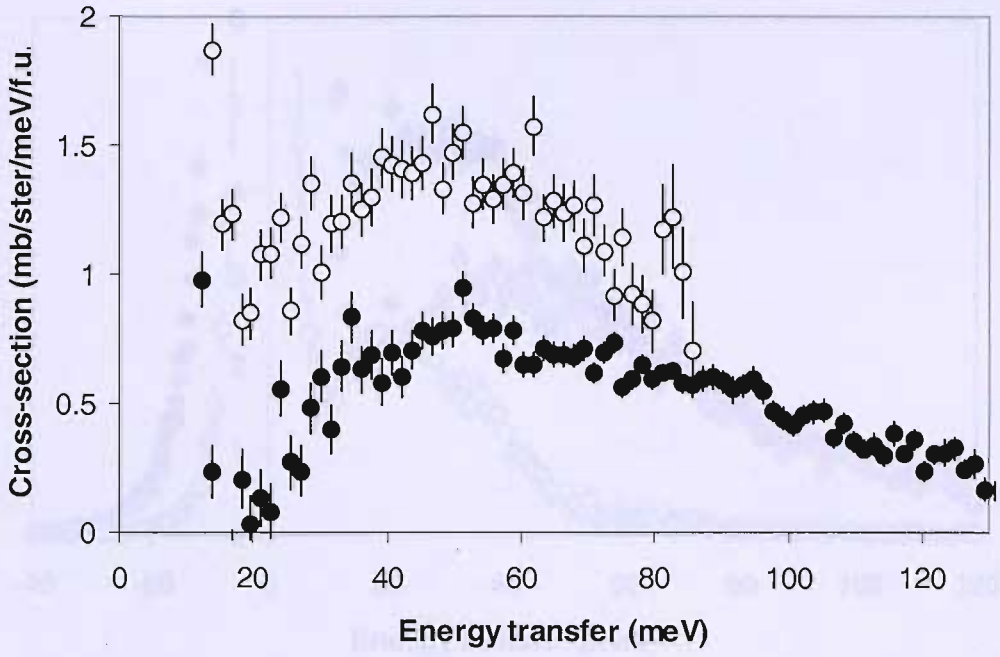

Figure 8.60: low-temperature magnetic response in YMn_4Al_8, showing the 27meV gap. Finite cross-section (now thought to be due to a lattice contribution) is observed for $1Å^{-1} \leq q \leq 3Å^{-1}$ (open circles), whereas the gap opens fully for $3Å^{-1} \leq q \leq 6Å^{-1}$ (black circles)

Inelastic spectra have similarly been obtained for $CeMn_4Al_8$: in this case a complete spin gap is not observed in the wavevector range $1Å^{-1} \leq \boldsymbol{q} \leq 6Å^{-1}$, while a well-defined maximum as occurs in YMn_4Al_8 is seen at 40meV.

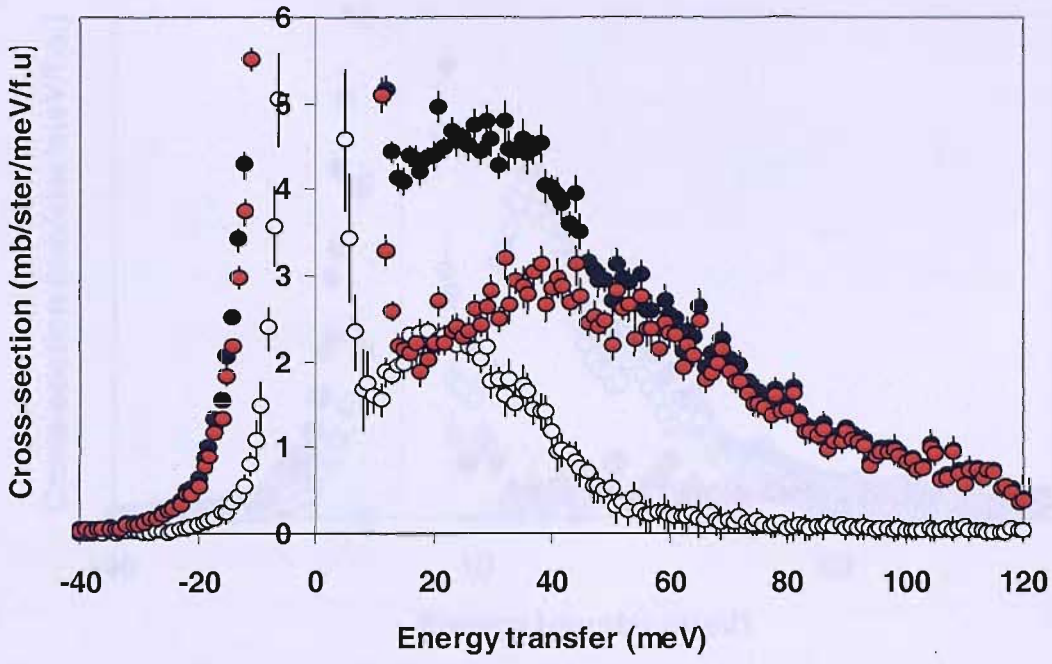

Figure 8.61: low-temperature inelastic neutron data measured in $CeMn_4Al_8$ for wavevector transfers $1Å^{-1} \leq q \leq 6Å^{-1}$. The key is as for YMn_4Al_8

Since the cerium in $CeMn_4Al_8$ has been shown to be in an intermediate valent state [23], it is possible that an underlying broad, flat response from the cerium that is difficult to separate from the Mn spin fluctuation response is masking the gap. Hybridization between the Ce 4f and Mn 3d electrons should also be considered as a possible mechanism for destroying the gap.

A weak magnetic response has also been observed in $ScMn_4Al_8$:

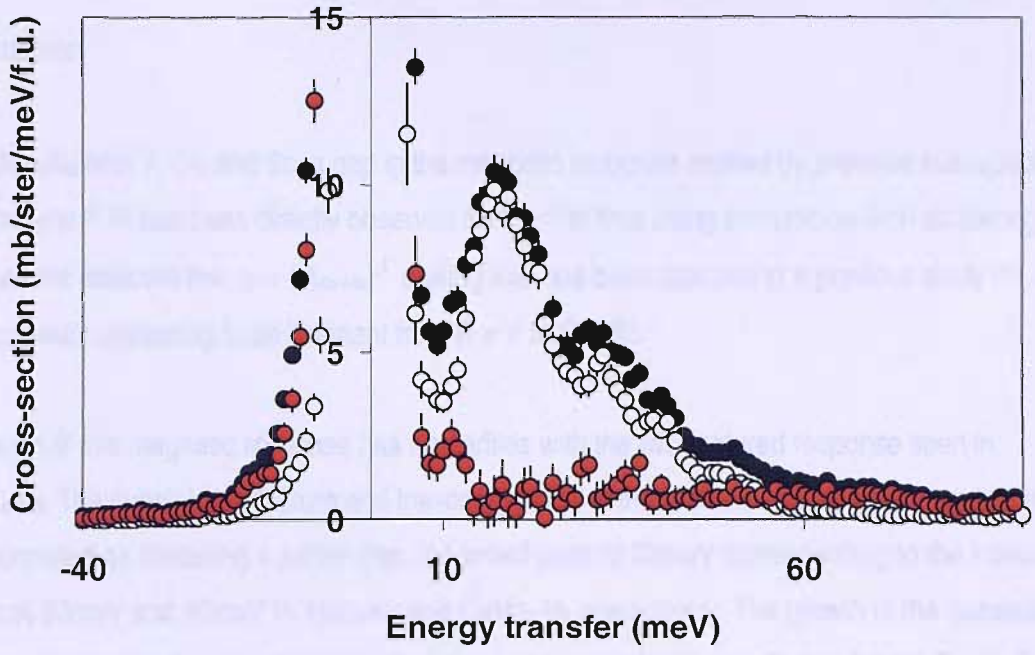

Figure 8.62: low-temperature inelastic neutron data measured in $ScMn_4Al_8$ for wavevector transfers $1Å^{-1} \leq q \leq 6Å^{-1}$. The key is as previously

This compound exhibits a fully open gap in the magnetic response as for YMn_4Al_8. According to previous studies [42] a scaling of gap width with $d_{Mn\text{-}Mn}$ should be expected. However, the responses for YMn_4Al_8 and $ScMn_4Al_8$ are almost identical:

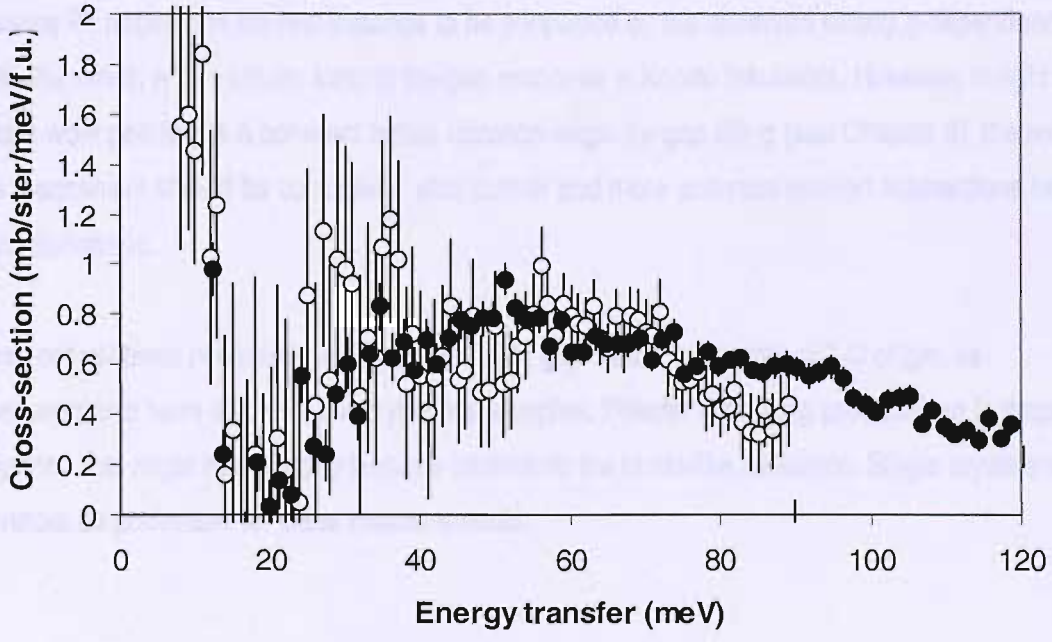

Figure 8.63: comparison of high-q magnetic data in YMn_4Al_8 (black circles) and $ScMn_4Al_8$ (open circles)

Discussion

For RMn_4Al_8 with Y, Ce and Sc, a gap in the magnetic response implied by previous susceptibility experiments [6, 22] has been directly observed for the first time using inelastic neutron scattering. This gap has not reflected the $\Delta \propto (d_{Mn\text{-}Mn})^{-\Gamma}$ scaling that has been reported in a previous study [42], with the gap width appearing to be invariant from R = Y to R = Sc.

This form of this magnetic response has similarities with the two-featured response seen in $LaMn_4Al_8$. The quasielastic feature and low-energy side of the broad magnetic peak may in this case be interpreted as bordering a partial gap, the broad peak at 30meV corresponding to the inelastic peaks at 50meV and 40meV in YMn_4Al_8 and $CeMn_4Al_8$ respectively. The growth of the quasielastic feature with temperature is reflected in the increasing quasielastic contribution for the R = Y, Sc compounds, which obscures the gap at high temperatures.

The origin of the gap remains a subject for debate. Hybridization interactions are certainly of importance in $CeMn_4Al_8$, resulting in an intermediate valent Ce ion and renormalization of states within the spin gap. The sample consequently fails to show a fully open spin gap for any range of wavevector transfer. It is worth noting that the concept of Kondo hybridization as applied to 4*f* systems [20] is supported by the observed strong $\boldsymbol{q}$-dependence in YMn_4Al_8, which is of a similar form to the gap response in Kondo insulators. The concept of Kondo hybridization as applied to 4*f* systems [20] appears in the first instance to be supported by the observed strong $\boldsymbol{q}$-dependence in YMn_4Al_8, which is of a similar form to the gap response in Kondo insulators. However, in light of recent work pointing to a coherent lattice vibration origin for gap-filling (see Chapter 9), the nature of this mechanism should be considered after further and more accurate phonon subtractions have been performed.

It has not yet been possible to assess these spin gap features in terms of 1-D origin, as measurements have involved polycrystalline samples. Powder averaging produces an isotropic response that might remove any features intrinsic to the chain-like sublattice. Single crystals would therefore be preferable for these measurements.

The results discussed in this section have been published in:

- C. J. Leavey, B. D. Rainford, J. R. Stewart and D. T. Adroja, Physica B **378-380** (2006) 675
- C. J. Leavey, B. D. Rainford, J. R. Stewart and D. T. Adroja, J. Magn. Magn. Mater. **310** (2007) 1041

References

[1] J. V. Florio, R. E. Rundle and A. I Snow, Acta. Cryst. **5** (1952) 449

[2] K. H. J. Buschow and A. M. van der Kraan, J. Phys. F: Metal Phys. **8** (1978) 921

[3] P. Schobinger-Papamantellos, P. Fischer, C. H. de Groot, F. R. de Boer and K. H. J. Buschow, J. Alloys Comp. **232** (1996) 154

[4] G. Baio, O. Moze, G. Amoretti, R. Sonntag, N. Stüβer and K. H. J. Buschow, Z. Phys. B **102** (1997) 449

[5] T. Yamasaki, K. Matsui, H. Nakamura and M. Shiga, Solid State Comm. **119** (2001) 415

[6] H. Nakamura, S. Giri and T. Kohara, J. Phys. Soc. Japan **73** (2004) 2971

[7] H. Nakamura, Y. Muro, S. Giri, J. Umemura, H. Kobayashi, T. Koyama and T. Kohara, J. Phys. Soc. Japan **74** (2005) 2421

[8] Y. Muro, H. Nakamura and T. Kohara, J. Phys. Cond. Matt. **18** (2006) 3931

[9] H.-S. Li and J. M. D. Coey, in: *Handbook of Magnetic Materials*, Vol. 6, Elsevier, Amsterdam (1994) Ed. K. H. J. Buschow, p.1

[10] I. Felner and I. Nowik, J. Phys. Chem. Sol. **40** (1979) 1035

[11] K. H. J. Buschow, J. H. N. van Vucht and W. W. van den Hoogenhof, J. Less Comm. Met. **50** (1976) 145

[12] J. Deportes, D. Givord, B. Kebe, J. Phys. **C5** (1979) 154

[13] A. M. van der Kraan and K. H. J. Buschow, Physica **86** (1977) 93

[14] H. Wada, H. Nakamura, K. Yoshimura, M. Shiga and Y. Nakamura, J. Mag. Mag. Mater. **70** (1987) 134

[15] J. Deportes, D. Givord, R. Lemaire, H. Nagai, Physica **86** (1977) 69

[16] M. Coldea, R. Coldea and G. Borodi, IEEE Transactions on Magnetics **30** (1994) 855

[17] O. Moze, R. M. Ibberson, R. Caciuffo and K. H. J. Buschow, J. Less Comm. Met. **166** (1990) 329

[18] I. Felner, J. Less Comm. Met. **72** (1980) 241

[19] I. Felner and I. Nowik, J. Magn. Magn. Mater **54-57** (1986) 163

[20] T. Moriya, J. Magn. Magn. Mater. **14** (1979) 1

[21] R. Coldea, M. Coldea and I. Pop, IEEE Trans. Magn. **30** (1994) 852

[22] M. Coldea , M. Neumann, S. Lütkehoff, S. Mähl and R. Coldea, J. Alloys Comp. **278** (1998) 72

[23] J. M. Lawrence, P. S. Riseborough, R. D. Parks, Rep. Prog. Phys. 44 (1981) 1

[24] R. Nirmala, V. Sankaranarayanan, K. Sethupathi, T. Geethakumary, M. C. Valsakumar, Y. Hariharan and A. V. Morozkin, Physica B 329 – 333 (2003) 673

[25] I. H. Hagmusa, J. C. P. Klaasse, E. Brück, F. R. de Boer, K. H. J. Buschow, J. Alloys Comp. **297** (2000) 21

[26] I. H. Hagmusa, F. E. Kayzel, E. Brück, K. H. J. Buschow, J. Appl. Phys. **83** (1998) 7136

[27] I. H. Hagmusa, E. Brück, K. H. J. Buschow, J. Alloys Comp. **278** (1998) 80

[28] T. Shinkoda, K. Kumagai, K. Asayama, J. Phys. Soc. Jpn. **46** (1979) 1754

[29] H. Wada, M. Shiga, Y. Nakamura, Physica B **161** (1989) 197

[30] M. Katayama, S. Akimoto, K. Asayama, J. Phys. Soc. Japan **42** (1977) 97

[31] Y. Kohori, Y. Noguchi, T. Kohara, J. Phys. Soc. Japan **62** (1993) 447

[32] K. Yoshimura, H. Nakamura, M. Takigawa, H. Yasuoka, M. Shiga, Y. Nakamura, J. Magn. Magn. Mater. **70** (1987) 142

[33] H. Nakamura, Y. Kitaoka, K. Yoshimura, Y. Kohori, K. Asayama, M. Shiga, Y. Nakamura, J. Physique **49** (1988) C8 – 257

[34] A. Solontsov, A. Vasil'ev, H. Nakamura, M. Shiga, Physica B **259 –261** (1999) 922

[35] J. G. Bonner and M. E. Fisher, Phys. Rev. **135A** (1964) 640

[36] K. Ueda and T. Moriya, J. Phys. Soc. Japan **38** (1975) 32

[37] Y. Muro, S. Giri, G. Motoyama, H. Nakamura and T. Kohara, J. Phys. Soc. Japan **74** (2005) 1135

[38] L. P. Le, A. Keren, G. M. Luke, B. J. Sternlieb, W. D. Wu, Y. J. Uemura, J. H. Brewer, T. M. Riseman, R. V. Upasani, L. Y. Chiang, W. Kang, P. M. Chaikin, T. Csiba and G. Grüner, Phys. Rev. B **48** (1993) 7284

[39] V. Jaccarino, G. K. Wertheim, J. H. Wernick, L. R. Walker and S. Arajs, Phys. Rev. **160** (1976) 476

[40] S. Takagi, H. Yasuoka, S. Ogawa and J. H. Wernick, J. Phys. Soc. Japan **50** (1981) 2539

[41] M. Corti, S. Aldrovandi, M. Fanciulli and F. Tabak, Phys. Rev. B **67** (2003) 172408

[42] Y. Muro, H. Nakamura and T. Kohara, J. Phys. Cond. Matt. **18** (2006) 3931

[43] V. Heine, Phys. Rev. **153** (1967) 673

[44] M. Shiga, K. Fujisawa and H. Wada, J. Phys. Soc. Japan **62** (1993) 1329

[45] H. Nakamura, K. Yoshimoto, M. Shiga, M. Nishi and K. Kakurai, J. Phys. Cond. Matt. **9** (1997) 4701

9. Conclusions

Studies of β-$Mn_{1-x}M_x$ Systems

In summary, studies of β-$Mn_{1-x}M_x$ alloys with M = Co and Ru have been shown to enter a static magnetic ground state at finite temperature, for all concentrations investigated. This is primarily evidenced by muon spin relaxation and polarised neutron data: in the β-$Mn_{1-x}Co_x$ alloys, stretched exponential relaxation is observed for $0.05 \leq x \leq 0.25$, in which the relaxation rate λ^{β} diverges at a concentration-dependent temperature. A gradual decrease in initial asymmetry with decreasing temperature does not however support a well-defined, critical transition. A stretched exponential form for longitudinal field relation is typical of a spin glass phase, characterised by a distribution of relaxation times. This scenario is supported by the diffuse scattering measured with polarised neutrons, indicating a degree of magnetic disorder.

Magnetometry data for both alloy systems appear to provide further indication of entry to a spin glass state at low temperatures on first inspection, with a bifurcation of field- and zero field-cooled susceptibilities. However, in most of the samples studied it is likely that the low temperature response is masked by those of oxide impurities. Above this region, the susceptibilities display a very slight increase with increasing temperature, and do not reflect any change to a Curie-Weiss regime corresponding to moment localisation as seen in β-$Mn_{1-x}Al_x$ [1]. This form of the zero-field cooled dc susceptibility confirms the nature of the response reported in a previous study [2]. It is noted that this study highlights the limitations of $\chi(0)$ measurements where strong antiferromagnetic correlations persist up to high temperatures.

These results constitute an important finding, as μSR evidence of spin glass order had previously only been observed for systems in which the impurity substitutes onto Site II [3]. Cobalt and ruthenium impurities have both been confirmed to preferentially occupy lattice Site I in this study, in agreement with previous studies [e.g. 2]. The solute atoms do not therefore introduce local disorder to the magnetic Site II sublattice that might be responsible for lifting the configurational degeneracy associated with this site. This is highlighted by the values for atomic positional parameter *y* derived from Rietveld analysis, with an average value of 0.2025 for the three β-$Mn_{1-x}Co_x$ concentrations studied, and an average of 0.2033 for β-$Mn_{1-x}Ru_x$.These are close, especially in the case of the

ruthenium alloys, to the critical value of 0.2035 established [4] as the requirement for a perfect equilateral triangular magnetic sublattice.

In β-$Mn_{1-x}Ru_x$, examined for the first time using muon spin relaxation techniques, further evidence has emerged for the long-range antiferromagnetic order originally observed in susceptibility, diffraction and specific heat studies [2]. This emerges as a secondary peak in the relaxation rate λ^{β}, occurring for $x \geq 0.12$ at temperatures higher than those of the corresponding spin glass transitions. Discontinuities are observed in the ZFC susceptibilities in the vicinity of T_N as deduced from μSR data. Two possible scenarios are that of a re-entrant spin glass, whereby antiferromagnetic order in these high-concentration samples gives way to a spin glass state at a lower temperature, or a co-existent spin glass phase that emerges within the long-range ordered state. Re-entrant phases occur where systems undergo a freezing of the transverse components of the magnetic moments, leading to finite correlation lengths and the breakdown of long-range order. It would however be reasonable to assume in the case of the β-$Mn_{(1-x)}Ru_x$ that the spin glass and antiferromagnetically ordered states are co-existent, as there appears to be no loss of AF order parameter as the system goes through the spin glass temperature, as established by polarized neutron spectra.

These experimental investigations have enabled the following magnetic phase diagram to be produced for the β-$Mn_{1-x}Ru_x$ alloy series:

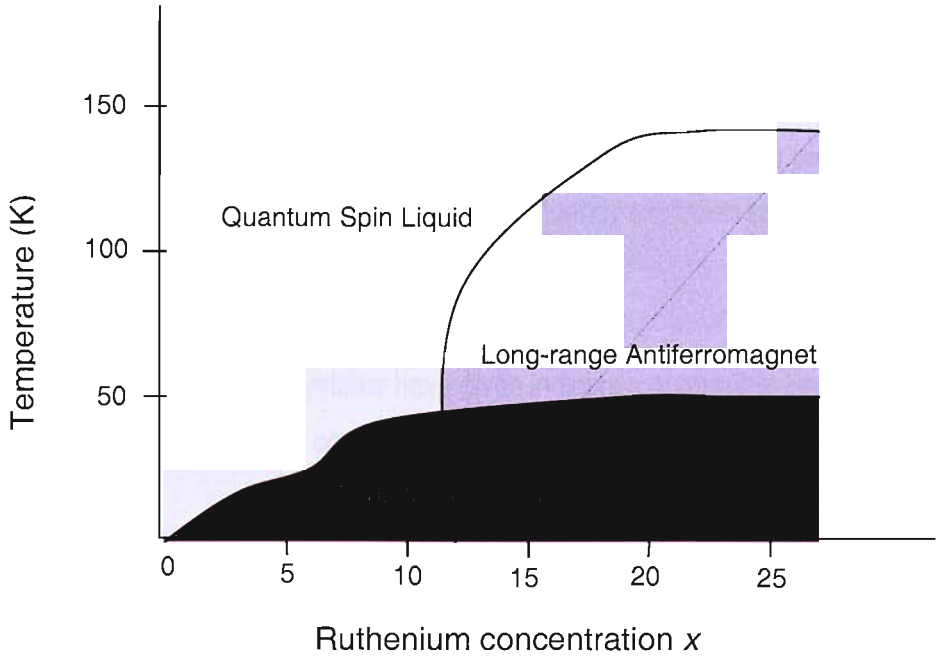

Figure 9.1: magnetic phase diagram for the β-$Mn_{1-x}Ru_x$ alloy series, showing magnetic phase as a function of temperature and nominal impurity concentration

Further measurements also indicate long-range order in the ruthenium alloys: magnetic Bragg peaks occur in low temperature neutron powder diffraction spectra, which are found to be incommensurate with the crystal cell. Using diffraction data recorded as part of these studies, it has been possible to determine the magnetic structure in β-$Mn_{1-x}Ru_x$, which takes the form of a complex helical configuration. This structure is consistent with the expected magnetic model for β-Mn systems, in which significant moments are associated entirely with the Site II sublattice, although it has not been possible to rule out entirely some possible magnetic contribution from Site I.

Specific heat data obtained for two alloys of this series have shown a cooperative anomaly at 78K in β-$Mn_{0.88}Ru_{0.12}$, and a sharp anomaly at 133K in β-$Mn_{0.81}Ru_{0.19}$. In both cases these features occur at temperatures coinciding with susceptibility cusps, with the high temperature peaks in the μSR data, and with the approximate temperatures at which magnetic Bragg peaks appear. The specific heat results are in good agreement with those reported for Ru alloys in a previous study [2], and despite a lack of evidence elsewhere to suggest moment localization, offer some support to the conjecture that these systems approach an intermediate state towards the localized limit.

Inelastic neutron scattering from β-$Mn_{1-x}Ru_x$ samples has shown a magnetic response featuring a quasielastic component that narrows as the temperature is decreased, accompanied by an increase in elastic intensity. Systems with a high degree of magnetic frustration are expected to have a large density of low-frequency modes, associated with the degeneracies of the excitation spectra in the Brillouin zone [5]. It is not apparent how this spectral weight becomes distributed in the case of long-range antiferromagnetic order emerging from a frustrated ground state. The present observations suggest that a significant weight persists in the low-frequency excitation spectrum of antiferromagnetically ordered β-$Mn_{1-x}Ru_x$ alloys.

Both β-$Mn_{1-x}Co_x$ and β-$Mn_{1-x}Ru_x$ systems have given indication of possible Fermi liquid scaling over (in the case of Ru systems) a wide concentration range, via fitting of inelastic neutron data to the function

$$S(\ ,\omega) = \frac{N\hbar}{g^2\mu_B^2\pi}[1+n(\omega)]\chi''(\ ,\omega)$$

where the imaginary part of the dynamical susceptibility is given by the Bernhoeft function [6]. The spin relaxation rate distribution limits Γ_1 and Γ_2 are then found to exhibit the expected non-Fermi

liquid temperature dependences in β-$Mn_{1-x}Ru_x$, while the NFL parameter $D(\Gamma)/\Gamma_1\Gamma_2$ diverges towards the antiferromagnetic transition. The parameter Γ_1, corresponding to the lower limit of the relaxation rate distribution, is found to be independent of wavevector transfer $\boldsymbol{q}$, while in the high-frequency limit Γ_2 there is a strong $\boldsymbol{q}$-dependence.

However, while this observed behaviour is consistent with a spatially correlated NFL system, with an associated broad distribution of relaxation times (as reflected elsewhere in these studies, e.g. muon spin relaxation data), it cannot be conclusively stated that these samples constitute examples of non-Fermi liquids. The concept of spherical averaging over a polycrystalline sample was introduced in Chapter 7 as a possible source of misleading results in this case, where the system in question supports strong antiferromagnetic correlations [12]. This is expanded upon in Appendix C.

Studies of RMn_4Al_8 Systems

Evidence for a magnetic phase transition in the compound $LaMn_4Al_8$ has been obtained for the first time, as a result of muon spin relaxation studies. The low temperature, zero-field response has a stretched exponential form, with the depolarization rate λ^{β} rising to a peak at approximately 4.5K. This is accompanied by a drop in the relaxation exponent β and a smooth decrease in initial asymmetry. Initial indications are of a spin glass transition; however as for the β-$Mn_{1-x}Co_x$ systems the decrease in a_0 towards low temperatures is not sudden, and hence does not support a well-defined transition. In addition, the exponent β does not reach a final value of around 1/3 as may be expected, instead reaching ~ 0.5 at 10K (where λ^{β} begins to rise and a_0 begins to drop) then continuing to decrease at lower temperatures. A lack of oscillatory asymmetry is considered to be more likely due to the existence of short-range order than a cancellation of internal fields due to antiferromagnetic sublattices, as an oscillatory muon response has been observed in the isostructural $PrMn_4Al_8$.

The scenario of short range order is supported in $LaMn_4Al_8$ by a diffuse background observed in the magnetic scattering measured using neutron polarization analysis. Very weak Bragg peaks are seen to be superimposed upon this background at low temperature, which indicate the presence of a small component of 3-d long range order. Extra Bragg peaks with strong temperature dependence also emerge in conventional neutron powder diffraction patterns; however, these are not indexable on the $ThMn_{12}$-type tetragonal unit cell. While this may imply a complicated incommensurate magnetic structure that does not correspond to a simple scaling of the antiferromagnetic wavevector, it is

perhaps more likely that an impurity phase may be responsible for these low temperature magnetic reflections, since a number of extra peaks persist at room temperature. The existence of some form of static ground state is nonetheless obvious, with the transition observed in the μSR data echoed in a ZFC susceptibility peak at 8.5K (close to that previously reported [7]), and bifurcation of ZFC and FC data at around 7K.

The compounds with R = Y and Ce display no evidence of magnetically correlated spin fluctuations in the muon time window, with a motionally-narrowed response observed down to 1.2K. These findings are in keeping with the smaller susceptibilities measured in these systems as part of this work, as well as the comparatively low values of the Sommerfeld constant reported previously [8]. In contrast, $PrMn_4Al_8$ shows an oscillatory muon response below 35K, which can be fitted to the form of a Bessel function. Crystal field analysis facilitated by inelastic neutron measurements has shown this ordering to be due entirely to the manganese sublattice, since the Pr^{3+} ion is found to occupy a singlet ground state. The question remains as to why the Mn moment should be more stable in the praseodymium than the lanthanum system, with the latter possessing a more expanded sublattice due to the increased R atomic radius.

In heavy rare earth systems, muon spin relaxation assumes a dual response consisting of two distinct asymmetry components. These have been attributed to two different implantation sites, at which the muons couple to either slow rare-earth spin fluctuations or faster manganese fluctuations, being less able to follow the latter and giving rise to a slower relaxation. Coincidence of several features in the temperature dependence of the fitted relaxation parameters has provided the first evidence of coupling between the manganese and rare earth sublattices.

Inelastic neutron scattering studies have yielded direct evidence for spin gaps in the excitation spectra of YMn_4Al_8, $CeMn_4Al_8$ and $ScMn_4Al_8$, as initially suggested in earlier studies involving susceptibility and NMR measurements [e.g. 9,10]. The gapped magnetic response in these compounds bears a strong resemblance to that observed in $LaMn_4Al_8$, which comprises an inelastic, temperature-independent component and a narrower quasielastic feature. The quasielastic lineshape has a Lorentzian form, and is found to decrease smoothly with temperature, suggesting a critical narrowing of the spin fluctuation response as the system moves towards the static ground state. An estimated contribution to the wavevector-dependent static susceptibility appears to show a weak temperature dependence, which would fall in line with prior interpretations that a certain degree of localized character is inherent to this compound [e.g. 11].

The source of the spin gap is an issue that as yet remains unresolved. The consequences of hybridization effects in these systems, closely linked to aspects of gap behaviour mean that such mechanisms cannot be ignored as a possible source. The effect of a low dimensional sublattice cannot however be conclusively ruled out, despite the failure of these studies to reproduce the $(d_{Mn\text{-}Mn})^{-\Gamma}$ scaling of gap width reported previously [11].

Reduced dimensionality is nonetheless of unquestionable importance in these alloys: with the existence of strong magnetic correlations confirmed by these studies, coupled with a near-critical separation of the manganese atoms that place $LaMn_4Al_8$ on the brink of local moment stability, this continues to represent the likely mechanism for suppressing the formation of long range ordered states.

Suggestions for Further Work

As mentioned in Chapter 7, accurate temperature analysis of the quasielastic magnetic response observed in β-$Mn_{1-x}M_x$ systems has been precluded by the limited energy resolution available to date. High-resolution inelastic neutron scattering work in the low-frequency regime has therefore been planned (and very recently carried out, using the time-focussed cold neutron IN6 spectrometer at ILL). These experiments are anticipated to provide further insight into the non-Lorentzian lineshapes, originally attributed to a non-Fermi-liquid state, exhibited by the β-$Mn_{1-x}M_x$ alloys.

In addition, for the specific case of the β-$Mn_{1-x}Ru_x$ alloys it is necessary to establish the critical impurity concentration for stabilising antiferromagnetic order. This will be identified by the manufacture and experimental investigation of further samples representing small increments of x.

A great deal of further, more detailed analysis is possible for all samples investigated using experimental data already gathered, where time constraints have not allowed this to date. The complementarity of muon spin relaxation and neutron scattering techniques was discussed in Chapter 3: comparison of muon spin relaxation rates and neutron linewidths (when these are accurately evaluated) may highlight important scaling relationships. Very little quantitative analysis of polarized neutron data has as yet been carried out. Previous studies of the diffuse scattering associated with disordered ground states have yielded a detailed description of the crystallographic and magnetic character of β-$Mn_{1-x}Al_x$. This includes establishing the concentration dependence of the range of magnetic correlations, as well as concentration fluctuations of solute atoms. It would be desirable to replicate these analyses in the β-$Mn_{1-x}M_x$ systems.

Concerning the RMn_4Al_8 compounds, the effect of Mn-Mn separation on the spin gap should be investigated further with a range of samples covering a broad range of atomic R radius. This is already underway in the form of inelastic neutron studies of $LuMn_4Al_8$. These studies, together with additional experiments performed on YMn_4Al_8 and $ScMn_4Al_8$ have shed some light on the wavevector-dependence of the pseudogap: measurements at incident energies of 68meV and 155meV in these three samples using the IN4 spectrometer have identified clear coherent lattice oscillations below $3Å^{-1}$.

In both types of intermetallic system, the value of single crystal studies is recognized if this research is to be furthered in a meaningful fashion. For the RMn_4Al_8, this will primarily help to establish whether observed behaviour is truly due to low dimensionality. In cases where the nature of the low temperature exchange coupling is in doubt (as has been suggested for $TbMn_4Al_8$), acquisition of single crystal samples would allow independent measurements of susceptibilities parallel and perpendicular to the crystal c-axis.

In β-$Mn_{1-x}M_x$ systems, the simpler form of the associated diffraction patterns should greatly assist in a confirmation of the magnetic structure. Very recent experiments[1] on single crystals of β-$Mn_{1-x}Ru_x$ performed using the D7 instrument at the ILL have enabled mapping of the magnetic diffuse scattering within the Brillouin zones.

[1] Experiments performed by B. D. Rainford, J. R. Stewart and A. Linne

References

[1] J. R. Stewart, *Moment Localisation in β-$Mn_{1-x}Al_x$* (PhD Thesis), Chapter 4

[2] K. Sasao, R.Y. Umetsu and K. Fukamichi, J. Alloys. Comp. **325** (2001) 24

[3] J.R. Stewart and R. Cywinski, Phys. Rev. B **59** (1999) 4305

[4] M. O'Keefe and S. Andersson, Acta Cryst. **A33** (1977) 914

[5] B. Canals and C. Lacroix, Phys. Rev. B **61** (2000) 11251

[6] N. Bernhoeft, J. Phys. Cond. Mat. **13** (2001) R771

[7] T. Yamasaki, K. Matsui, H. Nakamura and M. Shiga, Solid State Comm. **119** (2001) 415

[8] I. H. Hagmusa, J. C. P. Klaasse, E. Brück, F. R. de Boer, K. H. J. Buschow, J. Alloys Comp. **297** (2000) 21

[9] H. Nakamura, S. Giri and T. Kohara, J. Phys. Soc. Japan **73** (2004) 2971

[10] Y. Muro, H. Nakamura and T. Kohara, J. Phys. Cond. Matt. **18** (2006) 3931

[11] Y. Muro, H. Nakamura and T. Kohara, J. Phys. Cond. Matt. **18** (2006) 3931

[12] B. D. Rainford, *private communication*

Appendix A

Corrections to Neutron Time-of-Flight Spectra

Attenuation

For slab geometry (applicable for all measurements reported in this thesis), the neutron attenuation on passing a distance *dx* through the sample of thickness *t* may be given by

$$d\phi = -\phi\mu dx$$
$$\rightarrow \int_{\phi_0}^{\phi} \frac{d\phi}{\phi} = -\mu \int_0^t dx = -\mu t$$
$$\rightarrow \phi = \phi_0 e^{-\mu t}$$

where μ is an attention coefficient.

The scattering from an elementary layer of thickness *dx*, located at a depth *x* into a slab sample will be subject to an attenuation along the path l_1 shown in the diagram:

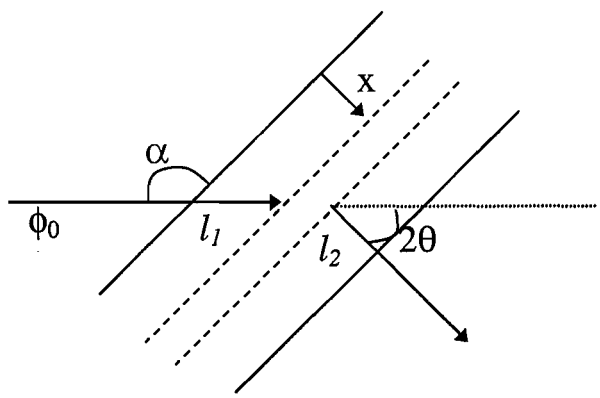

where

$$dl_1 = \frac{dx}{\sin\alpha}$$

The attenuation is given by $\phi = \phi_0 e^{-\mu_1 l_1}$ where $\mu_1 = N(\sigma_{incoherent} + \sigma_{absorption})$, the absorption cross-section corresponding to the elastic energy.

The outgoing beam is subject to absorption only, with the attenuation given by $\phi = \phi_0 e^{-\mu_2 l_2}$ and $\mu_2 = N\sigma_{absorption}(inelastic)$. The path length l_2 corresponds to $(t-x)/\sin(\alpha - 2\theta)$.

For a flux incident ϕ upon a slab of thickness *t*, the scattered neutron flux into solid angle $\Delta\Omega$ is

$$N(\Delta\Omega) = \phi n\left(\frac{d\sigma}{d\Omega}\right)t\Delta\Omega$$

where *n* is the number density of scattering centres and the cross-section given is per scattering centre. It then follows that for an element of depth *x* and thickness *dx*, the neutron flux into solid angle $\Delta\Omega$ at an angle 2θ from the slab is

$$dN_s(\Delta\Omega, x) = \phi_0 \exp\left[-\frac{\mu_1 x}{\sin\alpha}\right] n\left(\frac{d\sigma}{d\Omega}\right) dx \cos ec\alpha \exp\left[-\frac{\mu_2(t-x)}{\sin(\alpha - 2\theta)}\right]\Delta\Omega \text{ cosec}$$

The total scattering into this solid angle is obtained by performing an integration over the sample thickness, leading to the following expression

$$N_s(\Delta\Omega) = \phi_0 n\left(\frac{d\sigma}{d\Omega}\right)\frac{\Delta\Omega}{\sin\alpha}\frac{1}{\mu_{eff}}\left\{\exp\left[-\frac{\mu_2 t}{\sin(\alpha - 2\theta)}\right] - \exp\left[-\frac{\mu_1 t}{\sin\alpha}\right]\right\}$$

where

$$\mu_{eff} = \frac{\mu_1}{\sin\alpha} - \frac{\mu_2}{\sin(\alpha - 2\theta)}$$

In the limit of $\mu_1 = \mu_2 \rightarrow 0$, the term in parentheses reduces to $\mu_{eff}t$: hence an attenuation or *self-shielding factor* may be defined for a sample of thickness t_s

$$A_s = \frac{1}{\mu_{eff} t_s}\left\{\exp\left[-\frac{\mu_2 t_s}{\sin(\alpha - 2\theta)}\right] - \exp\left[-\frac{\mu_1 t_s}{\sin\alpha}\right]\right\}$$

The corrected counts are then obtained simply by dividing $N_s(\Delta\Omega)$ by A_s.

Vanadium normalization

The counts into $\Delta\Omega$ corresponding to the elastic peak in the vanadium spectrum, i.e.

$$N_V(\Delta\Omega) = \phi_0 A_V(\Delta\Omega) n_V \left(\frac{d\sigma}{d\Omega}\right)_V \frac{\Delta\Omega}{\sin\alpha} t_V$$

are corrected for attenuation, then used to normalize the corrected sample counts

$$\frac{C_s(\Delta\Omega\Delta\tau)}{C_V(\Delta\Omega)} = \frac{n_s\left(\frac{d^2\sigma}{d\Omega d\tau}\right)_s \Delta\pi_s}{n_V\left(\frac{d\sigma}{d\Omega}\right)_V t_V}$$

where $\Delta\tau$ is the time channel width associated with the time-of-flight inelastic cross-section.

The absolute cross-section is then

$$\left(\frac{d^2\sigma}{d\Omega d\tau}\right)_s = \frac{n_V t_V}{n_s t_s}\left(\frac{d\sigma}{d\Omega}\right)_V \frac{1}{\Delta\tau}\frac{C_s(\Delta\Omega\Delta\tau)}{C_V(\Delta\Omega)}$$

where $\left(\frac{d\sigma}{d\Omega}\right)_V = \frac{5.08}{4\pi}$ barns/steradian.

This may be converted to a form given in terms of scattering function:

$$\frac{d^2\sigma}{d\Omega dE} = \frac{k_f}{k_i} S(\ \ , \omega) = \frac{\tau_f^{\ 3}}{m} \frac{d^2\sigma}{d\Omega d\tau}$$

Appendix B

Calculations of Crystal Field States of Pr^{3+} in $PrMn_4Al_8$

The trivalent praseodymium ion has $J = 4$, which for a free ion corresponds to a 9-fold degeneracy of m_J states. This degeneracy will be lifted in the presence of a crystal field of the form:

$$V = \sum_{l,m} B_l^m O_l^m$$

where O represent the crystal field parameters and B are the Stevens operators, both of which are functions of m_J and orbital angular momentum l. The Stevens operators transform in an analogous fashion to spherical harmonics to give a polar coordinate form dependent on J. An example is the operator O_2^0, which transforms as $3J^2 - J(J+1)$. These operate on the m_J states of the Pr^{3+} ion to give the new eigenstates produced by mixing due to the crystal field. The coupling of these states is represented by

$$\langle m_J | J_z | m_J \rangle$$

where the m_J form the elements of a 9 x 9 matrix, and the J_z operator components are obtained from

$$V = \sum_{l,m} B_l^m O_l^m = B_0^0 O_0^0 + B_0^1 O_0^1 + B_0^2 O_0^2 + B_0^3 O_0^3 ..... + B_1^0 O_1^0 .....$$

in which all odd terms are zero for this crystal field symmetry.

The result is that only the diagonal and two off-diagonal matrix elements are non-zero.

	$\|4\rangle$	$\|3\rangle$	$\|2\rangle$	$\|1\rangle$	$\|0\rangle$	$\|-1\rangle$	$\|-2\rangle$	$\|-3\rangle$	$\|-4\rangle$
$\|4\rangle$	A	0	0	0	α	0	0	0	0
$\|3\rangle$	0	B	0	0	0	β	0	0	0
$\|2\rangle$	0	0	C	0	0	0	γ	0	0
$\|1\rangle$	0	0	0	D	0	0	0	β	0
$\|0\rangle$	α	0	0	0	E	0	0	0	α
$\|-1\rangle$	0	β	0	0	0	D	0	0	0
$\|-2\rangle$	0	0	γ	0	0	0	C	0	0
$\|-3\rangle$	0	0	0	β	0	0	0	B	0
$\|-4\rangle$	0	0	0	0	α	0	0	0	A

The new eigenvalues attained by coupling of certain m_J states are then obtained by solving

$$M\varphi = \lambda\varphi$$

for the set of smaller matrices:

	$\|4\rangle$	$\|0\rangle$	$\|-4\rangle$
$\|4\rangle$	A	α	0
$\|0\rangle$	α	E	α
$\|-4\rangle$	0	α	A

	$\|3\rangle$	$\|-1\rangle$
$\|3\rangle$	B	β
$\|-1\rangle$	β	D

	$\|2\rangle$	$\|-2\rangle$
$\|2\rangle$	C	γ
$\|-2\rangle$	γ	C

	$\|1\rangle$	$\|-3\rangle$
$\|1\rangle$	D	β
$\|-3\rangle$	β	B

For the first matrix, three solutions are obtained, corresponding to

$$\lambda_1 = A$$

$$\lambda_{2,3} = \frac{A + E \pm \sqrt{(A+E)^2 + 4(AE + 2\alpha^2)}}{2}$$

The 2x2 matrices yield four more eigenvalues:

$$\lambda_{4,5} = \frac{(D+B) \pm \sqrt{(B-D)^2 + 4\beta^2}}{2}$$

$$\lambda_{6,7} = C \pm \gamma$$

The eigenfunctions of these 7 new crystal field states may then be obtained. Taking the first of the 2x2 matrices above as an example, it can be seen that the new functions will be a mixture of $|3\rangle$ and $|-1\rangle$ states:

$$\varphi_+ = a|3\rangle + b|-1\rangle = \cos\theta|3\rangle + \sin\theta|-1\rangle$$
$$\varphi_- = a|-1\rangle - b|3\rangle = \cos\theta|-1\rangle - \sin\theta|3\rangle$$

where the coefficients are given as *sin* and *cos* functions to ensure orthogonal solutions:

$$\langle\varphi_+|\varphi_+\rangle = \langle\varphi_-|\varphi_-\rangle = 1$$
$$\langle\varphi_+|\varphi_-\rangle = 0$$

In this case

$$\cos\theta = \frac{1}{\sqrt{2R\left(R \pm \sqrt{R^2-1}\right)}} \quad \text{and} \quad \sin\theta = \frac{R \pm \sqrt{R^2-1}}{\sqrt{2R\left(R \pm \sqrt{R^2-1}\right)}}$$

where

$$R = \frac{D-B}{2\beta}$$

The resulting set of basis states may be represented by:

$|2^s\rangle \,\&\, |2^a\rangle$ → two singlet states where *s* and *a* denote symmetric and antisymmetric wavefunctions arising from a linear combination of degenerate states

$\alpha|\pm 3\rangle \pm |\mp 1\rangle$ → two doublet states

$|4^a\rangle$ → singlet state

$\alpha|4^s\rangle + \beta|0\rangle$
$\alpha|0\rangle - \beta|4^s\rangle$ → two singlet states

Appendix C

Spherical Averaging Cross Section for Strong Antiferromagnetic Correlations

In the β-$Mn_{1-x}M_x$ alloys discussed in this thesis, diffuse scattering measurements show the presence of strong antiferromagnetic correlations, leading to relatively sharp diffuse peaks in $S(\boldsymbol{q})$ in the low temperature spin-glass state. In the case of β$Mn_{1-x}Ru_x$ alloys a transition to long range antiferromagnetism occurs for alloys with Ru concentrations above 12%, with well defined Bragg peaks. As the Néel temperature is approached from higher temperatures, the spin dynamics will reflect the proximity of the AF critical point; one would expect to observe an increase in the correlation length ξ (the inverse correlation length $\kappa \rightarrow 0$ as $T \rightarrow T_N$) and a critical slowing down of the dynamics. However these experiments have been made on polycrystalline samples, so to be able to compare with experiment it is necessary to perform a spherical average of the magnetic cross section.

The geometry is shown in the figure on the following page. Here the scattering triangle is represented superimposed on the magnetic Brillouin zone centred on the reciprocal lattice vector $\boldsymbol{G}$. The BZ is represented approximately as a sphere of radius q_m. $\boldsymbol{Q}$ represents the scattering vector and the spherical average consists of integrating over all values of $\boldsymbol{Q}$ that lie in this BZ, keeping $|\boldsymbol{Q}|$ constant.

Now the form of the line shape in the cross section can be taken to be Lorentzian:

$$\frac{1}{\omega}\operatorname{Im}\chi(q,\omega) = \frac{\chi(q)\Gamma(q)}{\Gamma(q)^2 + \omega^2}.$$

Within Moriya's SCR theory the linewidth is expected to have the form:

$$\Gamma(q) = \Gamma_0\left(q^2 + \kappa^2\right)$$

in the case of systems close to an AF critical point. Also the susceptibility has the form

$$\chi(q) = \frac{\chi_0 \kappa^2}{q^2 + \kappa^2}.$$

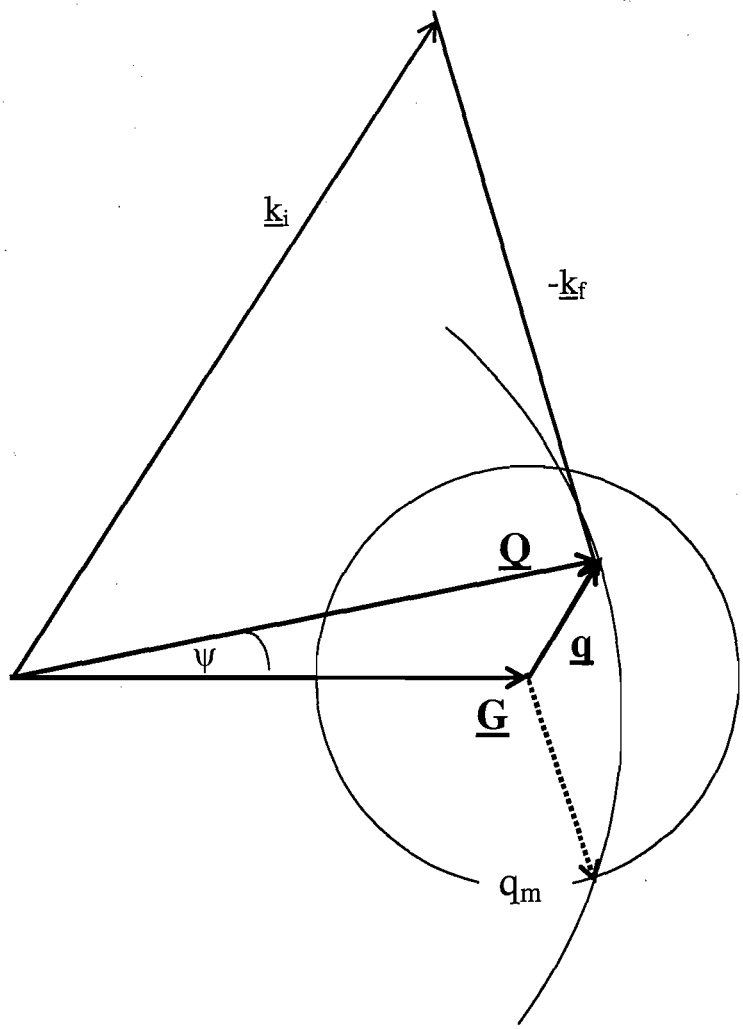

It follows that the product $\chi(\boldsymbol{q})\Gamma(\boldsymbol{q})$ is independent of q:

$$\chi(q)\Gamma(q) = \chi_0 \kappa^2 \Gamma_0.$$

The spherical average now becomes:

$$\left\langle \frac{1}{\omega}\mathrm{Im}\,\chi(q,\omega)\right\rangle = \frac{\chi_0\kappa^2\Gamma_0\int_0^{\psi_m} 2\pi Q^2\sin\psi\left[\Gamma(q)^2+\omega^2\right]^{-1}d\psi}{\int_0^{\psi_m}2\pi Q^2\sin\psi\, d\psi}$$

$$= \frac{\chi_0\kappa^2\Gamma_0}{1-\cos\psi_m}\int_0^{\psi_m}\frac{\sin\psi\, d\psi}{\left[\Gamma(q)^2+\omega^2\right]} = \frac{\chi_0\kappa^2}{(1-\cos\psi_m)\Gamma_0}\int_0^{\psi_m}\frac{\sin\psi\, d\psi}{\left[(q^2+\kappa^2)^2+(\omega/\Gamma_0)^2\right]}$$

From the figure above it may be seen that;

$$q^2 = Q^2+G^2-2QG\cos\psi\,.$$

Also

$$q_m{}^2 = Q^2+G^2-2QG\cos\psi_m, \quad so\ that$$

$$\cos\psi_m = \frac{Q^2+G^2-q_m{}^2}{2QG}$$

It follows that

$$\left\langle \frac{1}{\omega}\mathrm{Im}\,\chi(q,\omega)\right\rangle = \frac{2QG\chi_0\kappa^2}{\Gamma_0\left[q_m^2-(Q-G)^2\right]}\int_0^{\psi_m}\frac{\sin\psi\, d\psi}{\left[(Q^2+G^2-2GQ\cos\psi+\kappa^2)^2+(\omega/\Gamma_0)^2\right]}$$

$$= A\int_0^{\psi_m}\frac{\sin\psi\, d\psi}{\left(a-b\cos\psi\right)^2+c^2} \quad where$$

$$a = Q^2+G^2+\kappa^2; \qquad b = 2GQ \quad and \quad c = \omega/\Gamma_0$$

Making the substitution:

$$c\tan\phi = a - b\cos\psi \quad then \quad c\sec^2\phi d\phi = b\sin\psi d\psi$$

the integral becomes:

$$\left\langle \frac{1}{\omega}\mathrm{Im}\,\chi(q,\omega)\right\rangle = A\int_0^{\theta_m}\frac{\sin\psi d\psi}{\left(a-b\cos\psi\right)^2+c^2} = A\int_{\phi_1}^{\phi_2}\frac{(c/b)\sec^2\phi d\phi}{c^2\left(1+\tan^2\phi\right)} = \frac{A}{bc}\left[\phi_2-\phi_1\right]$$

$$where \quad \phi_2 = \tan^{-1}\left[\left(a-b\cos\psi_m\right)/c\right] = \tan^{-1}\left[\Gamma_0\left(q_m^2+\kappa^2\right)/\omega\right]$$

$$and \quad \phi_1 = \tan^{-1}\left[\left(a-b\right)/c\right] = \tan^{-1}\left[\Gamma_0\left((G-Q)^2+\kappa^2\right)/\omega\right]$$

The result can be written in terms of the complements of the angles φ_1, φ_2, since

$$\tan^{-1}(p/q)-\tan^{-1}(r/s) = -\tan^{-1}(q/p)+\tan^{-1}(s/r).$$

Finally the contribution to the scattering arising from this particular Brillouin zone is determined:

$$\left\langle \frac{1}{\omega}\mathrm{Im}\,\chi(q,\omega)\right\rangle = \frac{\chi_0\kappa^2}{\left[q_m^2-(Q-G)^2\right]}\frac{1}{\omega}\left[\tan^{-1}\left(\frac{\omega}{\Gamma_1}\right)-\tan^{-1}\left(\frac{\omega}{\Gamma_2}\right)\right]$$

$$where \quad \Gamma_1 = \Gamma_0\left[\left(Q-G\right)^2+\kappa^2\right] \quad and \quad \Gamma_2 = \Gamma_0\left[q_m^2+\kappa^2\right]$$

$$\therefore\left\langle \frac{1}{\omega}\mathrm{Im}\,\chi(q,\omega)\right\rangle = \frac{\chi_0\kappa^2\Gamma_0}{\Gamma_2-\Gamma_1}\frac{1}{\omega}\left[\tan^{-1}\left(\frac{\omega}{\Gamma_1}\right)-\tan^{-1}\left(\frac{\omega}{\Gamma_2}\right)\right]$$

It can be seen that the spherically-averaged lineshape has a form identical to the Bernhoeft function.

The presence of non-Lorentzian lineshapes therefore does not *necessarily* imply non-Fermi liquid behaviour, but arises naturally in polycrystalline samples as a consequence of spherical averaging of the cross section.

The figure below shows a simulation of the lineshape as a function of *q/G*.

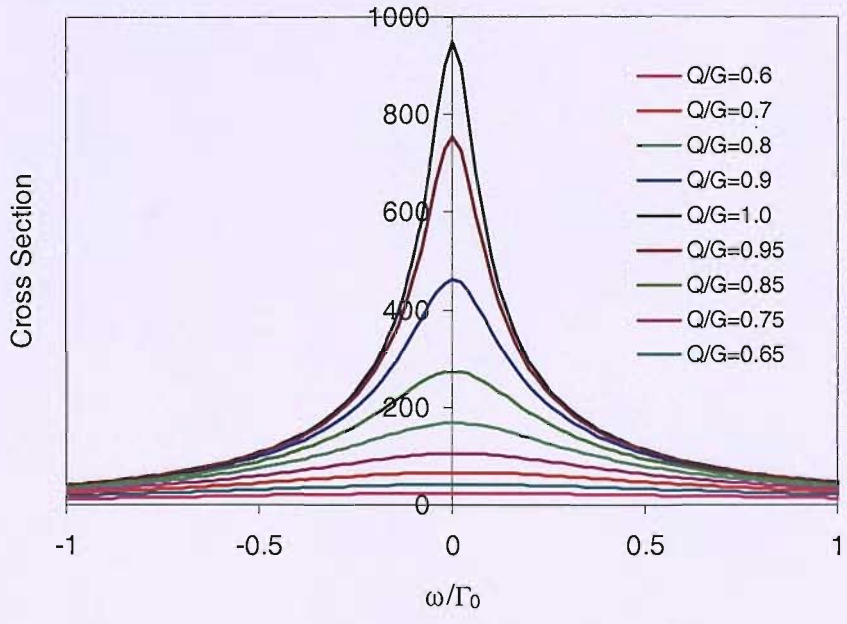

From private communication with B. D. Rainford.
Lineshape simulations as a function of q/G performed by B. D. Rainford.